Relationship between Micro and Macro Mechanical Properties of Cemented Artificial Conglomerate

by

Yuan Li

A thesis submitted in partial fulfillment of the requirements for the degree of

Doctor of Philosophy

in

GEOTECHNICAL ENGINEERING

Department of Civil and Environmental Engineering
University of Alberta

Abstract

Micromechanics modeling is becoming more popular in geotechnical analysis. It allows engineers to understand the deformation and failure processes at the microscopic level. Due to the advancement of computer capacities and numerical methods for micromechanics analysis, engineers are able to perform micromechanics analysis on more practical problems. In order to perform these analysis, it is necessary to determine the micro mechanical parameters of the material. This research is focused on the theoretical and experimental development to determine the micro mechanical parameters of cemented granular material.

In the theoretical analysis, the micro mechanical properties of geomaterials consist of several components. The contribution of each of these components to the overall macro behavior is dependent on the characteristics of each component. The strength of a cemented granular material consists of frictional strength between the grains, the bonding strength between the grains and the cement, and the bonding strength of the cement. It is assumed that the voids in a cemented granular material are occupied by cement, and the overall strength of the material can be calculated from the strength of each individual component. In this study, the theoretical relationship that relates the strength of each component to the overall macro mechanical strength of the cemented granular material has been developed.

Experiments were conducted to measure the micro and macro mechanical parameters in the theoretical relationship for cemented granular material. Artificial conglomerate made up of steel balls and Portland cement was used to minimize the variation of grains and cementation properties in natural materials, and the possibility of crushing of grains under high stress. Direct shear, uniaxial/triaxial and Brazilian tensile tests were conducted to study the mechanical behavior and

measure the macro parameters of artificial conglomerates. Microscopy analysis, 3D scanning and post-failure analysis were carried out to obtain the micro properties. In addition, an innovation approach was developed to measure the inter-particle friction angle of steel balls.

Numerical simulation was performed to study the micro mechanical behavior of cemented granular material and it was further used to examine the theoretical relationship that relates the micro and macro mechanical parameters. Using calibrated micro properties, the numerical results show good agreement between theoretical calculations and laboratory measurements under different normal stresses. However, different micro parameters are required for modelling tests with samples of different particle sizes. This is due to the size dependent progressive failure mechanism in the micro model.

Using measured micro properties as inputs, the calculated cohesions from the theoretical relationship are about 0.84 to 1.05 times of the measured values from direct shear tests. The calculated peak friction angles are about 10% to 15% higher than the measured values from direct shear tests. Since it is practically impossible to arrange particles in the experiment that is assumed in the theoretical relationship, this could be the reason that accounts for the differences between the calculated and measured values.

The calculated cohesion and friction agree with the measured values in the laboratory, which supports the existence of a relationship between the micro and macro mechanical properties. The macro parameters of cemented granular material can be calculated with measured micro properties using the derived theoretical relationship. In addition, this study also provides the laboratory procedures to measure the macro and micro properties of cemented granular material.

Acknowledgements

I would like to express my sincere gratitude and appreciation to my supervisor, Dr. Dave Chan. He not only devotes a tremendous amount of time to guide me in tackling the challenges in my research, but also provides much insights into critical thinking and how to become a good researcher. The work would not have been accomplished to this extent without his generous support.

I am very grateful to my co-supervisor, Dr. Alireza Nouri, for his technical guidance, valuable advices and kind encouragement during the course of my research work. He is always willing to share his knowledge and wisdom.

I wish to thank the other committee members: Dr. Lijun Deng, Dr. Alireza Bayat and Dr. Peijun Guo for reading this thesis and offering constructive comments. Your comments and advices on the thesis are much appreciated.

I also like to thank Christine Hereygers, Todd Kinnee, Tianran Ma, and Xin Xu for their assistance with the laboratory tests. My appreciation is also extended to my other friends and fellow graduate students for their help and company.

I am deeply indebted to my parents and my sister, for their endless love and support, and for encouraging me to pursue and complete this research.

Finally, I would like to thank my husband, Ying Zhang, without his consistent love, encouragement, understanding, and assistance throughout this long journey, the completion of this research work would not have been possible. I also want to thank my dear little daughter, Ellie Zhang, to bring so much joy and happiness into my life. I cherish every moment I spend with them.

Table of Contents

List of Figures

List of Tables

Chapter 1: Introduction

1.1 Background

1.1.1 Introduction to cemented granular material

Cemented granular material consists of a particle skeleton with cementing agent that bonds the particles together. A few examples of this class of materials are sedimentary rocks (e.g., sandstone, conglomerate and breccia) as well as artificial cemented sands (Delenne et al. 2009, Das et al. 2013). While cemented granular material is treated as a continuum at the macro scale, it is considered as an assembly of individual particles interacting with each other and with the cementing agent at the micro scale.

Researchers found that the macro mechanical behavior of cemented granular material is closely related to the behavior of individual particles. For instance, the bond between particles tends to break at low confining pressure and leads to strain softening of the cemented granular material. On the other hand, particle crushing occurs at high confining pressure and results in strain hardening. Particle crushing, cement degradation and fragment rearrangement are the key mechanical degradation processes at the micro scale (Menendez et al. 1996).

Extensive research has been conducted to study the mechanical behavior of cemented granular material at the micro scale, including studies on the effect of grain crushing, grain deformation, inter-particle contact force, fabric anisotropy, cementation, and inter-particle friction (Einav 2007, Christoffersen et al. 1981, Matsuoka 1974, Oda and konishi 1974, Nova et al. 2003, Oda 1974, Tobita and Oda 1999). However, much of the research is not physically verified, due to difficulties in the micro properties measurement. In addition, the relationship between micro and macro mechanical properties for the cemented granular material is still largely unknown, such as the relationship between micro bonding strength and macro mechanical properties.

This research is aimed to study the micro and macro mechanical properties of cemented granular material, and to improve the understanding of many practical problems, such as sand production in the petroleum industry. Sand production is the migration of sand from the sandstone due to the flow of oil in sandstone reservoir. It is an important concern since the produced sand can erode

vital components in the well system, plug the wellbore, and present significant disposal difficulties. On the other hand, sand production can boost oil productivity due to loosing of the rock. Knowing the relationship between the micro and macro mechanical properties can be very helpful in sand production management.

1.1.2 Mechanism of degradation process

Despite the small volume fraction that cementing agent usually occupies in cemented granular material, the presence of cement substantially changes the mechanical response of the granular particle assembly. Particles will detach from cemented granular material when the bonding between particles and cementing agent breaks. Cementing agent is formed during the diagenetic process, which involves precipitation, dissolution, recrystallization, and pressure solution. Thus, bonds could be generated in different ways depending on the precipitating minerals, the depositional environment, stresses and temperature, resulting in different bond properties.

Nespereira et al. (2010) conducted uniaxial compression tests and thin sections analysis on Palaeocene sandstone and found that the bonding strength differs for different types of cementing agents. Palaeocene sandstone has mainly opal cementing agent, and it is considered as strong to very strong rock according to the uniaxial compression strength (UCS) distribution. For those with low UCS, it is due to the presence of more clayey cementation. Bernabe et al. (1992) studied the effect of cementing material on the strength of granular rock by performing triaxial tests on two types of synthetic granular material. One was made of Ottawa sand and halite cement, and the other one was composed of Ottawa sand and silica glass cement. Despite similar initial porosity (32% and 31.5%, respectively) of these two materials under same confining pressure (3.4 MPa), the silica-cemented samples had a much higher strength than those cemented by halite. In addition, the elastic bulk modulus for the silica-cemented material increased with the amount of cementing material, whereas this parameter was nearly identical for the halite-cemented samples.

Bell (1978) carried out petrographic examination on Fell sandstone (81% silicate cementing material) and revealed that its porosity increased with the amount of cement. However, the shear strength of the material deceased significantly with an increase in cement content, which could be explained by the increase in voids. Also, no evident relationship was found between cement content and elastic parameters. However, Dyke and Dobereiner (1991) stated that cementing agent

could considerably enhances the strength and stiffness of sandstone if the bonding material is silica. On the other hand, no evident trend exists between the amount of cementing material and the strength and deformability when the cementing agent is weak clay or carbonate. Clay matrix content (in the range of 3 to 35% of total solids) in sandstone also affects neither strength nor deformability (Dobereiner 1984). Regardless of these conflicting findings, the bond with silicate cementing agent is the strongest, followed by those with carbonate and ferrous cementing materials, and the bond with clayed cementing agent is the weakest.

Besides the type and amount of cementing material, the detachment of particles is also affected by several other factors including the type of grain-to-grain contact, ground/reservoir temperature, capillary force, seepage force, cyclic loading, and geostatic stress and strain field.

Dobereiner and Freitas (1986) postulated that the strength of weak sandstone increases with the grain contact ratio, which is defined as the ratio of contact length with neighboring grains to the total perimeter of grain particle in 2D view. When the grain contact ratio was higher than 55%, quartz over-growth was observed in the cementing agent, and the sandstone behaved like a hard rock. Dyke and Dobereiner (1991) proposed that the grain contact ratio related more to strength than the cementing material content. Both deformability and strength increase with the grain contact ratio. Jeng et al. (2004) stated that the grain area ratio, which represents the percentage of grain within rock, is a key parameter in determining the UCS of sandstone. An empirical equation of UCS in terms of grain area ratio and porosity was proposed.

Essam and Wally (2007) stated that the change in reservoir temperature usually leads to chemical reactions, and therefore affects the bonding strength between sand particles. For example, quartz hydrolysis is believed to reduce surface energy and cohesion. Its occurrence highly depends on temperature. In addition, carbonate cement becomes less soluble at higher temperature in deep formations, while silicate cement becomes more soluble. Both processes can directly affect the detachment of sand particles (Pettijohn et al. 1987).

Han and Dusseault (2002) and Essam and Wally (2007) investigated the influence of capillary force and seepage force on the bonding strength. Capillary pressure refers to the pressure difference across the free surface formed between two fluids. As one of the cohesive forces among sand particles, capillary force can contribute to the strength of sandstone. However, this force does

not always exist and could dissipate at some critical water saturation. Adversely, fluid gradient due to water flowing results in a seepage force that pushes the particle in the direction of fluid flow. It is one of major forces mobilizing sand particles. Calculations showed that the seepage force is always lower than the capillary force.

Ray et al. (1999) investigated the effect of cyclic loading and strain rate on the mechanical behavior of Chunar sandstone. Two types of tests were performed using a MTS closed loop servo-controlled stiff testing machine. The first type of test was increasing the applied stress on the samples with fixed number of cycles. The increase in applied stress results in decrease in UCS. The second type of test was increasing the number of cycles applied with fixed stress level. The increase in the loading cycles results in the decrease in UCS (9.4~34.5%). It is worth mentioning that cyclic loading can lead to strain hardening and higher strength when the applied stress does not cause failure after many cycles, although cyclic loading usually causes failure at a lower stress level than monotonic loading (Singh 1989).

1.2 Problem statement

Micromechanics modeling becomes more popular in geotechnical analysis. It allows us to understand the deformation and failure processes at the microscopic level. Currently, micromechanics analysis is widely used by geotechnical engineers due to the advancement of computer capacities and numerical methods. Thus, the micro mechanical parameters of the material are necessary to be determined for the micromechanics analysis. However, the measurement of micro properties is challenging and not commercially available, while the macro properties can be measured in most laboratories. Therefore, it would be very helpful and practical to relate the micro mechanical properties to macro parameters which could be readily determined.

Bonding strength consists of normal bonding strength and shear bonding strength, which are the primary parameters in determining rock strength (Tronvoll et al. 1997). Presently, shear bonding strength is usually assumed to be the same as the cohesion, and the normal bonding strength equals to the Brazilian tensile strength or direct tensile strength (Akram and Sharrock 2010, Tronvoll et al. 1997, Ding and Zhang 2014). However, Muhuri et al. (2004) stated that cohesion reflects the strength of the bonding between rock particles, and cohesion is therefore the combined magnitude of shear and normal bonding strength. Moreover, the normal and shear bonding strength are

generally set to be equal in most Discrete Element Modeling (Hsieh et al. 2008, Holt et al. 2003, Marketos and Bolton 2007). After all, no agreement on the micro-macro strength relationship has been made and further work should be carried out.

No model is found that can predict the critical condition of debonding of cemented granular material at the micro scale with macro mechanical behavior. However, there is some work on microstructural model, the research approach of which can be used for reference. In this research, a new theoretical relationship is developed to relate the micro mechanical properties of cemented granular material to the macro parameters which could be determined in the laboratory.

1.3 Research objectives and scope

The primary objectives of this research are to understand the mechanism of bond degradation in cemented granular material, such as sandstone, and to develop the theoretical relationship that can capture the critical condition of debonding of cemented granular material with conventional macro mechanical properties. Some specific objectives are to:

- Investigate the mechanisms of bonding and debonding between particles in cemented granular material, and understand the influence of cementation and other external factors on bonding;
- Formulate a new theoretical relationship to relate the micro mechanical properties of cemented granular material to macro parameters that could be readily determined using standard laboratory tests;
- Verify the developed theoretical relationship using laboratory results;
- Test the accuracy of proposed theoretical relationship with numerical simulation results.

To achieve the foregoing research objectives, the following work is performed:

- Understand the geotechnical properties and behavior of sandstone, which is a typical example of cemented granular material. Understand the mechanism of cementation and the role cementing agent plays in sandstone degradation;
- Calculate the normal and shear bonding strength using published data and a simplified physical model. Examine the existing correlations between micro bonding strength and macro parameters;

- Derive the theoretical relationship between the micro and macro mechanical properties;
- Prepare artificial samples, and measure the micro bonding strength and macro properties via laboratory tests;
- Verify the theoretical relationship with experiment results;
- Investigate whether the derived theoretical relationship can provide micro mechanical properties those can capture the macro behavior of cemented granular material with numerical simulation.

1.4 Outline of the thesis

The thesis is organized into seven chapters. A brief outline of the chapters is provided below.

Chapter 2 presents the literature review on sand, sandstone and diagenesis process, which helps to understand the mechanism of bonding and debonding of cemented granular material. Furthermore, the research conducted on the micro-macro relationships of granular material, the experiments conducted on artificial cemented granular samples, and the numerical investigation of cemented granular material are extensively reviewed to assist the current study.

Chapter 3 discusses the assessment of the normal and shear bonding strength using published data and a simple physical model. Then, with a simplified 2D model with rigid and uniform rods, two extreme packing conditions are analyzed separately. The theoretical relationship between the micro and macro mechanical properties is developed for the cemented granular material.

Chapters 4 and 5 describe the sample preparation procedure and all the experiments conducted in this study. With the prepared artificial conglomerate and cement paste samples, a series of laboratory tests are carried out to study the mechanical behavior of cemented granular material and collect all the measurements involved in the theoretical relationship. The macro parameters of the material are obtained with the conventional experiments, including direct shear testing, uniaxial/triaxial compression testing and Brazilian tensile testing. Innovative experiments and post-failure analysis on the failed samples are conducted to determine the micro parameters involved in the theoretical derivation.

Chapter 6 focuses on the verification of the theoretical relationship between the micro and macro mechanical properties of cemented granular material with the experiment results.

Chapter 7 presents the investigation of micro mechanical behavior of cemented granular material and the accuracy of proposed theoretical relationship with PFC^{2D}. Firstly, shearing of two different simple assemblies of particles are conducted to study the progressive failure mechanism. Then, with the trends learnt from parametric sensitivity study on the direct shear behavior, the numerical conglomerates similar to those prepared in the laboratory are generated and the micro parameters for different groups of numerical samples are calibrated. The numerical and laboratory results of direct shear tests are compared and discussed.

Chapter 8 summarizes major conclusions of this study and proposes some recommendations for the future work.

In addition, three appendixes have been attached at the end of the thesis. Appendix A provides an overview of sand and sandstone, including the definition, formation, classification, and mechanical behavior. Appendix B elaborates the calculation procedure of micro bonding strength using the published data. Moreover, the calculated normal and shear bonding strength is also compared with the corresponding commonly accepted macro parameters. Appendix C presents a brief introduction to the PFC^{2D} particle-flow model, which is used for the numerical simulation in this study.

Chapter 2: Literature Review

2.1 Introduction

One of the main objectives of this research is to develop the theoretical relationship that relates the micro and macro mechanical properties of cemented granular material. It is a prerequisite to understand the mechanisms of bonding and debonding in cemented granular material. Sandstone is chosen for the literate review as an example of cemented granular material in this chapter. To systematically understand the physical and micro mechanical properties of the material, an overview of sand and sandstone is provided, including the definition, formation, classification, and mechanical behavior (Appendix A). Sandstone is made up of sand particles and cementation that is derived from diagenesis processes. Then, the diagenesis process is reviewed to understand the formation of bonding in sandstone and its controlling factors.

Previous research work at the micro scale for granular materials is also examined to assist the current study for cemented granular material. In addition, published experimental work on artificial cemented granular samples is reviewed for potential use in the validation of the proposed theoretical relationship. Further review is presented on the micro mechanical numerical modeling of cemented granular material so as to choose a suitable numerical modeling software to test the accuracy of the proposed theoretical relationship.

2.2 Introduction to sand and sandstone

To understand the mechanical behavior of cemented granular material like sandstone, it is important to understand the individual constituents that make up the material. Sand has grain diameters between 1/16 and 2 mm, which is visible to the naked eye. The most common constituent of sand is silicate minerals, mainly quartz. Also, sand contains non-quartz silicates (e.g., feldspar), and sometimes sand-sized fragments of calcite and dolomite, or animal shells (Goodman 1993). Depending on the local rock sources and geological conditions, sand composition is highly variable.

Sandstone is a type of sedimentary rock consisting predominately of sand-sized particles. Geochemical assessments suggest that sandstone accounts for 15% of the sedimentary column (Pettijohn et al. 1965). The color of sandstone is greatly influenced by the local geological

environment; most sandstones are found in tan, brown and yellow colors. Sandstone has a high porosity that allows the storage of brines, ground water, natural gas, and petroleum. In addition, it mostly comes with a high permeability, which makes it possible for the migration of pore fluid. Appendix A presents the formation, components, classification, and the mechanical properties of sand and sandstone in detail.

2.3 Diagenesis process

Diagenesis is the process that transforms sediment into rock and sand into sandstone undergoing chemical, physical and biological changes. Freshly deposited sand has unstable grain packing and high porosity. Diagenesis can significantly reduce its porosity through compaction and cementation. Meanwhile, unstable detrital diminishes with formation of stable authigenic precipitates. Pettijohn et al. (1987) studied the diagenesis process systematically, and this process is summarized as below.

Diagenesis includes several post-depositional processes and is influenced by the increase of burial depth, temperature and pressure as follows. Sand assemblage first forms with high porosity at the ground surface. Then, compaction and possible chemical precipitation start to take place when the deposit is buried a few meters to tens of meters deep, exposed to interstitial water. Further compaction and cementation continue to greater buried depth (about 1000 meters), and the pore water may change to brine. After that, at thousands of meters depth, pressure solution, which occurs when high effective stresses are developed on the tangential contacts of quartz grains, becomes another factor contributing to porosity reduction. "High-grade" diagenesis or metamorphism starts when the deposit is buried nearly ten thousand meters. Growth of chlorite and other metamorphic minerals occur when considerable pressure solution takes place. However, porosity may increase due to decementation and weathering when the sandstone/rock is uplifted to near ground surface.

Diagenesis processes can be classified into physical diagenetic processes and chemical diagenetic processes.

2.3.1 Physical diagenetic processes

Compaction and bioturbation are the main physical diagenetic processes. Compaction could reduce the porosity of sediments significantly accompanying the occurrences of rotation, fracturing, translation, and plastic deformation of detrital grains (Pettijohn et al. 1987). Through the rearrangement of detrital grains, permeability would decrease too. Besides, the bulk density of sandstone, and the velocity of elastic waves in sandstone will increase due to compaction.

Bioturbation is the physical and biological activities occurred at or near the sediment surface, which cause the sediment to become resuspended and mixed. Burrowing and boring by organisms can increase the compaction of sediments and then reduce the porosity. Besides, during bioturbation, some organisms would precipitate minerals that act as cementing agents.

2.3.2 Chemical diagenetic processes

Compared with physical diagenetic processes, chemical changes are more important in altering the properties of sandstone after deposition.

(1) Precipitation

Precipitation is a process that various kinds of cements existed in the pore solutions precipitate onto the surfaces of the same or different mineral grains. Chemical precipitation of a binding agent and/or chemical welding of adjacent detrital grains could result in cementation and lithification.

Authigenic precipitates in sandstone can be classified into three groups. The most common precipitates are the minerals with the same chemical composition and structure as the primary detrital grains, like quartz, feldspar, clay, and zircon. There are also some minerals, which only have the same composition but different structure, such as opal and anatase overgrowths. The remainder precipitates are those not originally present in the detrital mix.

(2) Dissolution

There are two different dissolution processes: congruent dissolution and incongruent dissolution. Congruent dissolution is a homogenous process, resulting in unchanged composition of undissolved solid. However, incongruent dissolution is a selective dissolution process, and the undissolved solid would be altered in composition. Take the magnesian calcite as an example,

through the incongruent dissolution, while the dissolved solid has a much lower Ca/Mg ratio than the original solid, the undissolved solid is left with a much higher Ca/Mg ratio. Therefore, a magnesian calcite will gradually be converted to a purer calcite in this way.

Dissolution is an important part in both replacement and recrystallization processes. During these processes, the grains must be in contact with each other to continue to support the sandstone without collapse. This requires that dissolution of the replaced mineral and precipitation of the replacing mineral occur in a very thin film between the bounding surfaces of the two phases. The critical factor in this process is the rate of diffusion that moves the dissolved material out of, and the precipitated material into the film.

(3) Recrystallization

Recrystallization is achieved by dissolution of the precursor and precipitation of the final crystal. The substance of recrystallization is tending to achieve the minimum system Gibbs free energy. Then, a more stable form would be formed through recrystallization. The total Gibbs free energy of the chemical system is the sum of the energy contributed by the mass of all materials in the system, and the surface energy of all crystals. This relationship can help to explain why a single large crystal is formed from an aggregate of smaller crystals through recrystallization.

It is worth mentioning that during the recrystallization process, the unstable mineral will be converted to a stable one without change in chemical composition. For instance, since calcite has a lower Gibbs free energy than aragonite and it is more stable under the temperature and pressure conditions of most sandstones, aragonite would be recrystallized to calcite at last.

(4) Cementation

Cementation is almost the most important process in diagenesis of sandstone. Direct cementation between the grains is an unequivocal source of true cohesion. The cement is not merely a pore filling, but bonds detrital grains together (Barton et al. 1993). For various kinds of sandstones, the cementing minerals are quite variable. In most greywackes, the dominant cements are altered matrix and precipitated clay, zeolites and other silicates. However, in many arenites, the cements are mostly carbonate and silica.

Carbonate is more soluble than silica, and is unlikely to be found as detrital in most sandstones deposited by water. Much of carbonate content in sandstones is in the form of cement. Quartz arenites are the most typically carbonate-cemented. Also, most arkoses contain some carbonate cements. There are three main stages in the formation of carbonate cementation. Firstly, when sand is transported into a carbonate depositional environment, carbonate cements are the primary precipitate. Direct precipitation occurs and many kinds of carbonate cements exist in the newly deposited sand, like calcite, dolomite, aragonite, magnesian calcite and so on. Secondly, during the diagenesis process, some carbonate cements those are more soluble and less stable than pure calcite, such as aragonite and magnesian calcite, will be dissolved and reprecipitate as calcite cements. Thirdly, the solubility of carbonate decreases with increasing temperature, and with a smaller effect, increases with increasing pressure. Therefore, at the deep burial situation, carbonate becomes less soluble at higher temperature, and precipitates as cements (Pettijohn et al. 1987).

While calcite is the most common carbonate cementation, quartz overgrowth is the usual form of silica cementation in the sandstone. Similarly, silica cements could also be obtained from deposition of silica detritus from environment. The precipitation of quartz only happens under supersaturated pore water, which exceeds the equilibrium solubility of quartz. Therefore, some amorphous silica would precipitate quickly at first, even under unsaturated pore water. Then, this kind of unstable silica precipitates and some feldspar will be dissolved and reprecipitate as quartz. Pressure solution is another route contributing to reprecipitation of quartz. Besides, the silica solubility increases with the increase of pH (above 9) and temperature. So, when the sandstone become uplifted, pore water will cool and becomes supersaturated. The precipitation of quartz will accelerate at this situation.

Besides, the abundant clay can reduce the amount of cements in the sandstone. At first, the clay matrix would cause the decrease in permeability, and lead to lower precipitation rate. Another reason is that the widely existence of clay tends to reduce the possibility of pressure solution. There would be few grain-to-grain contacts between rigid quartz and/or carbonate grains, which are common in lithic sandstones and greywackes.

(5) Pressure solution

Pressure solution occurs when high effective stresses are developed on the tangential contacts of quartz grains, resulting in higher solubility at those points. The pressure solution process heightens at the presence of clay film. Pressure solution can reduce the porosity of sandstone, and is related to depth of burial and time. However, pressure solution process is not involved in all sandstone diagenesis. Relatively uncompacted sandstone filled with quartz cements has little or no pressure solution (Pettijohn et al. 1987).

2.4 Research methodology

Cemented granular material consists of a particle skeleton and a solid matrix partially filling the interstitial space. A few examples of this class of materials are mortar, concrete, asphalt, grouted soil, and sedimentary rocks (e.g., sandstone, conglomerate and breccia) (Delenne et al. 2009). Cemented granular material can be idealised as an assembly of granular particles with cementing agent. For uncemented granular material, it can be treated as frictional granular assembly in which the forces are transmitted among contact points. To assist the current study, the research conducted on the micro-macro relationships of both cemented and uncemented granular materials are reviewed in this section.

The mineral composition of natural cemented granular material is very diverse due to the complex diagenesis process. Both particles and cementing materials are highly variable in physical and mechanical properties. Natural materials are also usually non-uniform, anisotropic and heterogeneous. Moreover, micro cracks could form during sample retrieval (i.e., drilling disturbance and stress relief). Thus, it is very difficult to produce repetitive laboratory test results. In addition, it is challenging to identify the effect of a specific parameter among many potential influencing parameters using natural samples, such as particle shape, gradation, packing pattern, composition of cementing materials, and void ratio. Therefore, the usage of artificial samples has always been considered a simple and proper approach to understand the mechanical behaviors of cemented granular material at both micro and macro scales (Akram 2010). In this section, the experimental studies conducted on various artificial cemented granular materials are discussed.

Numerical simulation has been extensively used in micro mechanical investigation. The macro behavior can be predicted with proper input of micro mechanical properties of the material. Thus, numerical simulation can be utilized to test the accuracy of proposed theoretical relationship by

inputting the micro properties provided by the theoretical relationship, and comparing the captured macro numerical behavior with laboratory results. In this section, numerical investigation of the cemented granular material is also reviewed with the aim to choose a suitable numerical modeling software for this study.

2.4.1 Research on micro-macro relations of cemented/uncemented granular material

While the cemented/uncemented granular material is treated as a continuum at the macro scale, it is considered as an assembly of individual particles interacting with each other at the micro scale, with or without cementing agent. Researchers have realized that the macroscopic mechanical behavior of cemented/uncemented granular material is closely related to the behavior of individual particles. Extensive research has been conducted to study the mechanical behavior of cemented /uncemented granular material at the micro scale, including studies on the effect of grain crushing, grain deformation, inter-particle contact force, the fabric anisotropy, cementation, and inter-particle friction.

The thermodynamics-based constitutive models such as continuum breakage mechanics (Einav 2007) explicitly correlate the grain crushing process with macro mechanical behavior of granular material. Das et al. (2013) improved this model to include the effect of cement in granular material with a new definition of damage for the cement phase. Kruyt et al. (2015) developed a micro mechanical expression for the average displacement gradient of granular material, which is formulated in terms of grain displacement and rotation for the 2D case.

Based on the principle of virtual work and the equilibrium of contact forces of the granular assembly, Christoffersen et al. (1981) represented the macro stresses of granular assembly by the inter-particle contact forces and the vectors which connect the centroids of adjacent contacting granules. They assumed the granular material is a medium carrying a set of macroscopic stresses through forces transmitted across contact points among the rigid particles at microscopic scale. In addition, some studies were performed on the relations between macro stresses and inter-particle contact forces of granular material under shear. Matsuoka (1974) performed direct shear tests on rods assembly and derived the relationship between the shear-normal stress ratio and normal-shear strain increment ratio on the mobilized plane by considering the change in the frequency distribution of contact orientations. Matsuoka (1974) also related the macro shear-normal stress

ratio on the spatial mobilized plane to the distribution of the inter-particle contact force and the micro dilation angle with a simple physical model. Oda and Konishi (1974) carried out simple shear tests on photoelastic rods assembly and found that the frequency distribution of contact orientation of granular material tends to concentrate around the major principal stress axis.

With the assumption that the degradation processes only affect the internal variables, Nova et al. (2003) developed an elastoplastic strain hardening model for the mechanical behavior of cemented granular material. The model can predict the mechanical behavior of the bonded material through the change of internal variables including bonding strength and plastic strain due to the weathering and chemical degradation. However, a wide set of parameters are used which are difficult to be physically identified. Nardelli and Coop (2015) studied the micro mechanical behavior of artificial cemented sand samples with a custom-built inter-particle loading apparatus. Two kinds of bonds, namely thick bond and thin bond were tested to study the influence of geometrical properties of the cementing agent. Through the tests, different breakage modes are identified, which are related to the thickness of the cement bond.

Oda (1974) derived a statistical model of granular material using the static equilibrium of mean forces at the contact points between particles. The model relates the mobilized principal stress ratio to the fabric index which represents the fabric anisotropy of granular material. With the assumption that the deformation of granular material is only caused by relative sliding and rolling of granules, Nemat-Nasser (2000) developed a micro mechanically based constitutive model for inelastic deformation of granular material. The deformation of frictional granular masses during simple shearing is considered to depend on the microstructure, which is defined in terms of the fabric anisotropy of granular material and its evolution. Li et al. (2009) investigated three aspects of the micro-macro relation of granular material, including the internal structure, the stress tensor and the strain tensor. The internal structure is the geometrical system at the micro scale. The micro structural definitions of the stress and strain tensors are derived, which relates the macro stress tensor with the contact forces, and the macro strain tensor with the relative displacements at contact.

The inter-particle friction is the resistance against the sliding and rolling of the grains at the contact points. This friction plays a dominant role in controlling the macro deformation and strength behaviors of granular materials (Tobita and Oda 1999). The relationship between the micro and macro friction of granular material has been studied by many researchers. With the assumption

15

that sliding occurs simultaneously on contact faces inclined in all the tangential directions of a spherical surface in the ultimate state, Caquot (1934) derived an equation between the inter-particle friction angle ϕ_μ and bulk friction angle at the critical state ϕ_{cv}, as shown in Eq. 2.1, by integrating forces acting in two orthogonal directions over a spherical surface:

$$\tan \phi_{cv} = \frac{1}{2} \pi \tan \phi_\mu \qquad [2.1]$$

A dense granular soil dilates during shear. The shearing resistance of uncemented granular soils was separated into two components (Taylor 1948, Bishop 1954): the internal frictional component between particles, which is a combination of rolling and sliding friction, and the additional component arising from shearing against interlocked particles. Bishop (1954) developed an approximate solution in the form of Eq. 2.2.

$$\sin \phi_{cv} = \frac{15 \tan \phi_\mu}{10 + 3 \tan \phi_\mu} \qquad [2.2]$$

There are also many researchers who have published various shearing models of uncemented granular materials to separate the total shearing resistance into fundamental components (Newland and Allely 1957, Rowe 1962, Horne 1965, Tobita and Oda 1999). Tobita and Oda (1999) developed an equation after Newland and Allely (1957), as shown in Eq. 2.3. It shows that the total shearing resistance of uncemented granular material was supplied by inter-particle friction at sliding contacts and dilatancy:

$$\tau = \sigma_n \tan(\phi_\mu + i) \qquad [2.3]$$

where τ and σ_n are the shear and normal stresses, respectively, ϕ_μ is the inter-particle friction angle, and i is dilatancy angle.

Hence, a rough quantitative relationship of micro to macro friction of uncementd granular material can be made based on their derivation as:

$$\phi = \phi_\mu + i \qquad [2.4]$$

where ϕ is the friction angle of the uncemented granular assembly at the peak state.

Rowe (1962) discussed the dilatancy behavior of an assembly of rigid and cohesionless particles, and developed the stress-dilatancy theory for granular materials. Based on static equilibrium, regular packing of uniform rigid rods was chosen firstly for the theoretical study at the micro scale. Then, the developed equation was extended to random packing using the principle of least work, and the energy ratio was related to the critical angle of sliding between particles. Horne (1965) examined the deformation mechanism of Rowe's theory and obtained the consistent formulation with Rowe's equation for the round, rigid and cohesionless particles assembly. The stress-dilatancy equation from Rowe (1962) is shown in Eq. 2.5, which is essentially the same as Eq. 2.3 for direct shear (Rowe et al. 1964).

$$\frac{\sigma_1}{\sigma_3(1 + d\varepsilon_v/d\varepsilon_1)} = tan^2\left(\frac{\pi}{4} + \frac{1}{2}\phi_\mu\right) \qquad [2.5]$$

where σ_1 and σ_3 are the major and minor effective principal stresses, and the term $1 + d\varepsilon_v/d\varepsilon_1$ represents the dilatancy.

The literature review indicates that many research work has been conducted on the micro-macro relationships of cemented/uncemented granular material. However, for the cemented granular material, the relationship of micro-macro strength properties is still largely unknown. Moreover, some research approaches on the micro structural models can be used for reference in the current study.

2.4.2 Experimental study on artificial cemented granular material

Artificial cemented granular material is widely used for two primary reasons: the elimination of the heterogeneities that occur in natural materials and the reproducibility of test results (Akram 2010). Various artificial samples are used in the laboratory to study the mechanical properties of cemented granular material as discussed below.

Cemented sand is the mostly used artificial cemented granular material in research, which could simulate the rock with sand sized grains, such as sandstone. Haeri et al. (2002) carried out large direct shear tests on artificial cemented gravely sand using lime as the cementing agent. The experiment results revealed a curved failure envelope for the cemented sand. Ismail et al. (2002) studied the effects of cement type on the mechanical behavior of cemented fine sandy soil. They introduced the uniaxial compressive strength as a measure of the effect of cementing bonds on the

shear behavior. It was found that the cement type significantly affects the shear behavior. The Portland cement was found to be the most ductile cementing agent compared with gypsum and calcite, and the sample prepared with Portland cement has the highest shear strength. Haeri et al. (2006) studied the behavior of a cemented gravely sand using triaxial compression tests. Gypsum, Portland cement and lime were used as cementing agents in the sample preparation. Three cement contents of 1.5%, 3.0% and 4.5% were selected. Drained and undrained triaxial compression tests were conducted under different confining pressures to examine the effect of cementing agent and cement content on the failure modes, shear strength, stress strain behavior, and volume and pore pressure changes. Consoli et al. (2009) carried out uniaxial compression and triaxial compression tests on artificial cemented sand with bender elements measurements to investigate the influence of voids/cement ratio on the initial shear modulus and Mohr-Coulomb effective strength parameters. The void/cement ratio was found to be an appropriate parameter to assess both initial stiffness and effective strength of the sand-cement mixture. In addition, the mechanical behavior of cemented sands with different cementing agents were also studied by some other researchers (Asghari et al. 2003, Clough et al. 1981, Coop and Atkinson 1993, Huang and Airey 1998, Saxena and Lastrico 1978, Schnaid et al. 2001, Marri 2010).

Cemented gravel is another commonly used artificial cemented granular material. Kongsukprasert et al. (2005) conducted a series of drained triaxial compression tests on a well-graded gravel of crushed sandstone mixed with Portland cement. The effect of water content, compaction effort, cement to gravel ratio by weight, and curing period on the stress-strain behavior of cemented gravel samples were investigated. Haeri et al. (2005) also performed a series of undrained triaxial and uniaxial compression tests on the artificial cemented gravel samples to study their mechanical behavior. Taheri et al. (2012) prepared the artificial cemented sample with Chiba gravel and standard proctor, and then the effect of loading histories on the stress-strain properties of cemented well-graded gravelly soil was studied.

Some other artificial materials have also been used. Delenne et al. (2009) prepared artificial cemented samples using lightweight expanded clay aggregate beads and joint seal paste as cementing matrix to investigate the strength and failure properties of cemented granular material. Nakagawa and Myer (2001) studied the mechanical and acoustic properties of weakly cemented granular rock using artificial samples fabricated with cementing sand and glass beads with sodium

silicate binder. To verify the bond contact model used in numerical simulation of cemented sands, a series of cemented granules were tested, which are idealized by a pair of aluminum rods glued together with calcium aluminate cement by Jiang et al. (2012). With a new auxiliary loading device, the mechanical relationships between the cemented rods were investigated. Amini and Hamidi (2014) conducted triaxial compression tests under both consolidated drained and undrained conditions to study the mechanical behavior of cemented granular material. The artificial samples are cemented poorly graded sand-gravel mixture (containing 30% gravel and 70% sand) with the Portland cement as the cementing agent.

To study the mechanical behavior of conglomerate containing mainly gravel, cobble and boulder embedded in a cementing agent, Akram (2010) prepared synthetic conglomerate samples with steel balls as clasts and Portland cement paste as the cement matrix. Uniaxial, triaxial, Brazilian tensile, and shear box tests were used to measure the mechanical properties. Using steel ball as clast can eliminate the effect of particle crushing, cracking and particle shape on the mechanical behavior. The current study focuses on the effect of micro bonding strength on the macro mechanical behavior of cemented granular material. Therefore, the artificial conglomerate comprised of high strength spherical particles and a controlled proportion of cement is preferred to investigate the mechanical behavior of cemented granular material.

2.4.3 Numerical simulation investigation of cemented granular material

Numerous numerical techniques have been extensively applied in soil and rock mechanics and in other science and engineering disciplines. These techniques can be divided into those based on continuum mechanics, such as the finite difference method (FDM), finite element method (FEM) and boundary element method (BEM), and the methods based on discontinuum mechanics, like the discrete element method (DEM). The continuum methods are generally used to model the granular material with the assumption of a homogeneous and isotropic microstructure. However, for the research on rocks like conglomerates, the continuum methods are not considered suitable (Akram 2010).

The main difference between continuum and discontinuum methods is the representation of a contact or interface between the discrete bodies that comprises the system. This interface may be soft to allow deformation along the contact, or rigid to restrain deformation along the contact. The

selection of contact type mainly depends on the physics of the system (Cundall and Hart 1993). The DEM was defined by Cundall and Hart (1993) as the numerical schemes which allow finite displacement and rotation of discrete bodies including complete detachment and can recognize new contacts automatically as calculation progresses. Since DEM evolves macro behavior of a granular system based on the interaction and movement of the discrete particles, it is considered appropriate for the study of cemented granular material.

Various DEM programs have been developed based on particle geometry, and the most common programs used to model granular materials are UDEC, 3DEC and Particle Flow Codes (PFC^{2D} and PFC^{3D}). UDEC (Cundall 1980) and 3DEC (Cundall 1988) deal with angular objects, and it is assumed that the medium is divided into a finite number of polygonal blocks by the intersection of the discontinuities. Particle flow codes (PFC^{2D} and PFC^{3D}) model the movement and interaction of circular particles. The particles can be bonded to their neighbors to model solids. Moreover, the medium in PFC can be represented by the assembly of circular discs (2D) or spheres (3D) with a set of micro mechanical properties that specifies the contact and bond conditions. Comparing with the other DEM programs in modeling cemented granular material, PFC has two main advantages. Firstly, it is potentially more efficient, since contact detection between circular objects is much simpler than that between angular objects. Also, it is possible for the blocks to break since they are composed of bonded particles, while the blocks modeled with UDEC or 3DEC cannot break (Itasca 2008). Therefore, PFC is a suitable program with increasing popularity to model nature or artificial cemented granular material.

Akram (2010) conducted numerical modelling with PFC^{3D} to better understand the conglomerate strength and deformation parameters. Numerical samples were prepared using measured and known micro parameters obtained from uniaxial, triaxial, Brazilian tensile, and direct shear tests. While the strength obtained from these tests matched the experimental results, the Young's modulus and Poisson's ratio in uniaxial and triaxial tests, the angle of dilation in shear box tests, and the failure mechanism in the Brazilian tests did not match with laboratory testing results. These differences were explained by the presence of the cement matrix in physical samples. Besides, numerical simulation was also conducted to investigate multiple factors in controlling the mechanical response of a clast supported conglomerate, including sensitivity of the cement matrix, the clasts' properties, specimen size, and size distribution of the clasts.

Rahmati (2013) conducted numerical study to investigate the effect of the micro and macro parameters on the failure mechanism and the geometry of the wellbore breakout using PFC^{3D}. A systematic methodology was developed for calibrating material micro properties. PFC^{3D} was also used in a series of parametric simulations of drilling conditions in sandstone reservoir. Holt (2001) conducted a study to address the main discrepancies associated with laboratory measured and in situ virgin compaction using synthetic sandstone and PFC^{2D} and PFC^{3D} modelling. Jiang et al. (2013) carried out a numerical study with PFC^{2D} on the mechanical behavior and strain localization of loose cemented granular material. Shen et al. (2016) developed a 3D bonded contact model with PFC^{3D} to simulate the mechanical behavior of cemented sand. Based on the observations of the micro structure of cemented sand, two types of bonded contact, namely, parallel bond contact and serial bond contact, were identified and modeled. The effect of bond geometry, the complete interactions in the normal, tangential, rolling, and torsional directions, and the coupled effect of loads in four directions were considered in the bond failure criterion. PFC^{3D} was also used to study the behavior of Antler Sandstone by selecting the micro mechanical properties with the inverse modelling approach (Gil et al. 2005).

Besides, it is possible to create particles of arbitrary shape by attaching two or more particles together in PFC, using the clump logic. The particles comprising the clump remain at a fixed distance from each other, and internal contacts within the clump are skipped during the calculation cycle. A clump acts as a rigid body that does not break apart, regardless of the forces acting upon it (Itasca 2008). Some researchers have used the clump logic to model rocks or granular materials to get true interlocking of the particles in the assembly (Fu 2005, Cho et al. 2007, 2008).

Fu (2005) developed a clustering DEM model to investigate the micro-macro behavior of real granular material with irregular particle shape configurations. PFC^{3D} was used to generate the clustering DEM model, and to simulate the compression test and the direct shear test, which demonstrated a good capability of predicting both the micro and macro behaviors of granular material, including dilation, strength, particle kinematics, and fabric evolution. Cho et al. (2007) developed a clumped particle model to simulate the behavior of rock with PFC. The clumped particle geometry was found to improve the predictive capabilities of the particle code significantly. For both Lac du Bonnet granite and a weak synthetic rock, the particle code calibrated to uniaxial tests using the clumped-particle geometry predicts both the stress-strain behavior and the complete

nonlinear failure envelope. Cho (2008) conducted a series of direct shear laboratory tests using synthetic brittle rock to investigate shear zones. Numerical simulation was conducted using developed clumped particle geometry with PFC^{2D}. The development of shear zone in rock subjected to direct shear was explored with the clump generated simulation models. The results showed a reasonable correlation between the laboratory testing and PFC simulation.

2.5 Summary

To understand the bonding and debonding mechanism of cemented granular material, such as sandstone, a summary of sand and sandstone in several aspects is provided in this chapter, including the formation, classification, and mechanical properties. The physical and chemical diagenesis processes are also reviewed to study the influence of cementation and other external factors on the formation and properties of bonds.

Extensive literature review is conducted on the research of micro-macro relations of granular material. No constitutive model has been established to relate the micro bonding strength to conventional macro parameters of cemented granular material. However, the research approach of Rowe's (1962) work can be used for reference. The regular packing of uniform rigid rods is used for the theoretical derivation in the current study.

The proposed theoretical relationship between micro and macro mechanical properties of cemented granular material needs to be verified with experiment results in this study. Therefore, the experimental work on artificial cemented granular samples is reviewed. The artificial conglomerate made with steel balls and Portland cement paste (Akram 2010) is chosen over several other options. The use of steel balls could eliminate the effect of particle crushing, cracking and particle shape on the mechanical behavior of conglomerates. Portland cement paste is a commonly used cementing agent and its strength can be adjusted with different water to cement ratios.

Numerical simulation investigation of cemented granular material is also reviewed. Since the micro mechanical behavior of cemented granular material, and the accuracy of proposed theoretical relationship need to be investigated and tested with numerical modeling in this study. The 'Particle Flow Code', which is commonly known as PFC is chosen due to the suitable

application and widespread use. The numerical samples with rigid "particles" that bonded together at their contact points with "parallel bonds" can be generated and tested.

Chapter 3: Theoretical Derivation of the Relationship between Micro and Macro Mechanical Properties of Cemented Artificial Granular Materials

3.1 Introduction

Understanding the relationship between micro and macro mechanical properties of cemented granular material is truly important. It helps engineers perform micromechanics analysis on more practical problems. In this research, normal and shear bonding strength was calculated using a simplified physical model and published data on synthetic conglomerates, as shown in Appendix B. It reveals that the normal bonding strength between steel ball and cement is lower than the Brazilian tensile strength and direct tensile strength of synthetic conglomerate. In addition, the shear bonding strength between steel ball and cement is lower than the cohesion of the conglomerate. Therefore, the commonly accepted relationships between micro bonding strength and macro parameters may not be reliable and further investigation is warranted.

In this chapter, the theoretical relationship between micro bonding strength of cemented granular material and macro parameters that can be determined in the laboratory is developed and discussed. To minimize the variation of grains and cementation properties in natural materials, and the possibility of crushing of grains under high stress, a uniform packing consisting of rigid and uniform rods is used to generate a simplified 2D model. For elastic and plastic deformation, crushing and cracking are ignored in the analysis. Two extreme particle packing conditions are considered, namely, the densest and loosest packings.

3.2 Theoretical derivation using the densest packing

As shown in Figure 3.1, an assembly of circular rods is firstly analyzed to study the relationship between micro resisting forces and externally applied forces. If the assembly fails along line A-A, the resisting forces at the contact points 1, 2, 3 and 4 must be overcome by the externally applied forces N and F. All the bonds between rods and cementing agent are assumed to be broken at the same time, and the bonding strength and friction between rods are also assumed to fail simultaneously.
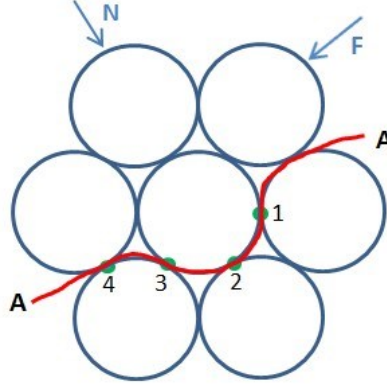
Figure 3.1 Typical group of rods for the densest packing condition

The movement at each contact point is shown in Figure 3.2. The symbol u denotes shear (tangential) movement and v denotes normal movement. φ_m is the micro dilation angle, and it is equal to 60° in the special densest packing configuration defined in this analysis at the beginning of shearing. The movement ratios of contact point 1 to contact point 4 at the beginning of shearing can be determined from:

$$\begin{cases} \dfrac{v_1}{u_1} = tan60° = \sqrt{3} \\ \dfrac{v_2}{u_2} = tan60° = \sqrt{3} \\ \dfrac{v_3}{u_3} = 0 \\ \dfrac{v_4}{u_4} = tan60° = \sqrt{3} \end{cases} \qquad [3.1]$$

It is evident that contact point 3 is only possible to fail in shear, and there is no normal movement at contact point 3. However, the failure modes of the other three contact points can be either shear failure or tensile failure, and need to be determined. Here, let $V_C = \dfrac{v\prime}{u\prime}$ be the movement criterion, which is the ratio of maximum normal movement to maximum shear movement at contact point before failure.

If $V_C \leq \sqrt{3}$, then $\begin{cases} \dfrac{v_1}{u_1} > \dfrac{v\prime}{u\prime} \\ \dfrac{v_2}{u_2} > \dfrac{v\prime}{u\prime} \\ \dfrac{v_4}{u_4} > \dfrac{v\prime}{u\prime} \end{cases}$, contact points 1, 2 and 4 all fail in tension, and contact point 3 fails

in shear.

If $V_C > \sqrt{3}$, then $\begin{cases} \dfrac{v_1}{u_1} < \dfrac{v\prime}{u\prime} \\ \dfrac{v_2}{u_2} < \dfrac{v\prime}{u\prime} \\ \dfrac{v_4}{u_4} < \dfrac{v\prime}{u\prime} \end{cases}$, contact points 1, 2, 3 and 4 all fail in shear.
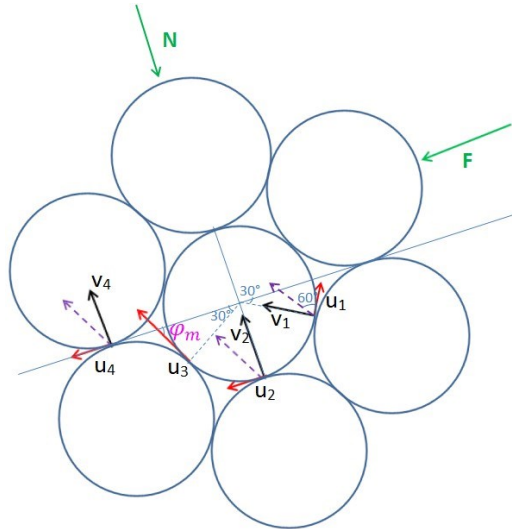
Figure 3.2 Movement of each contact point for the densest group of rods
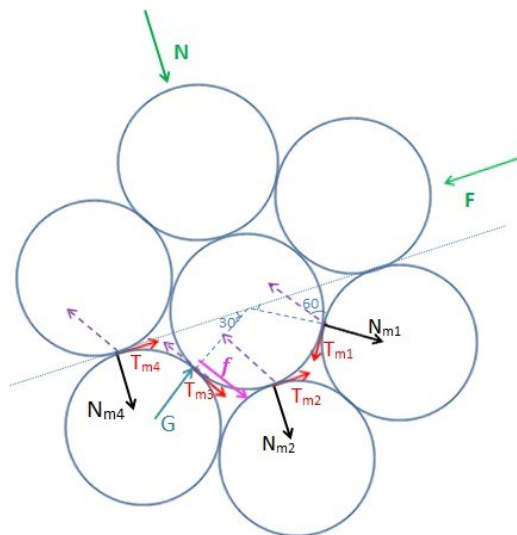
Figure 3.3 Resisting forces at each contact point for the densest group of rods

In both situations, force equilibrium must be satisfied. Therefore, the resisting forces at each point should be analyzed, as shown in Figure 3.3. T_m is the micro shear resisting force, N_m is the micro normal resisting force, T_m^p is the peak shear resisting force, and N_m^p denotes the peak normal resisting force. The bonding strength is assumed to be the same for all contacts. Therefore, the

peak shear resisting force T_m^p and peak normal resisting force N_m^p are constant. G is the supporting reaction force at contact point 3, $f = Gtan\phi_\mu$ is the friction force, and ϕ_μ is the inter-particle friction angle. As shown in Figure 3.4, the supporting reaction force G can be divided into two components along the directions of F and N with the micro dilation angle φ_m.
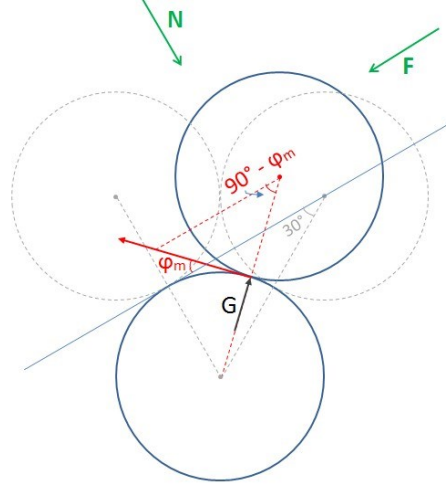
Figure 3.4 Relationship between the supporting reaction force and micro dilation angle

3.2.1 Contact points 1, 2 and 4 fail in tension, and contact point 3 fails in shear

The force equilibrium equations for the first situation of the densest packing are:

$$\begin{cases} N_m^p sin60° - T_{m1} \sin 30° + T_{m2} + T_m^p sin30° + T_{m4} + G \sin \varphi_m + f \cos \varphi_m = F \\ -N_m^p \sin 30° - T_{m1} \sin 60° - N_m^p - T_m^p \sin 60° - N_m^p + G \cos \varphi_m - f \sin \varphi_m = N \end{cases}$$ [3.2]

To simplify the equations:

$$\begin{cases} \dfrac{\sqrt{3}}{2} N_m^p - \dfrac{1}{2}T_{m1} + T_{m2} + \dfrac{1}{2} T_m^p + T_{m4} + G \sin \varphi_m + Gtan\phi_\mu \cos \varphi_m = F \\ -\dfrac{5}{2} N_m^p - \dfrac{\sqrt{3}}{2} T_{m1} - \dfrac{\sqrt{3}}{2} T_m^p + G \cos \varphi_m - Gtan\phi_\mu \sin \varphi_m = N \end{cases}$$ [3.3]

Based on the Eq. 3.3, there are another four unknowns (namely, T_{m1}, T_{m2}, T_{m4}, and G) besides N_m^p and T_m^p. An assumption is required to solve this equation. Assume the relationships between the resisting forces and corresponding movements are linear as shown in Figure 3.5, the

movement ratio $\frac{v}{u}$ equals to α times of the resisting force ratio $\frac{N_m}{T_m}$, $\frac{v}{u} = \alpha \frac{N_m}{T_m}$. Then, the shear resisting forces T_{m1}, T_{m2} and T_{m4} can be determined using the movement ratios in Eq. 3.1.

$$
\begin{cases}
T_{m1} = \dfrac{\alpha N_m^p}{tan60°} = \dfrac{\sqrt{3}}{3}\alpha N_m^p \\[2mm]
T_{m2} = \dfrac{\alpha N_m^p}{tan60°} = \dfrac{\sqrt{3}}{3}\alpha N_m^p \\[2mm]
T_{m4} = \dfrac{\alpha N_m^p}{tan60°} = \dfrac{\sqrt{3}}{3}\alpha N_m^p
\end{cases}
\qquad [3.4]
$$
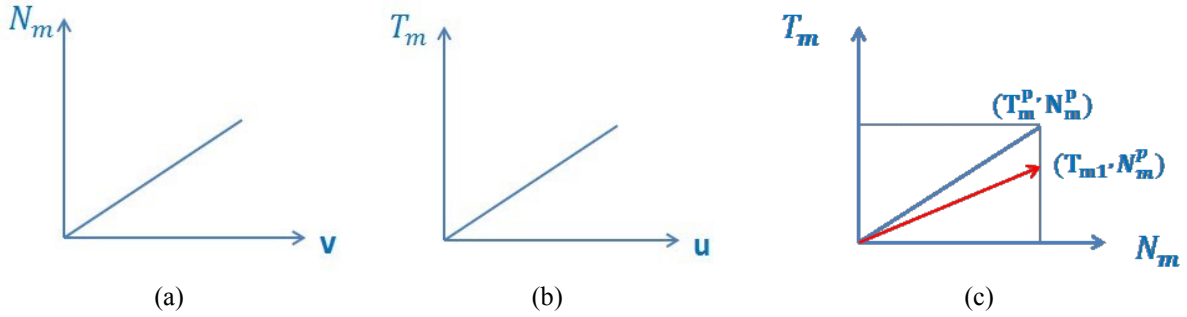
Figure 3.5 The linear relationships between resisting forces and corresponding movements

Combining Eq. 3.3 and Eq. 3.4, the relationships between the maximum micro resisting forces and the externally applied forces F and N are:

$$
\begin{cases}
\dfrac{\sqrt{3}(1+\alpha)}{2}N_m^p + \dfrac{1}{2}T_m^p + G\,(sin\,\varphi_m + tan\phi_\mu\,cos\,\varphi_m) = F \\[3mm]
-\dfrac{5+\alpha}{2}N_m^p - \dfrac{\sqrt{3}}{2}T_m^p + G\,(cos\,\varphi_m - tan\phi_\mu\,sin\,\varphi_m) = N
\end{cases}
\qquad [3.5]
$$

Since $V_C = \frac{v\prime}{u\prime}$ is the movement criterion, the ratio between peak normal resisting force and peak shear resisting force can be related to V_c ($V_c = \alpha \frac{N_m^p}{T_m^p}$). Then, the Eq. 3.5 can be written as:

$$
\begin{cases}
2G\,(sin\,\varphi_m + tan\phi_\mu\,cos\,\varphi_m) = 2F - (\dfrac{\sqrt{3}(1+\alpha)}{\alpha}V_c + 1)T_m^p \\[3mm]
2G\,(cos\,\varphi_m - tan\phi_\mu\,sin\,\varphi_m) = 2N + \left(\dfrac{5+\alpha}{\alpha}V_c + \sqrt{3}\right)T_m^p
\end{cases}
\qquad [3.6]
$$

Hence, the relationship between F, N and T_m^p is obtained:

$$\frac{2F - (\frac{\sqrt{3}(1+\alpha)}{\alpha}V_c + 1)T_m^p}{2N + \left(\frac{5+\alpha}{\alpha}V_c + \sqrt{3}\right)T_m^p} = \frac{tan\phi_\mu + tan\,\varphi_m}{1 - tan\phi_\mu\,tan\,\varphi_m} \qquad [3.7]$$

According to the trigonometric identities:

$$\frac{tan\phi_\mu + tan\,\varphi_m}{1 - tan\phi_\mu\,tan\,\varphi_m} = \tan(\phi_\mu + \varphi_m) \qquad [3.8]$$

Combining Eq. 3.7 and Eq. 3.8 results in:

$$\frac{2F - (\frac{\sqrt{3}(1+\alpha)}{\alpha}V_c + 1)T_m^p}{2N + \left(\frac{5+\alpha}{\alpha}V_c + \sqrt{3}\right)T_m^p} = \tan(\phi_\mu + \varphi_m) \qquad [3.9]$$

It is worth mentioning that the inter-particle friction angle and micro dilation angle must satisfy the condition that $\phi_\mu + \varphi_m \leq 90°$.

Let $A = \tan(\phi_\mu + \varphi_m)$, Eq. 3.9 can be written as:

$$2F = 2N * A + \left[\left(\frac{5+\alpha}{\alpha}V_c + \sqrt{3}\right) * A + \left(\frac{\sqrt{3}(1+\alpha)}{\alpha}V_c + 1\right)\right]T_m^p \qquad [3.10]$$

To convert forces F and N to stresses, P groups of rods of unit thickness along the failure surface is considered. As shown in Figure 3.6, the length of the specimen is denoted by L, and the thickness t is assumed to be 1. Let d be the diameter of the rod, then the length L is:

$$L \approx P * (2d\,sin60°) = \sqrt{3}dP \qquad [3.11]$$

The combined force PF in Figure 3.6 can be converted to shear stress τ as $\tau = \frac{PF}{Lt}$, and PN can be related to normal stress σ as $\sigma = \frac{PN}{Lt}$. Therefore, the Mohr-Coulomb criterion can be expressed as:

$$\frac{PF}{Lt} = c + \frac{PN}{Lt}\tan\phi_P \qquad [3.12]$$
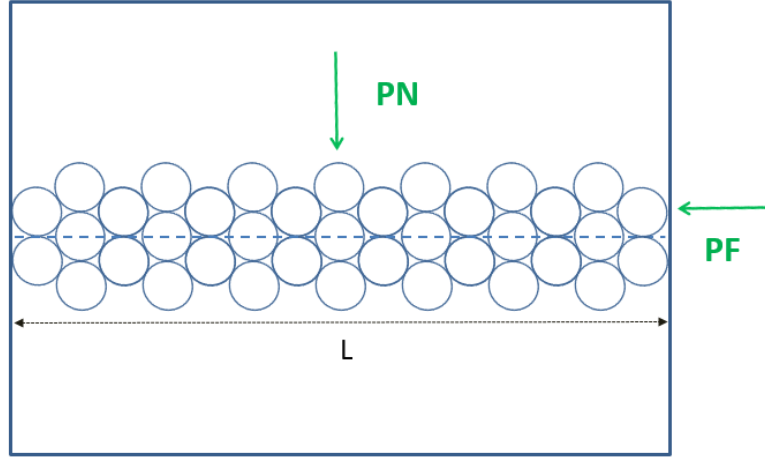
Figure 3.6 The direct shear failure surface consisting of P groups of rods (densest packing)

Because all the bonds and friction are assumed to be overcome at the same time, the cohesion c and friction angle ϕ_P in Eq. 3.12 are corresponding to the peak state.

To compare the micro resisting force T_m^p and inter-particle friction angle ϕ_μ with Mohr-Coulomb parameters, Eq. 3.10 is re-arranged as follows:

$$\frac{PF}{Lt} = \frac{PN}{Lt} * A + \left[\left(\frac{5+\alpha}{\alpha}V_c + \sqrt{3}\right) * A + \left(\frac{\sqrt{3}(1+\alpha)}{\alpha}V_c + 1\right)\right] * \frac{T_m^p * P}{2Lt} \qquad [3.13]$$

To obtain the shear bonding strength, the contact area between rod and cementing agent for each contact point should be known. In this formulation, it is assumed that the contact area is equal to $a_c = \omega dt$, where ω is the contact area coefficient. Since it is assumed that all the bonds are broken at the same time in the derivation, tensile failure and shear failure will take place at the same time. Therefore, the contact areas for tension and shear failure are assumed to be the same. The peak resisting force T_m^p can be converted into shear bonding strength τ_m as shown in Eq. 3.14.

$$\frac{PF}{Lt} = \frac{PN}{Lt} * A + \left[\left(\frac{5+\alpha}{\alpha}V_c + \sqrt{3}\right) * A + \left(\frac{\sqrt{3}(1+\alpha)}{\alpha}V_c + 1\right)\right] * \frac{\tau_m * wdP}{2L} \qquad [3.14]$$

Substituting L in Eq. 3.11 into Eq. 3.14 results in:

$$\frac{PF}{Lt} = \frac{PN}{Lt} * A + \left[\left(\frac{5+\alpha}{\alpha}V_c + \sqrt{3}\right) * A + \left(\frac{\sqrt{3}(1+\alpha)}{\alpha}V_c + 1\right)\right] * \frac{\tau_m * w}{2\sqrt{3}} \qquad [3.15]$$

It is clear from a comparison of Eq. 3.12 and Eq. 3.15 that the micro bonding strength and inter-particle friction angle can be related to the Mohr-Coulomb parameters when considering two extreme conditions.

When only friction is considered, the cohesion c and shear bonding strength τ_m are set to be zero. Then the Eq. 3.12 and Eq. 3.15 are simplified to:

$$\frac{PF}{Lt} = \frac{PN}{Lt} \tan \phi_P = \frac{PN}{Lt} * A \qquad [3.16]$$

Hence, the macro peak friction angle can be related to term A, which involves the inter-particle friction angle and micro dilation angle.

$$\tan \phi_P = \tan(\phi_\mu + \varphi_m) \qquad [3.17]$$

Similarly, when only considering the effect of cementing agent, the inter-particle friction angle, micro dilation angle and macro friction angle are all set to zero. The term A equals to zero. Eq. 3.12 and Eq. 3.15 are simplified to:

$$\frac{PF}{Lt} = c = \left(\frac{\sqrt{3}(1 + \alpha)}{\alpha} V_c + 1 \right) * \frac{\tau_m * w}{2\sqrt{3}} \qquad [3.18]$$

Therefore, the cohesion term c can be related to shear bonding strength τ_m, the movement coefficient α and criterion V_c as shown below.

$$c = \left(\frac{1 + \alpha}{2\alpha} V_c + \frac{\sqrt{3}}{6} \right) w * \tau_m \qquad [3.19]$$

3.2.2 Contact points 1, 2, 3 and 4 all fail in shear

The force equilibrium equations can be expressed as:

$$\begin{cases} -T_m^p \sin 30° + N_{m1} \cos 30° + T_m^p + T_m^p \cos 60° + T_m^p + G \sin \varphi_m + f \cos \varphi_m = F \\ -T_m^p \cos 30° - N_{m1} \sin 30° - N_{m2} - T_m^p \sin 60° - N_{m4} + G \cos \varphi_m - f \sin \varphi_m = N \end{cases} \qquad [3.20]$$

To simplify the equations:

$$\begin{cases} -\dfrac{1}{2}T_m^p + \dfrac{\sqrt{3}}{2}N_{m1} + T_m^p + \dfrac{1}{2}T_m^p + T_m^p + G\sin\varphi_m + G\tan\phi_\mu\cos\varphi_m = F \\ -\dfrac{\sqrt{3}}{2}T_m^p - \dfrac{1}{2}N_{m1} - N_{m2} - \dfrac{\sqrt{3}}{2}T_m^p - N_{m4} + G\cos\varphi_m - G\tan\phi_\mu\sin\varphi_m = N \end{cases} \qquad [3.21]$$

Similar as the derivation in the first situation of densest packing, the normal resisting forces N_{m1}, N_{m2} and N_{m4} can be determined using the movement ratios in Eq. 3.1.

$$\begin{cases} N_{m1} = \dfrac{T_m^p\,tan60°}{\alpha} = \dfrac{\sqrt{3}T_m^p}{\alpha} \\ N_{m2} = \dfrac{T_m^p\,tan60°}{\alpha} = \dfrac{\sqrt{3}T_m^p}{\alpha} \\ N_{m4} = \dfrac{T_m^p\,tan60°}{\alpha} = \dfrac{\sqrt{3}T_m^p}{\alpha} \end{cases} \qquad [3.22]$$

Combining Eq. 3.21 and Eq. 3.22:

$$\begin{cases} \dfrac{4\alpha + 3}{2\alpha}T_m^p + G\sin\varphi_m + G\tan\phi_\mu\cos\varphi_m = F \\ -\dfrac{2\sqrt{3}\alpha + 5\sqrt{3}}{2\alpha}T_m^p + G\cos\varphi_m - G\tan\phi_\mu\sin\varphi_m = N \end{cases} \qquad [3.23]$$

The peak resisting force T_m^p can be related to F and N:

$$\dfrac{2F - \dfrac{4\alpha+3}{\alpha}T_m^p}{2N + \dfrac{2\sqrt{3}\alpha+5\sqrt{3}}{\alpha}T_m^p} = \dfrac{tan\phi_\mu + tan\,\varphi_m}{1 - tan\phi_\mu\,tan\,\varphi_m} \qquad [3.24]$$

Combining Eq. 3.8 and Eq. 3.24 results in:

$$\dfrac{2F - \dfrac{4\alpha+3}{\alpha}T_m^p}{2N + \dfrac{2\sqrt{3}\alpha+5\sqrt{3}}{\alpha}T_m^p} = tan(\phi_\mu + \varphi_m) \qquad [3.25]$$

And the Eq. 3.25 is re-arranged as follows:

$$2F = 2N * A + \left(\dfrac{2\sqrt{3}\alpha + 5\sqrt{3}}{\alpha}A + \dfrac{4\alpha + 3}{\alpha}\right)T_m^p \qquad [3.26]$$

where $A = tan(\phi_\mu + \varphi_m)$.

For P groups of rods as shown in Figure 3.6, the relationship between PF and PN can be expressed as:

$$\frac{PF}{Lt} = \frac{PN}{Lt} * A + \left(\frac{2\sqrt{3}\alpha + 5\sqrt{3}}{\alpha} A + \frac{4\alpha + 3}{\alpha}\right) * \frac{T_m^p * P}{2Lt} \qquad [3.27]$$

As mentioned in the derivation of the first situation, the contact area for each contact point can be represented by $a_c = \omega \mathrm{d}t$. Substituting $T_m^p = \tau_m w \mathrm{d}t$, and $L = \sqrt{3}\mathrm{d}P$ into Eq. 3.27 results in:

$$\frac{PF}{Lt} = \frac{PN}{Lt} * A + \left(\frac{2\sqrt{3}\alpha + 5\sqrt{3}}{\alpha} A + \frac{4\alpha + 3}{\alpha}\right) * \frac{\tau_m * w}{2\sqrt{3}} \qquad [3.28]$$

Eq. 3.28 shows that the externally applied forces are related to the micro bonding strength τ_m, inter-particle friction angle ϕ_μ, micro dilation angle φ_m, and movement coefficient α and criterion V_c.

When only friction is considered, cohesion c and bonding strength τ_m are set to zero. Eq. 3.12 and Eq. 3.28 are simplified into:

$$\frac{PF}{Lt} = \frac{PN}{Lt}\tan\phi_P = \frac{PN}{Lt} * A \qquad [3.29]$$

Then, the peak friction angle ϕ_P from Mohr-Coulomb criterion can be related to the inter-particle friction angle ϕ_μ and micro dilation angle φ_m. The relationship is the same as shown in Eq. 3.17.

$$\tan\phi_P = \tan(\phi_\mu + \varphi_m) \qquad [3.30]$$

When only cohesion and shear bonding strength are considered, both the friction angle and micro dilation angle are set to zero. Eq. 3.12 and Eq. 3.28 are simplified into:

$$\frac{PF}{Lt} = c = \frac{4\alpha + 3}{\alpha} * \frac{\tau_m * w}{2\sqrt{3}} \qquad [3.31]$$

Therefore, the relationship between cohesion term c and shear bonding strength τ_m is given by:

$$c = \frac{4\alpha + 3}{2\sqrt{3}\alpha} * w * \tau_m \qquad [3.32]$$

3.3 Theoretical derivation using the loosest packing

The loosest packing is shown in Figure 3.7. The group of rods shown in solid lines are analyzed. If the assembly of rods fails along line A-A, the resisting forces on the contact points 1 and 2 must be overcome by the externally applied forces N and F. Similar to the densest configuration, all the bonds between rods and cementing agent are assumed to be broken at the same time, and the bonding strength and friction are assumed to fail simultaneously.

The movement of contact points 1 and 2 is shown in Figure 3.8. Since elastic and plastic deformation is ignored due to the relative movement occurs between solid bodies, obviously only shear movement u_1 and u_2 exist for this special configuration. In addition, only shear resisting forces T_{m1} and T_{m2}, and friction f_1 and f_2 are generated to resist the movement at contact points, as shown in Figure 3.9. G_{m1} and G_{m2} are internal supporting reaction forces at contact points 1 and 2, and G_{E1} and G_{E2} are the external supporting reaction forces. Like the densest packing condition, both G_{m1} and G_{m2} can be divided into two components with the micro dilation angle φ_m, and $\varphi_m = 0$ for the loosest packing condition.
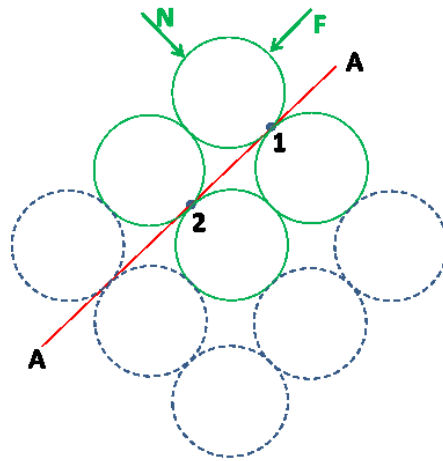
Figure 3.7 Typical group of rods for the loosest packing condition
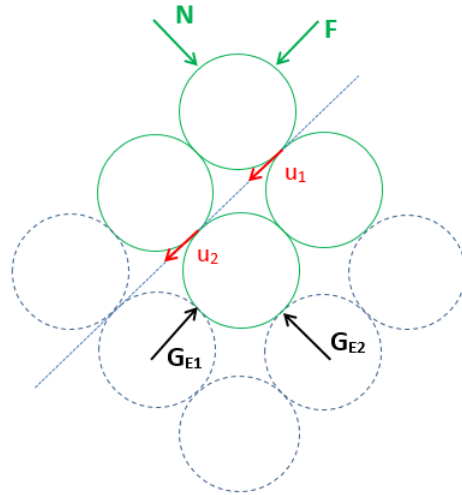
Figure 3.8 Movement at each contact point for the loosest packing of rods
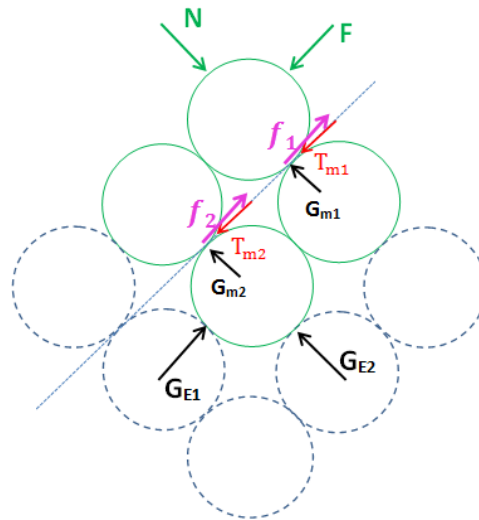
Figure 3.9 Resisting forces at each contact point for the loosest packing of rods

The peak shear resisting force T_m^p is constant and satisfies force equilibrium. Since all bonds are assumed to be broken simultaneously, the peak shear resisting forces at contact points 1 and 2 can be achieved at the same time.

$$\begin{cases} 2\,T_m^p + G_{m1}\sin\varphi_m + G_{m2}\sin\varphi_m + f_1\cos\varphi_m + f_2\cos\varphi_m = F \\ G_{m1}\cos\varphi_m + G_{m2}\cos\varphi_m - f_1\sin\varphi_m - f_2\sin\varphi_m = \text{N} \end{cases} \qquad [3.33]$$

Simplify the equations:

$$\begin{cases} 2T_m^p + (G_{m1} + G_{m2}) * (\sin \varphi_m + tan\phi_\mu \cos \varphi_m) = F \\ (G_{m1} + G_{m2}) * (\cos \varphi_m - tan\phi_\mu \sin \varphi_m) = N \end{cases} \qquad [3.34]$$

The peak shear resisting force T_m^p can be related to F and N:

$$\frac{F - 2 T_m^p}{N} = \frac{tan\phi_\mu + tan \varphi_m}{1 - tan\phi_\mu \tan \varphi_m} \qquad [3.35]$$

Combining Eq. 3.8 and Eq. 3.35 results in:

$$\frac{F - 2 T_m^p}{N} = \tan(\phi_\mu + \varphi_m) \qquad [3.36]$$

Let $A = \tan(\phi_\mu + \varphi_m)$, Eq. 3.36 can be written as:

$$F = N * A + 2T_m^p \qquad [3.37]$$

To convert F and N to stresses, P groups of rods in the unit thickness failure surface are analyzed, as shown in Figure 3.10. The length of the sample is denoted by L, and the thickness t is 1. Let d be the diameter of the rod, then the length L is:

$$L = P * 2d = 2dP \qquad [3.38]$$
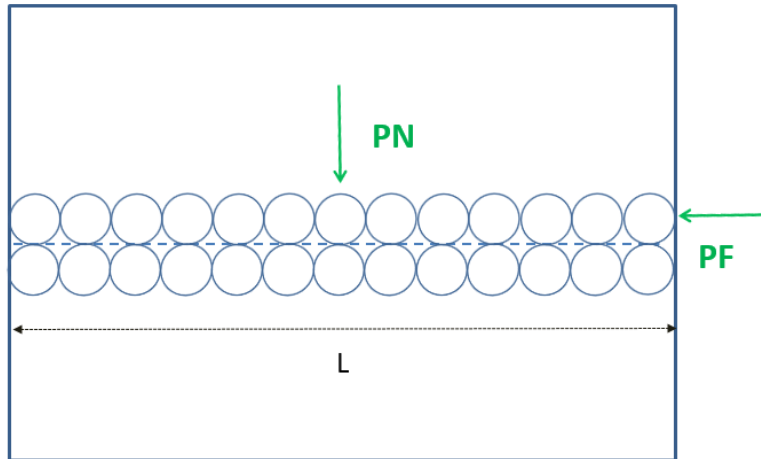
Figure 3.10 Direct shear failure surface consisting of P groups of rods (loosest packing)

For P groups of rods as shown in Figure 3.10, the forces PF and PN can be converted to stresses as follows:

$$\frac{PF}{Lt} = \frac{PN}{Lt} * A + 2\frac{T_m^p * P}{Lt} \qquad [3.39]$$

Similar to the derivation in the densest packing condition, the peak shear resisting force T_m^p can be represented by the shear bonding strength τ_m and the contact area a_c. Then, Eq. 3.39 can be written as:

$$\frac{PF}{Lt} = \frac{PN}{Lt} * A + 2\frac{\tau_m * wdP}{L} \qquad [3.40]$$

Substituting L in Eq. 3.38 into Eq. 3.40 results in:

$$\frac{PF}{Lt} = \frac{PN}{Lt} * A + \tau_m * w \qquad [3.41]$$

Comparing Eq. 3.12 and Eq. 3.41, the relationship between micro and macro parameters can be derived. When only friction is considered, the cohesion c and shear bonding strength τ_m are set to zero. The following relationship is obtained:

$$\frac{PF}{Lt} = \frac{PN}{Lt}\tan \phi_P = \frac{PN}{Lt} * A \qquad [3.42]$$

Therefore, the same relationship between ϕ_P, and ϕ_μ and φ_m as the densest packing is obtained.

$$\tan \phi_P = \tan(\phi_\mu + \varphi_m) \qquad [3.43]$$

When only the effect of cementing agent is considered, Eq. 3.12 and Eq. 3.41 are simplified into:

$$\frac{PF}{Lt} = c = \tau_m * w \qquad [3.44]$$

Then, the relationship between cohesion and shear bonding strength for the loosest packing is given by:

$$c = \tau_m * w \qquad [3.45]$$

3.4 Relationship between micro and macro strength properties

Microscopically shear strength consists of two components based on the Mohr Coulomb criterion, namely, cohesion and friction. At the micro scale, as shown in our derivation, the shear strength

consists of two components: bonding strength and micro friction that includes inter-particle friction and micro dilation, which is consistent with the Mohr Coulomb criterion.

According to Eq. 3.17, Eq. 3.30 and Eq. 3.43, the macro peak friction angle ϕ_P has the same relationship with the inter-particle friction angle and micro dilation angle for both densest packing and loosest packing.

$$\tan \phi_P = \tan(\phi_\mu + \varphi_m) \qquad [3.46]$$

The relationship between cohesion c and shear bonding strength τ_m in Eq. 3.19 and Eq. 3.32 for the densest packing, and Eq. 3.45 for the loosest packing are highly analogical. In addition, the equations can be written in the same form as shown in Eq. 3.47 if the term that relates to movement coefficient α and criterion V_c, and contact area coefficient w is represented by B. Term B mainly depends on the packing condition.

$$c = B * \tau_m \qquad [3.47]$$

where $B = \begin{cases} \left(\frac{1+\alpha}{2\alpha} V_c + \frac{\sqrt{3}}{6}\right) w & \text{for the densest packing} \\ w \text{ for the loosest packing} \end{cases}$, and the movement criterion V_C is given $\sqrt{3}$

when $V_C > \sqrt{3}$.

3.5 Summary

It is widely accepted that the shear bonding strength between particles is the same as cohesion, as defined in the Mohr Coulomb failure criterion in analyzing cemented granular material. For tensile failure, Brazilian tensile strength or direct tensile strength is usually used to determine the normal bonding strength between particles. In this chapter, using a simplified physical model and some published data on synthetic conglomerate, the normal and shear bonding strength between the particles and cementing agent were calculated and compared with the macro tensile strength and cohesion of the material. The results show that both normal and shear bonding strength is smaller than the corresponding commonly accepted macro parameters.

To investigate the relationship between the micro and macro mechanical properties of cemented granular material, two extreme regular packing conditions of uniform and rigid rods, namely, the

densest and loosest packings, are considered to develop the theoretical relationship. The derivation process is given in details in this chapter.

For the densest and loosest groups of rods, the movement and resisting forces of all contact points along the failure surface were analyzed firstly. By considering force equilibrium, the micro peak resisting force on the contact point was related to the externally applied load on the group of rods. To convert the externally applied load to the stresses involved in the Mohr-Coulomb criterion, P groups of rods of unit thickness along the direct shear failure surface were considered. In addition, a contact area between rod and cementing agent was assumed to calculate the micro bonding strength from the micro peak resisting force. Finally, by comparing the theoretical equations based on micromechanics with the Mohr-Coulomb criterion for macro behavior, the micro bonding strength and inter-particle friction angle of cemented granular material can be related to macro parameters which can be determined in laboratory experiments as shown in Eq. 3.46 and Eq. 3.47.

Chapter 4: Mechanical Properties of Cemented Granular Material

4.1 Introduction

To verify the theoretical relationship which relates the micro mechanical properties to the macro parameters of cemented granular material, all the measurements involved should be obtainable from laboratory tests, including the peak friction angle ϕ_p, cohesion c corresponding to the peak strength, the inter-particle friction angle ϕ_μ, movement coefficient α and criterion V_c, the contact area coefficient w, and the bonding strength τ_m and σ_m. The determination of these parameters is divided into two chapters. In this chapter, the experiments conducted to obtain the macro mechanical properties of artificial samples are discussed. Direct shear tests have been performed to obtain the peak friction angle and cohesion corresponding to the peak strength. Uniaxial and triaxial tests have been conducted to confirm the results from direct shear testing. Brazilian tensile tests have been conducted to measure the macro tensile strength. Moreover, the inter-particle friction angle and movement criterion are determined with designed innovative testing programs and introduced in this chapter.

4.2 Objectives of the experiments

The experiments on artificial conglomerate are aimed at achieving the following objectives:

- Study the macro mechanical behavior of artificial conglomerate (with steel balls and Portland cement) and cement paste samples using various laboratory tests.
- Measure the inter-particle friction angle and movement criterion, and determine the bonding strength between the steel ball and Portland cement through post failure analysis.
- Verify the theoretical relationship between micro and macro mechanical parameters with laboratory results.

4.3 Sample preparation

4.3.1 Materials

Steel balls and Portland cement were used to prepare the artificial samples.

- Steel ball is used as the granular particle mainly for two reasons. Firstly, it has significantly higher strength than the cementing agent and remains intact during testing. This makes the post-failure analysis more feasible without considering the effect of particle crushing on the mechanical properties of samples. Secondly, the spherical shape of steel ball eliminates the effect of particle shape on the mechanical behavior.
- Portland cement is chosen firstly because its strength can be adjusted using different water-cement ratios. Secondly, Portland cement was used in related research and the results from this study can be compared with the published data.

4.3.2 Sample preparation procedures

In this study, artificial conglomerate samples and cement paste samples were prepared for a series of laboratory tests including direct shear, uniaxial/triaxial and Brazilian tensile tests. The dimensions of cylindrical shaped samples for the laboratory testing are shown in Table 4.1.

Table 4.1 Dimensions of samples for laboratory testing

Tests	Diameter/length or thickness (mm)	
	Artificial conglomerate	Cement paste sample
Direct shear test	63.5/127	63.5/127
Uniaxial/Triaxial test	63.5/127	63.5/127
Brazilian tensile test	63.5/40	63.5/40

Split moulds with diameter of 63.5 mm (2.5 inch) were used as shown in Figure 4.1(a). To eliminate the effect of sample size on test results, steel balls with diameters of 3.2 mm (1/8 inch) and 4.8 mm (3/16 inch) were chosen as per ASTM D5607 and ASTM D3967's recommendation. The least cross-sectional dimension of the sample should be no less than 10 times the largest grain size in the sample. Steel balls were compacted to the densest state (porosity = 38.5%) during all conglomerate samples preparation. The amount of steel balls required for different sample sizes was calculated based on the total volume and porosity. Two types of Portland cement paste with water-cement ratio (W/C) of 0.6 and 0.45 were used in this study.
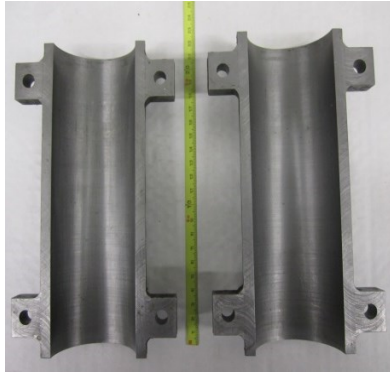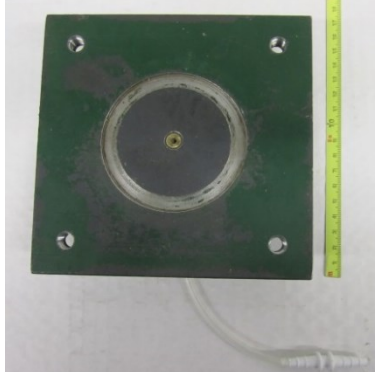
(a) Split mould   (b) Mould pedestal   (c) Slotted steel plate
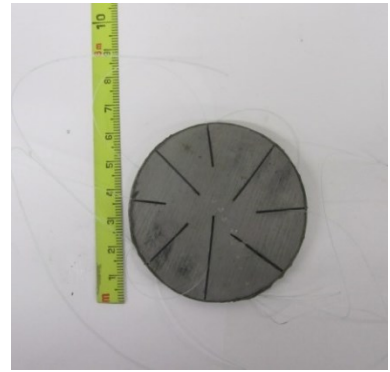
(d) Cellophane attached to mould   (e) Assembled mould   (f) Mould and steel balls

(g) Dead load and vibrating table   (h) Sieving   (i) Injecting cement

Figure 4.1 The stepwise procedure of sample preparation

Detailed sample preparation procedures are given in Figures 4.1(b) to 4.1(i). A 3-mm hole was drilled in the pedestal base and then connected to an injection tube as shown in Figure 4.1(b). A slotted steel plate as shown in Figure 4.1(c) was prepared to allow air to flow upwards freely during cement injection. A piece of cellophane was attached to the mould using silicon to minimize the friction between sample and mould as shown in Figure 4.1(d). A pre-determined amount of steel balls was poured into the assembled mould as shown in Figures 4.1(e) and (f). To achieve the densest state, vibrating table was used with a dead load sitting on the mould pedestal above the steel balls (Figure 4.1(g)). Portland cement was sieved through Sieve #200 (75μm) to exclude cement lumps (Figure 4.1(h)). High range water reducer (1g water reducer to 100 g cement) was added to cement and water paste to increase the flowability. The cement paste was then injected to the mould through the 3-mm hole in the base plate with the help of syringe as shown in Figure 4.1(i). Extra cement paste was injected to create a flat top surface. The sample was extracted after curing in the mould for 24 hours under room temperature. A 2-mm thick cement paste was left at the top part of the sample during cutting and grinding, see Figure 4.2. Similarly, the pure cement paste sample was prepared. All samples were then cured in the water tank for a minimum of 28 days.

Figure 4.2 The cement paste and artificial conglomerate samples

4.3.3 Sample treatment before testing

The degree of saturation and the corresponding treatment technique of the sample need to be considered before testing. Yurtdas et al. (2004a, b) studied the effect of drying on the mechanical behavior of mortar, which was made by sand, cement and water. After immersing the samples in

water for 6 months, all the mortar samples were treated in different ways. While some samples were protected from drying, some were dried at 60°C in oven and the rest of the samples were left to desiccate at 21°C and 45% humidity. Uniaxial compression tests were conducted on the samples to study the effect of drying. The results for the samples left in desiccation in Figure 4.3 show that the UCS strength increases with weight loss and approaches peak value after about 2.5~3% weight loss and stays constant afterwards. The peak strength is equal to that of the samples dried at 60°C in the oven. Therefore, the cemented granular samples are not necessarily completely dried to reach constant peak strength.
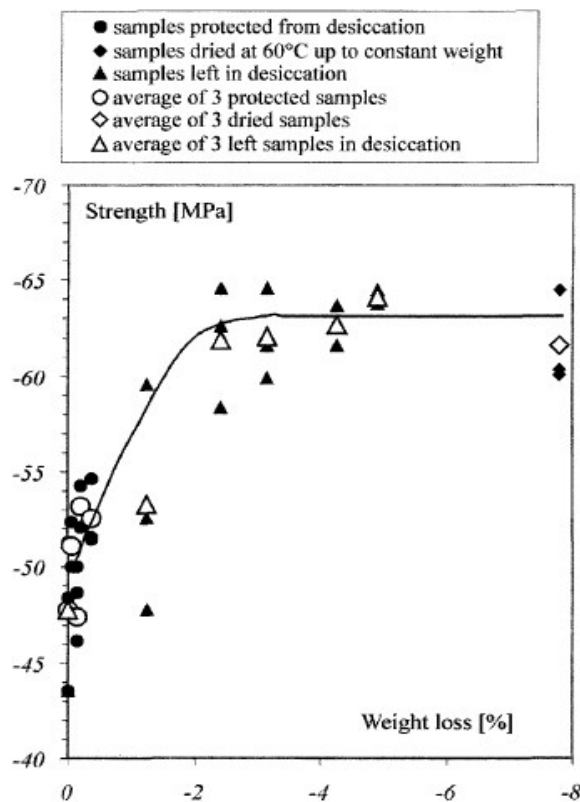
Figure 4.3 The UCS of mortar versus weight loss (Yurtdas et al. 2004a)

Skoczylas et al. (2007) investigated the effect of drying on strength and elastic properties of mortar using uniaxial compression tests. Mortar samples were divided into 3 groups after curing in water for 6 months. Group 1 samples were tested as saturated. Group 2 samples were dried at 60°C in the oven before testing. Group 3 samples were dried and re-saturated in ethanol before testing. As seen in Table 4.2, minor effects on Young's modulus and Poisson's ratio took place by comparing the results of dried and re-saturated samples. It implies that the pore fluid would not lead to obvious

44

difference in mechanical behavior. Moreover, negligible effect on the strength was found by comparing the mean UCS of saturated and re-saturated samples. It shows that the mortar pore structure remained nearly unchanged during the drying process. Bahador and Jong (2006) used CO_2 gas diffusivity to examine changes of pore structure of concrete samples under different drying conditions. Results show that the 105°C oven drying for 24 hours damages the pore structure both near sample surface and in the center, while the 40°C oven drying for a month and air drying for 3 months only deteriorate the near surface pore structure. It can be concluded that testing on air dried samples can generate consistent mechanical properties, and the pore fluid would not lead to much difference to the mechanical behavior when weight loss is beyond a critical value (e.g., 2.5 to 3%).

Table 4.2 Effect of drying on strength and elastic properties (Skoczylas et al. 2007)

Mortar samples	UCS (MPa)	Young's modulus (MPa)	Poisson's ratio
Saturated samples	50.4	36700	0.2
Dried samples	61.6	31800	0.15
Re-saturated samples	51	31800	0.15

It is difficult to determine if samples are fully saturated and drained testing is deemed necessary to eliminate the effect of air in samples. The estimated testing time is over 10 days for sample with height of 127 mm under drained condition, using Bishop and Henkel's (1957) equation (Eq. 4.1) and published data on cement properties. Table 4.3 lists the pros and cons of using air-dried and saturated samples. It is apparent that air-dried samples are favourable as the testing is simple and efficient while producing consistent results.

$$t_f = \frac{h^2}{\eta c_v \cdot 0.05}$$

[4.1]

where t_f is the requisite time to failure for a drained test,

h is ½ height of the sample,

c_v is the coefficient of consolidation, and

η is a factor depending upon drainage conditions at the sample boundaries.

Table 4.3 Comparison of using air-dried samples and saturated samples

Comparison	Air-dried samples	Saturated samples
Pros	• Simple and efficient; • Consistent in results; • Provide all parameters required; • Lots of published data for comparison;	• Measure pore pressure; • Minimal micro cracks; • Provide all parameters required;
Cons	• Micro cracks; • Possible effect of pore water pressure; • Required time for air drying;	• Difficult to achieve fully saturated; • Time consuming; • Complicated testing procedures;

In this research, five artificial conglomerate samples were prepared with steel balls of 4.8 mm and cementing paste with water-cement ratio of 0.6. Samples were air-dried for various periods under constant ambient temperature (21°C) and tested with uniaxial compression test. Figure 4.4 presents the strength with various drying time and indicates that 15 days of air-drying is sufficient to produce consistent results. Therefore, all the prepared samples were air-dried for minimum 15 days before testing in this study.
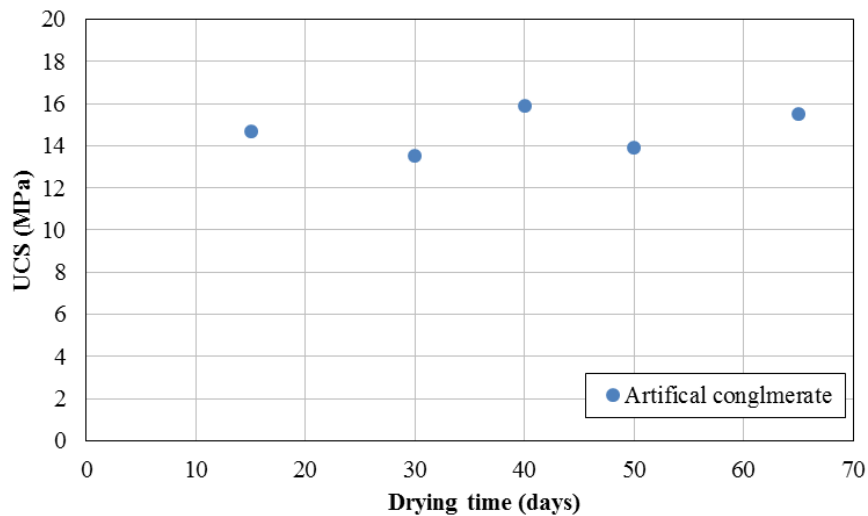
Figure 4.4 Unconfined compressive strength versus drying time of artificial conglomerates

4.4 Direct shear, Uniaxial/Triaxial and Brazilian tensile testing

Direct shear tests, uniaxial/triaxial compression tests and Brazilian tensile tests were conducted to study the macro mechanical behavior of artificial conglomerates. Also, all tests were conducted

on cement paste samples, and the main focus is to determine the cohesion and tensile strength of cement used in the post failure analysis. The required measurements for each type of test are listed in Table 4.4. In addition, the failure surfaces from direct shear testing and Brazilian tensile tests were used in the post failure analysis to obtain the micro bonding strength between cement and steel balls.

Table 4.4 Measurements required and the corresponded tests

Tests	Parameters	
	Artificial conglomerate	Cement paste sample
Direct shear test	Peak strength, peak cohesion, peak friction angle, and micro shear bonding strength	Peak strength and peak cohesion
Uniaxial/Triaxial test	Peak strength, peak cohesion and peak friction angle	Peak strength and peak cohesion
Brazilian tensile test	Tensile strength and micro normal bonding strength	Tensile strength

Table 4.5 Summary of types of samples and number of samples for different testing

Artificial samples	Type of sample	Number of direct shear test	Number of Uniaxial/Triaxial test	Number of Brazilian tensile test
Group 1	Conglomerate with 4.8 mm steel balls and w/c ratio of 0.6 cement paste	5	4	4
Group 2	Conglomerate with 3.2 mm steel balls and w/c ratio of 0.6 cement paste	5	4	4
Group 3	Conglomerate with half of 3.2 mm and half of 4.8 mm steel balls, and w/c ratio of 0.6 cement paste	5	4	4
Group 4	Conglomerate with 4.8 mm steel balls and w/c ratio of 0.45 cement paste	5	4	4
Group 5	Cement paste sample with w/c ratio of 0.6	5	4	6
Group 6	Cement paste sample with w/c ratio of 0.45	5	4	6

For the artificial conglomerate, the effects of several factors on the macro relationship were investigated: particle size, uniform or non-uniform particle size distribution and cementing strength. For each group of samples, five direct shear tests and four uniaxial/triaxial tests (one uniaxial test and three triaxial tests) were conducted at different normal/confining stresses, and four or six Brazilian tensile tests were carried out to obtain the tensile strength. The factors studied and corresponding number of tests are shown in Table 4.5.

4.4.1 Direct shear tests

Based on ASTM 5607 standard, 6 groups of artificial samples were tested with the RDS-100 direct shear system (Figure 4.5). The test specimen was mounted inside the shear box with the shear gap smeared with manufacturer-provided modeling clay, and the normal and shear loads were controlled by the syringe pumps. The maximum normal load and shear load can be applied by this system are 50 kN and 100 kN, respectively. The maximum allowable shear displacement is 10 mm. For each group of samples, 4 specimens were tested under the normal stresses of 0.5, 2, 5 and 10 MPa to ensure the applied shear loads were within the apparatus's limits. Also, one extra test was repeated at one of the normal stresses to check the consistent of the results. To avoid any movement of steel balls during testing, a constant low axial displacement rate of 0.001mm/s was applied in all the tests. The shear stress, shear displacement and vertical displacement were monitored at a recording rate of 6 readings per second.

Figure 4.5 The RDS-100 direct shear system

The shear stress versus shear displacement plots and the vertical displacement versus shear displacement plots for the 6 groups of samples are shown in Figures 4.6 through 4.17. The distinct shear planes lead to obvious strain softening behavior for all the samples. With the increase of the normal stress, both the peak shear stress and the corresponding shear displacement increase. For each group of artificial conglomerates, the stress-strain curves under different normal stresses before the peak point are parallel to each other. The reason is that the steel balls within the conglomerate are nearly incompressible and the number of contacts among the balls does not increase with the normal stress, which leads to similar stiffness of the conglomerate under different normal stresses. Besides, the brittle stress-strain relationship indicates that the peak strength is mainly contributed by breaking the cement bonds. After the peak point, the softening behavior is affected by the decrease in dilation rate. During the shearing, all the artificial conglomerates and cement paste samples show volumetric contraction, which is followed by a subsequent volumetric dilation. The amount of contraction during shearing is increased with the normal stress for every group of samples. While the artificial conglomerates failed gradually after peak with no cracking sound, the cement pastes failed abruptly with loud cracking noise. As shown in Figures 14 and 16, the steep curves after peak points are due to the rapid release of energy of the machine after the cement-cement bonds are totally broken.

The shear strength under different normal stresses and the calculated macro dilation angles are summarized in Table 4.6. The tests show a good reproducibility of the results. Also, the peak shear strength of artificial conglomerates and cement paste samples are plotted against the corresponding normal stresses in Figure 4.18 and 4.19, respectively, to determine the Mohr-Coulomb's strength parameters. For the artificial conglomerates, the cohesion is in the range of 2.3 to 3.2 MPa, and the friction angle is between 55.9° and 59.5°. Furthermore, as shown in Figure 4.18, no distinct difference can be observed among the failure envelops of different groups of conglomerates. As discussed in Section 4.3, all the conglomerates were made with the densest steel balls packing structure with 38.5% of the whole volume being occupied by steel balls. It seems that for the artificial conglomerates with the same structure of steel balls assembly, the effect of particle size and uniform/non-uniform particle size distribution on the strength and mechanical behavior is not obvious. This finding is consistent with the theoretical relationship developed in Chapter 3, which shows that the macro friction angle and cohesion have no relationship with particle size.

For the cement paste samples, the w/c ratio of 0.45 cement paste samples have a higher cohesion (4.40 MPa) than that of cement paste samples with w/c ratio of 0.6 (4.00 MPa), but the friction angles of the two groups of cement paste sample are very similar (62.6° and 62.4°, respectively). This is consistent with Hyett et al. (1992) and Contreras et al. (2008)'s statement that the strength of Portland cement sample decreases with increase of w/c ratio after a limited w/c ratio. However, since the difference between the two groups of cement paste samples is not obvious, the effect of cementing strength on the macro mechanical behavior cannot be concluded, and the failure envelopes of group 1 and group 4 artificial conglomerates are found similar.

As shown in Table 4.6, the macro dilation angle of all tested artificial conglomerates is in the range of 58.7° to 67.2°, and those almost parallel dilation curves in Figures 4.7, 4.9, 4.11 and 4.13 show that the dilation is insensitive to the normal stress. The variation of normal stress only changes the onset of dilation but does not affect its magnitude. The high macro dilation angle in the direct shear test is due to the presence of steel balls. While the cement matrix would be crushed during shearing along the failure surface, the steel balls on the shear plane are incompressible and the sliding between steel balls leads to the high macro dilation angle. Also, the failed particle and cement fabric may give a more dilatant behavior during shearing compared with pure steel balls assembly. For the cement paste samples, the macro dilation angle has a very large range, from 0° to 87.6°. Also, the macro dilation angle decreases significantly with the increase of normal stress for the two groups of samples.

As shown in Figure 4.20, the shear surfaces of failed samples were preserved for post failure analysis. The predominant failure was found along the steel ball-cement contacts in all the artificial conglomerate failure surfaces, which indicates that the shear bond between steel ball and cement is much weaker than that of the cement matrix. In addition, for some of the shear planes, the failure surfaces extended a little to the sample halves, which shows the existing of secondary failure cracks.
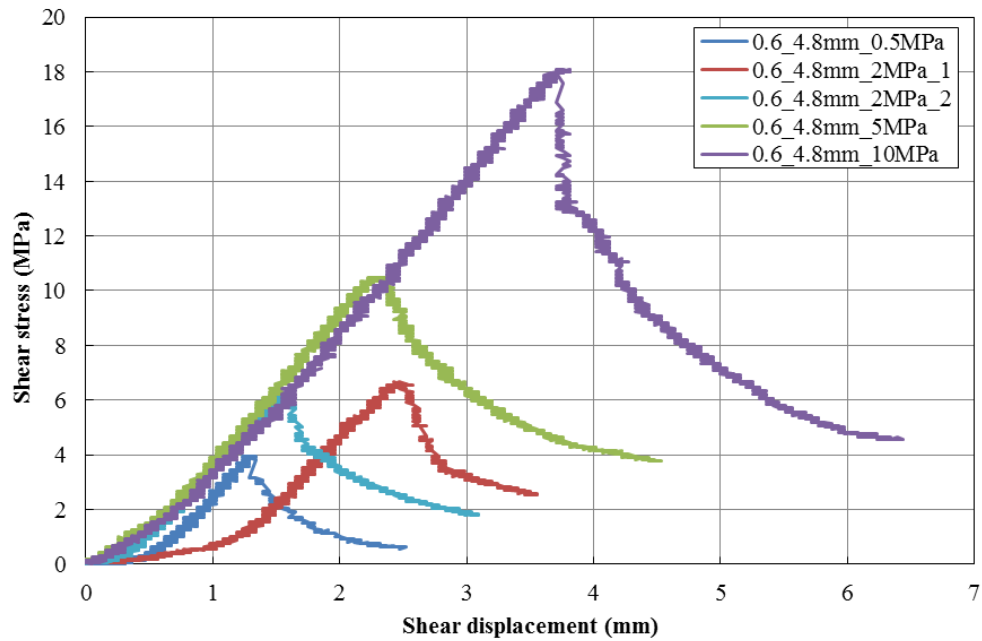
Figure 4.6 Shear stress versus shear displacement of group 1 artificial conglomerates
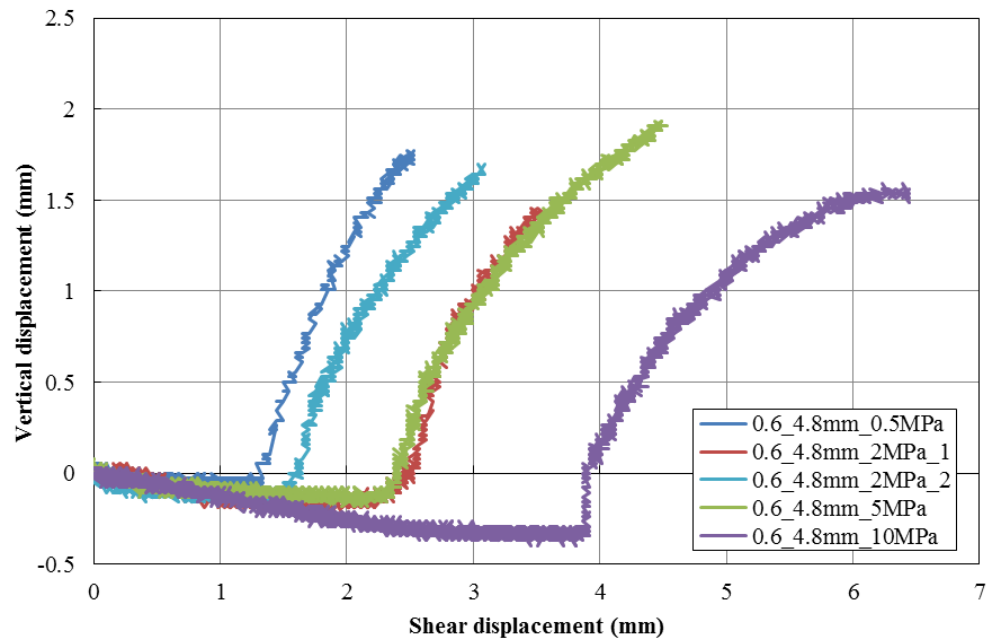
Figure 4.7 Vertical displacement versus shear displacement of group 1 artificial conglomerates
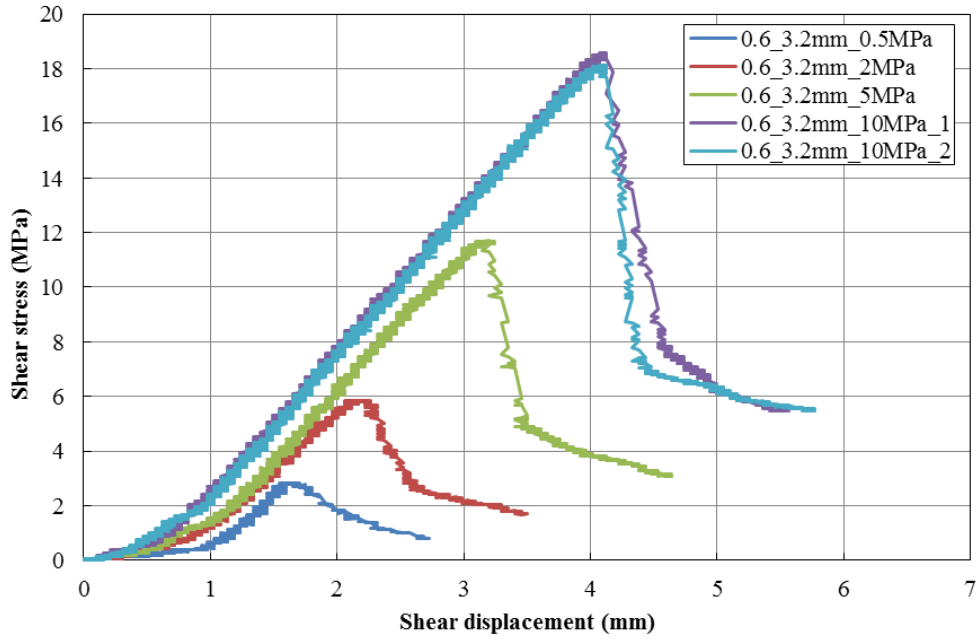
Figure 4.8 Shear stress versus shear displacement of group 2 artificial conglomerates
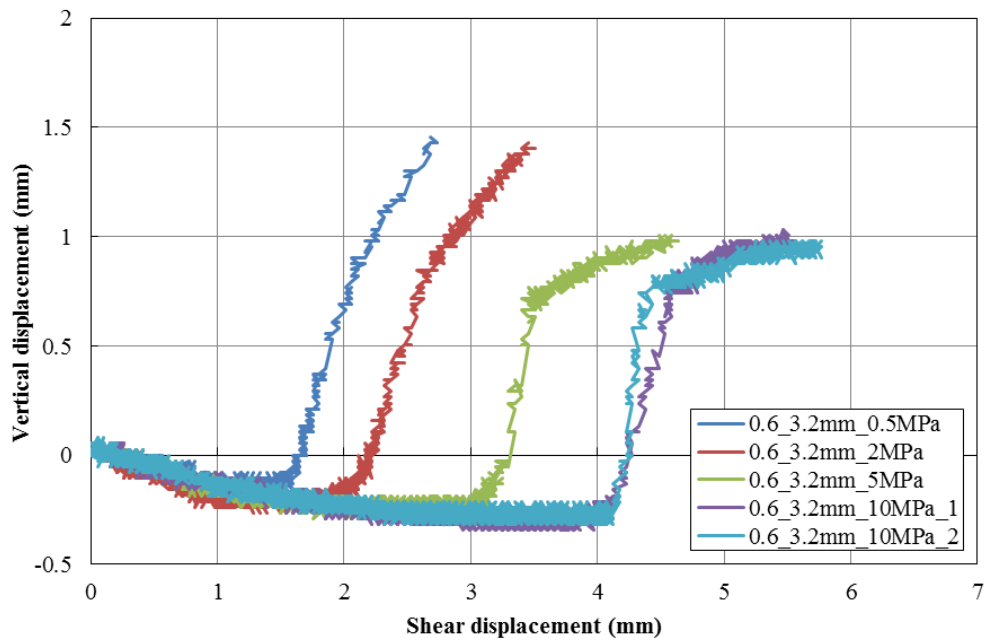
Figure 4.9 Vertical displacement versus shear displacement of group 2 artificial conglomerates
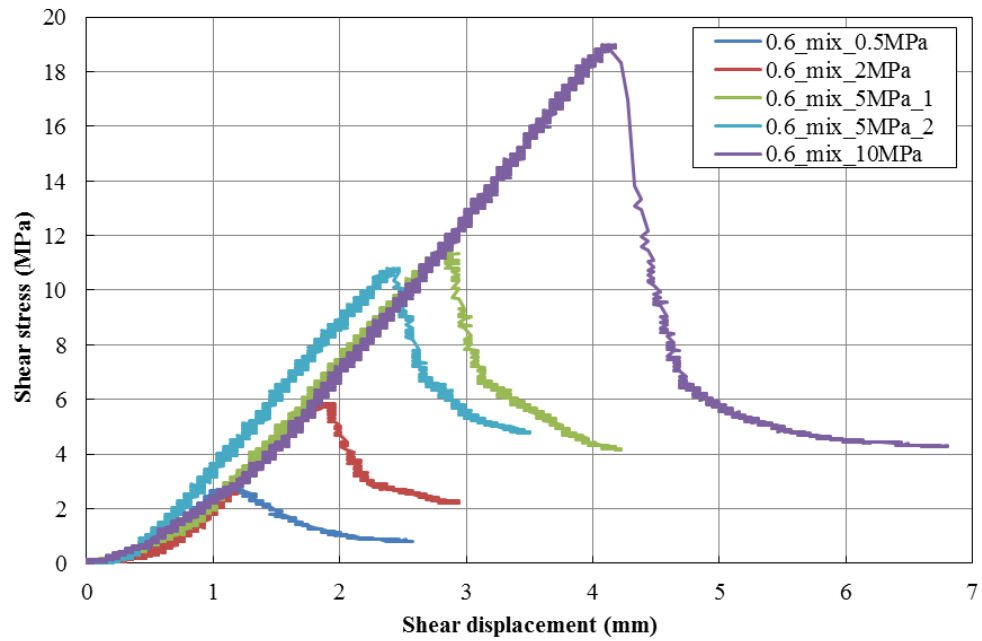
Figure 4.10 Shear stress versus shear displacement of group 3 artificial conglomerates
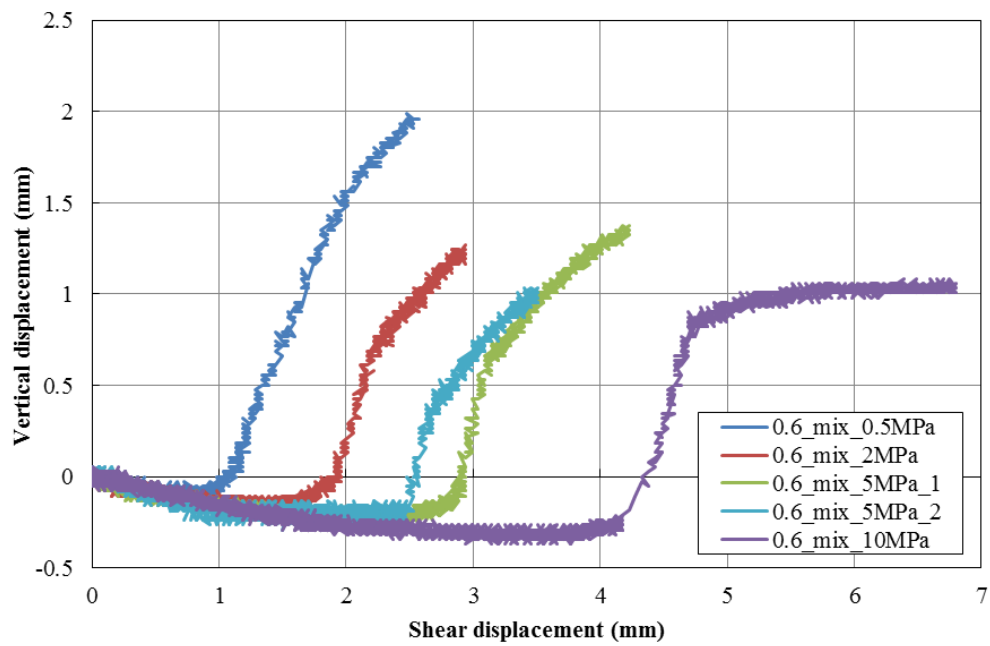
Figure 4.11 Vertical displacement versus shear displacement of group 3 artificial conglomerates
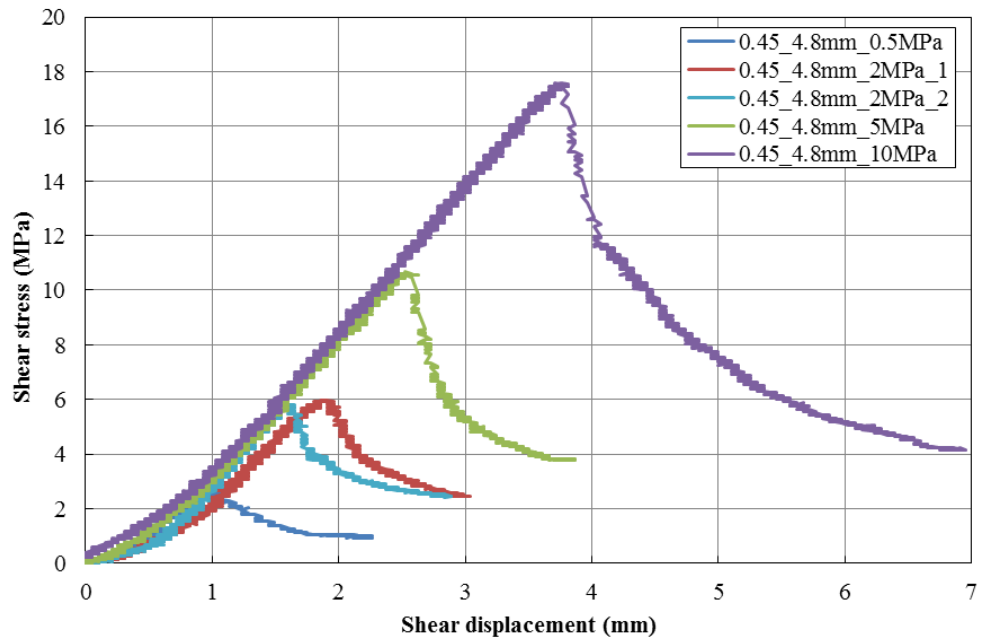
Figure 4.12 Shear stress versus shear displacement of group 4 artificial conglomerates
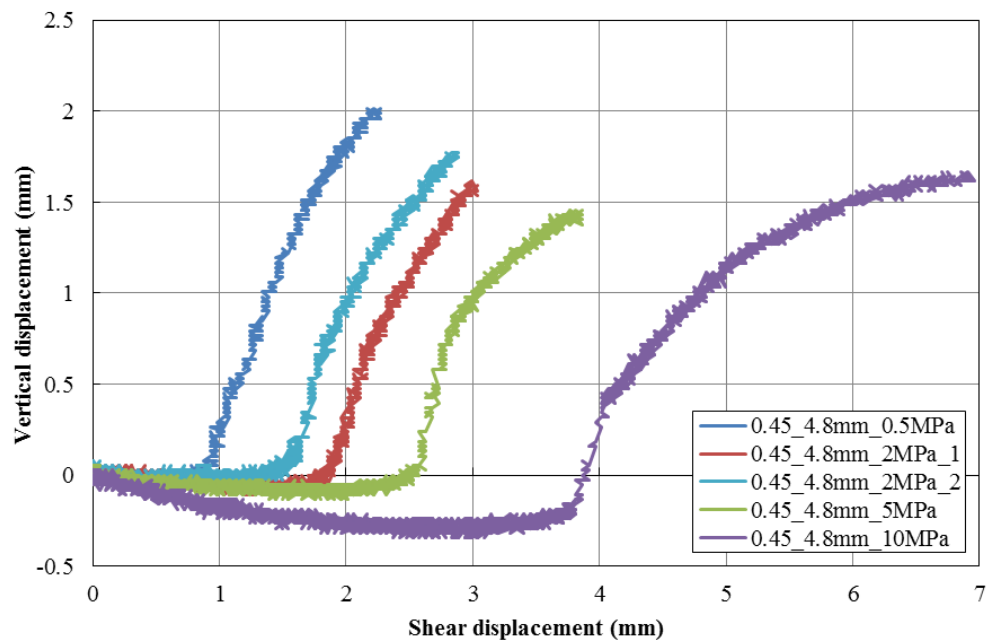
Figure 4.13 Vertical displacement versus shear displacement of group 4 artificial conglomerates
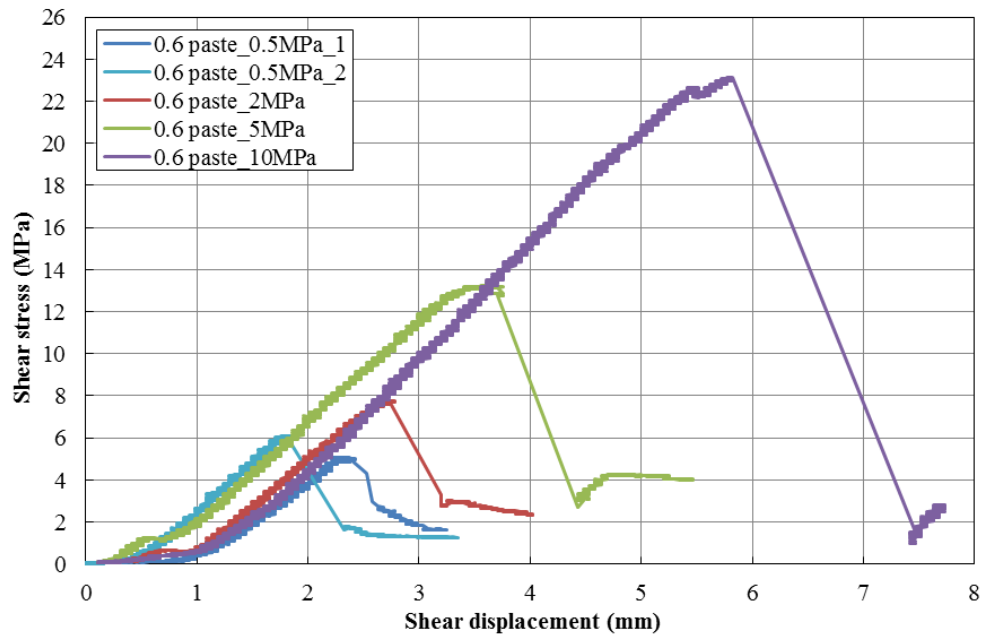
Figure 4.14 Shear stress versus shear displacement for cement paste samples with water-cement ratio of 0.6

Figure 4.15 Vertical displacement versus shear displacement for cement paste samples with water-cement ratio of 0.6
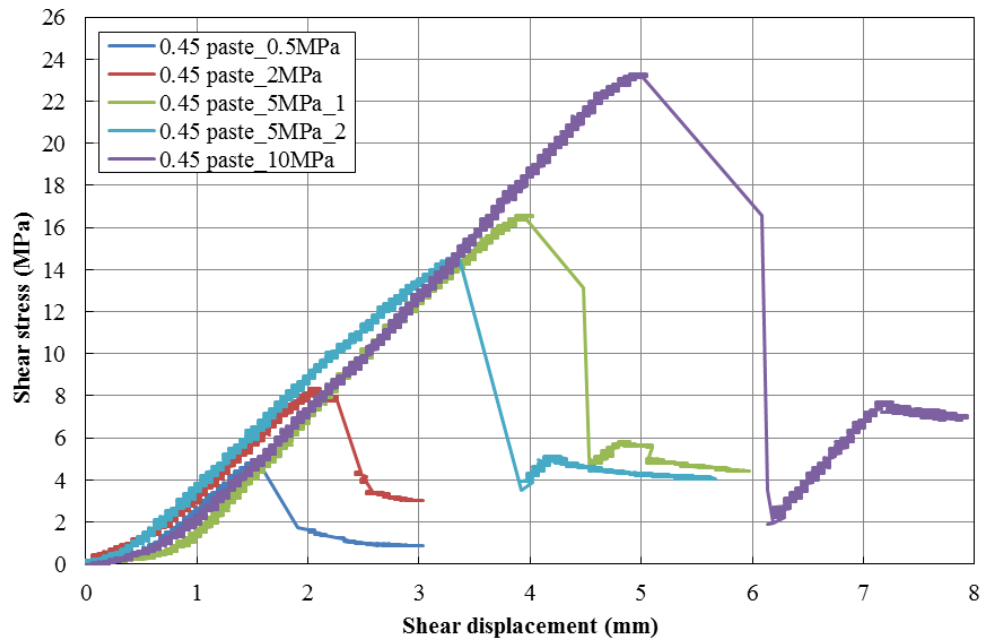
Figure 4.16 Shear stress versus shear displacement for cement paste samples with water-cement ratio of 0.45
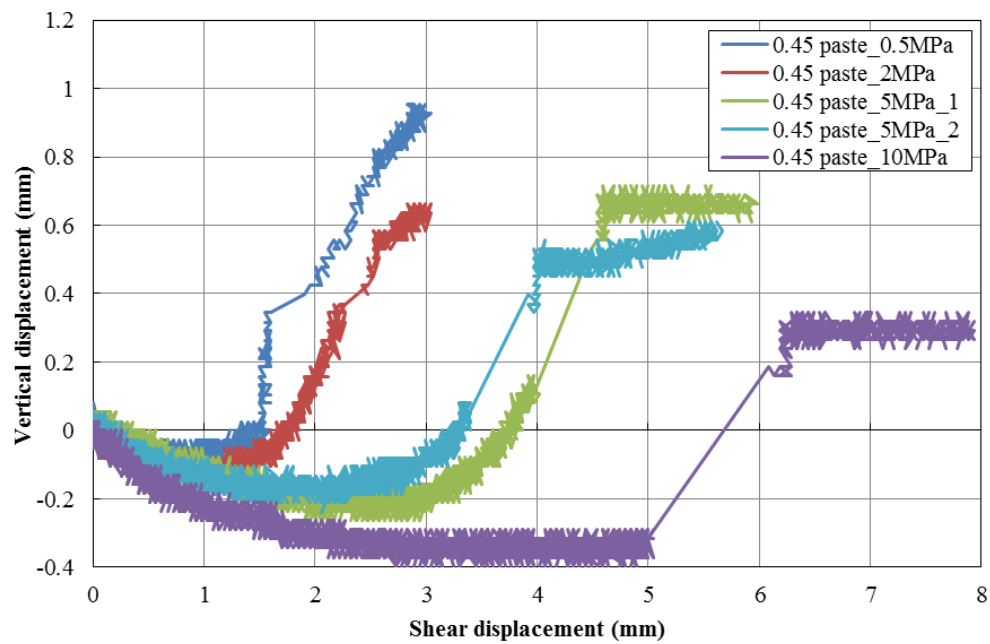
Figure 4.17 Vertical displacement versus shear displacement for cement paste samples with water-cement ratio of 0.45

Table 4.6 Summary on direct shear testing results

Artificial samples	Sample No.	Normal stress (MPa)	Shear strength (MPa)	Macro Dilation angle (°)	Cohesion (MPa)	Friction angle (°)
Group 1	0.6_4.8mm_1	0.5	3.96	63.8	3.22	55.91
	0.6_4.8mm_2	2	6.49	66.5		
	0.6_4.8mm_3	5	10.39	62.9		
	0.6_4.8mm_4	10	18.08	58.7		
	0.6_4.8mm_5	2	6.04	63.3		
Group 2	0.6_3.2mm_1	0.5	2.84	62.9	2.64	57.95
	0.6_3.2mm_2	2	5.86	61.6		
	0.6_3.2mm_3	5	11.72	60.1		
	0.6_3.2mm_4	10	18.56	60.6		
	0.6_3.2mm_5	10	18.13	63.4		
Group 3	0.6_mix_1	0.5	2.78	62.6	2.33	59.45
	0.6_mix_2	2	5.86	63.1		
	0.6_mix_3	5	11.35	65.3		
	0.6_mix_4	10	19.00	61.4		
	0.6_mix_5	5	10.79	62.8		
Group 4	0.45_4.8mm_1	0.5	2.71	63.4	2.59	56.82
	0.45_4.8mm_2	2	5.98	63.7		
	0.45_4.8mm_3	5	10.67	67.2		
	0.45_4.8mm_4	10	17.60	63.1		
	0.45_4.8mm_5	2	5.80	64.5		
Group 5	0.6 paste_1	0.5	5.06	85.2	4.00	62.37
	0.6 paste_2	2	7.77	54.8		
	0.6 paste_3	5	13.38	45.8		
	0.6 paste_4	10	23.13	16.7		
	0.6 paste_5	0.5	6.00	73.8		
Group 6	0.45 paste_1	0.5	4.94	87.6	4.40	62.61
	0.45 paste_2	2	8.33	55.5		
	0.45 paste_3	5	16.40	34.3		
	0.45 paste_4	10	23.31	0		
	0.45 paste_5	5	14.74	32.9		
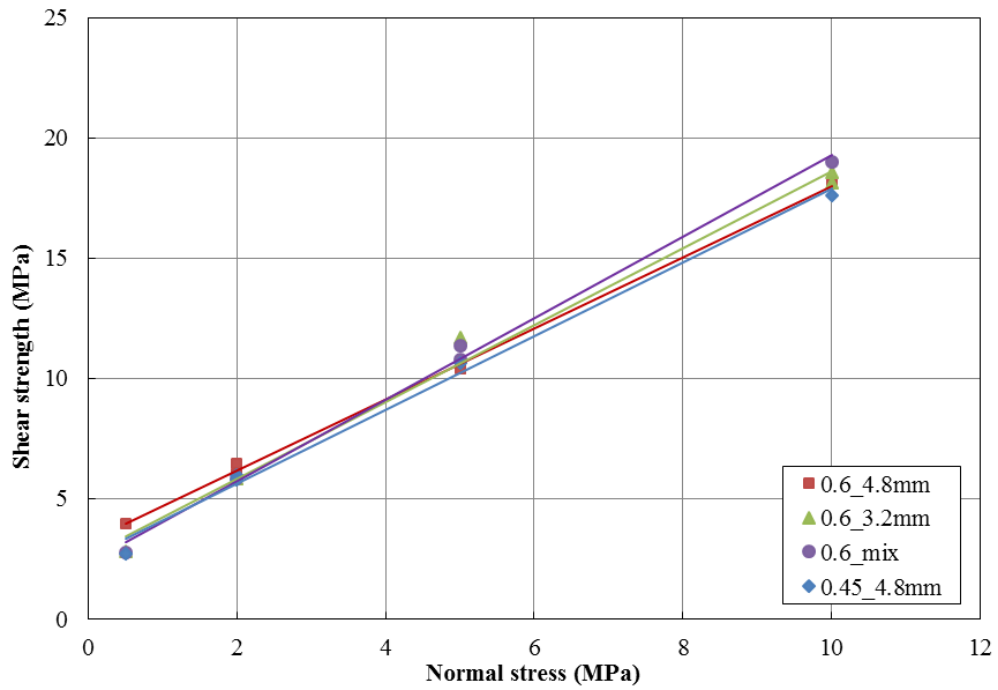
Figure 4.18 Shear strength versus normal stress of the artificial conglomerates
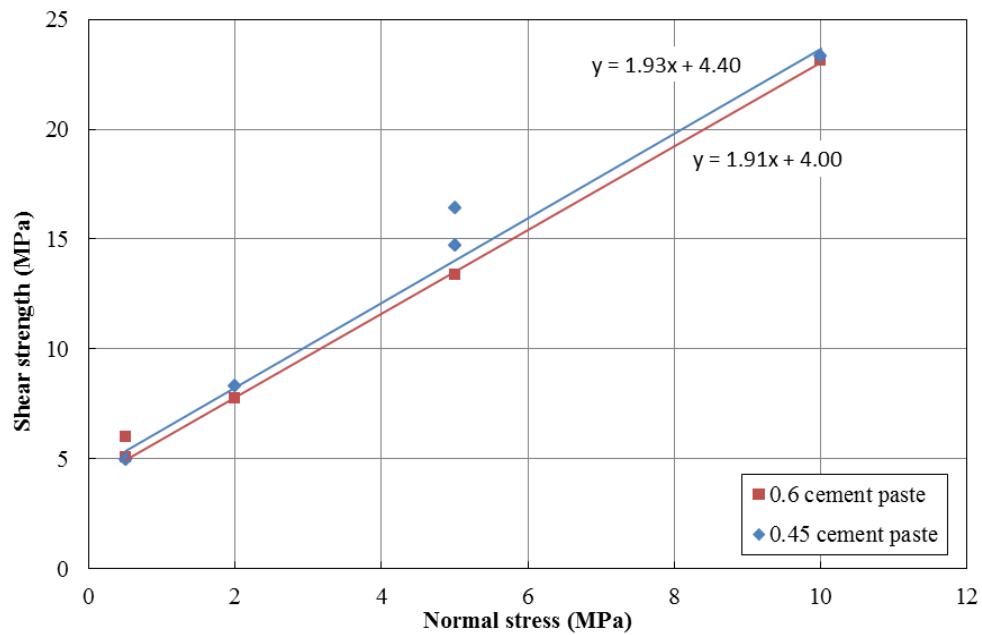
Figure 4.19 Shear strength versus normal stress of the cement paste samples

58
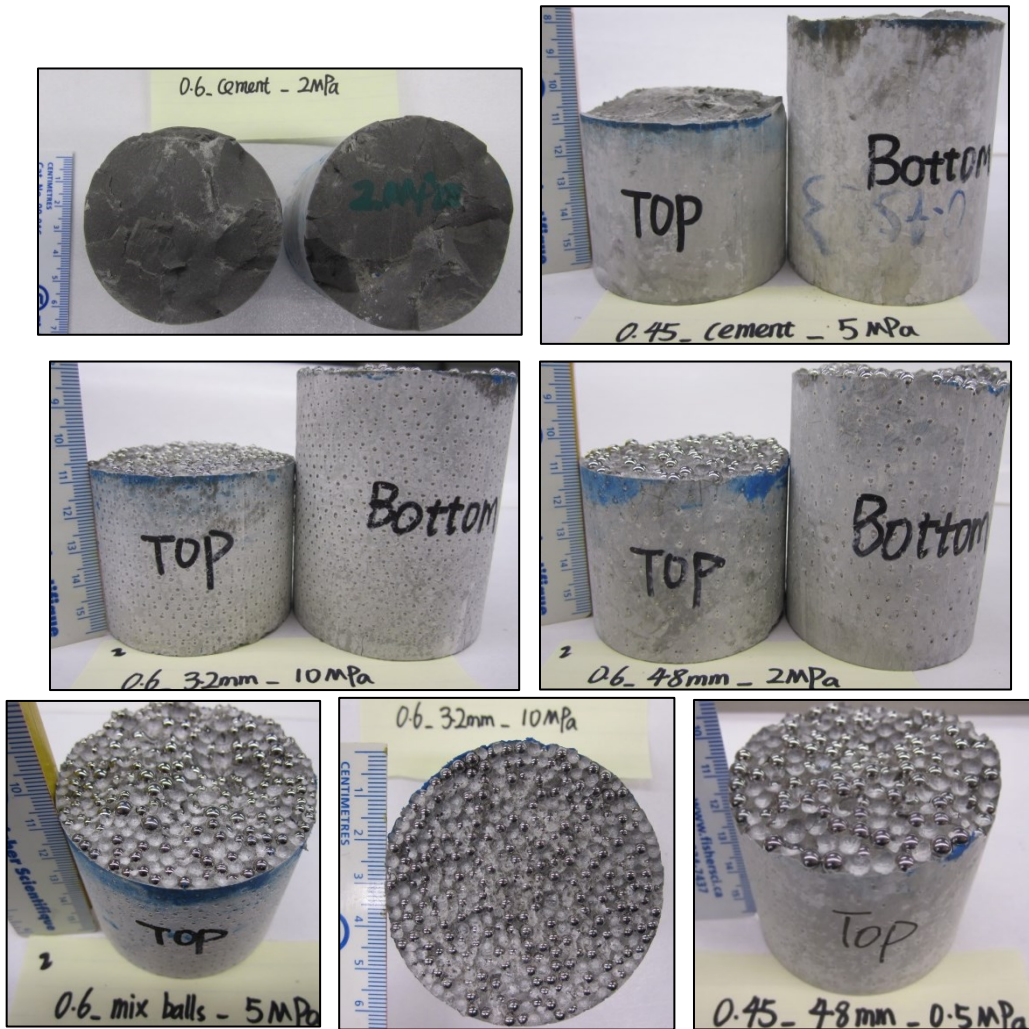
Figure 4.20 Examples of shear surfaces from direct shear testing

4.4.2 Uniaxial/Triaxial tests

Six UCS tests and 18 triaxial tests were performed to obtain the strength parameters listed in Table 4.4. For the first 5 groups of samples, the confining stresses applied were 0.5, 2 and 5 MPa. Due to safety concern, group 6 samples were only tested up to confining stress of 2 MPa. Figure 4.21 shows the key testing procedures and the testing apparatus INSTRON 500 tons. Like a typical triaxial test, the sample was fitted inside nitrile membrane (D = 2.5 inch) to isolate the sample from cell fluid (Figure 4.21(a)). It was then placed between base pedestal of the cell and loading rod and sealed with 3 O-rings on each side (Figure 4.21(b)). The cell and cap were mounted subsequently. Silicon oil was used as the cell fluid to transmit confining pressure to sample (Figure 4.21(c)). The remaining air in the cell was expelled completely using ISCO pumps. Protecting shield must be in

place prior to applying any load (Figure 4.21(d)). A constant shear displacement rate of 0.001 mm/s was used for all the tests. The axial load and axial displacement were monitored at the recording rate of one reading per second.

(a)   (b)   (c)   (d)
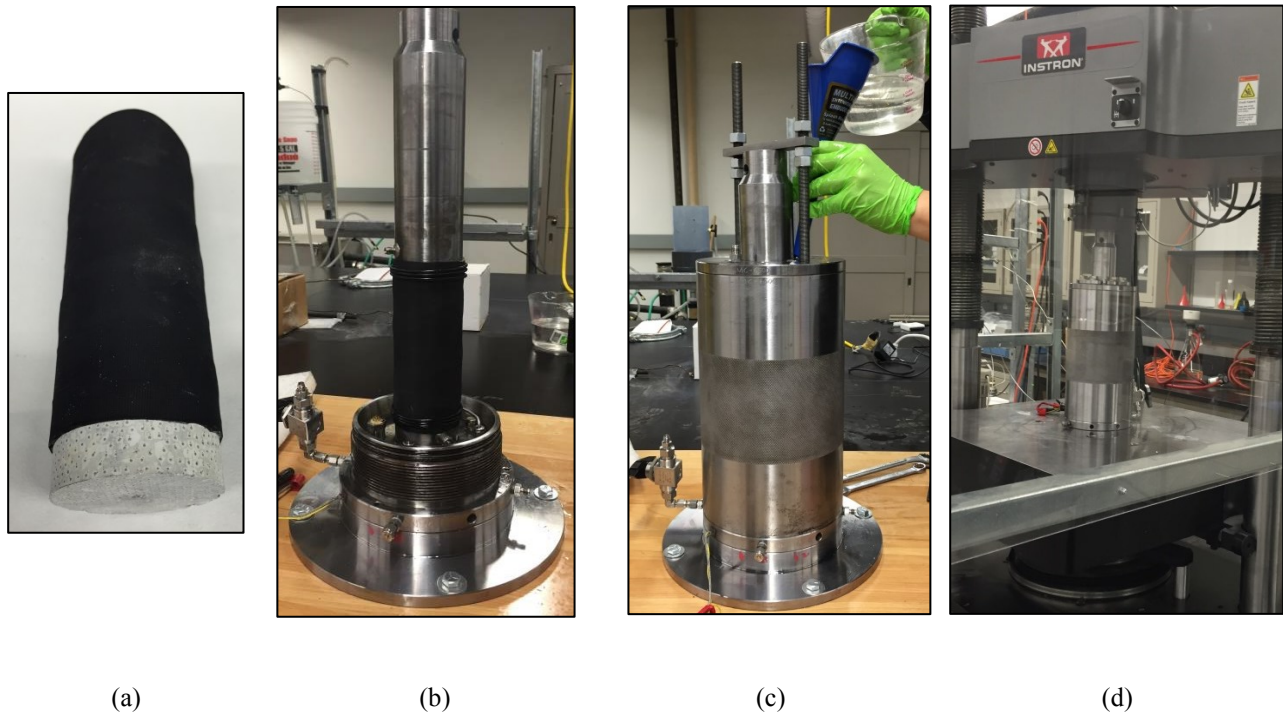
Figure 4.21 The triaxial testing apparatus: (a) Specimen wrapped with the nitrile membrane; (b) Specimen mounted inside the cell; (c) The vessel filled by the silicon oil; (d) The triaxial testing in progress.

The axial stress-strain plots of artificial conglomerates are shown in Figures 4.22 to 4.25. All curves show similar strain softening behavior. Both the magnitudes of peak strength and axial yield strain increase with the confining stress. The stress-strain behavior is brittle under low confining stresses. It is because the bonding between the steel balls and cement contributes more to the strength than the friction between particles under low confining stress. On the other hand, if the confining stress is higher, the stress-strain behavior could become more ductile due to the increased contribution of friction to the strength. Figures 4.22 through 4.25 also demonstrate that the stress-strain curves for different confining stresses have similar slopes before reaching peak stress. For natural cemented granular material, it is known that the stiffness of sample increases with confining stress due to the increases in particle contacts. However, the steel balls within the artificial conglomerate are "incompressible" and in the densest packing condition. The contacts

between the spherical steel balls would not increase with the confining stress, therefore, there is negligible change in the stiffness.

The axial stress-strain plots of cement paste samples are given in Figures 4.26 and 4.27. For group 5 cement paste samples in Figure 4.26, the stress-strain curve for the 2 MPa confining stress demonstrates a strain hardening behavior, while the other two curves for the 0.5 MPa and 5 MPa confining stresses show strain softening behaviors. The micro cracks developed during drying could contribute to this difference. Although all samples were dried for the same period of time, the size and intensity of micro cracks are different in each sample. However, all group 6 samples show strain softening behavior in Figure 4.27, with loud cracking sound. This brittle stress-strain relationship and distinct softening behavior is evident in the cement paste samples with low water-cement ratio (Harsh et al. 1990).

To obtain the best fit Mohr-Coulomb failure envelop, the $(\sigma_1 - \sigma_3)/2$ versus $(\sigma_1 + \sigma_3)/2$ plot is used based on the following Mohr-Coulomb relationships.

$$\frac{\sigma_1 - \sigma_3}{2} = c * \cos \phi + \frac{\sigma_1 + \sigma_3}{2} \sin \phi \qquad [4.2]$$

$$\tau = c + \sigma \tan \phi \qquad [4.3]$$

where σ_1 is the axial stress, MPa

$\quad$ σ_3 is the confining stress, MPa

$\quad$ c is the cohesion, MPa

$\quad$ ϕ is the friction angle, °

$\quad$ τ is the shear strength, MPa, and

$\quad$ σ is the normal stress, MPa.

The $(\sigma_1 - \sigma_3)/2$ versus $(\sigma_1 + \sigma_3)/2$ plot for the first group of artificial conglomerates is shown in Figure 4.28, from which the Mohr-Coulomb strength parameters (c and ϕ) corresponding to the peak shear strength can be calculated based on Eq. 4.2. Then the best fit Mohr-Coulomb failure envelop with the Mohr-circles is easily determined according to Eq. 4.3, as shown in Figure 4.29. Similarly, the Mohr-Coulomb failure envelops for the other groups of samples are shown in Figure 4.30 through 4.34. The shear strength and Mohr-Coulomb strength parameters for all the six groups of samples are summarized in Table 4.7. For the artificial conglomerates, the cohesion and friction

angle are in the range of 2.7 to 3.5 MPa and 57.1° to 59.6°, respectively. The strength parameters are consistent with those obtained from direct shear tests. It is worth mentioning that all group 6 samples and the samples for UCS testing within group 5 samples were prepared using one bag of Portland cement, while the other samples for the uniaxial/ triaxial tests and all the samples used for direct shear and Brazilian tensile testing were made with another bag of Portland cement. This seems to be the main reason for the inconsistent results of group 5 samples in Table 4.7 and the inconsistent cohesions measured from triaxial testing and direct shear testing for group 6 samples.

The failure envelopes of all four groups of artificial conglomerates are plotted in Figure 4.35. No distinct difference can be observed among the failure envelops, which agrees with the findings from direct shear tests. As shown in Figure 4.36, the failure envelops of groups 5 and 6 cement paste samples are nearly parallel to each other, which indicates that the two groups of cement samples have similar friction angles.

For the cement paste samples, the primary failure modes are spalling and splitting as shown in Figure 4.37, regardless of the magnitude of confining stress. The samples have a larger number of cracks and could be disintegrated into several fragments. The cracks on some of the cement paste samples are highlighted as red lines. Comparing with the conglomerates, the cracks in the cement paste samples are relatively planar. The failed artificial conglomerates from UCS and triaxial tests are shown in Figure 4.38. The failure mode for the UCS samples is mainly axial splitting. The cracks propagated from top to bottom and are parallel or sub-parallel to the loading axis. With the increase of confining stress, the failure mode changes to shear failure, and the shear plane became more evident. In addition, the conglomerates with smaller steel balls have more integral shear planes than those with larger balls.
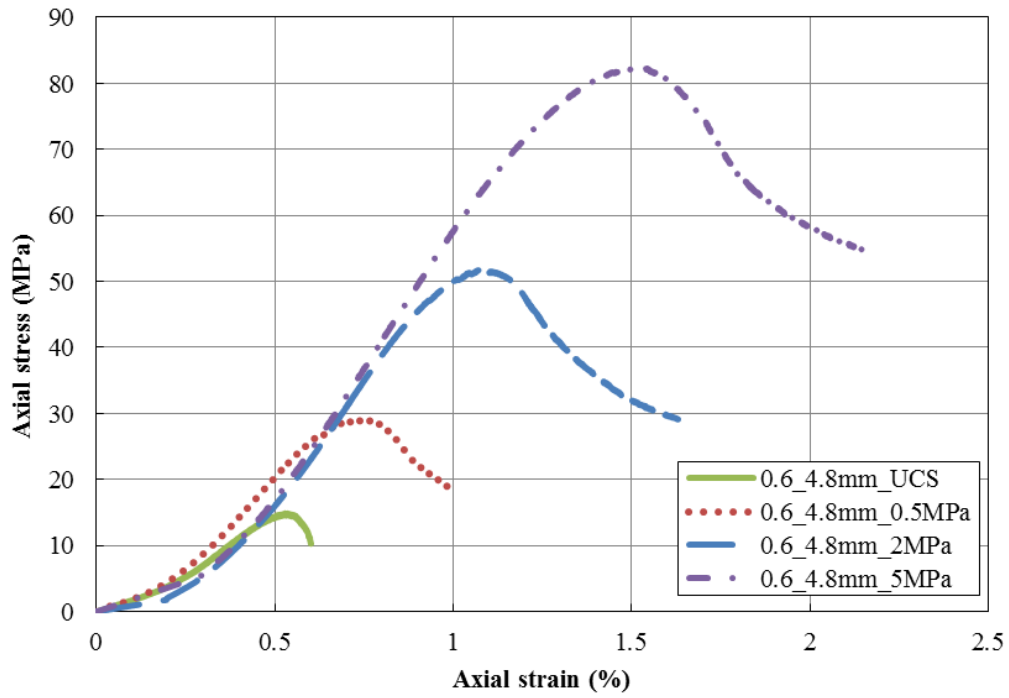
Figure 4.22 Axial stress versus axial strain plot of group 1 artificial conglomerates
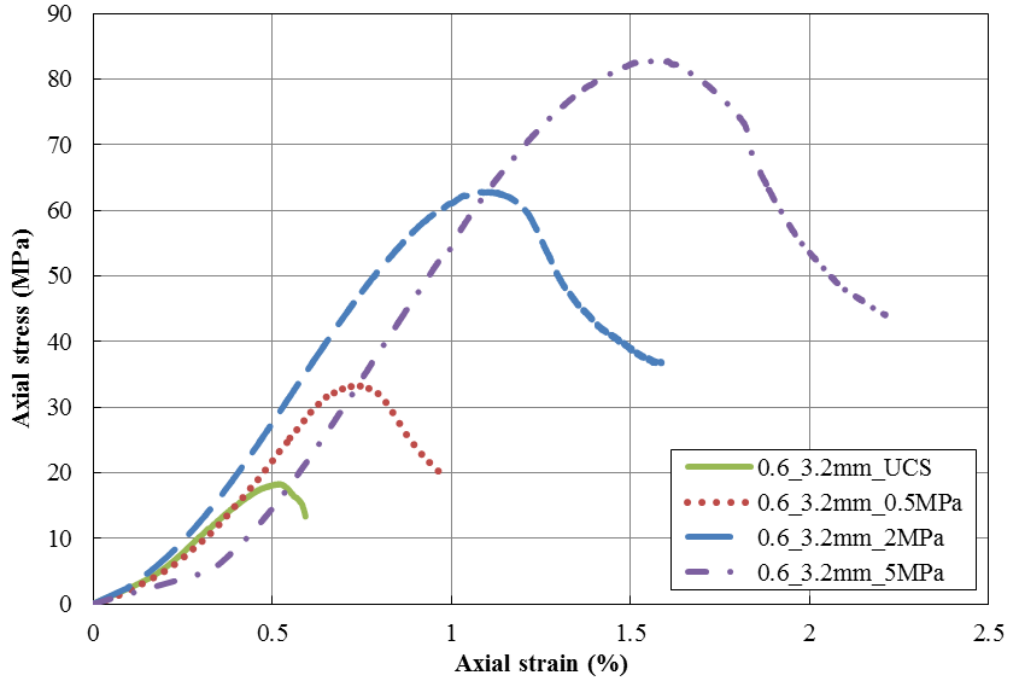
Figure 4.23 Axial stress versus axial strain plot of group 2 artificial conglomerates
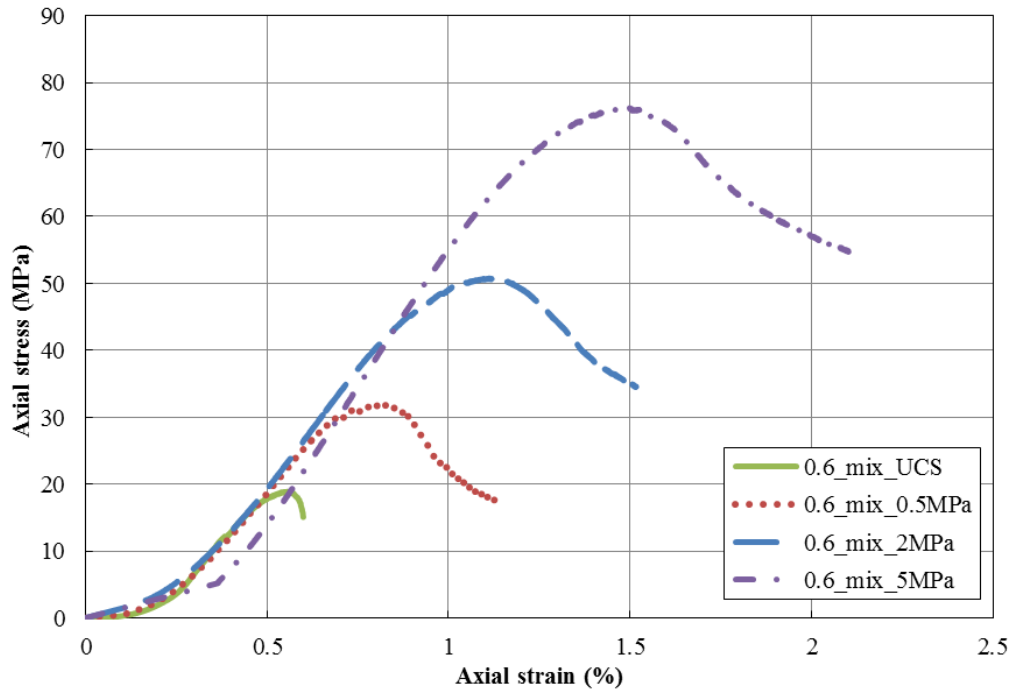
Figure 4.24 Axial stress versus axial strain plot of group 3 artificial conglomerates
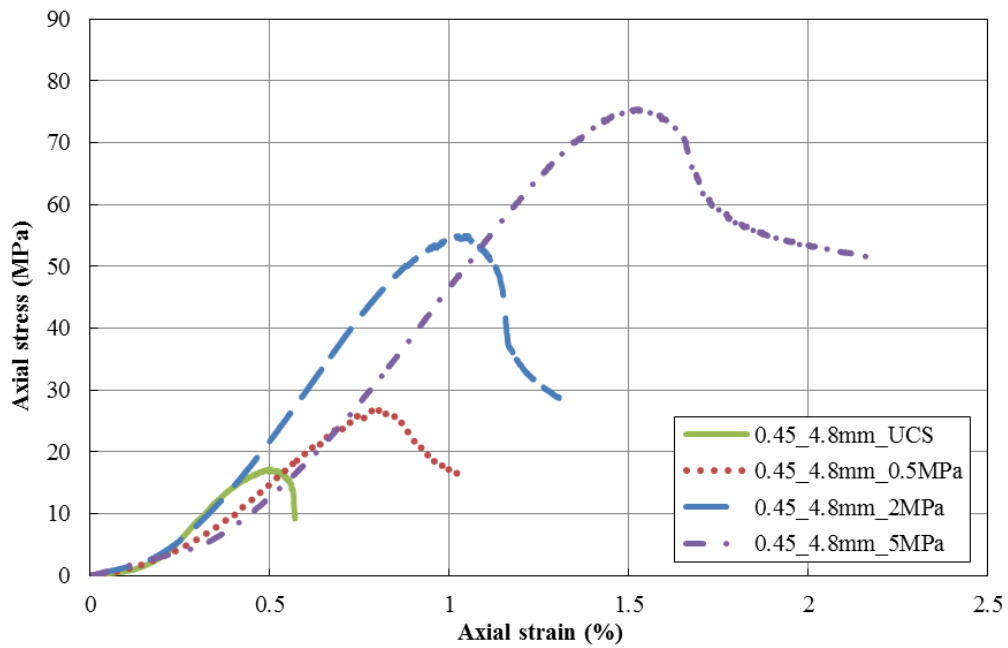
Figure 4.25 Axial stress versus axial strain plot of group 4 artificial conglomerates

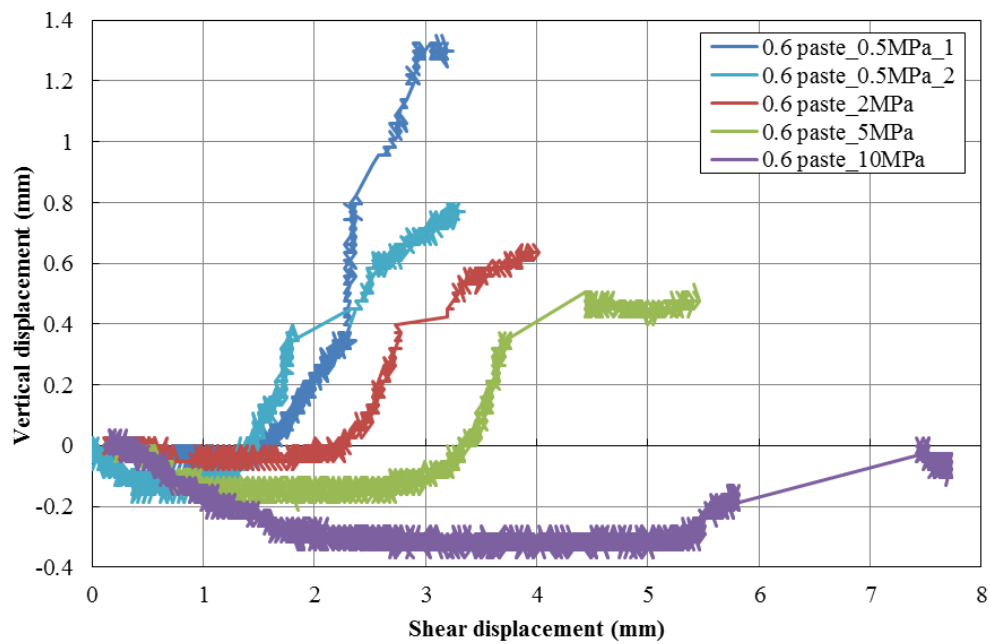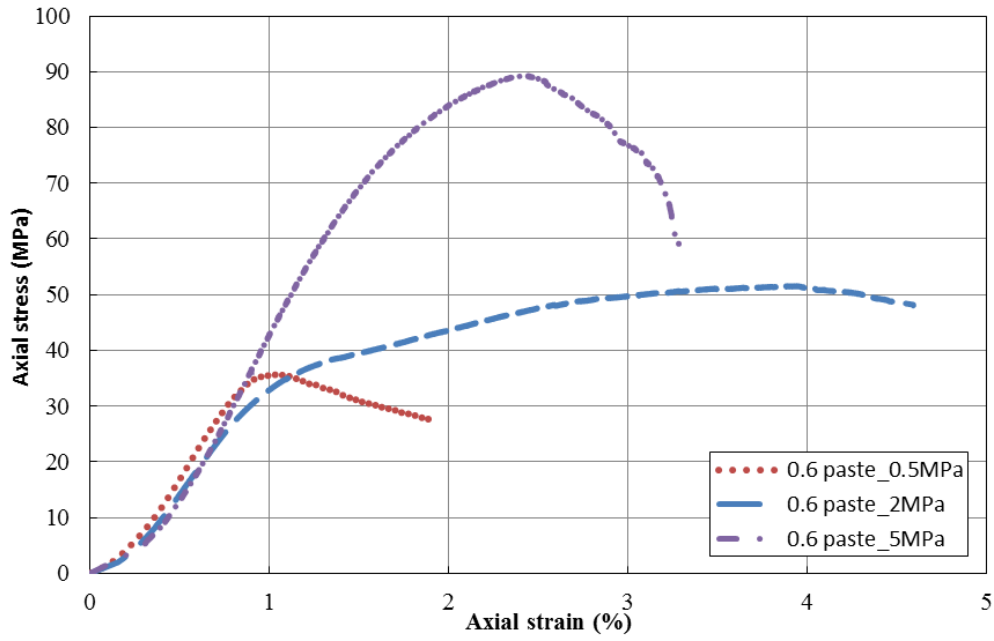Figure 4.26 Axial stress versus axial strain plot for cement paste samples with water-cement ratio of 0.6
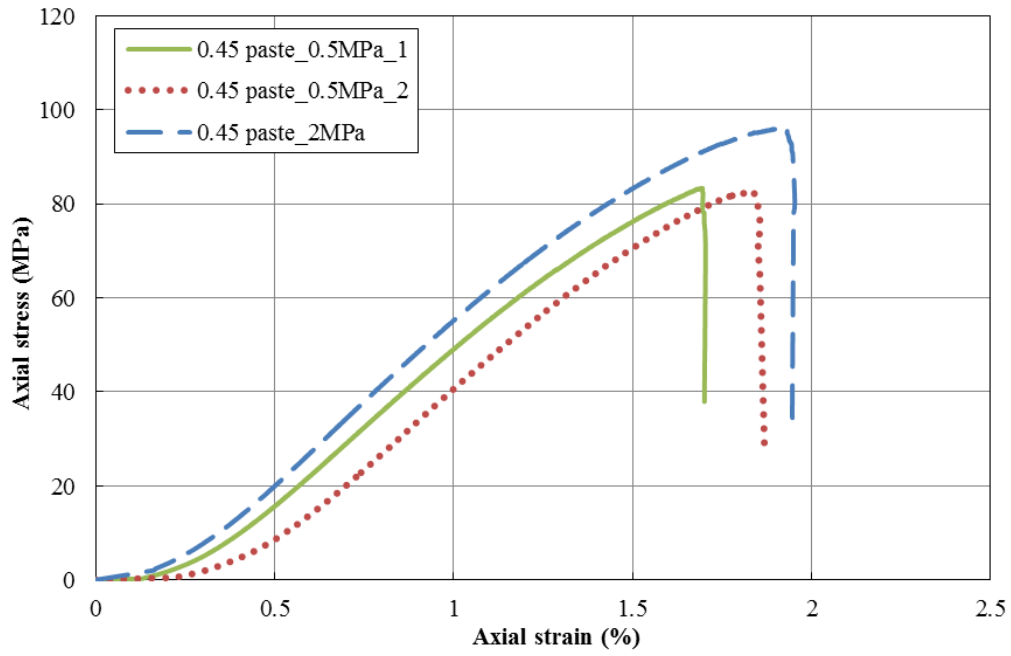
Figure 4.27 Axial stress versus axial strain plot for cement paste samples with water-cement ratio of 0.45

Table 4.7 Summary on Uniaxial/Triaxial testing results

Artificial samples	Sample No.	Confining stress (MPa)	Shear strength (MPa)	Cohesion (MPa)	Friction angle (°)
Group 1	0.6_4.8mm_1	0	14.91	2.70	59.26
	0.6_4.8mm_2	0.5	29.00		
	0.6_4.8mm_3	2	51.91		
	0.6_4.8mm_4	5	82.27		
Group 2	0.6_3.2mm_1	0	18.26	3.27	59.60
	0.6_3.2mm_2	0.5	33.31		
	0.6_3.2mm_3	2	62.90		
	0.6_3.2mm_4	5	82.92		
Group 3	0.6_mix_1	0	18.83	3.52	57.14
	0.6_mix_2	0.5	31.91		
	0.6_mix_3	2	50.77		
	0.6_mix_4	5	76.20		
Group 4	0.45_4.8mm_1	0	17.21	3.00	57.98
	0.45_4.8mm_2	0.5	27.18		
	0.45_4.8mm_3	2	55.02		
	0.45_4.8mm_4	5	75.49		
Group 5	0.6 paste_1	0	60.00	4.16	57.80
	0.6 paste_2	0.5	35.81		
	0.6 paste_3	2	51.49		
	0.6 paste_4	5	89.30		
Group 6	0.45 paste_1	0	69.78	10.09	59.09
	0.45 paste_2	0.5	81.80		
	0.45 paste_3	2	96.32		
	0.45 paste_4	0.5	83.27		
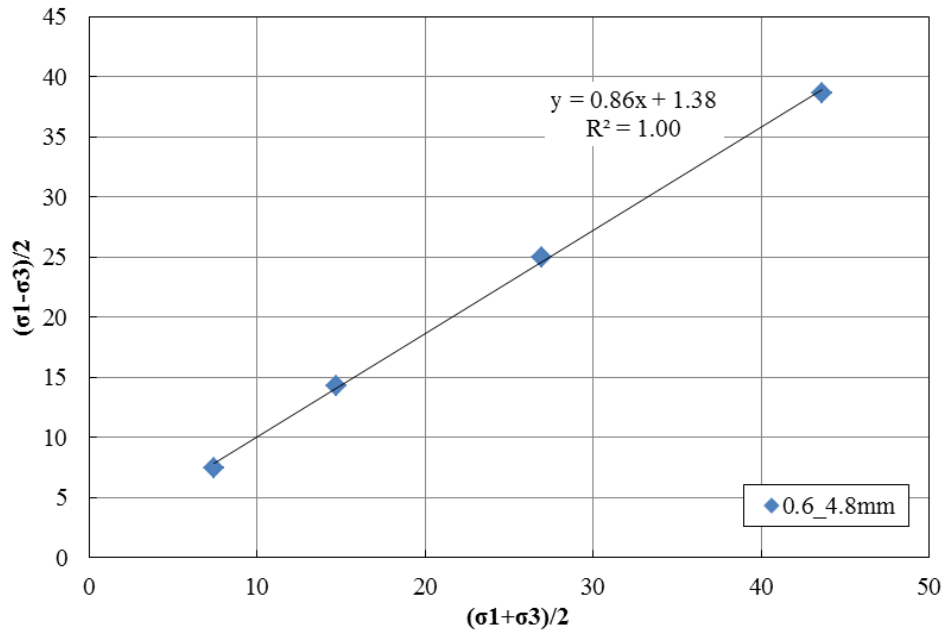
Figure 4.28 The $(\sigma_1 - \sigma_3)/2$ versus $(\sigma_1 + \sigma_3)/2$ plot for group 1 artificial conglomerates
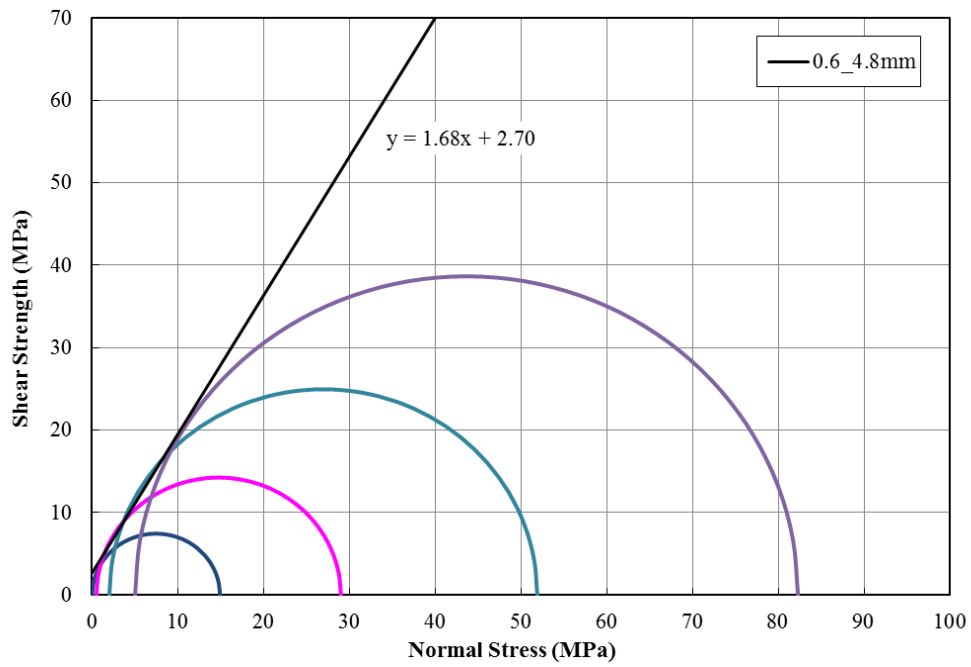
Figure 4.29 Mohr circles and failure envelope for group 1 artificial conglomerates
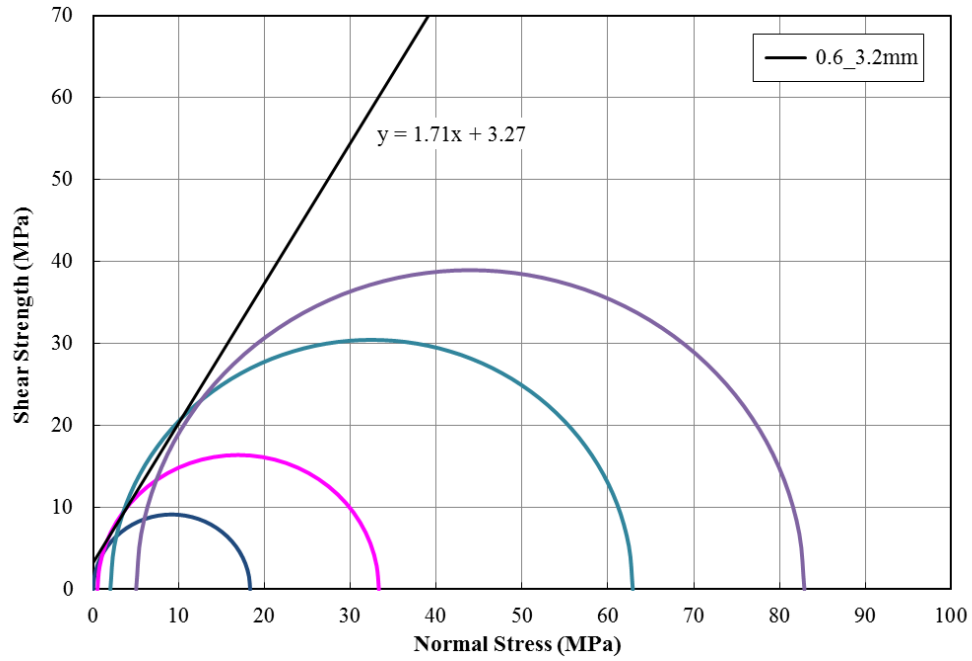
Figure 4.30 Mohr circles and failure envelope for group 2 artificial conglomerates
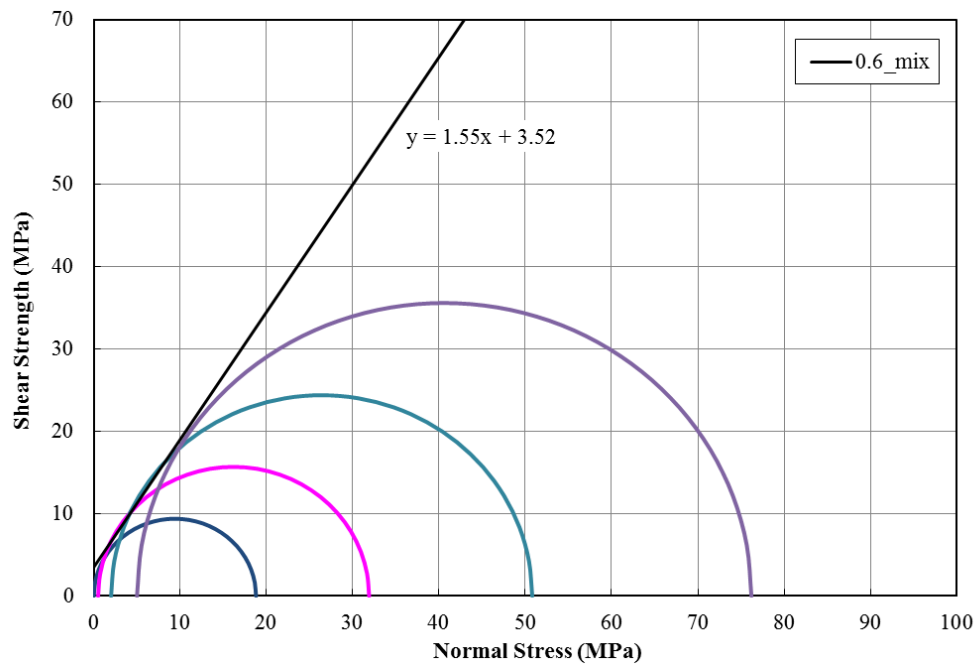
Figure 4.31 Mohr circles and failure envelope for group 3 artificial conglomerates
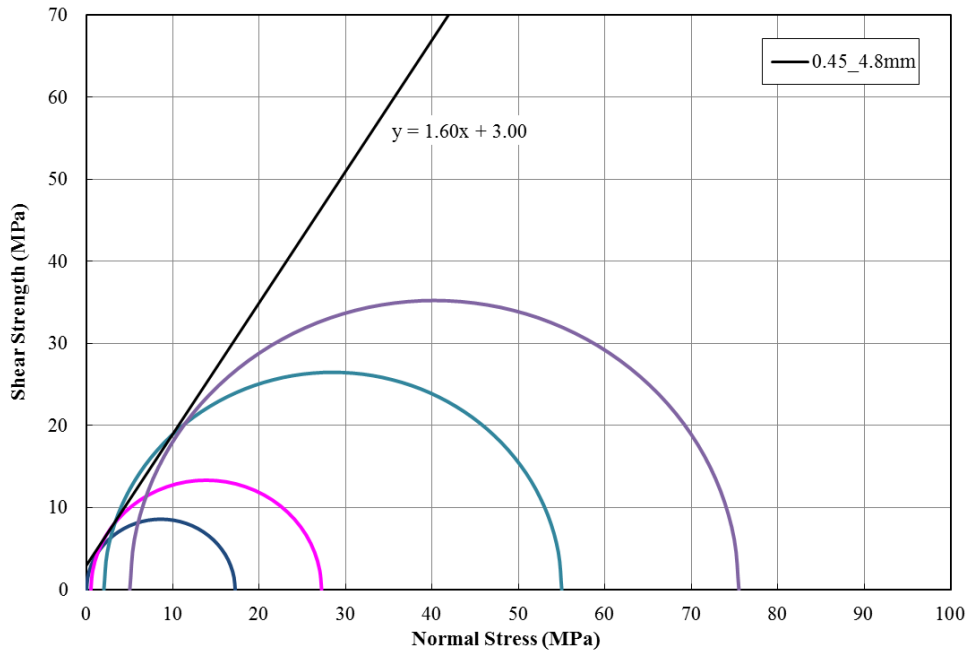
Figure 4.32 Mohr circles and failure envelope for group 4 artificial conglomerates
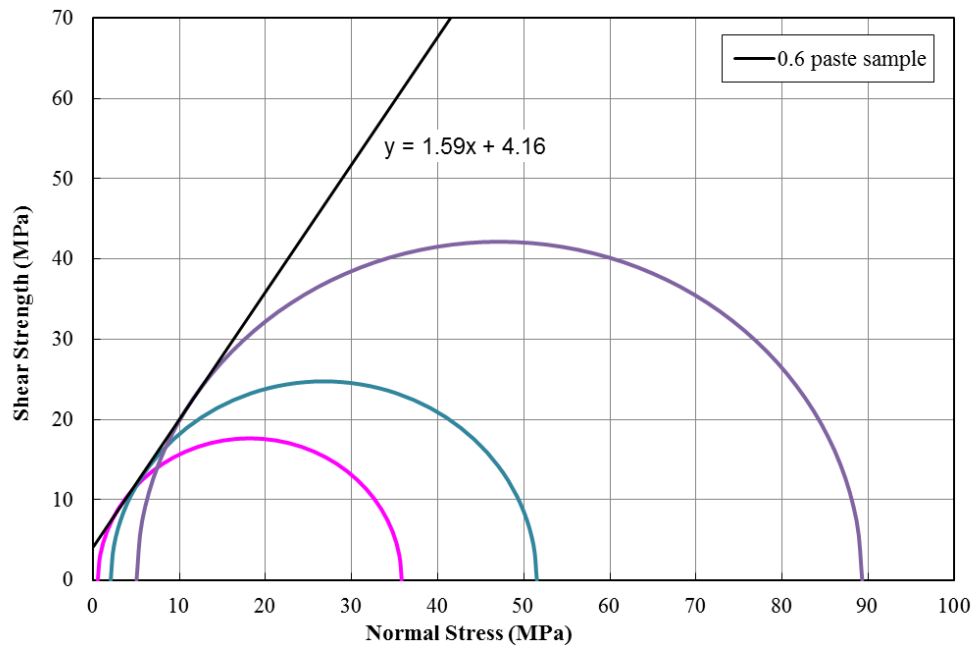
Figure 4.33 Mohr circles and failure envelop for cement paste samples with water-cement ratio of 0.6
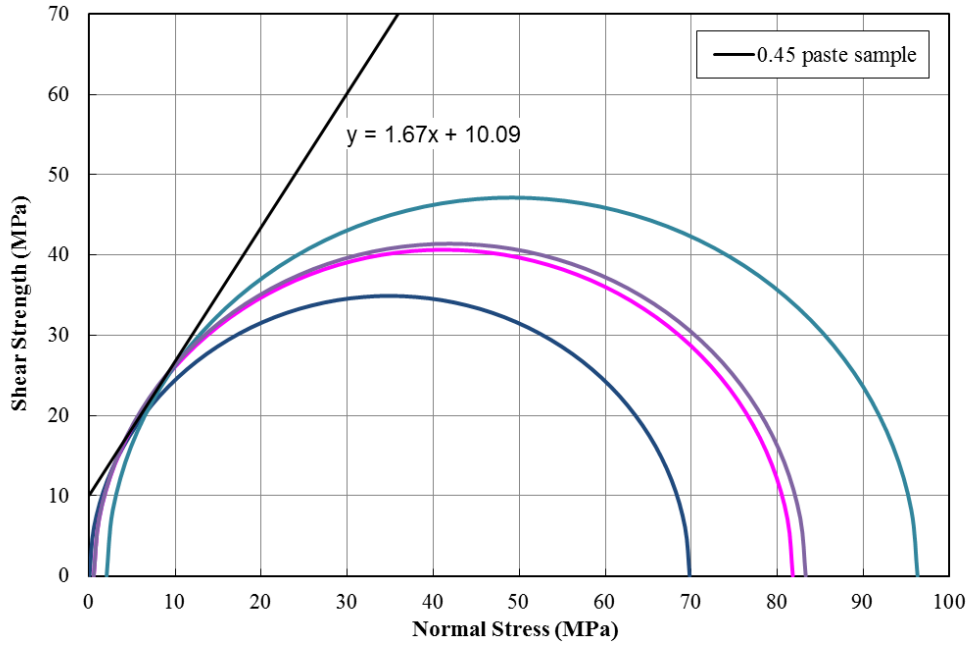
Figure 4.34 Mohr circles and failure envelope for cement paste samples with water-cement ratio of 0.45
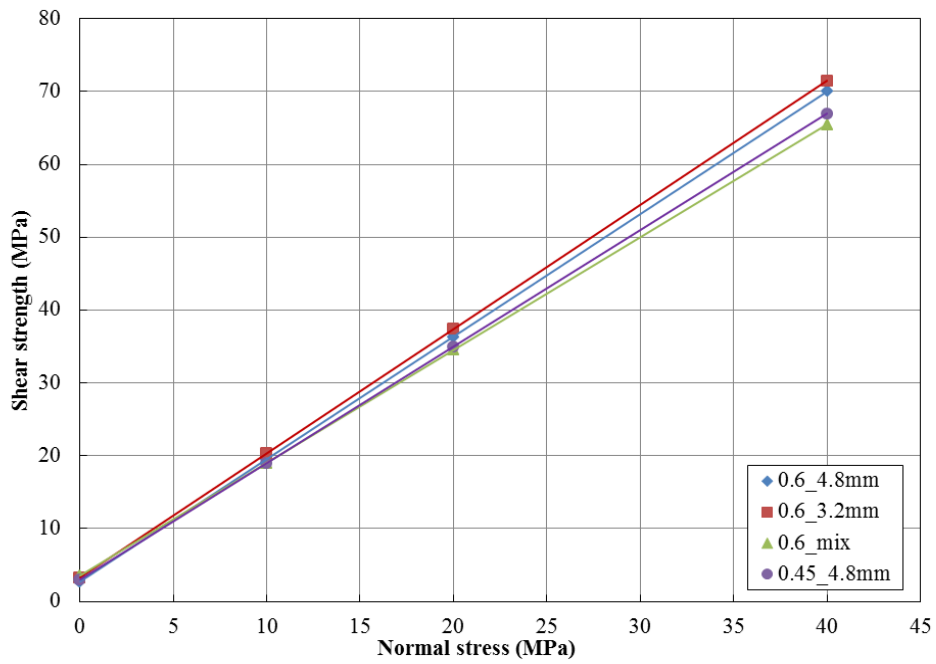
Figure 4.35 Failure envelopes for the artificial conglomerates
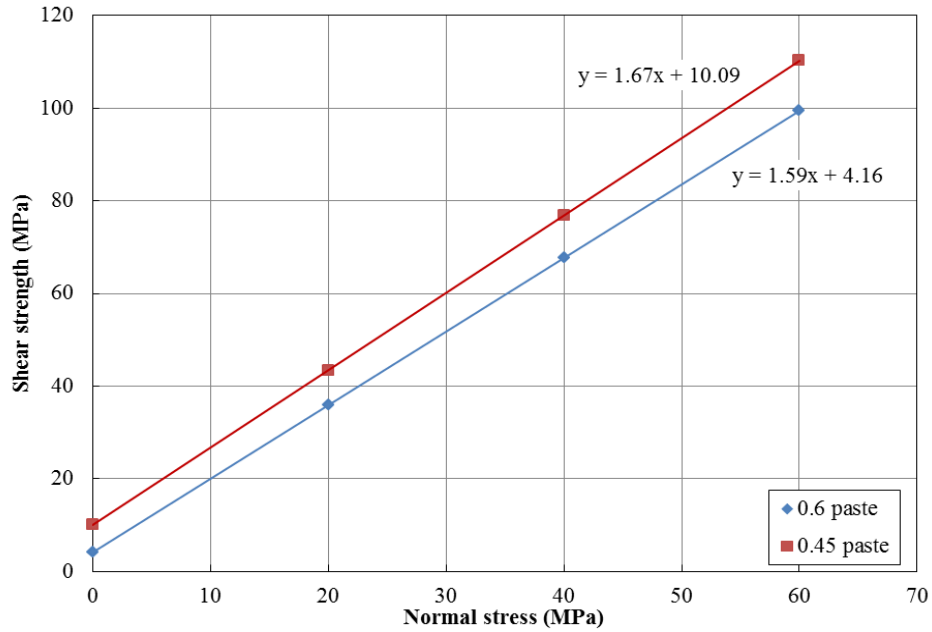
Figure 4.36 Failure envelopes for the cement paste samples

| (a) | (b) | (c) | (d) |
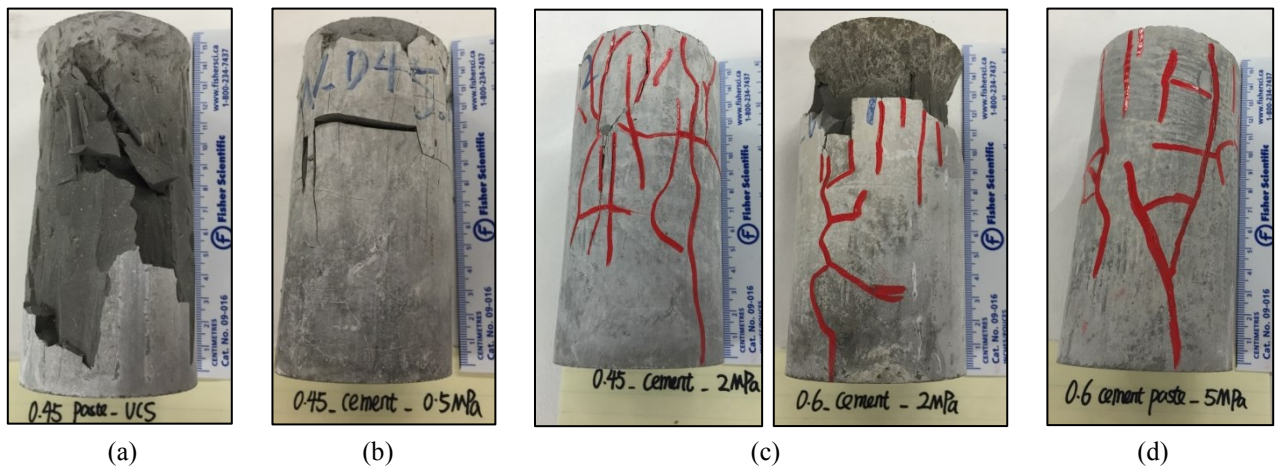
Figure 4.37 The UCS/triaxial testing failure samples (cement paste samples): (a) under UCS testing condition; (b) under 0.5MPa confining stress; (c) under 2MPa confining stress; (d) under 5MPa confining stress.
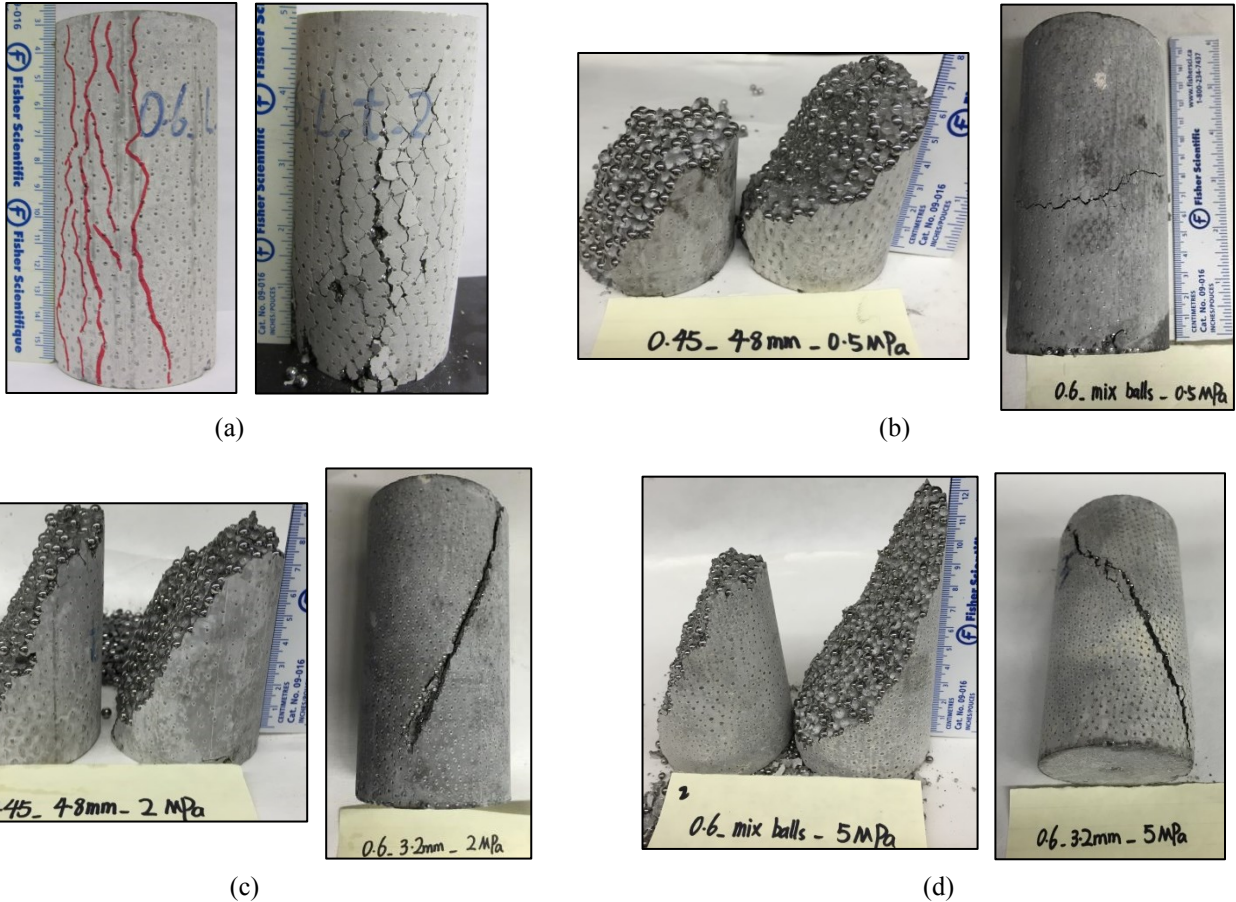
Figure 4.38 The UCS/triaxial testing failure samples (artificial conglomerates): (a) under UCS testing condition; (b) under 0.5MPa confining stress; (c) under 2MPa confining stress; (d) under 5MPa confining stress.

4.4.3 Brazilian tensile tests

Brazilian tensile tests were conducted on artificial conglomerates and cement paste samples to determine the indirect tensile strength. Based on the ASTM D3967, samples were axially loaded under compression at a constant loading rate of 2000 N/min to ensure the failure occurs within 10 minutes of loading. The applied load and axial displacement with time were monitored with INSTRON testing equipment (Figure 4.39(a)).

The splitting tensile strength should be calculated as follows (ASTM D3967):

$$\sigma_t = 2P/\pi LD \qquad\qquad [4.4]$$

where σ_t is the splitting tensile strength, MPa

P is the maximum applied load, Newton

L is the thickness of the specimen, mm, and

D is the diameter of the specimen, mm.

A total of 16 artificial conglomerates and 12 cement paste samples were tested, and the measured Brazilian tensile strength are summarized in Table 4.8. The tensile stress versus displacement curves of artificial conglomerates are shown in Figures 4.40 through 4.43. The curves for cement paste samples are plotted in Figure 4.44 and 4.45. Unlike the results from the triaxial and direct shear tests, the values of the Brazilian tensile strength show some variabilities. The main reason is that a thin cement paste layer was left on top of the sample during sample preparation, it is difficult to keep a constant thickness of this layer for sample consistency. However, the general trend of the results is reasonable. For instance, the cement paste sample with w/c of 0.45 has a higher tensile strength (3.7 MPa) than that with w/c of 0.6 (3.3 MPa).

(a)   (c)

(b)
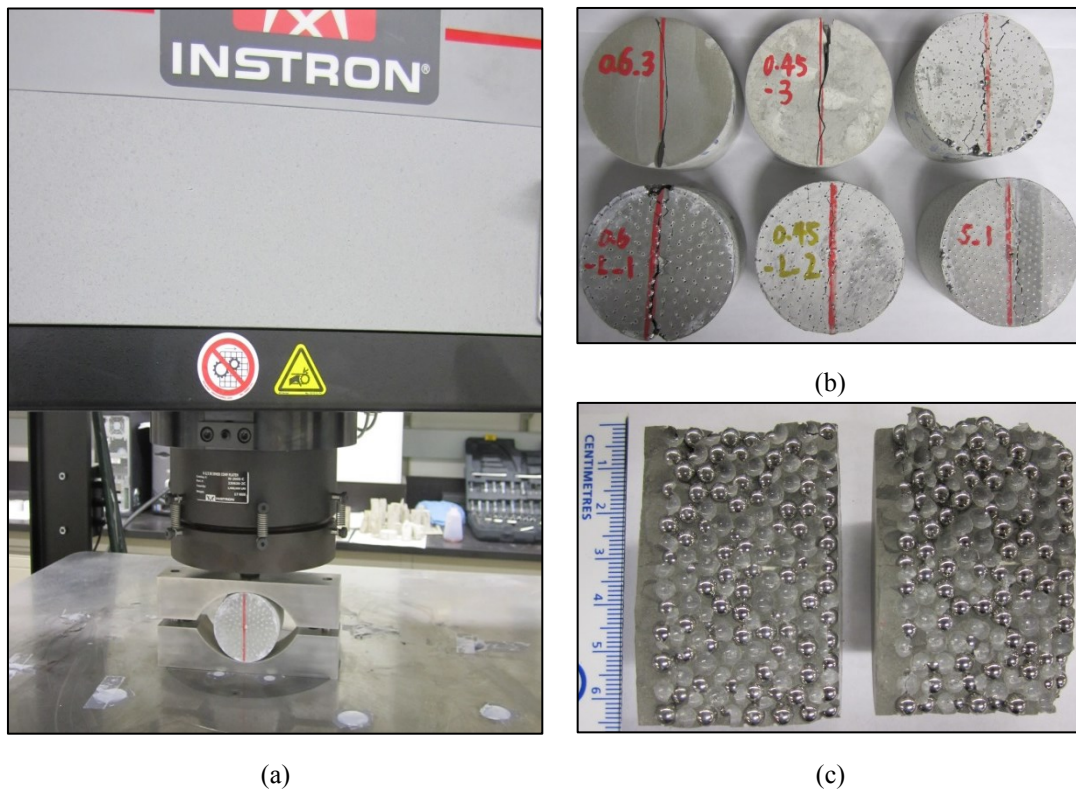
Figure 4.39 (a) The INSTRON testing machine used for the Brazilian tensile testing; (b) The samples after failure with distinct cracks; (c) The failure surface of artificial conglomerate.

73

As shown in Table 4.8, the tensile strength of all types of artificial conglomerates is in the range of 1.55 to 1.77 MPa. It is not clear that if the small difference among the tensile strength is because of particle size and/or cementing strength. Like the findings in the direct shear and uniaxial/triaxial testing results, the effect of particle size and uniform/non-uniform particle size distribution on the macro tensile strength is not evident.

Figure 4.39(b) shows well-developed axial cracks indicating a typical tensile splitting failure mode in the cement paste samples. However, several distinct cracks were observed after failure for the artificial conglomerates, indicating the existence of narrow shear zones. The reason is that the artificial conglomerates are much more ductile than the cement paste samples, due to the contacts between the steel balls and cement. It is also found that the dominant failure mode of the sample is along the steel ball to cement contact boundaries (Figure 4.39(c)). This observation indicates that the normal bonding strength between steel ball and cement in the artificial conglomerate is lower than the tensile strength of cement paste.
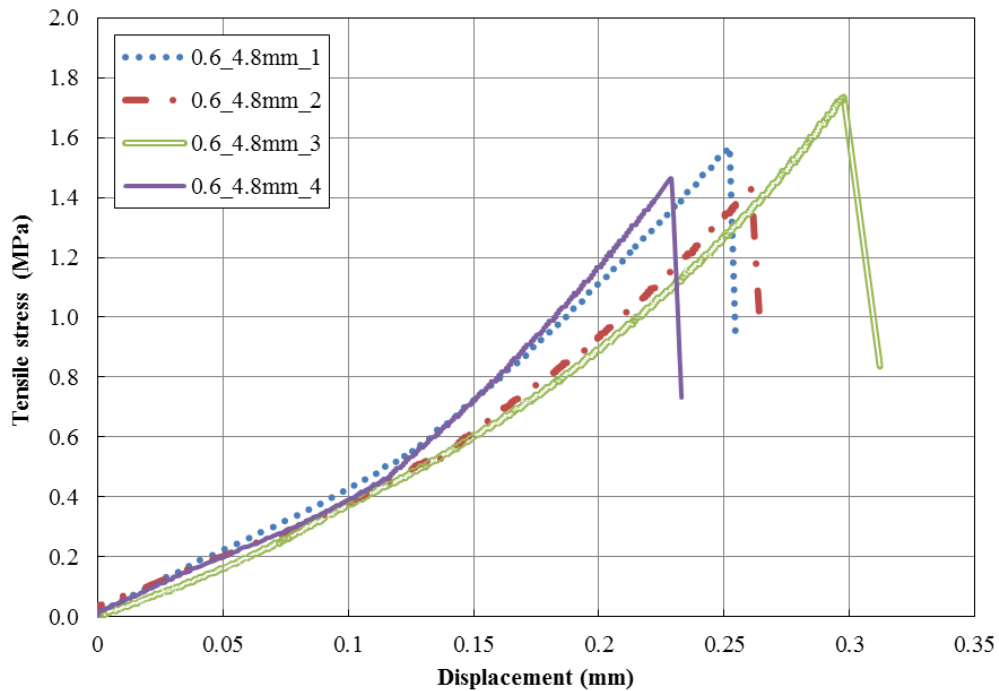
Figure 4.40 The Brazilian tensile test results for group 1 artificial conglomerates
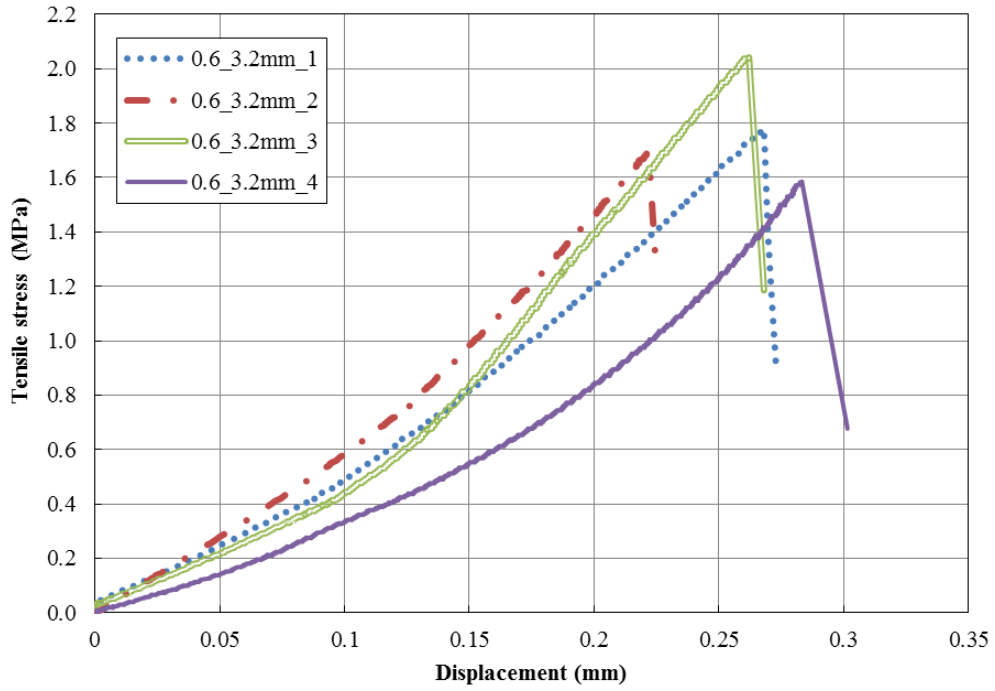
Figure 4.41 The Brazilian tensile test results for group 2 artificial conglomerates
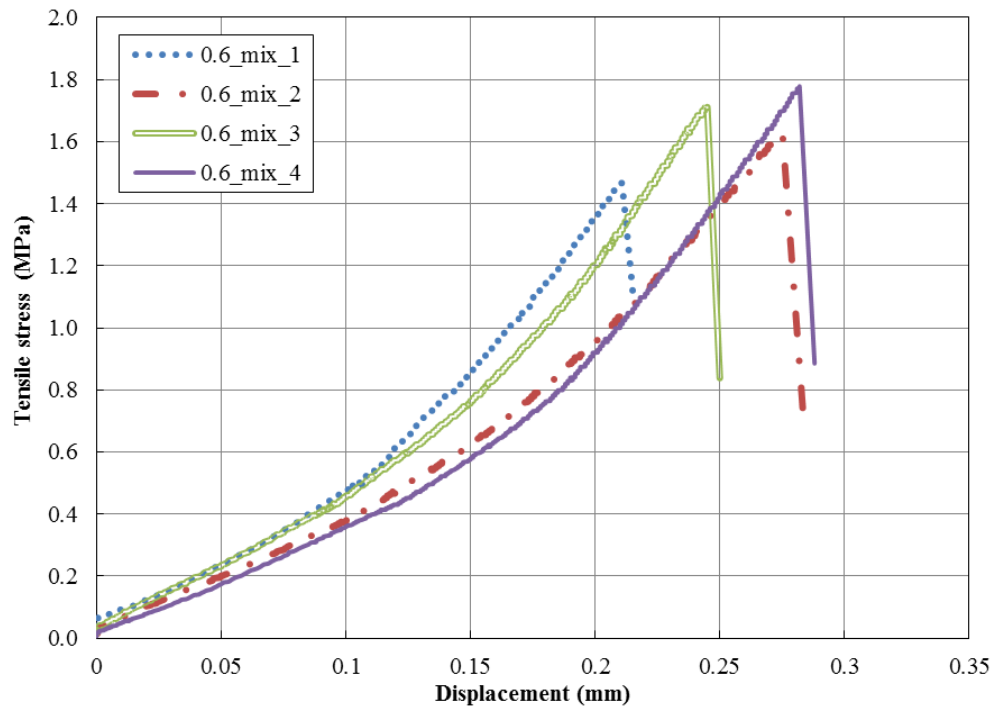
Figure 4.42 The Brazilian tensile test results for group 3 artificial conglomerates
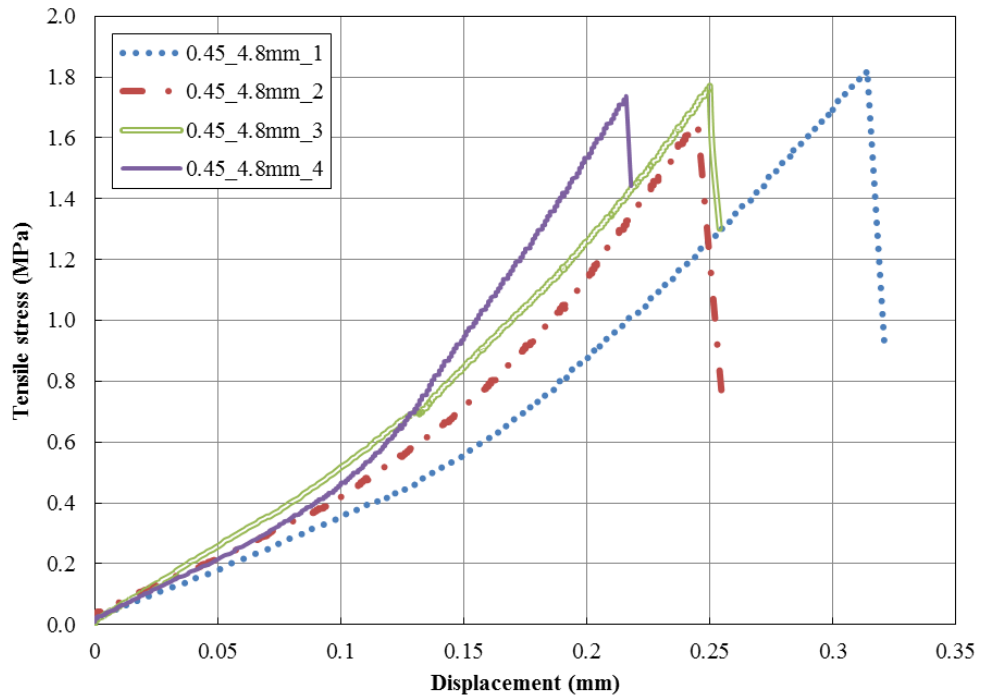
Figure 4.43 The Brazilian tensile test results for group 4 artificial conglomerates
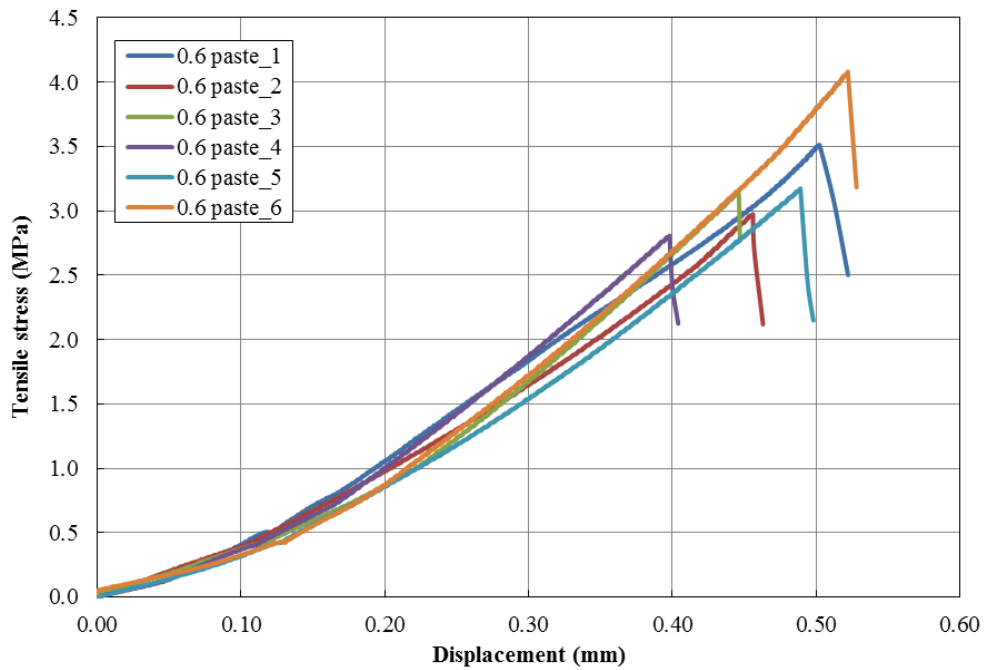
Figure 4.44 The Brazilian tensile test results for cement paste samples with water-cement ratio of 0.6
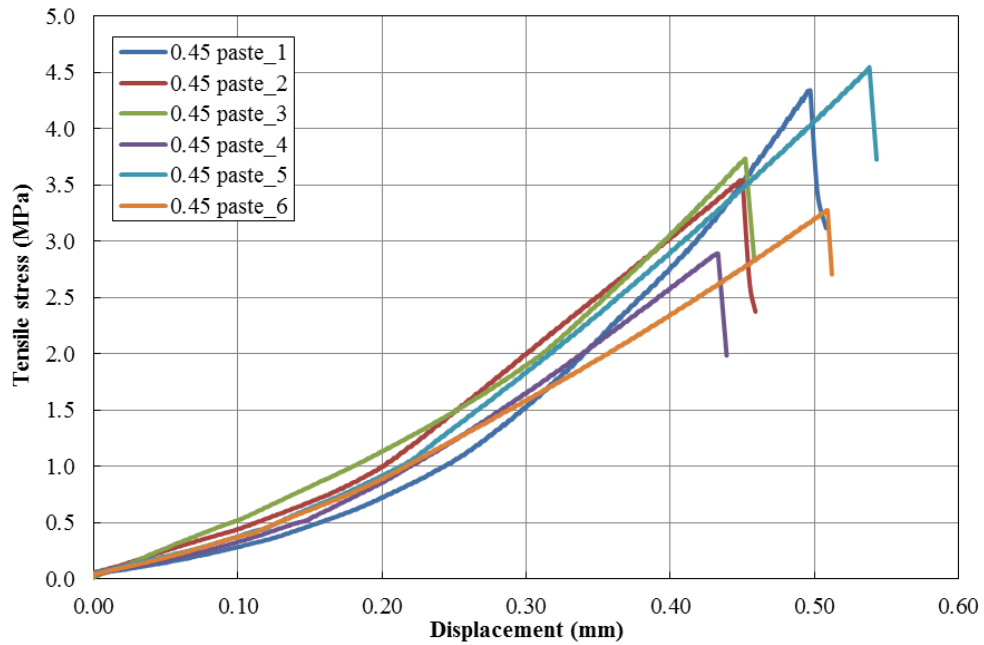
Figure 4.45 The Brazilian tensile test results for cement paste samples with water-cement ratio of 0.45

Table 4.8 Summary of Brazilian tensile testing results

Artificial samples	Sample No.	Tensile strength (MPa)	Average tensile strength (MPa)
Group 1	0.6_4.8mm_1	1.57	1.55
	0.6_4.8mm_2	1.43	
	0.6_4.8mm_3	1.74	
	0.6_4.8mm_4	1.46	
Group 2	0.6_3.2mm_1	1.78	1.77
	0.6_3.2mm_2	1.68	
	0.6_3.2mm_3	2.04	
	0.6_3.2mm_4	1.59	
Group 3	0.6_mix_1	1.47	1.65
	0.6_mix_2	1.63	
	0.6_mix_3	1.71	
	0.6_mix_4	1.78	

	0.45_4.8mm_1	1.82	
Group 4	0.45_4.8mm_2	1.65	1.75
	0.45_4.8mm_3	1.77	
	0.45_4.8mm_4	1.74	
Group 5	0.6 paste_1	3.51	3.28
	0.6 paste_2	2.97	
	0.6 paste_3	3.14	
	0.6 paste_4	2.81	
	0.6 paste_5	3.17	
	0.6 paste_6	4.08	
Group 6	0.45 paste_1	4.34	3.72
	0.45 paste_2	3.54	
	0.45 paste_3	3.73	
	0.45 paste_4	2.89	
	0.45 paste_5	4.55	
	0.45 paste_6	3.28	

4.5 Measuring inter-particle friction and movement criterion for shear-normal failure

Besides the macro parameters that can be measured from direct shear, uniaxial/triaxial and Brazilian tensile tests, the inter-particle friction angle of steel balls and the movement criterion for shear-normal failure of cement should be determined.

4.5.1 Inter-particle friction angle of steel balls

The inter-particle friction angle is one of the micro parameters involved in the theoretical relationship derivation which should be determined independently of other parameters. In this study, direct shear tests were carried out on steel balls with one inch diameter. The steel balls have the same surface treatment as those used in the artificial conglomerate. As shown in Figure 4.46, three one-inch diameter steel balls were embedded in the center of the bolt anchor sulfaset paste plate which is placed in the bottom half of the shear box. All the three steel balls are in contact with each other and the bolt anchor sulfaset paste was poured into the shear box mould above the

mid-height of the ball to provide strong bonding. Another steel ball was treated similarly to fit in the upper shear box and rested on the bottom half with point contacts. Besides, glue was smeared around the contact area between steel balls and paste plate to avoid the occurrence of rolling. The direct shear apparatus used for the inter-particle friction measurement is shown in Figure 4.47. Two sets of tests were conducted to ensure test consistency under normal loads of 60, 100 and 200 N.
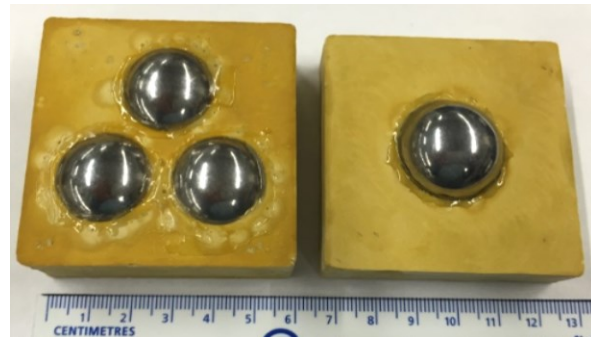
Figure 4.46 The embedded steel balls for inter-particle friction measurement
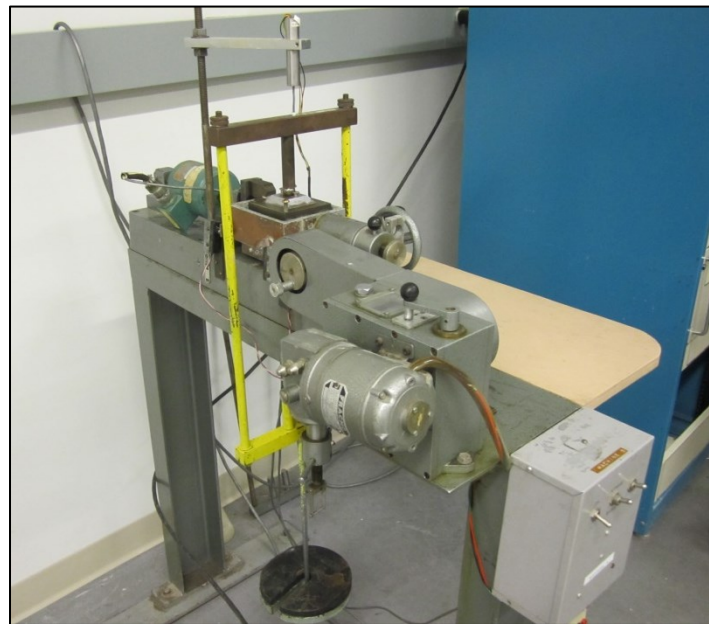
Figure 4.47 The direct shear apparatus used for inter-particle friction measurement

As shown in Figure 4.48, points B, C and D are used to represent the centers of steel balls in the bottom half of shear box. While point A stands for the center of steel ball in the upper half of shear box, point Axy is the projection of ball center A in the xy plane. At first, Ball A is set on the center

of bottom shear box and contacts with all the three steel balls. Then, with a constant strain rate (0.005 mm/s), the ball A would climb over steel balls B and C during the test. Since both geometric conditions and mechanical relationships among these steel balls can be determined, the inter-particle friction angle could be determined by relating to the measured horizontal force and applied normal force. The derivation process is given below in detail.
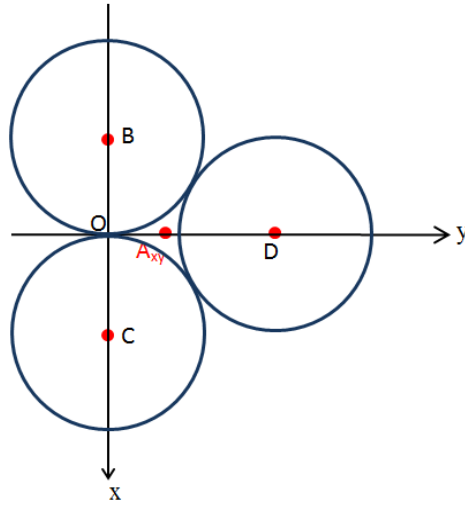
Figure 4.48 The projection of the steel balls on the xy plane

Cartesian coordinate system is used as shown in Figure 4.49. At each moment, all the forces applied on the ball A should be in equilibrium, including the external force F, contact force F_a at contact point a between balls A and B, and contact force F_b at contact point b between steel balls A and C. The externally applied force F consists of two components, namely vertical force F_v and horizontal force F_H. In the direct shear test, the vertical force F_v is the applied normal load, and the horizontal force F_H is the measured force in the horizontal direction. The contact force F_a is the combined force of local normal force N_a and friction force f_a at contact point a. Similarly, the force F_b can be divided into local normal force N_b and friction force f_b at contact point b.

The external vertical force and horizontal force are:

$$\begin{cases} \overrightarrow{F_v} = 0\hat{\imath} + 0\hat{\jmath} - F_v\hat{k} \\ \overrightarrow{F_H} = 0\hat{\imath} - F_H\hat{\jmath} - 0\hat{k} \end{cases} \qquad [4.5]$$

Then, the external resultant applied force F is:

$$\vec{F} = 0\hat{\imath} - F_H\hat{\jmath} - F_v\hat{k} \qquad [4.6]$$
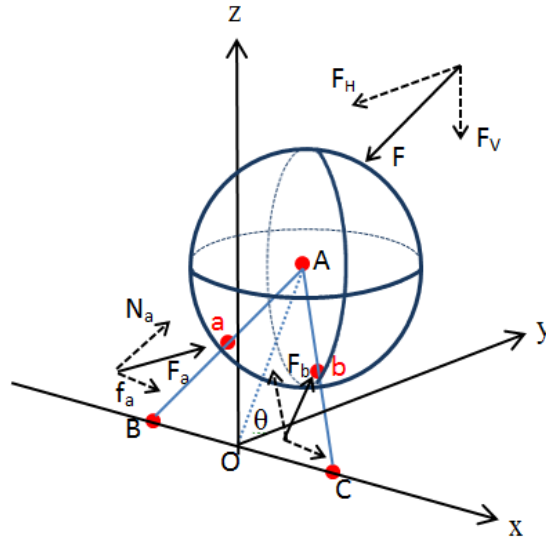
Figure 4.49 The forces applied on steel ball in the upper shear box
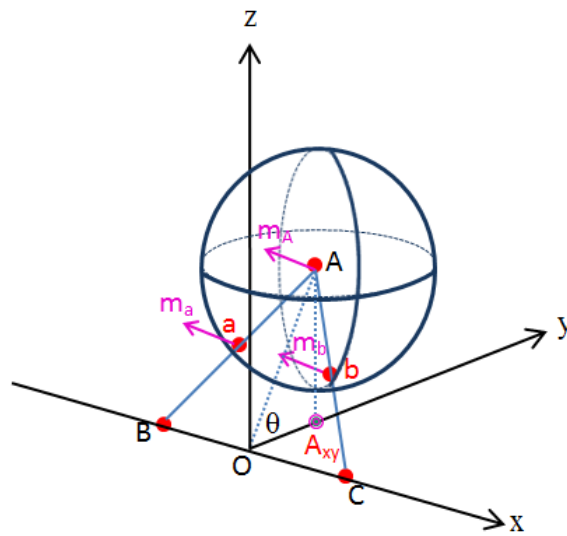
Figure 4.50 The movement conditions of steel ball in the upper shear box

The movement conditions of ball center A, and contact points a and b are shown in Figure 4.50. Let r be the radius of the steel ball and θ denotes the angle between line AO and xy plane, the coordinates of all the points involved are:

$$\begin{cases} O = (0,0,0) \\ A = \left(0, \sqrt{3}r\cos\theta, \sqrt{3}r\sin\theta\right) \\ B = (-r,0,0) \\ C = (r,0,0) \\ a = \left(-\frac{r}{2}, \frac{\sqrt{3}}{2}r\cos\theta, \frac{\sqrt{3}}{2}r\sin\theta\right) \\ b = \left(\frac{r}{2}, \frac{\sqrt{3}}{2}r\cos\theta, \frac{\sqrt{3}}{2}r\sin\theta\right) \end{cases} \qquad [4.7]$$

Therefore, the unit vectors along the BA and CA directions can be written as:

$$\begin{cases} \overrightarrow{u_{BA}} = \dfrac{\overrightarrow{BA}}{|\overrightarrow{BA}|} = \dfrac{1}{2}\hat{\imath} + \dfrac{\sqrt{3}}{2}\cos\theta\,\hat{\jmath} + \dfrac{\sqrt{3}}{2}\sin\theta\,\hat{k} \\[3mm] \overrightarrow{u_{CA}} = \dfrac{\overrightarrow{CA}}{|\overrightarrow{CA}|} = -\dfrac{1}{2}\hat{\imath} + \dfrac{\sqrt{3}}{2}\cos\theta\,\hat{\jmath} + \dfrac{\sqrt{3}}{2}\sin\theta\,\hat{k} \end{cases} \qquad [4.8]$$

Since the movement vector at point A is:

$$\overrightarrow{m_A} = 0\hat{\imath} - \sqrt{3}r\sin\theta\,\hat{\jmath} + \sqrt{3}r\cos\theta\,\hat{k} \qquad [4.9]$$

Then the unit vector along the movement direction of steel ball A can be determined:

$$\overrightarrow{u_{m_A}} = \overrightarrow{u_{m_a}} = \overrightarrow{u_{m_b}} = \frac{\overrightarrow{m_A}}{|\overrightarrow{m_A}|} = -\sin\theta\,\hat{\jmath} + \cos\theta\,\hat{k} \qquad [4.10]$$

Let N and f be the magnitudes of the local normal force and friction force at contact point a, respectively, then the normal force and friction force applied to the steel ball A at contact point a can be represented as:

$$\begin{cases} \overrightarrow{N_a} = N * \overrightarrow{u_{BA}} = N * \left(\dfrac{1}{2}\hat{\imath} + \dfrac{\sqrt{3}}{2}\cos\theta\,\hat{\jmath} + \dfrac{\sqrt{3}}{2}\sin\theta\,\hat{k}\right) \\[3mm] \overrightarrow{f_a} = f * \left(-\overrightarrow{u_{m_a}}\right) = f * (\sin\theta\,\hat{\jmath} - \cos\theta\,\hat{k}) \end{cases} \qquad [4.11]$$

Hence the contact force F_a at contact point a is:

$$\overrightarrow{F_a} = \overrightarrow{N_a} + \overrightarrow{f_a} = \frac{1}{2}N\hat{\imath} + \left(\frac{\sqrt{3}}{2}N\cos\theta + f\sin\theta\right)\hat{\jmath} + \left(\frac{\sqrt{3}}{2}N\sin\theta - f\cos\theta\right)\hat{k} \qquad [4.12]$$

Since balls B and C are symmetrical about the Y axis, the magnitudes of the local normal force and friction force at contact point a should be the same as those at contact point b. Similarly, the contact force F_b at contact point b is given by:

$$\overrightarrow{F_b} = \overrightarrow{N_b} + \overrightarrow{f_b} = -\frac{1}{2}N\hat{\imath} + \left(\frac{\sqrt{3}}{2}N\cos\theta + f\sin\theta\right)\hat{\jmath} + \left(\frac{\sqrt{3}}{2}N\sin\theta - f\cos\theta\right)\hat{k} \qquad [4.13]$$

Because the externally applied force F, and contact forces F_a and F_b in Eq. 4.6, Eq. 4.12 and Eq. 4.13 should be in equilibrium, the following relationships must be satisfied:

$$\begin{cases} \frac{\sqrt{3}}{2}N\cos\theta + f\sin\theta = \frac{1}{2}F_H \\ \frac{\sqrt{3}}{2}N\sin\theta - f\cos\theta = \frac{1}{2}F_v \end{cases} \qquad [4.14]$$

The magnitudes of the local normal force N and friction force f are obtained and related to externally applied vertical force F_v and horizontal force F_H:

$$\begin{cases} N = \frac{\sqrt{3}}{3}(F_H\cos\theta + F_v\sin\theta) \\ f = \frac{1}{2}(F_H\sin\theta - F_v\cos\theta) \end{cases} \qquad [4.15]$$

At the micro scale, the local normal force N and friction force f can be related with the inter-particle friction, as shown in Eq. 4.16, where ϕ_μ is the inter-particle friction angle.

$$f = N * \tan\phi_\mu \qquad [4.16]$$

Substituting N and f in Eq. 4.15 into Eq. 4.16, the inter-particle friction can be related to the known F_v and measured F_H:

$$\tan\phi_\mu = \frac{f}{N} = \frac{\sqrt{3}}{2} * \frac{F_H\sin\theta - F_v\cos\theta}{F_H\cos\theta + F_v\sin\theta} \qquad [4.17]$$

As shown in Eq. 4.17, to obtain the inter-particle friction angle, besides the applied vertical force and measured horizontal force, the angle θ between the line 0A and xy plane must be determined based on the geometry relationship.

As shown in Figure 4.48, the length of OA_{xy} is equal to $\frac{\sqrt{3}}{3}r$ at the starting point, and then it decreases with time during the test. By measuring the length of OA_{xy}, angle θ can be calculated

based on the relationship of $\theta = cos^{-1}(\frac{OA}{OA_{xy}})$, where the length of OA is always equal to $\sqrt{3}R$. In addition, the variation of vertical displacement can be determined by calculating the change in the length AA_{xy}. Some of the calculation results are shown in Table 4.9, where ΔOA_{xy} is the change in horizontal displacement, ΔAA_{xy} is the change in vertical displacement. According to the calculation results, both the angle θ and vertical displacement increase with the increase in horizontal displacement.

Table 4.9 The calculation of angle θ based on the geometry relationship

Horizontal displacement ΔOA_{xy} (mm)	Angle θ (°)	Vertical displacement ΔAA_{xy} (mm)
0	70.53	0
1	73.27	0.33
2	75.97	0.60
3	78.64	0.83
4	81.29	1.00
$\sqrt{3}/3$ r	90.00	1.26

The experimental results are shown in Figures 4.51 and 4.52. While the first group tests' results are shown in solid lines, the results of the second group tests are shown in dash lines. Obviously, the two groups' results are very consistent. Based on the test results, the calculation of angle θ in Table 4.9 and the relationship in Eq. 4.17, the inter-particle frictions are summarized in Table 4.10. The average friction coefficient is 0.12 and the inter-particle friction angle is about 6.84°. To verify the derivation results, the theoretical curves are drawn based on the calculated friction coefficient of 0.12 and several selected horizontal displacements. As shown in Figure 4.53 and Figure 4.54, the theoretical curves (drawn with straight lines and marks) are very consistent with the laboratory data.

Table 4.10 The calculation of inter-particle friction under different vertical applied forces

Vertical applied force (N)	Inter-particle friction $\tan \phi_\mu$ at different horizontal displacement				Mean Inter-particle friction angle ϕ_μ
	0 mm	1mm	2mm	3mm	
60_1	0.11	0.12	0.12	0.13	6.84°
60_2	0.11	0.13	0.11	0.11	
100_1	0.12	0.13	0.13	0.13	
100_2	0.12	0.13	0.13	0.13	
200_1	0.11	0.13	0.12	0.12	
200_2	0.12	0.12	0.12	0.13	
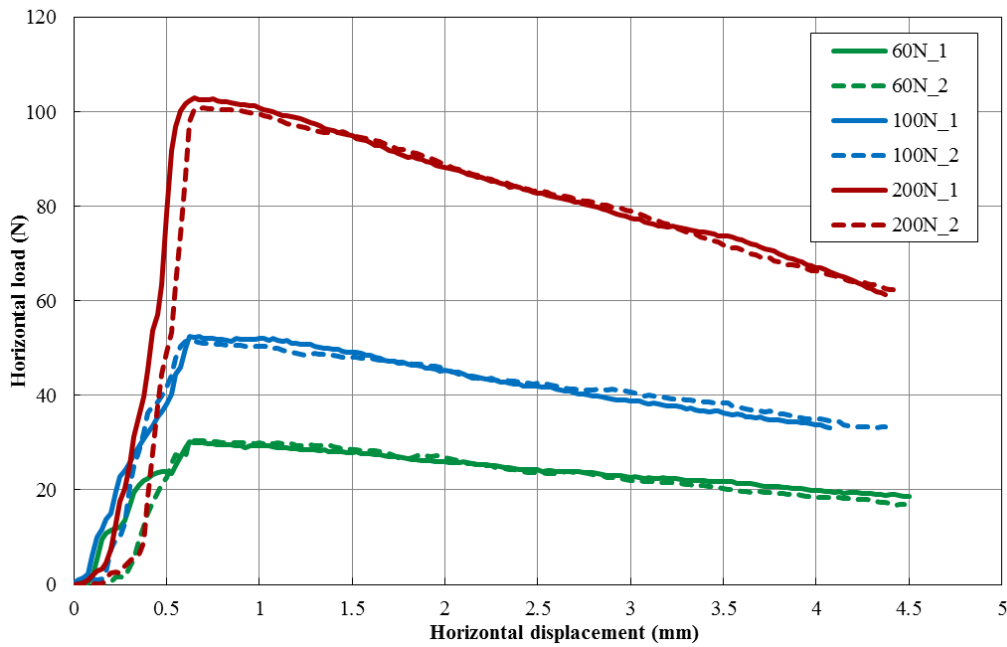
Figure 4.51 The variation of horizontal load with horizontal displacement for two groups of tests
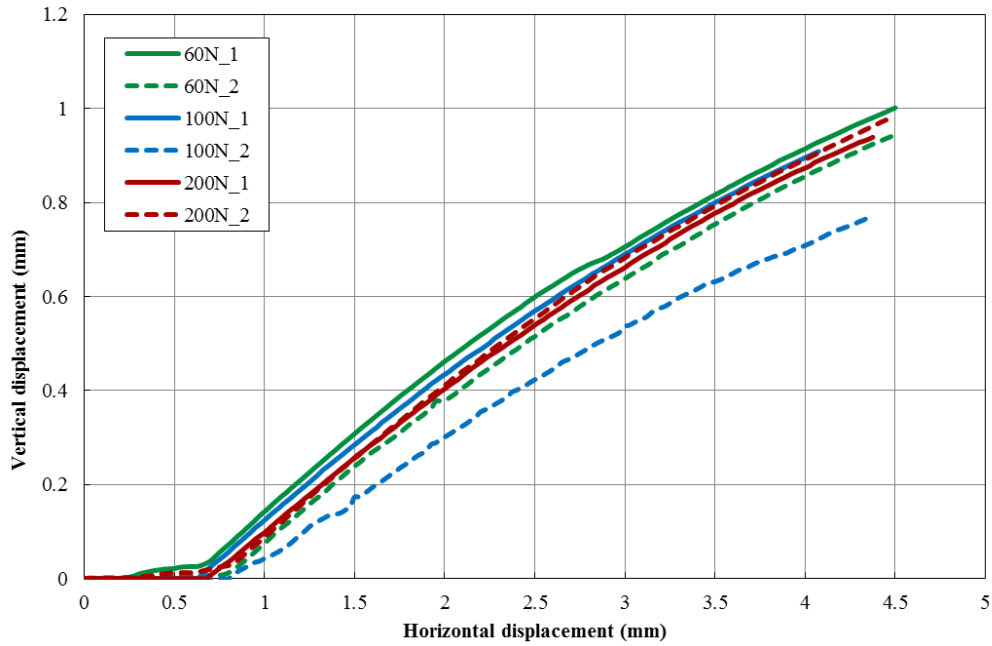
Figure 4.52 The change of vertical displacement with horizontal displacement for two groups of tests
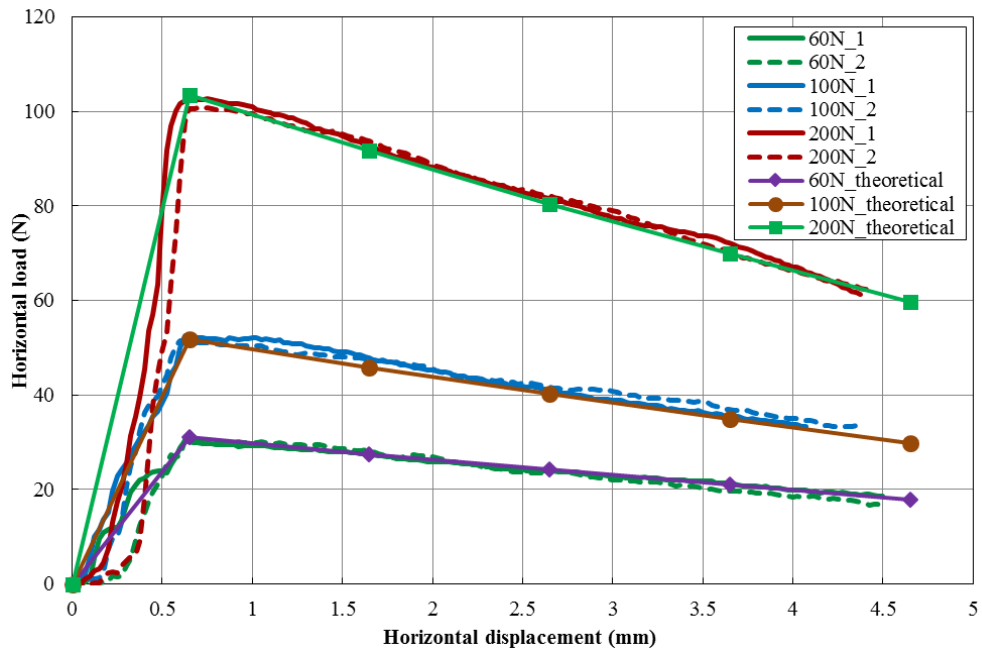
Figure 4.53 Comparison between measured and theoretical horizontal load curves based on the calculated inter-particle friction angle
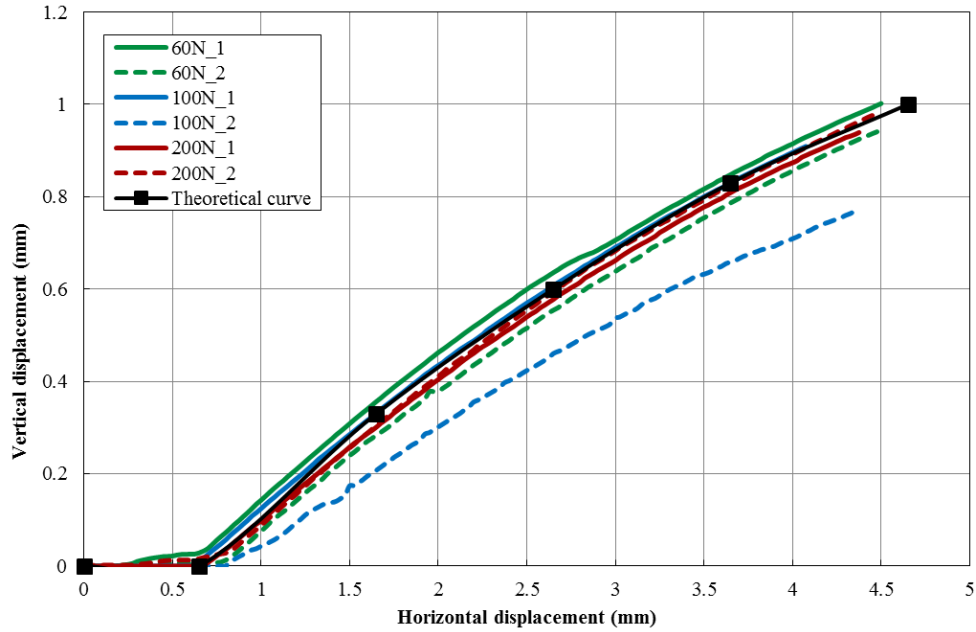
Figure 4.54 Comparison between measured and theoretical vertical displacement curves based on the calculated inter-particle friction angle

4.5.2 The movement criterion of cement paste sample

The movement criterion is defined as $V_c = \frac{v'}{u'}$, where v' and u' denote the maximum normal movement and maximum shear movement before failure, respectively. In this research, the movement criterion of cement to steel ball contact is assumed to be the same as that of cement-cement contact. In the laboratory, UCS test was conducted on the cement paste sample to obtain the maximum shear displacement, while Brazilian tensile test was used to measure the maximum normal displacement with the use of strain gauges. Then, the movement criterion of cement can be obtained.

UCS tests were conducted on cement paste samples with w/c ratios of 0.6 and 0.45 at the axial displacement rate of 0.001 mm/s. The Humboldt H-2919 Extensometer was used to measure the accurate axial strain ε_1 and radial strain ε_2. The test results are shown in Figures 4.55 and 4.56. Based on the Mohr's circle for the plane strain (Figure 4.57), the maximum shear strain γ_{max} occurs at the 45° shear plane, which equals to $(\varepsilon_1 - \varepsilon_2)$. Therefore, the maximum shear strain can be calculated and it is found to be 0.63% for the 0.6 cement paste sample and 0.65% for the 0.45 cement paste sample.

To obtain the maximum shear displacement, the thickness of the shear failure zone must be determined. An Olympus SZ61 microscope was used to investigate the tensile and shear cracks. Figure 4.58 shows the tensile failure zone from different Brazilian tensile test failure samples. The shear cracks from different uniaxial/triaxial test failure samples are shown in Figure 4.59. Since the maximum magnification that can be achieved with this microscope is 45X, and the smallest resolvable size for the human eye is about 0.1 mm (Cooper 2011), only the micro crack larger than 0.002 mm can be observed. The observed micro cracks are concentrated in the highlighted failure zone. The thickness of the tensile failure zone is around 0.20 mm and the shear failure zone thickness is about 0.19 mm on average. The maximum shear displacements of 0.6 and 0.45 cement paste samples can be determined by multiplying the thickness of shear failure zone by the corresponding maximum shear strains, which are 1.20×10^{-3} mm and 1.24×10^{-3} mm, respectively.
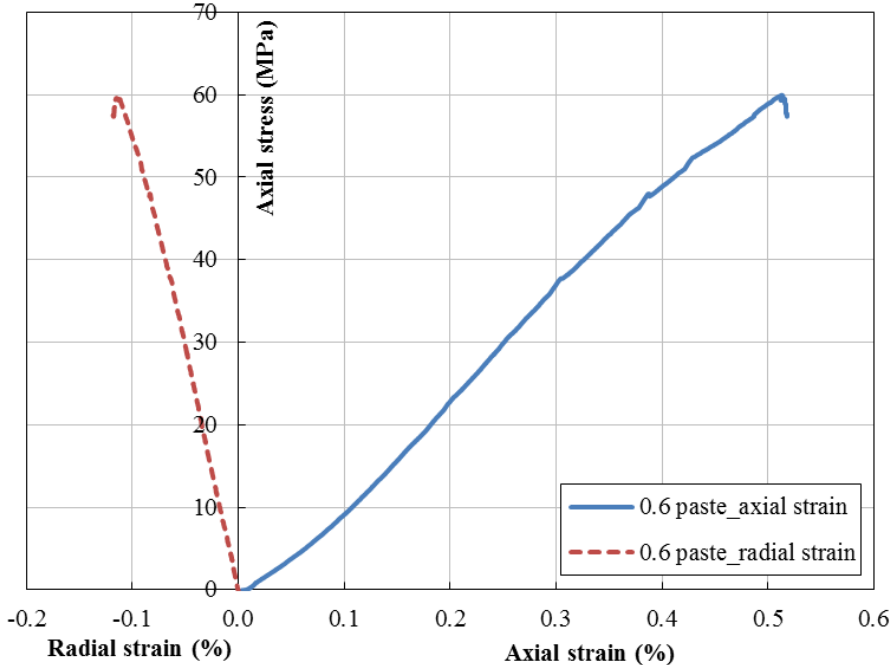
Figure 4.55 The axial and radial strain measurements for cement paste sample with water-cement ratio of 0.6
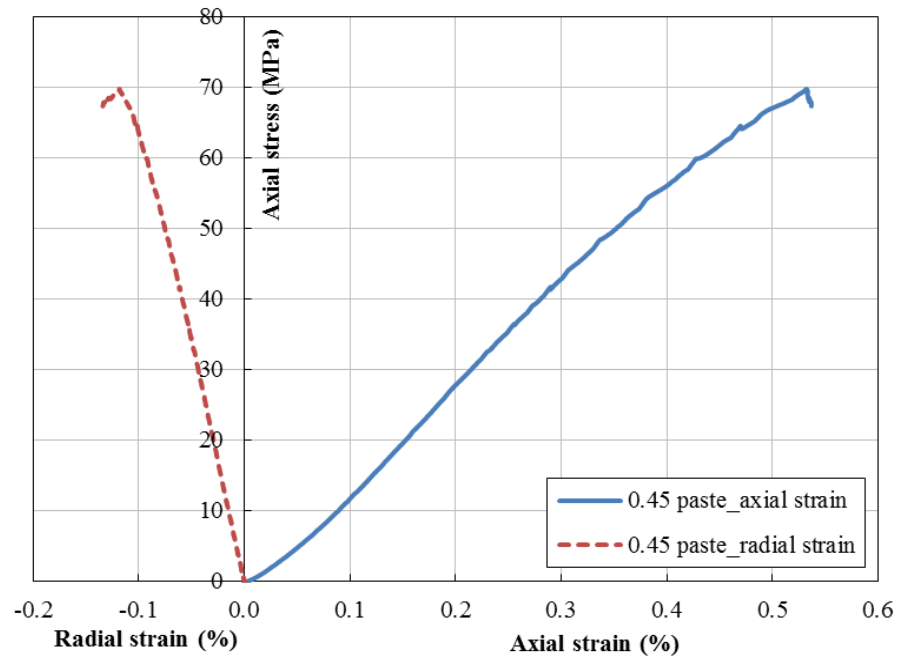
Figure 4.56 The axial and radial strain measurements for cement paste sample with water-cement ratio of 0.45
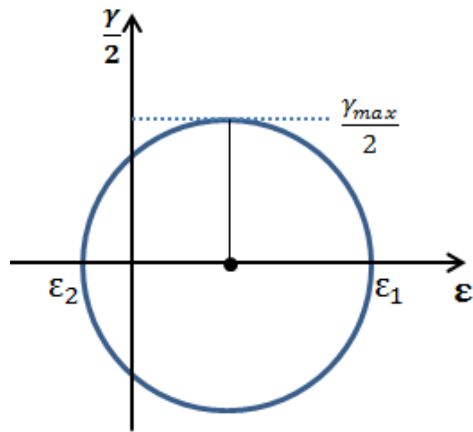
Figure 4.57 The Mohr Circle for the plane strain
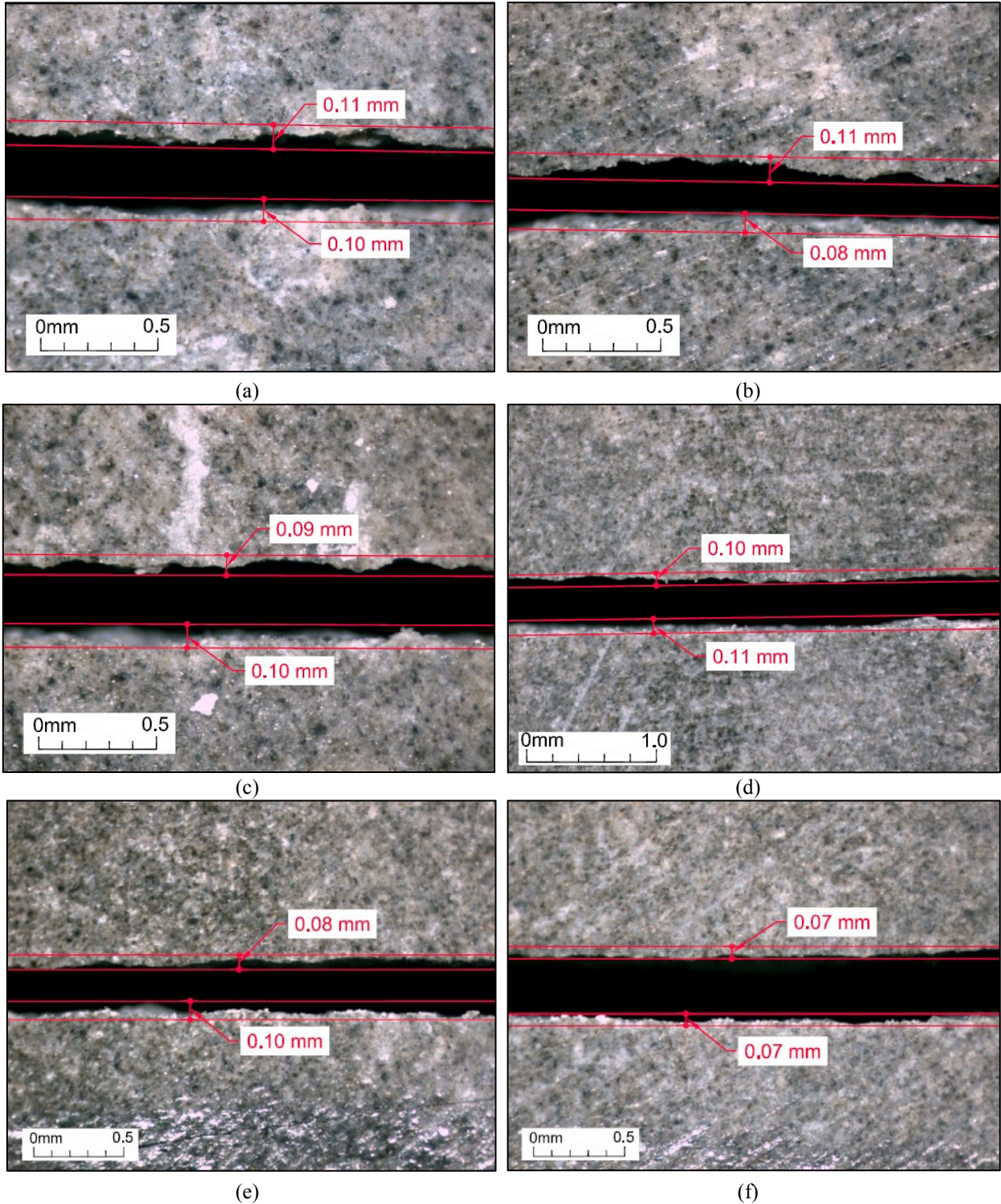
Figure 4.58 Pictures of tensile cracks from different samples or different locations under the microscope. (a) (b) (c) Cracks in cement paste samples with water-cement ratio of 0.6 at magnification of 45X; (d) Cracks in cement paste sample with water-cement ratio of 0.45 at magnification of 25X; (e) (f) Cracks in cement paste samples with water-cement ratio of 0.45 at magnification of 35X
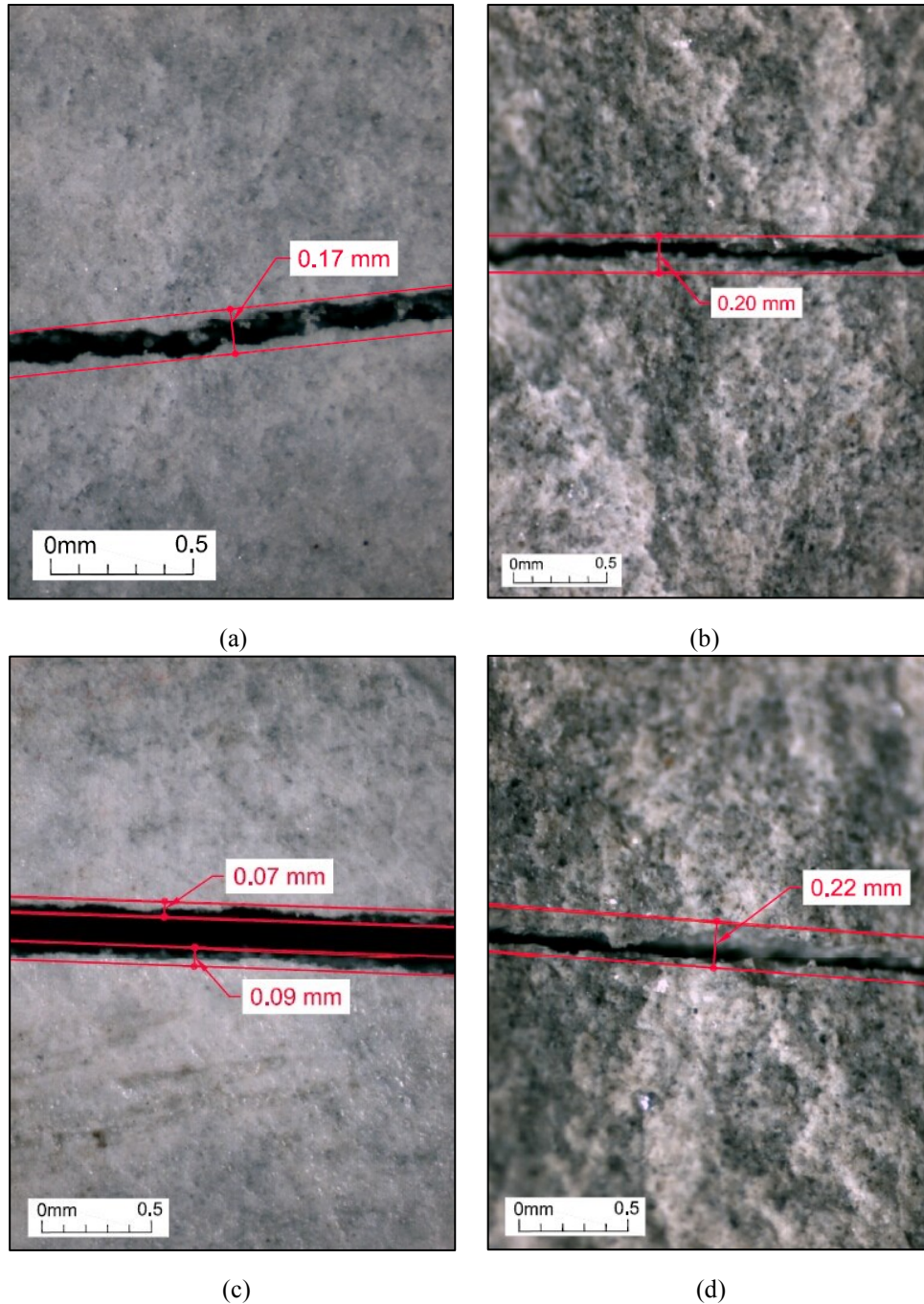
Figure 4.59 Pictures of different shear cracks under the microscope. (a) Cracks in cement paste sample with water-cement ratio of 0.6 at magnification of 45X; (b) Cracks in cement paste sample with water-cement ratio of 0.45 at magnification of 30X; (c) (d) Cracks in cement paste samples with water-cement ratio of 0.45 at magnification of 35X.

Three cement paste samples with w/c ratio of 0.6 and three samples with w/c ratio of 0.45 were tested to measure the maximum normal displacement. Samples were loaded at a constant

displacement rate of 0.002 mm/s in the Brazilian tensile tests as shown in Figure 4.60(a). Showa Measuring Instruments Co. strain gauges (Model No: N11-MA-5-350-11, gauge factor of 2.14±1%, and Resistance of 350±0.3% Ω) with length of 5 mm were used to record the traverse strains using a quarter Wheatstone bridge circuit. All the strain gauges were attached to the center of the samples with X60 Superglue from HBM (Figure 4.60(b)). The data acquisition system in the Mining laboratory at University of Alberta was used to measure the traverse stain and the applied load with time.

(a)   (c)
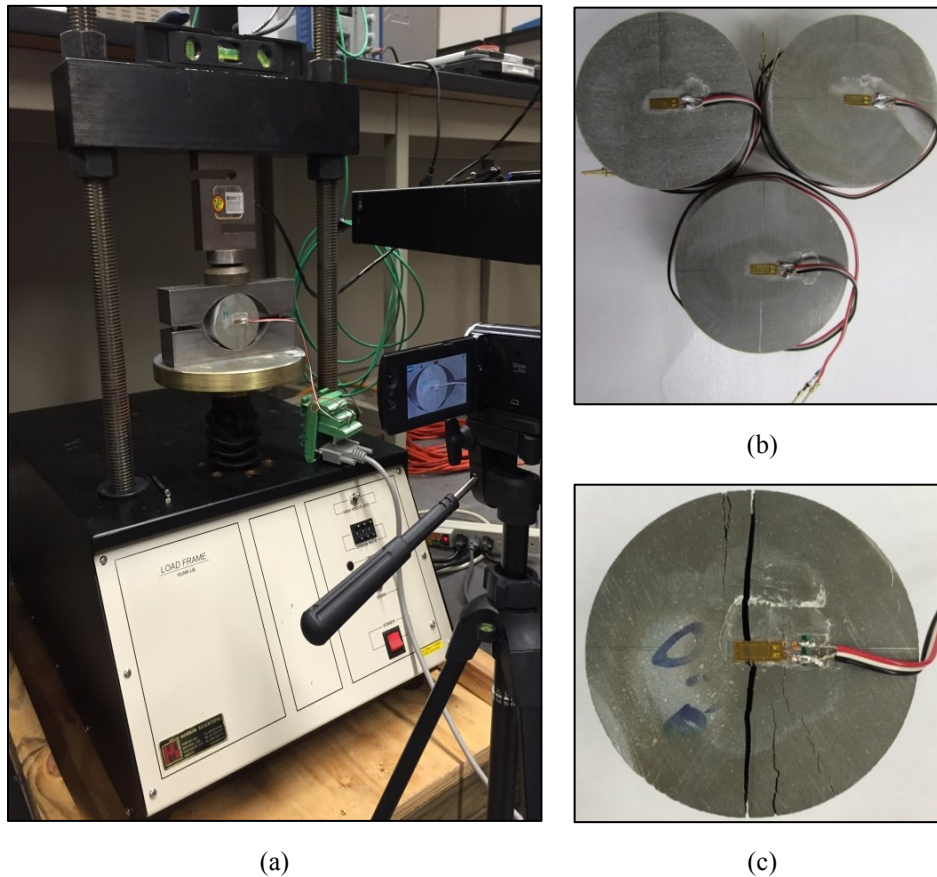
Figure 4.60 (a) The Brazilian tensile test in process with strain measurement; (b) The samples with strain gauges attached; (c) The post failure Brazilian tensile samples.

The test results for cement paste samples with w/c ratio of 0.45 and 0.6 are shown in Figure 4.61 and Figure 4.62. Since the results show scatter, the average slope method is used. The plots with averaged slopes of tensile strength versus strain curves are also shown in the figures, from which the maximum normal strains can be obtained based on the measured averaged Brazilian tensile strength (from Section 4.4.3). Therefore, the maximum normal strain ε_n is around 0.05% for 0.6

cement paste sample and around 0.06% for the 0.45 cement paste sample. Because the strain is calculated based on the strain gauge length (5 mm), the maximum normal displacement v' can be determined by multiplying the maximum normal strain by the strain gauge length, which is around 2.50×10^{-3} mm for the 0.6 cement paste sample and 3.00×10^{-3} mm for the 0.45 cement paste sample.

All the measurements and calculation results are summarized in Table 4.11. With the determined maximum normal and shear displacements before failure, the movement criterion can be calculated. For the cement paste sample with w/c ratio of 0.6, the movement criterion is 2.08. For the cement paste sample with w/c ratio of 0.45, the movement criterion is 2.42.
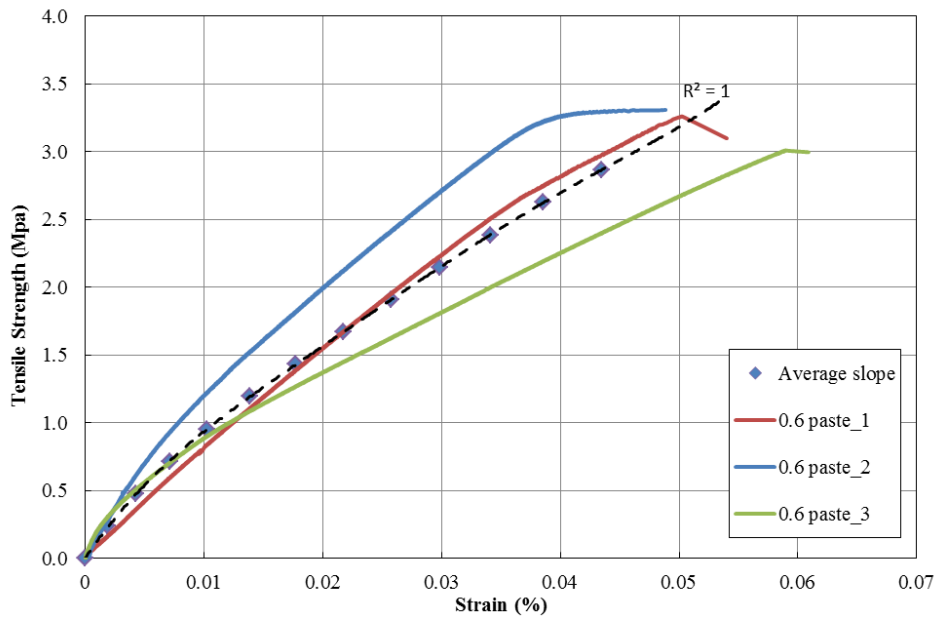
Figure 4.61 Tensile strength versus strain of cement paste samples with water-cement ratio of 0.6
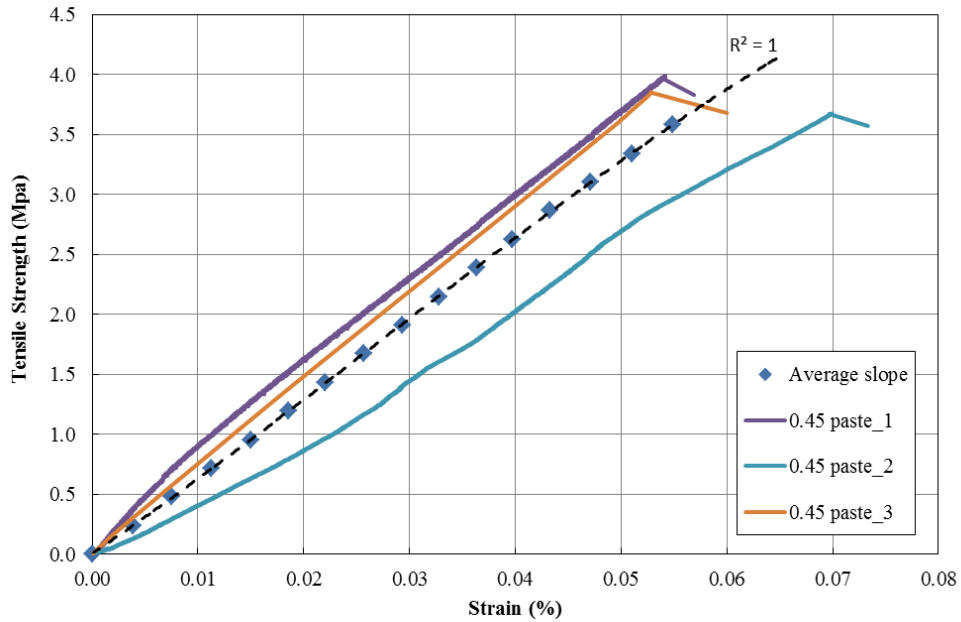
Figure 4.62 Tensile strength versus strain of cement paste samples with water-cement ratio of 0.45

Table 4.11 The calculation of movement criterion of cement paste samples

Samples	Maximum shear displacement u' (mm)	Maximum normal displacement v' (mm)	Movement criterion V_c
0.6 cement paste samples	1.20×10^{-3}	2.50×10^{-3}	2.08
0.45 cement paste samples	1.24×10^{-3}	3.00×10^{-3}	2.42

4.6 Summary

Several experiments were conducted to study the mechanical behavior of the cemented granular material and determine the measurements involved in the theoretical relationship. In this chapter, laboratory tests conducted to obtain the mechanical properties of the material are described in detail and the corresponding results are presented and interpreted.

Steel balls and Portland cement were chosen to prepare the artificial conglomerate and cement paste samples. To check the effect of particle size, uniform or non-uniform particle size distribution and cementing strength on the mechanical behavior of artificial conglomerate, two different sizes

of steel balls (diameters of 4.8 mm and 3.2 mm) and two w/c ratios of the cementing paste (w/c=0.6 and 0.45) were used to make the samples. To obtain consistent results, all the samples were air-dried under constant temperature for minimum 15 days before testing.

Direct shear, uniaxial/triaxial and Brazilian tensile tests were conducted on four different groups of artificial conglomerates and two groups of cement paste samples. The testing results from direct shear and uniaxial/triaxial testing are consistent, except for the cement paste samples with w/c ratio of 0.45 made from two different bags of Portland cement. For the artificial conglomerates, the post-peak stress-strain relationship is brittle, which indicates the primary contribution of the broken bonds to the peak stress. Due to nearly incompressible steel balls and the dense structure of steel balls assembly in the artificial conglomerate, not much change in the stiffness of the samples was found under the applied normal stresses and confining stresses, which is different from the behavior of natural conglomerates. In addition, no distinct difference was observed among the failure envelops of different groups of conglomerates. It implies that for the artificial conglomerate with the same structure of steel balls assembly, the effect of particle size and uniform/non-uniform particle size distribution on the strength and mechanical behavior is not obvious. This finding is also supported by the Brazilian tensile testing results. Since the difference between the two groups of cement paste samples is not obvious, the effect of cementing strength on the macro mechanical behavior cannot be concluded based on the experimental results.

Besides the measured macro parameters, including the peak friction angle ϕ_p, cohesion c and the tensile strength σ_t, the inter-particle friction angle ϕ_μ and movement criterion V_c are also required to verify the relationship derived in Chapter 3. In this study, an innovative method was designed to determine the inter-particle friction angle using a modified direct shear test. The steel balls were embedded in the bolt anchor sulfaset paste plate to fit in the upper and bottom halves of the shear box. With the known geometry conditions and mechanical relationships among those embedded steel balls, an equation was developed to relate the inter-particle friction angle to the applied normal load and measured horizontal load. The measured inter-particle friction angle ϕ_μ of steel balls used in this research is about 6.84°. For the determination of movement criterion of cement paste samples, Brazilian tensile tests with transverse strain measurement and UCS tests with the shear strain measurement were conducted. To obtain the maximum shear displacement, a

microscope was used to determine the thickness of shear failure zone. For cement paste sample with w/c of 0.6 and 0.45, the movement criterion is found to be 2.08 and 2.42, respectively.

Chapter 5: Post-Failure Analysis of the Failure Surface and Determination of Micro Bonding Strength

5.1 Introduction

Post-failure analysis was carried out on the failure surfaces of samples tested in direct shear and Brazilian tensile tests to obtain the micro bonding strength, contact area coefficient and the movement coefficient.

Tensile strength of the artificial conglomerate consists of the cement's tensile strength and the normal bonding strength between steel balls and cement as:

$$\sigma_t = \frac{\sigma_c \, A_C}{A} + \frac{\sigma_m \, A_B}{A} \qquad\qquad [5.1]$$

where σ_t is the tensile strength of artificial conglomerate, σ_c is the tensile strength of Portland cement paste sample, σ_m is the normal bonding strength between steel ball and cement, A_C is the area occupied by the cement-cement contact on the failure surface, A_B is the area occupied by the steel ball-cement contact on the failure surface, and A is the total area of failure surface of the artificial conglomerate.

Similarly, shear strength of the artificial conglomerate consists of two parts based on the Mohr Coulomb criterion, namely, cohesion and friction. Cohesion is due to the cohesive strength of cement and shear bonding strength between steel balls and cement along the failure surface as:

$$\tau = c + \sigma \tan \phi = \frac{\tau_c \, A_C}{A} + \frac{\tau_m \, A_B}{A} + \sigma \tan \phi \qquad\qquad [5.2]$$

where τ is the shear strength of artificial conglomerate, c is the cohesion of artificial conglomerate, σ is the normal stress, ϕ is the macro friction angle, τ_c is the cohesion of Portland cement paste sample, τ_m is the shear bonding strength between steel ball and cement, and A_C, A_B, and A are the same as defined above.

To obtain the shear bonding strength τ_m and normal bonding strength σ_m, the total area of the failure surface (A), and areas occupied by cement-cement contact (A_C) and steel ball-cement contact (A_B) should be determined from the post failure analysis of failure surface.

5.2 Measurement of total area of failure surface

In this study, the total area of failure surface is measured using 3D scanning. A portable and handheld 3D laser scanner named MAXscan, manufactured by Creaform (Figure 5.1(a)), was used to produce the 3D geometry of failed sample. The maximum resolution of this scanner is 0.1 mm and its maximum accuracy is 0.05mm. The scanner has a high measurement rate of 18,000 measurements/seconds and a volumetric accuracy of 0.020 mm + 0.025 mm/m. Since steel balls on the failure surface are reflective, before the scanning, the '3D scan spray' manufactured by Laser Design was used to apply evenly thin layer anti-reflection coating on the failure surface with minimal thickness (average particle size of 2.8 μm), as shown in Figure 5.2.

<table>
<tr><td>(a)</td><td>(b)</td></tr>
</table>

Figure 5.1 (a) 3D laser scanner (MAXscan); (b) Artificial reflective targets in the background.

The triangulation depth sensors used in the 3D scanner can calculate the depth of scanned point through trigonometry. The sample surface appears in the camera's field of view when the emitter of the scanner projects laser line on the sample's surface. The emitter, the point on the laser line, and the camera form a triangle. The depths of the points on the targeted surface corresponding to the laser line can be calculated using known angles and distances automatically. Besides, artificial highly reflective target points were used as reference background (Figure 5.1(b)). The 3D sensors can calculate the coordinates of artificial targets at high accuracy, which assists the precise calculation of the surface point coordinate of the sample. The use of artificial targets can improve the accuracy and data acquisition speed (Kainat 2014).

In this way, the position of scanned sample in space can be continuously calculated and the optimized surface information is captured through an automatic surface generation. At the same

time, the software 'VXelements' was used to monitor the data acquisition process on a laptop to achieve the real-time visualization of the scanned surface.

(a)   (b)
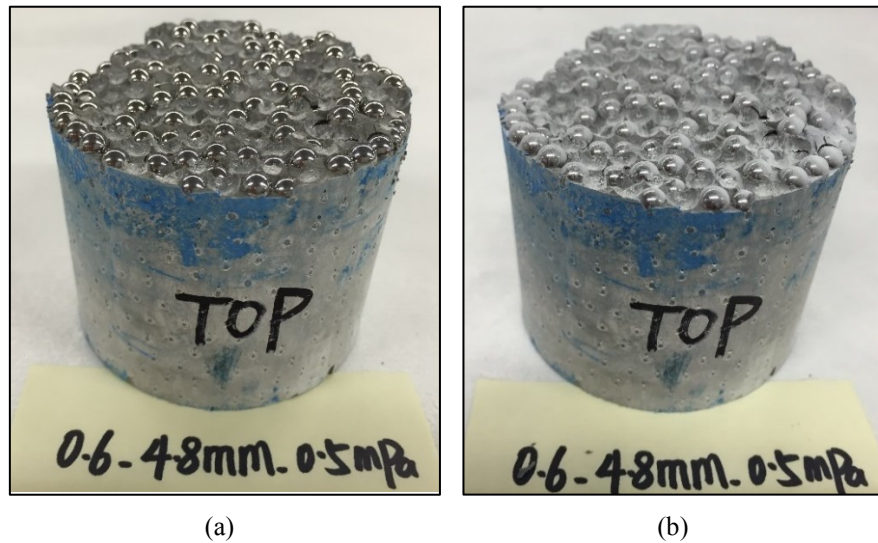
Figure 5.2 The failed artificial conglomerate from direct shear testing: (a) before treatment; (b) with anti-reflection coating.

The digital file from 3D scanning was imported and analyzed using the 'Geomagic control' software, as shown in Figure 5.3. The produced artificial conglomerate from direct shear test was trimmed for easy operation, and then the total area of the failure surface was chosen and calculated. Some of other analyzed failure surfaces are shown in Figures 5.4 and 5.5. The calculated total area of the highlighted failure surface from direct shear and Brazilian tensile samples are summarized in Table 5.1 and Table 5.2, respectively.

(a)   (b)
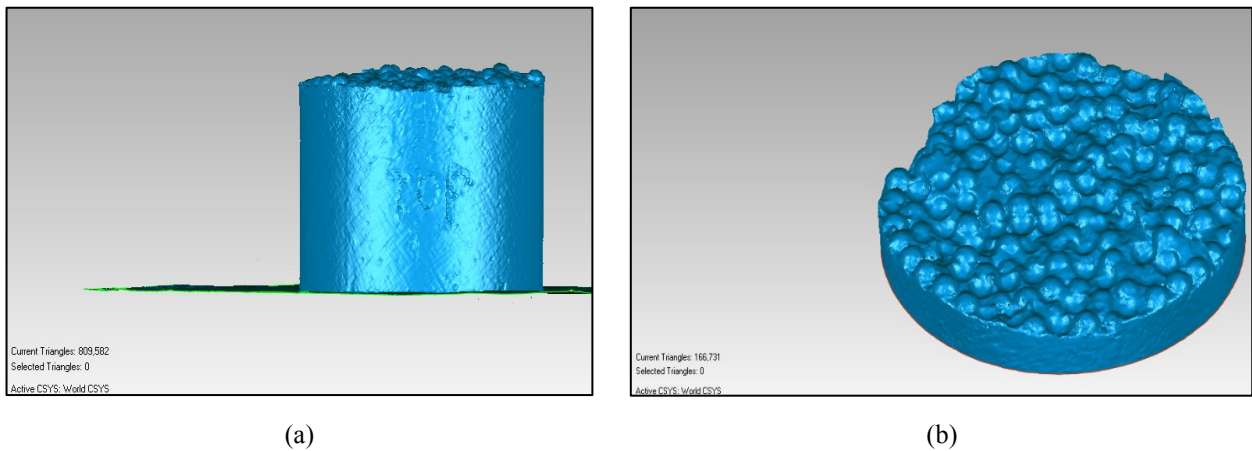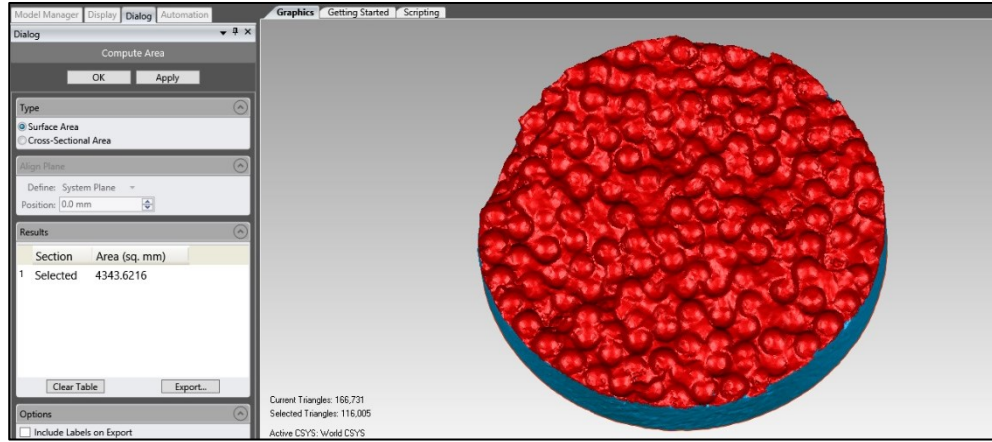
(c)

Figure 5.3 The direct shear testing failure surface analysis with the 'Geomagic control' software: (a) The produced group 1 artificial conglomerate under 0.5 MPa from 3D scanning; (b) Trimmed sample for easy operation; (c) Highlighted failure surface and the calculated total area of the failure surface.
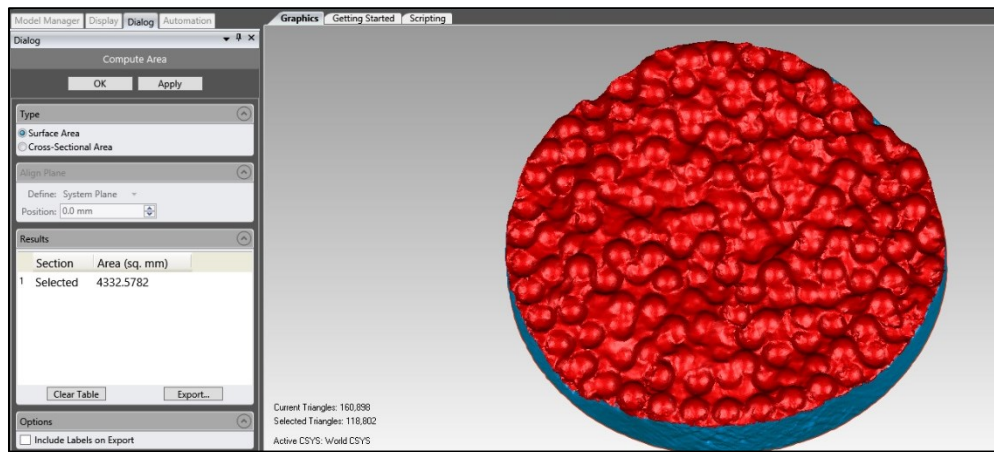
(a)
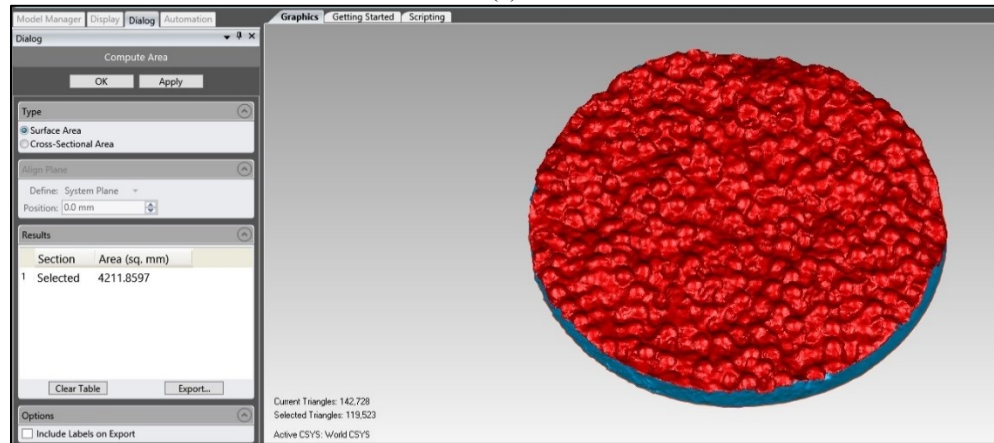
(b)
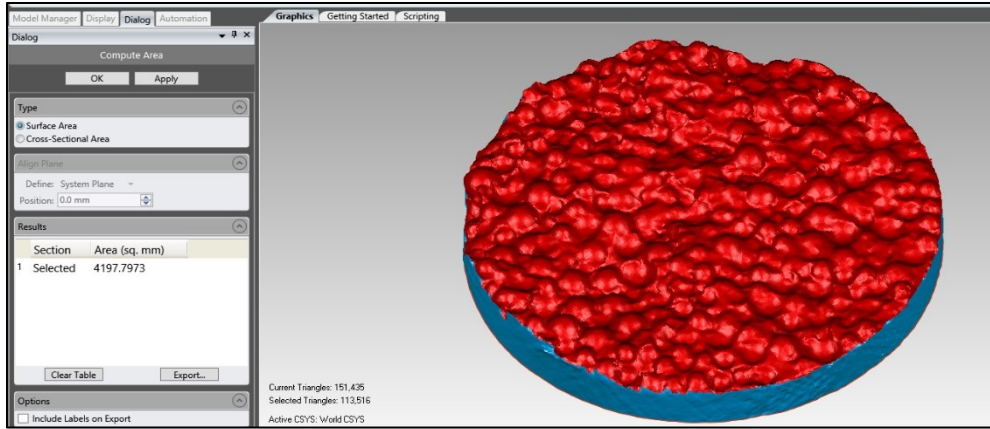
(c)
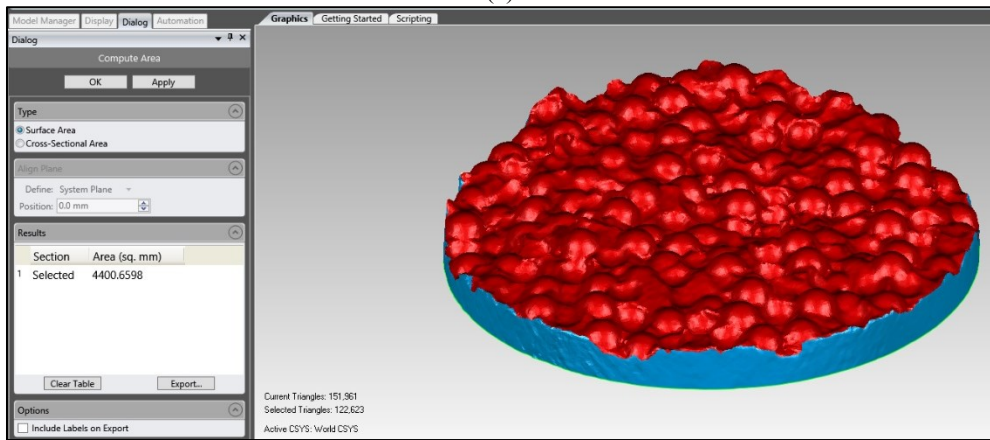
(d)

Figure 5.4 Total area of failure surface of direct shear testing samples under 2 MPa: (a) group 1 artificial conglomerate; (b) group 2 artificial conglomerate; (c) group 3 artificial conglomerate; (d) group 4 artificial conglomerate.
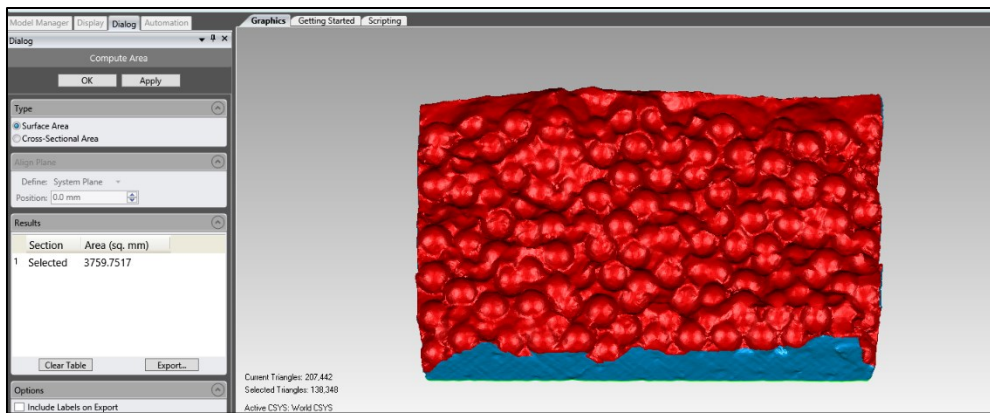
(a)
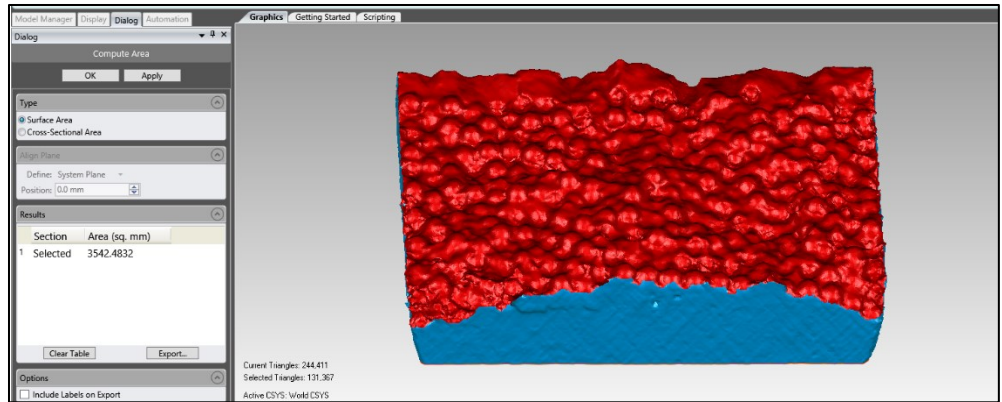
(b)
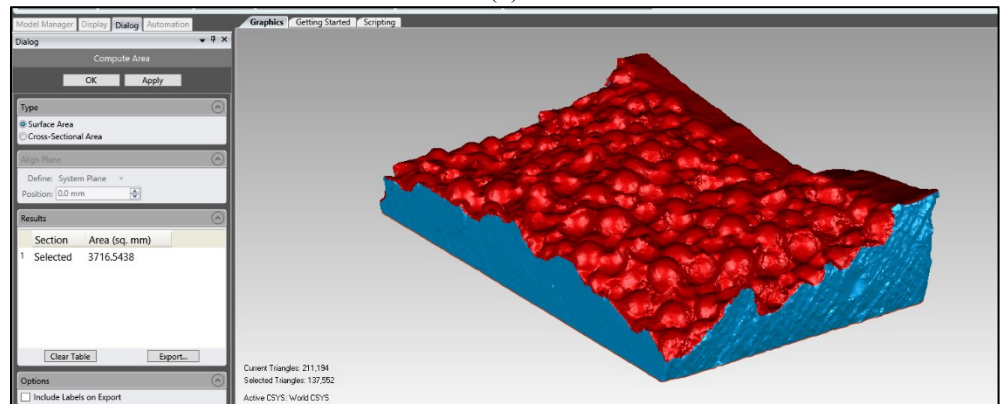
(c)
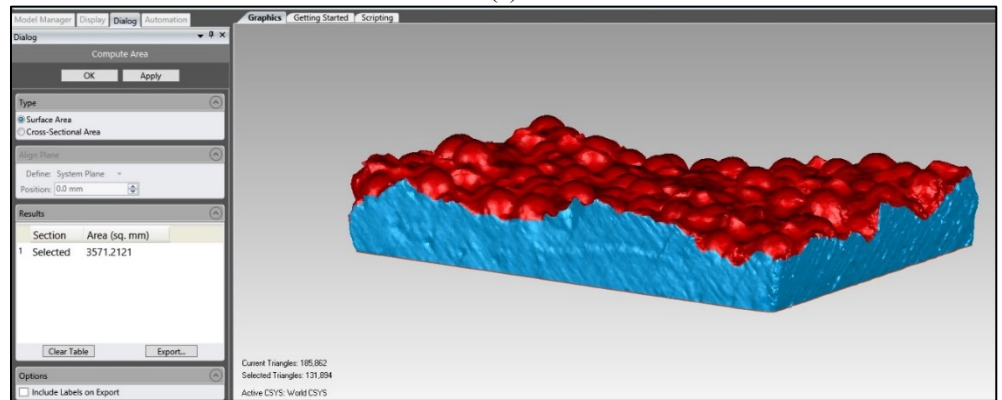
(d)

Figure 5.5 Total area of failure surface of Brazilian tensile testing samples: (a) group 1 artificial conglomerate; (b) group 2 artificial conglomerate; (c) group 3 artificial conglomerate; (d) group 4 artificial conglomerate.

Table 5.1 Total area of failure surface of direct shear testing samples

Artificial samples	Sample No.	Normal stress (MPa)	Total failure surface area A (mm^2)
Group 1	0.6_4.8mm_1	0.5	4343.62
	0.6_4.8mm_2	2	4332.58
	0.6_4.8mm_3	5	4223.44
	0.6_4.8mm_4	10	4338.18
	0.6_4.8mm_5	2	4276.93
Group 2	0.6_3.2mm_1	0.5	4208.17
	0.6_3.2mm_2	2	4211.86
	0.6_3.2mm_3	5	4251.08
	0.6_3.2mm_4	10	4101.28
	0.6_3.2mm_5	10	4119.56
Group 3	0.6_mix_1	0.5	4237.49
	0.6_mix_2	2	4197.80
	0.6_mix_3	5	4080.10
	0.6_mix_4	10	4192.77
	0.6_mix_5	5	4231.73
Group 4	0.45_4.8mm_1	0.5	4342.57
	0.45_4.8mm_2	2	4400.66
	0.45_4.8mm_3	5	4523.79
	0.45_4.8mm_4	10	4286.44
	0.45_4.8mm_5	2	4348.71

Table 5.2 Total area of failure surface of Brazilian tensile testing conglomerates

Artificial samples	Sample No.	Total failure surface area A(mm²)
Group 1	0.6_4.8mm_1	3759.75
	0.6_4.8mm_2	3682.79
Group 2	0.6_3.2mm_1	3542.48
	0.6_3.2mm_2	3611.81
Group 3	0.6_mix_1	3716.54
	0.6_mix_2	3723.47
Group 4	0.45_4.8mm_1	3571.21
	0.45_4.8mm_2	3671.05

5.3 Measurement of steel ball-cement contact area on the failure surface

Failure surface consists of steel ball-cement and cement-cement contact areas. Besides the total area of failure surface, the area occupied by the steel ball-cement contact is required for the micro bonding strength determination. As shown in Figure 5.6, the steel ball-cement contact area A_B has 2 components: the surface area of steel balls and the area of holes once occupied by steel balls. Based on the height h above/below the imaginary failure plane, the steel balls and holes on the failure surface were divided into five cases (Figure 5.7), namely $\frac{1}{4}r, \frac{1}{2}r, r, \frac{3}{2}r$ and $\frac{7}{4}r$, where r is the radius of steel ball. For example, Case 1 includes the steel ball with height about $\frac{1}{4}r$ above the imaginary failure plane and the hole that is around $\frac{1}{4}r$ below the imaginary failure plane. Since the numbers of steel balls and holes on the failure surface for each case can be counted, the steel ball-cement contact area on the failure surface (A_B) can be calculated based on Eq. 5.3 below.

$$A_B = \frac{1}{2}\pi r^2 N_1 + \pi r^2 N_2 + 2\pi r^2 N_3 + 3\pi r^2 N_4 + \frac{7}{2}\pi r^2 N_5 \qquad [5.3]$$

where A_B is the area occupied by the steel ball-cement contact on the failure surface,

r is the radius of steel ball on the failure surface,

N_1 is the number of steel balls and holes on the failure surface for Case 1, when $h = \frac{1}{4}r$,

N_2 is the number of steel balls and holes on the failure surface for Case 2, when $h=\frac{1}{2}r$,

N_3 is the number of steel balls and holes on the failure surface for Case 3, when $h=r$,

N_4 is the number of steel balls and holes on the failure surface for Case 4, when $h=\frac{3}{2}r$, and

N_5 is the number of steel balls and holes on the failure surface for Case 5, when $h=\frac{7}{4}r$.

Figure 5.8 presents some of the conglomerate pictures used for counting and calculation. The cases of steel balls and holes for each case were marked on enlarged pictures when studying the actual sample. Obviously, only steel balls above the imaginary failure plane exist for Case 4 and Case 5. The calculated steel ball-cement contact area from direct shear and Brazilian tensile testing samples are summarized in Table 5.3 and Table 5.4, respectively. It is worth mentioning that for the conglomerates with mixed steel balls (Group 3 artificial conglomerates), counting/calculation were conducted separately for each ball radius (r).

The area of holes once occupied by steel balls

The surface area of steel balls above the imaginary failure plane
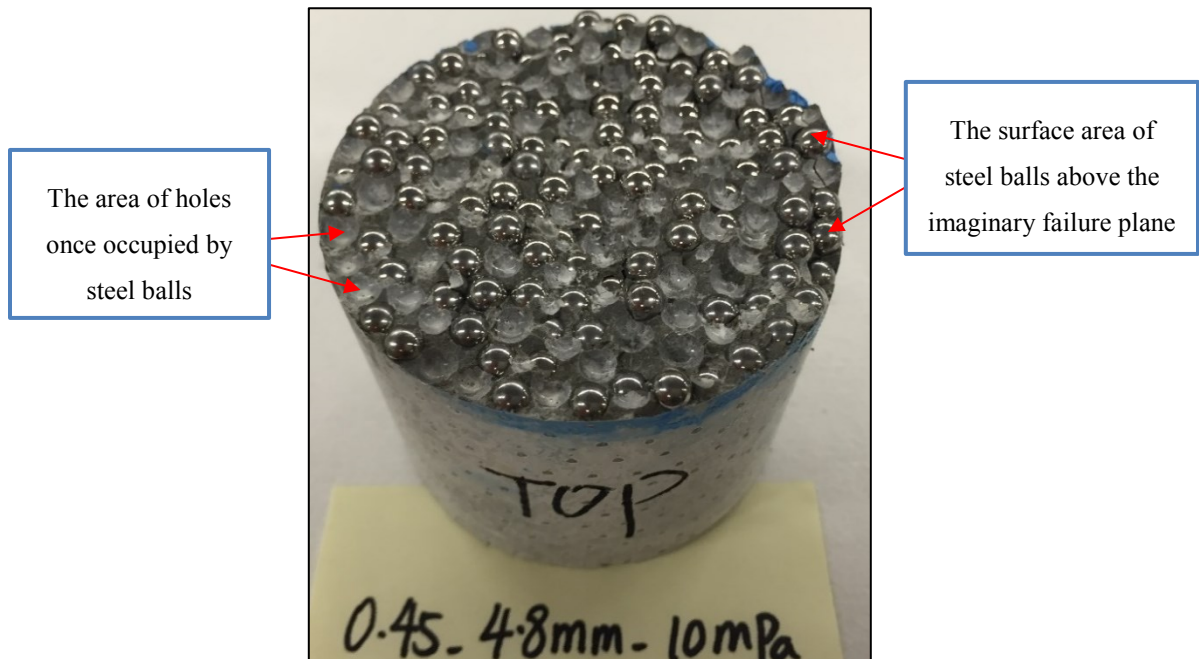
Figure 5.6 The two components of steel ball-cement contact area on the failure surface
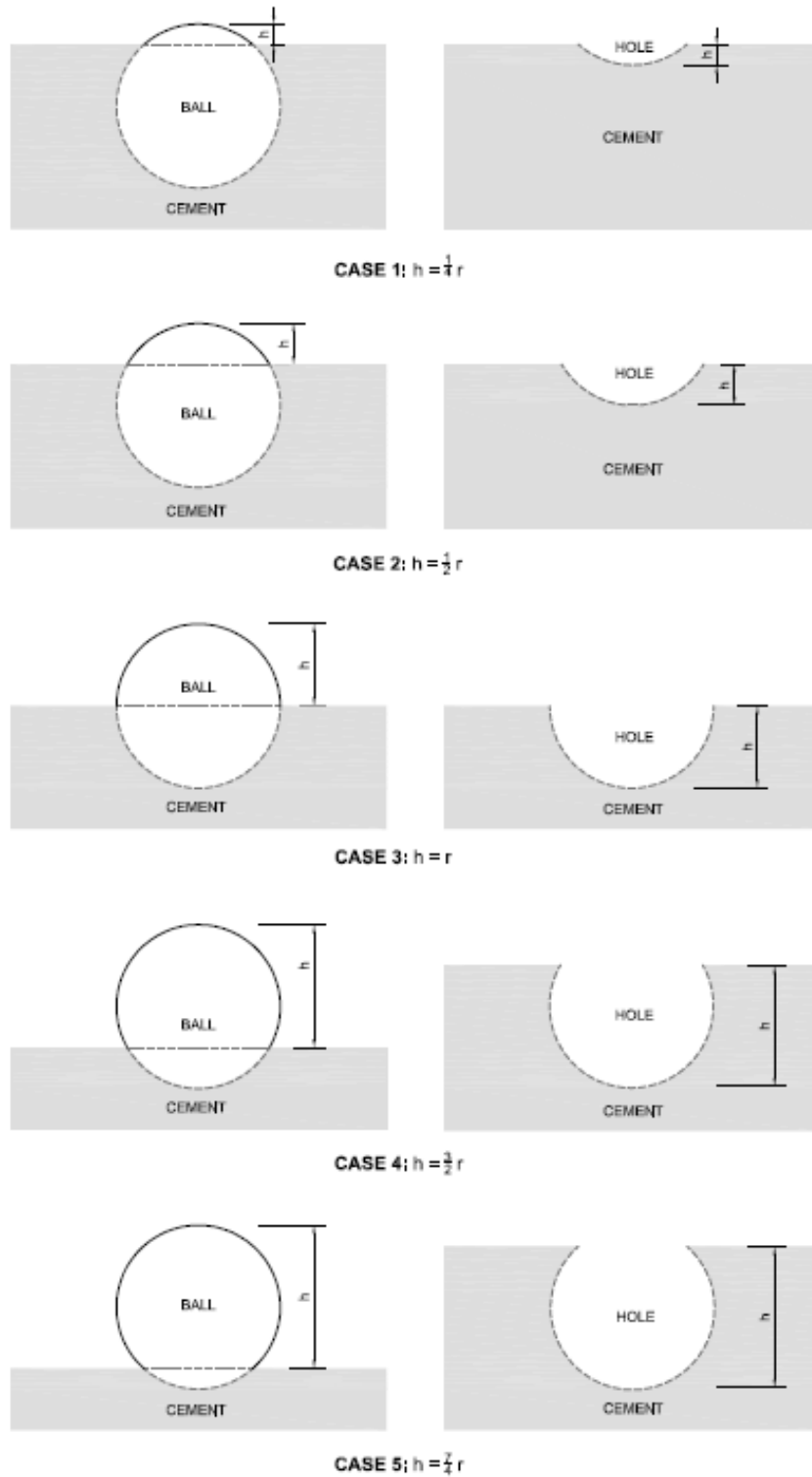
Figure 5.7 Five cases of steel balls and holes on the failure surface
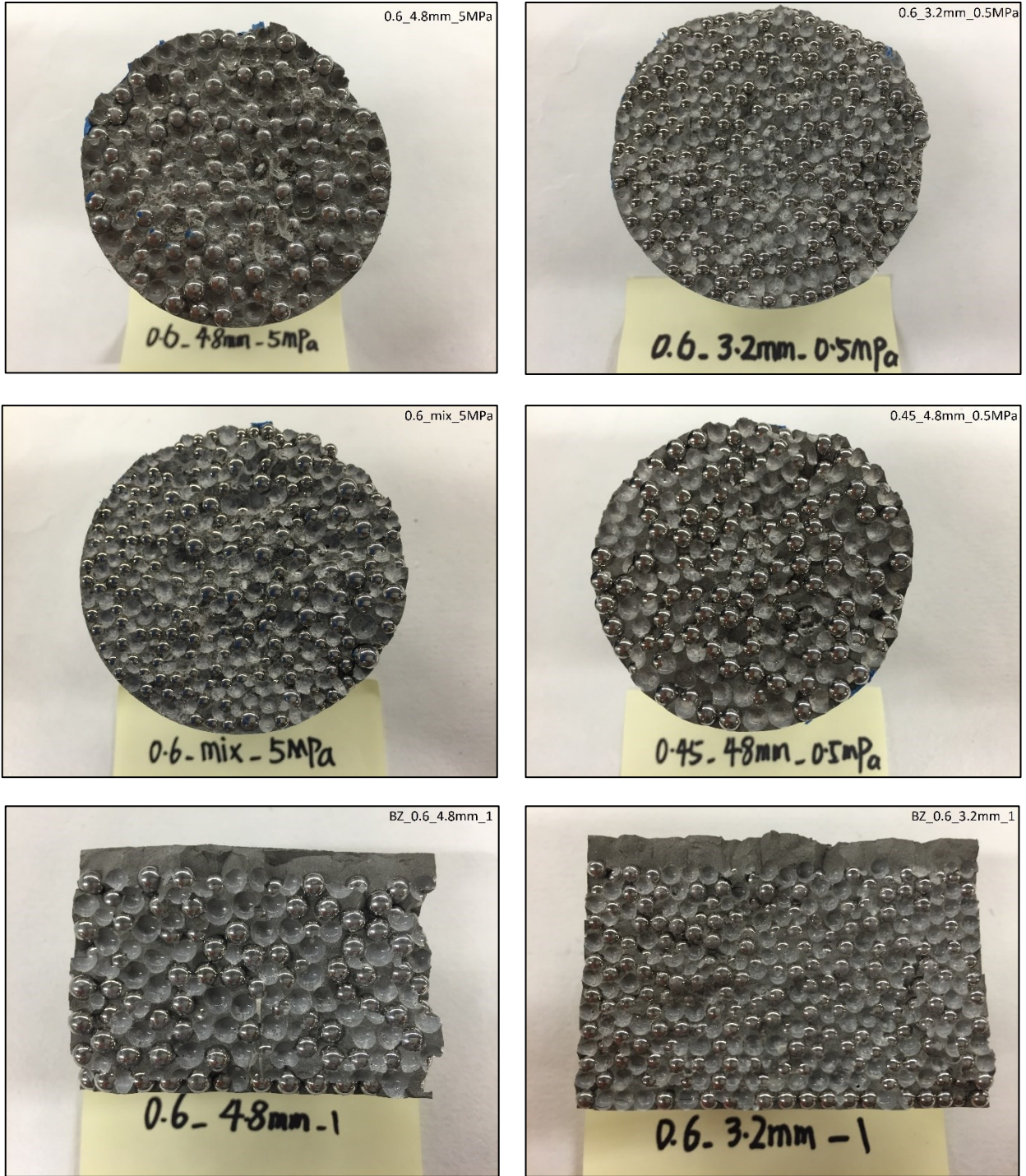
Figure 5.8 Some of the pictures used for the steel ball-cement contact area determination

Table 5.3 Calculated steel ball-cement contact area on the failure surface of direct shear testing conglomerates

Artificial samples	Sample No.	Normal stress (MPa)	No. of 4.8 mm balls/holes on the failure surface					No. of 3.2 mm balls/holes on the failure surface					Area occupied by steel ball-cement contact A_B (mm^2)
			Case 1	Case 2	Case 3	Case 4	Case 5	Case 1	Case 2	Case 3	Case 4	Case 5	
Group 1	0.6_4.8mm_1	0.5	75	52	33	2	0	-	-	-	-	-	2886.02
	0.6_4.8mm_2	2	98	66	23	3	0	-	-	-	-	-	3037.91
	0.6_4.8mm_3	5	112	54	22	0	0	-	-	-	-	-	2751.99
	0.6_4.8mm_4	10	95	59	24	4	0	-	-	-	-	-	2975.37
	0.6_4.8mm_5	2	114	58	19	2	0	-	-	-	-	-	2841.34
Group 2	0.6_3.2mm_1	0.5	-	-	-	-	-	228	142	37	6	0	2755.22
	0.6_3.2mm_2	2	-	-	-	-	-	220	136	26	12	0	2644.38
	0.6_3.2mm_3	5	-	-	-	-	-	243	128	29	9	1	2676.05
	0.6_3.2mm_4	10	-	-	-	-	-	225	114	40	9	0	2640.42
	0.6_3.2mm_5	10	-	-	-	-	-	213	131	38	12	0	2767.10
Group 3	0.6_mix_1	0.5	36	35	11	2	0	95	81	20	4	0	2876.55
	0.6_mix_2	2	44	28	8	1	0	122	71	21	4	0	2705.65
	0.6_mix_3	5	38	21	6	3	0	110	103	21	3	1	2772.50
	0.6_mix_4	10	39	25	9	3	0	108	88	24	7	0	2948.26
	0.6_mix_5	5	50	22	8	1	0	125	72	21	5	0	2695.59
Group 4	0.45_4.8mm_1	0.5	104	61	26	3	0	-	-	-	-	-	3109.39
	0.45_4.8mm_2	2	78	63	23	7	0	-	-	-	-	-	3020.04
	0.45_4.8mm_3	5	81	75	24	4	0	-	-	-	-	-	3136.20
	0.45_4.8mm_4	10	94	56	22	6	0	-	-	-	-	-	2948.56
	0.45_4.8mm_5	2	94	64	16	8	0	-	-	-	-	-	2984.30

Table 5.4 Calculated steel ball-cement contact area on the failure surface of Brazilian tensile testing conglomerates

Artificial samples	Sample No.	No. of 4.8 mm balls/holes on the failure surface					No. of 3.2 mm balls/holes on the failure surface					Area occupied by steel ball-cement contact A_B (mm^2)
		Case 1	Case 2	Case 3	Case 4	Case 5	Case 1	Case 2	Case 3	Case 4	Case 5	
Group 1	0.6_4.8mm_1	76	54	11	3	0	-	-	-	-	-	2198.02
	0.6_4.8mm_2	70	55	14	3	0	-	-	-	-	-	2269.50
Group 2	0.6_3.2mm_1	-	-	-	-	-	162	121	24	3	0	2050.58
	0.6_3.2mm_2	-	-	-	-	-	170	112	31	6	0	2193.09
Group 3	0.6_mix_1	38	36	7	3	0	63	45	13	4	0	2300.40
	0.6_mix_2	38	31	8	2	0	65	47	16	2	0	2216.93
Group 4	0.45_4.8mm_1	77	40	15	4	0	-	-	-	-	-	2153.35
	0.45_4.8mm_2	74	47	14	3	0	-	-	-	-	-	2162.28

5.4 Determination of micro bonding strength

As mentioned above, for the artificial conglomerate, the total area of the failure surface consists of the area occupied by the cement-cement contact (A_C) and the area occupied by the steel ball-cement contact (A_B). Therefore, the area ratios of $\frac{A_C}{A}$ and $\frac{A_B}{A}$ can be determined from the results presented in Section 5.2 and 5.3.

Based on Eq. 5.1, the normal bonding strength σ_m can be obtained from the tensile strength of artificial conglomerate σ_t, the tensile strength of Portland cement paste sample σ_c, and the area ratios of $\frac{A_C}{A}$ and $\frac{A_B}{A}$. Since σ_t and σ_c have been measured from the Brazilian tensile testing, the normal bonding strength σ_m was calculated and summarized in Table 5.5. For the four groups of artificial conglomerates, the normal bonding strength is in the range of 0.40 to 0.73MPa.

Similarly, the cohesion of artificial conglomerate c and the cohesion of Portland cement paste sample τ_c are determined from laboratory tests. Table 5.6 presents the shear bonding strength between steel ball and cement as calculated from Eq. 5.2. For group 1 to group 4 artificial conglomerates, the shear bonding strengths are 2.84, 1.89, 1.50 and 1.79 MPa, respectively.

Table 5.5 Calculation of the normal bonding strength of artificial conglomerates

Artificial samples	Sample No.	Total failure surface area A (mm^2)	Area occupied by steel ball-cement contact A$_B$ (mm^2)	A$_B$/A	Average A$_B$/A	Tensile strength (MPa)	Normal bonding strength σ_m (MPa)
Group 1	0.6_4.8mm_1	3759.75	2198.02	0.585	0.600	1.55	0.40
	0.6_4.8mm_2	3682.79	2269.50	0.616			
Group 2	0.6_3.2mm_1	3542.48	2050.58	0.579	0.593	1.77	0.73
	0.6_3.2mm_2	3611.81	2193.09	0.607			
Group 3	0.6_mix_1	3716.54	2300.40	0.619	0.607	1.65	0.60
	0.6_mix_2	3723.47	2216.93	0.595			
Group 4	0.45_4.8mm_1	3571.21	2153.35	0.603	0.596	1.75	0.41
	0.45_4.8mm_2	3671.05	2162.28	0.589			
Group 5	0.6 cement paste	-	-	-	-	3.28	-
Group 6	0.45 cement paste	-	-	-	-	3.72	-

Table 5.6 Calculation of the shear bonding strength of artificial conglomerates

Artificial samples	Sample No.	Normal stress (MPa)	Total failure surface area A (mm²)	Area occupied by steel ball-cement contact A_B (mm²)	A_B/A	Average A_B/A	Cohesion (MPa)	Shear bonding strength τ_m (MPa)
Group 1	0.6_4.8mm_1	0.5	4343.62	2886.02	0.664	0.673	3.22	2.84
	0.6_4.8mm_2	2	4332.58	3037.91	0.701			
	0.6_4.8mm_3	5	4223.44	2751.99	0.652			
	0.6_4.8mm_4	10	4338.18	2975.37	0.686			
	0.6_4.8mm_5	2	4276.93	2841.34	0.664			
Group 2	0.6_3.2mm_1	0.5	4208.17	2755.22	0.655	0.646	2.64	1.89
	0.6_3.2mm_2	2	4211.86	2644.38	0.628			
	0.6_3.2mm_3	5	4251.08	2676.05	0.629			
	0.6_3.2mm_4	10	4101.28	2640.42	0.644			
	0.6_3.2mm_5	10	4119.56	2767.10	0.672			
Group 3	0.6_mix_1	0.5	4237.49	2876.55	0.679	0.669	2.33	1.50
	0.6_mix_2	2	4197.80	2705.65	0.645			
	0.6_mix_3	5	4080.10	2772.50	0.680			
	0.6_mix_4	10	4192.77	2948.26	0.703			
	0.6_mix_5	5	4231.73	2695.59	0.637			
Group 4	0.45_4.8mm_1	0.5	4342.57	3109.39	0.716	0.694	2.59	1.79
	0.45_4.8mm_2	2	4400.66	3020.04	0.686			
	0.45_4.8mm_3	5	4523.79	3136.20	0.693			
	0.45_4.8mm_4	10	4286.44	2948.56	0.688			
	0.45_4.8mm_5	2	4348.71	2984.30	0.686			
Group 5	0.6 cement paste	-	-	-	-	-	4.00	-
Group 6	0.45 cement paste	-	-	-	-	-	4.40	-

5.5 Determination of the contact area coefficient w

In the 2D theoretical derivation, it is assumed that the contact area between rod and cement equals to $a_c = \omega dt$, where d and t are the diameter and thickness of the rod. In order to obtain the contact area coefficient w, the average contact area a_c must be determined.

Based on the results in Table 5.3, the average contact area between steel ball and cement a_{3D} can be determined by dividing the total area of steel ball-cement contact on the failure surface by the total number of contacts, as shown in Eq. 5.4.

$$a_{3D} = \frac{A_B}{N_1 + N_2 + N_3 + N_4 + N_5} \qquad [5.4]$$

where A_B is the area occupied by the steel ball-cement contact on the failure surface,

N_1 is the number of steel balls and holes on the failure surface for Case 1, when $h=\frac{1}{4}r$,

N_2 is the number of steel balls and holes on the failure surface for Case 2, when $h=\frac{1}{2}r$,

N_3 is the number of steel balls and holes on the failure surface for Case 3, when $h=r$,

N_4 is the number of steel balls and holes on the failure surface for Case 4, when $h=\frac{3}{2}r$, and

N_5 is the number of steel balls and holes on the failure surface for Case 5, when $h=\frac{7}{4}r$.

As shown in Figure 5.9, the average contact area a_{3D} can be treated as the surface area of spherical cap of steel ball. Let r be the radius of the steel ball and h be the height of the cap, then the surface area of steel ball spherical cap is:

$$a_{3D} = 2\pi r * h \qquad [5.5]$$

The curve L_{AB} is the projection of steel ball spherical cap on the YZ plane, which can be obtained from the actual average contact area a_{3D}. The length of the curve L_{AB} should be the same as the projection of the assumed 2D contact area a_c on the YZ plane. In this way, the contact area coefficient w can be obtained when the length of curve L_{AB} is determined.
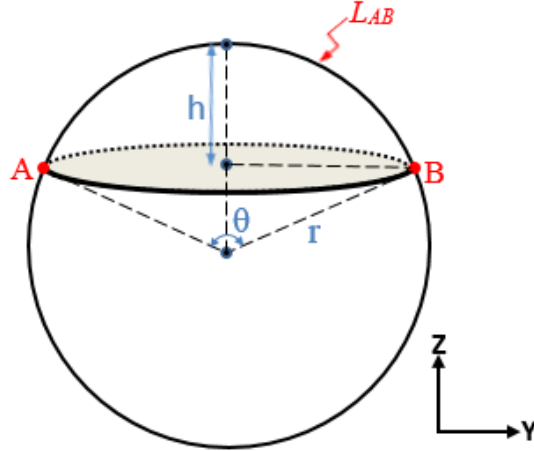
Figure 5.9 The spherical cap of steel ball

Let θ be the angle in degrees corresponding to the curve L_{AB} as shown in Figure 5.9. Then the angle θ can be calculated from the height h and the radius r as:

$$\cos\frac{\theta}{2} = \frac{r - h}{r} \tag{5.6}$$

Since the length of L_{AB} is related to the angle θ as follows:

$$L_{AB} = \frac{\pi\theta}{180°} * r \tag{5.7}$$

Combining Eq. 5.5, Eq. 5.6 and Eq. 5.7, the length of L_{AB} can be determined with known contact area a_{3D}:

$$L_{AB} = \frac{2\pi r}{180°}\cos^{-1}(1 - \frac{a_{3D}}{2\pi r^2}) \tag{5.8}$$

As mentioned above, the projection of the assumed 2D contact area on the YZ plane is $a_{cYZ} = \omega d$ and it should be equal to the length of curve L_{AB}. Hence, the contact area coefficient ω can be calculated from:

$$\omega = L_{AB}/d = \frac{\pi}{180°}\cos^{-1}(1 - \frac{a_{3D}}{2\pi r^2}) \tag{5.9}$$

The calculated contact area coefficients for group 1 to group 4 artificial conglomerates are summarized in Table 5.7, which are 0.98, 0.98, 0.99 and 1.01, respectively.

114

Table 5.7 Summary of the contact area coefficient of direct shear testing conglomerates

Artificial samples	Sample No.	Area occupied by steel ball-cement contact A_B (mm²)	The contact area a_c (mm²)	Average a_c (mm²)	The contact area coefficient w
Group 1	0.6_4.8mm_1	2886.02	17.81	15.90	0.98
	0.6_4.8mm_2	3037.91	15.99		
	0.6_4.8mm_3	2751.99	14.64		
	0.6_4.8mm_4	2975.37	16.35		
	0.6_4.8mm_5	2841.34	14.72		
Group 2	0.6_3.2mm_1	2755.22	6.67	6.75	0.98
	0.6_3.2mm_2	2644.38	6.71		
	0.6_3.2mm_3	2676.05	6.53		
	0.6_3.2mm_4	2640.42	6.81		
	0.6_3.2mm_5	2767.10	7.02		
Group 3	0.6_mix_1	2876.55	10.13	9.37	0.99
	0.6_mix_2	2705.65	9.05		
	0.6_mix_3	2772.50	9.06		
	0.6_mix_4	2948.26	9.73		
	0.6_mix_5	2695.59	8.87		
Group 4	0.45_4.8mm_1	3109.39	16.03	16.74	1.01
	0.45_4.8mm_2	3020.04	17.66		
	0.45_4.8mm_3	3136.20	17.04		
	0.45_4.8mm_4	2948.56	16.56		
	0.45_4.8mm_5	2984.30	16.40		

5.6 Determination of the movement coefficient α

In the theoretical derivation, it is assumed that the relationships between the resisting forces on the contact points and the corresponding movements are linear; therefore the movement criterion and coefficient have the relationship of $V_c = \alpha \frac{N_m^p}{T_m^p}$, where $\frac{N_m^p}{T_m^p}$ equals to the ratio of the peak normal resisting force to the peak shear resisting force at the steel ball-cement contact. As assumed in the

derivation, tensile failure and shear failure at different contact points take place at the same time. Therefore, the contact areas for tension failure and shear failure are the same. Then, the bonding strength equals to the peak resisting force divided by the contact area, and $\frac{N_m^p}{T_m^p}$ should equal to the ratio of the normal bonding strength to shear bonding strength $\frac{\sigma_m}{\tau_m}$. Therefore, the following relationship is obtained:

$$V_c = \alpha \frac{N_m^p}{T_m^p} = \alpha \frac{\sigma_m}{\tau_m} \qquad [5.10]$$

As shown in the Table 5.8, after substituting the measured movement criterion V_c and calculated normal to shear bonding strength ratio $\frac{\sigma_m}{\tau_m}$ into the Eq. 5.10, the movement coefficient α can be calculated. For the four groups of conglomerates, the movement coefficient is in the range of 5.25 to 14.82.

Table 5.8 Calculation of the movement coefficient of artificial conglomerates

Artificial samples	Movement criterion V_c	Normal bonding strength σ_m (MPa)	Shear Bonding strength τ_m (MPa)	$\frac{\sigma_m}{\tau_m}$	Movement coefficient α
Group 1	2.08	0.40	2.84	0.14	14.82
Group 2	2.08	0.73	1.89	0.39	5.37
Group 3	2.08	0.60	1.50	0.40	5.25
Group 4	2.42	0.41	1.79	0.23	10.46

5.7 Summary

According to the present knowledge, the tensile strength of artificial conglomerate consists of the tensile strength of cement paste sample and the normal bonding strength between steel balls and cement. Similarly, the cohesion of conglomerate is the combined cohesive strength of cement and shear bonding strength between steel balls and cement along the failure surface. As shown in Eq. 5.1 and Eq. 5.2, the macro tensile strength and cohesion can be related to the micro normal and shear bonding strength with known total failure surface area and the area occupied by steel ball-cement contact on the failure surface. Post failure analysis was carried out on the failure surfaces of direct shear and Brazilian tensile testing samples to determine the micro bonding

strength τ_m and σ_m. Firstly, the failure surface was scanned using a 3D scanner and then the total failure surface area A was calculated using the software 'Geomagic control'. All the steel balls and holes on the failure surface were divided into five categories based on the height above/below the imaginary failure plane, and the steel ball-cement contact area A_B equals to the sum of multiplying the contact area between steel ball and cement of each case by the corresponding counted number of steel balls/holes. For the four groups of artificial conglomerates, the normal bonding strength is found to be in the range of 0.40 to 0.73 MPa, and the shear bonding strength lies between 1.50 and 2.84 MPa. Besides, the contact area coefficient is calculated using the measured average contact area a_{3D} between steel ball and cement, which is about 1.0 for all the artificial conglomerates. Also, the movement coefficient is calculated based on the measured micro bonding strength and movement criterion to be in the range of 5.25 to 14.82.

All the parameters required in the theoretical relationship between the micro and macro mechanical properties of the cemented granular material have been determined.

Chapter 6: Verification of Theoretical Relationship using Experiment Results

6.1 Introduction

All the parameters required in the theoretical relationship between micro and macro mechanical properties of cemented granular material have been determined in the laboratory. In this chapter, the relationship between the inter-particle friction angle and macro peak friction angle, and the relationship between micro bonding strength and the macro cohesion are verified with the measured parameters.

6.2 Verification of the relationship between micro and macro friction angles

The peak friction angle can be considered as the sum of contributions from inter-particle friction, particle rolling and dilation. As shown in Caquot's (1934) equation (Eq. 2.1), the critical state friction angle for granular material depends on the inter-particle friction and the effect of particle rolling. However, this study is focused on cemented granular material and there is no particle rolling during shearing in cemented material. Equation 3.46 represents the theoretical relationship between macro peak friction angle and inter-particle friction angle and micro dilation angle, which agrees with the equation (Eq. 2.3) developed by Tobita and Oda (1999).

The inter-particle friction angle of steel balls ϕ_μ has been measured directly in the laboratory, which is found to be 6.84°. The micro dilation angle φ_m is calculated to be 60° for the densest packing at the peak state, and the macro peak friction angle ϕ_P is found to be 66.84° based on Eq. 3.46. The calculated and measured peak friction angle of the artificial conglomerates are summarized in Table 6.1.

Table 6.1 The theoretical and measured peak friction angles of artificial conglomerates

Artificial samples	Sample name	Inter-particle friction angle ϕ_μ (°)	Micro dilation angle φ_m (°)	Theoretical peak friction angle (°)[1]	Measured peak friction angle (°)
Group 1	0.6_4.8mm				55.91
Group 2	0.6_3.2mm	6.84	60.00	66.84	57.95
Group 3	0.6_mix				59.45
Group 4	0.45_4.8mm				56.82

Note 1: The theoretical peak friction angle is calculated using Eq. 3.46.

Cement content was found to have no effect, or negligible effect, on the peak friction angle (Clough et al. 1981, Marri 2010, Amini et al. 2014, Wang and Leung 2008). Therefore, the peak friction angle of artificial conglomerate is considered the same as the peak friction angle of uncemented steel ball assembly. Compared with the experiment results, the calculated theoretical peak friction angle (66.84°) is about 10%~15% higher than the measured peak friction angle for groups 1 to 4 artificial conglomerates from direct shear tests. The difference could be due to the steel ball assembly in the conglomerate samples not being the densest packing condition that is assumed in the theoretical derivation. In addition, the measured friction angle (55.91°~59.45°) indicates that the actual micro dilation angle of the artificial conglomerate is around 50°, which is reasonable.

6.3 Verification of the relationship between micro bonding strength and macro cohesion

Equation 3.47 represents the theoretical relationship between micro bonding strength and macro cohesion from the Mohr-Coulomb criterion. To verify this relationship, the shear bonding strength τ_m, movement criterion V_c and coefficient α, and the contact area coefficient w were determined in Chapters 4 and 5 (see Table 6.2). Since the measured movement criterion V_C is greater than $\sqrt{3}$, the value $V_C = \sqrt{3}$ is used for the verification.

The theoretical cohesion is calculated by substituting the parameters in Table 6.2 into Eq. 3.47, resulting in about 0.84 to 1.05 times the measured cohesion from direct shear testing. The calculated theoretical cohesion versus measured cohesion is plotted in Figure 6.1. It clearly shows that the theoretical cohesion obtained from the derived equation agrees with the measured cohesion. Therefore, the relationship between cohesion and micro shear bonding shown in Eq. 3.47 is valid.

In addition, as shown in Eq. 3.47, the micro bonding strength and macro cohesion are related to the term B. The contact area coefficient w in B is highly dependent on the porosity of the ball skeleton. In the artificial conglomerate used in the laboratory, the steel balls are in a very dense packing and the porosity of balls skeleton is equal to 38.5%. The contact area coefficient of unity is obtained from the post failure analysis, and with the measured movement criterion and movement coefficient, the value of term B is in the range of 1.2 to 1.3 for the artificial conglomerates.
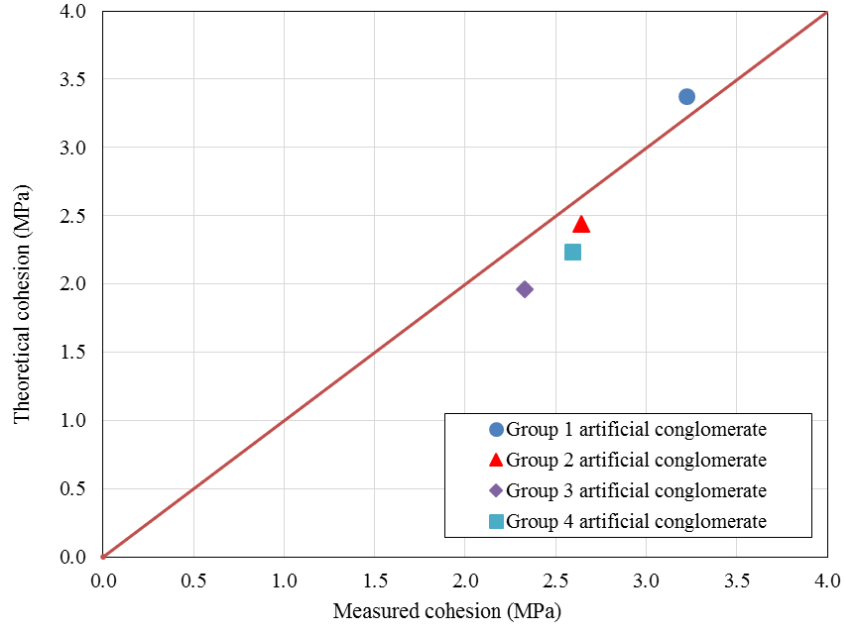
Figure 6.1 Calculated theoretical cohesion vs measured cohesion plot of artificial conglomerates
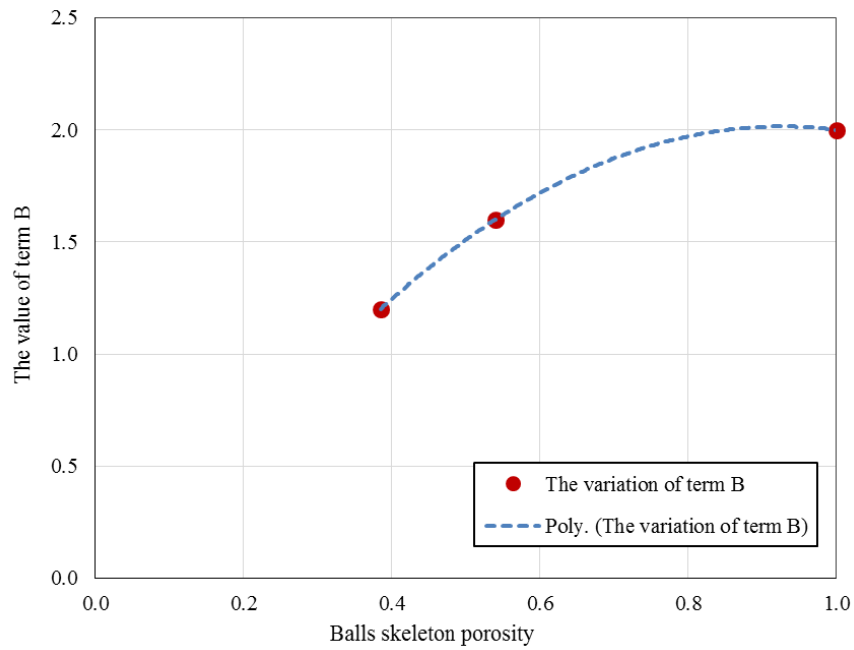
Figure 6.2 The variation of term B with the balls skeleton porosity

For the loosest packing in the theoretical equation, the porosity of particles skeleton is around 54.0%, and the contact area coefficient can be obtained from the definition of contact area of $a_c = \omega dt$. Since the contact area of the loosest packing equals to $a_c = \pi dt/2$, the contact area

coefficient ω can be calculated and is around 1.6. Moreover, if an extreme loose condition is considered, and there is only one steel ball in the sample, the porosity of balls skeleton is around 100%. The shear bonding strength τ_m is not changed with an average value of 2.0 MPa. However, the macro cohesion of this extremely loose sample should approximately equal to the cohesion of cement paste, which is around 4.0 MPa. Therefore, the term B is about 2.0 based on the Eq. 3.47 for this extreme case.

As shown in the plot of term B versus the porosity of the ball skeleton (Figure 6.2), B increases nonlinearly with the increase of porosity. It reveals that with the constant shear bonding strength, the macro cohesion would increase with porosity, which is reasonable. Furthermore, for the samples made with the same particles and cementing material used in the laboratory, the macro cohesion is about 1.2 to 2.0 times of the micro shear bonding strength. Based on this relationship, the micro bonding strength of tested material can be obtained from the measured macro cohesion.

Theoretically, B should always be larger than 1.0 when most of the voids of particles skeleton are filled with cementing material. The macro cohesion of cemented granular material consists of cohesive strength of cementing agent and shear bonding strength between particles and cementing agent. Since the cohesive strength of the cementing agent is larger than the micro bonding strength, B must be larger than 1.0 for this case. However, for the extreme case that there are lots of voids on the failure surface, B can be less than 1.0. The reason is that the macro cohesion is usually obtained by the shear force divided by the total area of the failure surface in the laboratory, and it is possibly smaller than the micro bonding strength between particles and cementing agent.

6.4 Summary

In this chapter, the theoretical relationship between the micro and macro mechanical properties of cemented granular material is verified using the laboratory measurements.

Equation 3.46 represents the relationship between the inter-particle friction angle and macro peak friction angle. Since the contribution of particle rolling is not allowed in the cemented conglomerates, the macro peak friction angle of cemented granular material is directly related to the inter-particle friction angle and the micro dilation. The calculated theoretical peak friction angle is about 10% -15% higher than the measured value from direct shear testing. The discrepancy can be due to the difficulty in reaching the densest packing condition in the laboratory experiment.

Equation 3.47 represents the relationship between the micro bonding strength and the macro cohesion. Based on the analysis of term B, this relationship is found to be related to the porosity of particle skeleton and particle surface properties. Using the measured micro properties, the calculated macro cohesions are about 0.84 to 1.05 times of the measured cohesions from direct shear testing.

The calculated macro cohesion and friction agree well with the measured values in the laboratory, which verifies the derived relationship between the micro and macro mechanical properties. The macro parameters of cemented granular material can be calculated with measured micro properties using the derived theoretical relationship. Further, the micro bonding strength and inter-particle friction for the tested material can be calculated with the measured macro parameters, as shown in the verification. Furthermore, the macro cohesion should be larger than the micro bonding strength for the cemented granular material, when the void ratio of the material is small. Presently, the shear bonding strength is typically assumed to be the same as the cohesion, which results in an overestimation of the micro bonding strength.

Table 6.2 The theoretical and measured cohesion of artificial conglomerates

Artificial samples	Sample name	Movement criterion Vc	Movement coefficient α	The contact area coefficient w	Shear bonding strength τ_m (MPa)	Theoretical cohesion (MPa)	Measured cohesion (MPa)
Group 1	0.6_4.8mm	2.08	14.82	0.98	2.84	3.38	3.22
Group 2	0.6_3.2mm	2.08	5.37	0.98	1.89	2.44	2.64
Group 3	0.6_mix	2.08	5.25	0.99	1.50	1.96	2.33
Group 4	0.45_4.8mm	2.42	10.46	1.01	1.79	2.24	2.59

Chapter 7: Numerical Simulation and Comparison with Laboratory Results

7.1 Introduction

To investigate the micro mechanical behavior of cemented granular material, and test the accuracy of the derived theoretical relationship, a numerical model for the conglomerate sample was built by using 'Particle Flow Code', which is commonly known as PFC.

This chapter presents a brief introduction to the PFC^{2D} Particle-Flow model based on Itasca (2008). Two simple models with two rows of particles were created to investigate the progressive failure mechanism in micro modeling. The effects of micro parameters on the macroscopic direct shear behavior are also discussed. Numerical direct shear testing was then conducted on the four groups of samples as prepared in the laboratory. The procedures for sample generation and numerical direct shear testing are presented, and the numerical simulation results for all groups of samples are summarized and compared with the laboratory results.

7.2 The PFC^{2D} Particle-Flow model

PFC^{2D} models the movement and interaction of circular particles by the Distinct Element Method (DEM), as described by Cundall and Strack (1979). It allows finite displacements and rotations of discrete bodies, and recognizes new contacts automatically as the calculation progresses. In DEM, the interaction of the particles is treated as a dynamic process with states of equilibrium developing whenever the internal forces balance. The dynamic behavior is represented numerically by a time-stepping algorithm in which the velocities and accelerations are assumed constant within each time-step.

The PFC^{2D} model is composed of distinct particles, usually referred as "balls" or "particles", which displace independently of one another. More complex behavior can be modeled by allowing the particles to be bonded together at their contact points with "bonds". When the inter-particle forces acting at any bond exceed the bond strength, the bond is broken. In addition to "particles" and "bonds", the PFC^{2D} particle-flow model also includes "walls". The velocity boundary conditions can be applied with walls to assemblies of balls for purposes of compaction and confinement.

In Appendix C, the calculation cycle and basic assumptions, the slip behavior along unbonded particles, the particle-cement behavior, and also the clumped particle model in PFC^{2D} are discussed in detail.

7.3 Numerical investigation of shearing of an assembly of particles

When an assembly of particles is sheared, the bonds generated among the particles would not be mobilized at the same time, which results in progressive failure. Progressive failure is the term describing the condition when different parts of a failure surface reach failure at different time. Two groups of shearing tests were conducted with PFC^{2D} to investigate the progressive failure mechanism in the micro modeling.

Since a whole assembly of particles are complicated to study, two simple models are created with two rows of particles. The first model is clump-clump testing model, in which the two rows of particles are modified into two clumps, and the installed parallel bonds between the clumps can be broken at the same time. The other model is particle-clump testing model, in which only one row of particles is modified into a clump, and the installed parallel bonds among particles would be mobilized at different times. The testing methods and results are shown in detail below.

7.3.1 Clump-Clump test

The clump logic provides a means to create a group of glued particles that behave as a single rigid body in a clump. Contacts internal to the clump are skipped during the calculation cycle, while the contacts with particles external to the clump are not affected. In this section, a clump-clump testing model is created, and the parallel bonds between the clumps are supposed to be broken at the same time in the direct shear testing, as assumed in the theoretical derivation.

As shown in Figure 7.1, two samples with two rows of particles are generated at first. Each row of Sample A contains 10 particles with the diameter of 4.8 mm, while Sample B consists of 15 particles in each row with the particle diameter of 3.2 mm. The widths of Samples A and B are kept the same to study the effect of particle size on the numerical simulation result. The input parameters in PFC^{2D} are shown in Table 7.1 and the direct shear testing procedure is given in Figure 7.2.
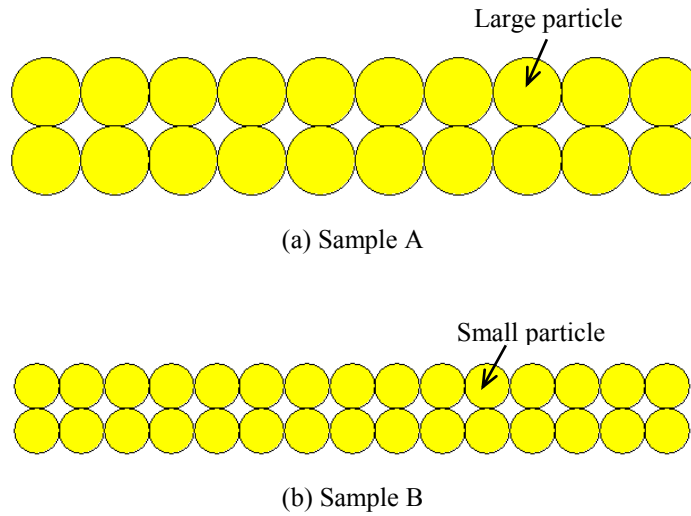
(a) Sample A

(b) Sample B

Figure 7.1 Samples A and B with two rows of particles

Table 7.1 Summary of parameters used for clump-clump tests and particle-clump tests

Particles properties	Value	Parallel bond properties	Value
Particle diameter (mm)	4.8/3.2	Normal strength $\bar{\sigma}_c$ (MPa)	2.0
Particle density (kg/m³)	7850	Shear strength $\bar{\tau}_c$ (MPa)	2.0
Friction coefficient μ	0.12	Normal stiffness $\bar{k}^n$ (GPa)	6.0
Normal stiffness k^n (GPa)	3.0	Stiffness ratio $\bar{k}^n / \bar{k}^s$	0.5
stiffness ratio k^n/k^s	2.5	Bond-radius multiplier $\bar{\lambda}$	1.0

Four walls are created around the particles assembly and parallel bonds are applied among the particles as shown in red lines in Figure 7.2(a). Then, a normal stress of 1 MPa is applied on the Wall 3. To make all the bonds to break at the same time, the particles are grouped into two clumps as shown in Figure 7.2(b). The new Walls 2, 4 and 5 are created to substitute the original lateral walls for the direct shear testing. Finally, the sample is sheared as shown in Figure 7.2(c) with a constant velocity applied on Wall 4. At the same time, the generated shear force at Wall 4 during shearing and the corresponding shear displacement are recorded.

The loading rate applied in the numerical simulation in this study is chosen to be 0.005 m/s. Different from the strain rate used in the laboratory, this loading rate is slow enough in numerical simulation to ensure that the sample remains in quasi-static equilibrium throughout the test. Since the calculation logic in PFC is fundamentally based on the dynamic mode governed by Newton's

second law of motion, the time step used in each calculation cycle is infinitely small (e.g. 10^{-8} sec) (Potyondy and Cundall 2004, Cho 2008).

(a)

(b)

(c)
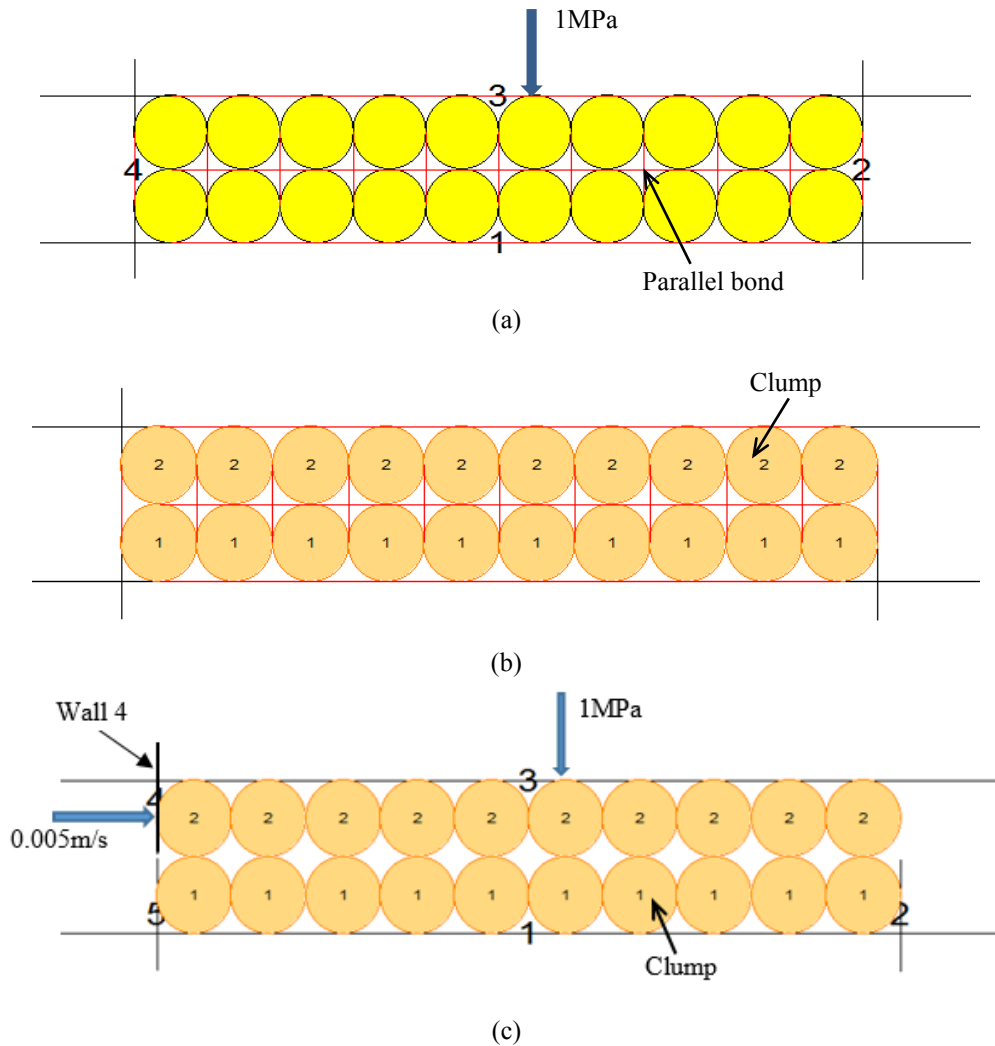
Figure 7.2 The clump-clump model testing procedure

The failed samples are shown in Figure 7.3 with shear cracks, and the shear force versus shear displacement plots are shown in Figure 7.4. Obviously, for the clump-clump testing model, all the parallel bonds are broken at the same time, which contributes to the peak shear force. The same shear force versus shear displacement plots obtained from Samples A and B indicates that, with the same bonding strength and bond-radius multiplier, the particle size has no effect on the direct shear testing results.
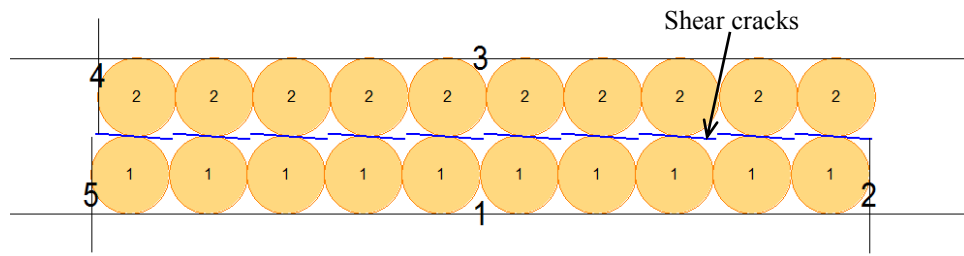
(a) The failed Sample A
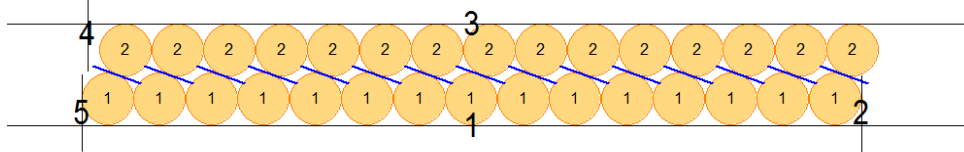
(b) The failed Sample B

Figure 7.3 The failure surfaces of Samples A and B
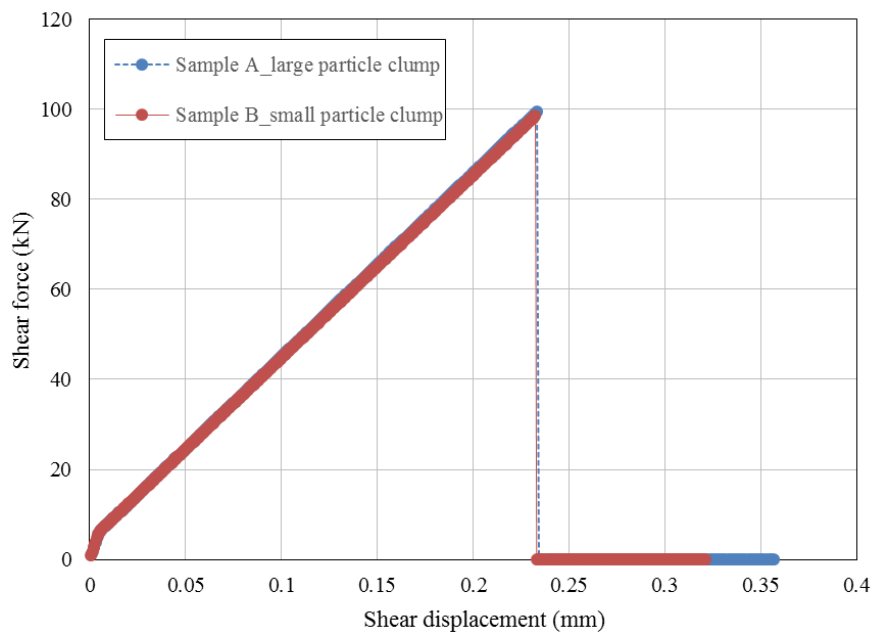
Figure 7.4 The shear force versus shear displacement plots of Samples A and B

7.3.2 Particle-Clump test

A group of particles that are bonded together differs from a clump. The parallel bonds among the particles maybe broken at different time, which results in the progressive failure mode. In this section, a particle-clump testing model is generated, and the testing results are compared with those of clump-clump testing model.

As shown in Figure 7.5, Samples C and D are prepared for the particle-clump direct shear testing. Similarly, Sample C is composed of 4.8 mm diameter particles, and Sample D consists of particles with 3.2 mm diameter. While the upper row of particles are bonded with parallel bonds, the bottom row of particles are grouped into a clump. The same parameters as the clump-clump testing model are used, as shown in Table 7.1. To keep the normal stress applied on each particle constant during the shearing, a constant normal force is applied on every particle to achieve the 1 MPa normal stress. With a constant velocity applied on Wall 4 (0.005m/s), the sample is sheared as shown in Figure 7.6.

The samples at failure state are shown in Figure 7.7. Like Samples A and B, Samples C and D also fail with shear cracks. However, the parallel bonds among the particles and clump are broken at different time. Therefore, the shear force versus shear displacement plots (Figure 7.8) have several peaks before the softening stage, and the peak shear force of Sample C is higher than that of Sample D.
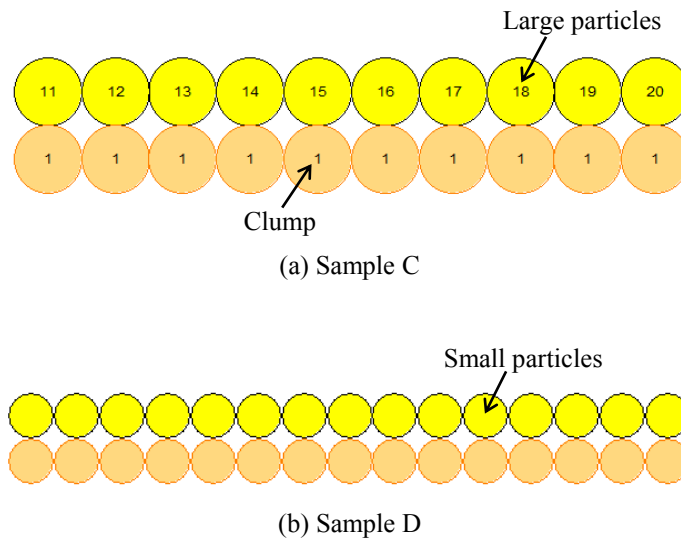
(a) Sample C

(b) Sample D

Figure 7.5 Particle-clump testing model for Samples C and D
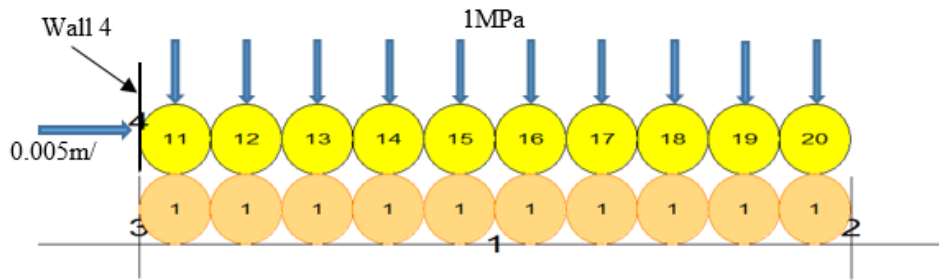
Figure 7.6 The particle-clump direct shear testing model
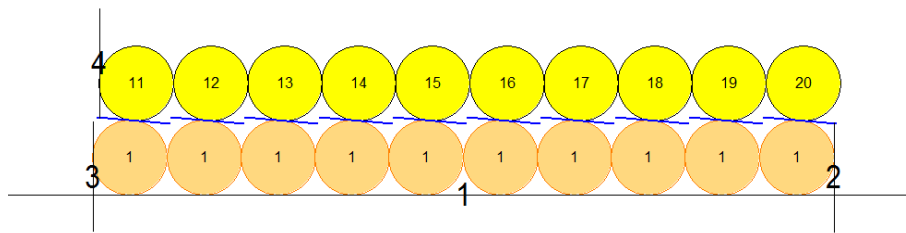
(a) Sample C at failure state
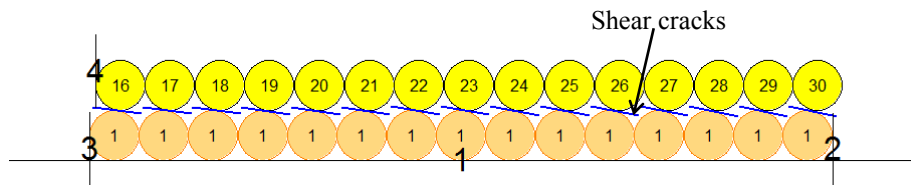
(b) Sample D at failure state

Figure 7.7 Shear failure locations for Samples C and D
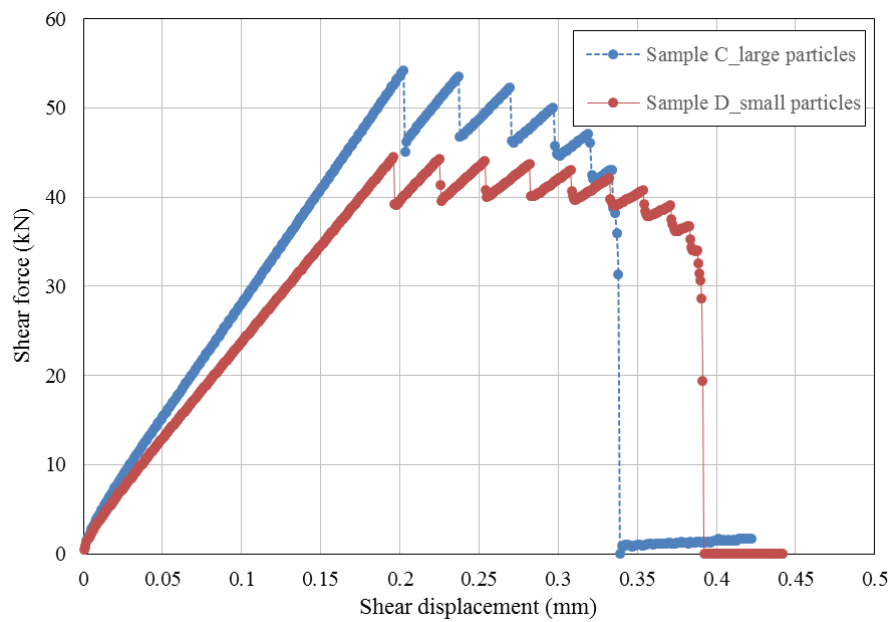
Figure 7.8 Shear force versus shear displacement plots for Samples C and D

7.3.3 Effect of progressive failure mode

For the particle-clump testing model, the parallel bonds among the particles progressively break along the failure surface, which is the progressive failure mode. Comparing the plots in Figure 7.4 and Figure 7.8, the peak shear forces of Samples C and D are much lower than those of Samples A and B. This indicates the progressive failure mode can significantly reduce the peak shear force.

Using the same material parameters, samples in the clump-clump test reach the same peak shear force, and their shear force versus shear displacement plots are the same. However, Sample C with large particles achieves a higher peak force than that of Sample D with small particles. Also, the two curves in the Figure 7.8 have different shapes. Therefore, for the progressive failure mode, the particle size affects the testing results significantly. In other words, the progressive failure mechanism is particle-size dependent.

7.4 Parametric sensitivity study on the direct shear behavior

In PFC^{2D}, the cemented granular material is represented as an assembly of circular disks bonded with parallel bonds at contacts. The particles are assumed to be rigid but particles can overlap at the contacts under compression. The parallel bonds can be specified by shear and tensile bonding strength. It is worth mentioning that once the bond is broken either by shear or rotation, the shear strength is set to its residual value if the particles stay in contact, which is a function of compression normal force and coefficient of friction at the contact. However, once a tensile bond is broken, the tensile strength of particle bonding is set to zero regardless of its contact condition. All the values assigned to those micro parameters can influence the macro strength of the sample and the nature of cracking and failure that occurs during loading (Cho 2008). In this section, the effect of micro parameters on the macro mechanical behavior are examined using direct shear testing on the particle-clump testing model with 3.2 mm diameter particles.

The micro parameters used for the parametric study is shown in Table 7.1. When the effect of one parameter is being investigated, the rest of the parameters are kept constant.

7.4.1 Effect of particle stiffness

Four simulations are carried out with the particle normal stiffness k^n varies between 1.0 GPa and 9.0 GPa. Figure 7.9 shows the direct shear testing results in terms of shear force versus shear

displacement. It is noted that with the increase in particle stiffness, the peak shear force increases significantly, while the shear displacement corresponding to the peak shear force decreases. However, when the particle stiffness is higher than 6 GPa, the growth in the peak shear force with particle stiffness decreases with the increase in particle stiffness. Moreover, although all the plots have the same number of peaks, the progressive failure phenomenon becomes less obvious with the increase of particle stiffness.

The normal to shear particle stiffness ratio $\frac{k^n}{k^s}$ is varied from 1.0 to 5.0 to check the sensitivity of particle stiffness ratio on the macroscopic behavior of particle-clump testing model. As shown in Figure 7.10, the results indicate that the particle stiffness ratio has negligible effect on the direct shear behavior.
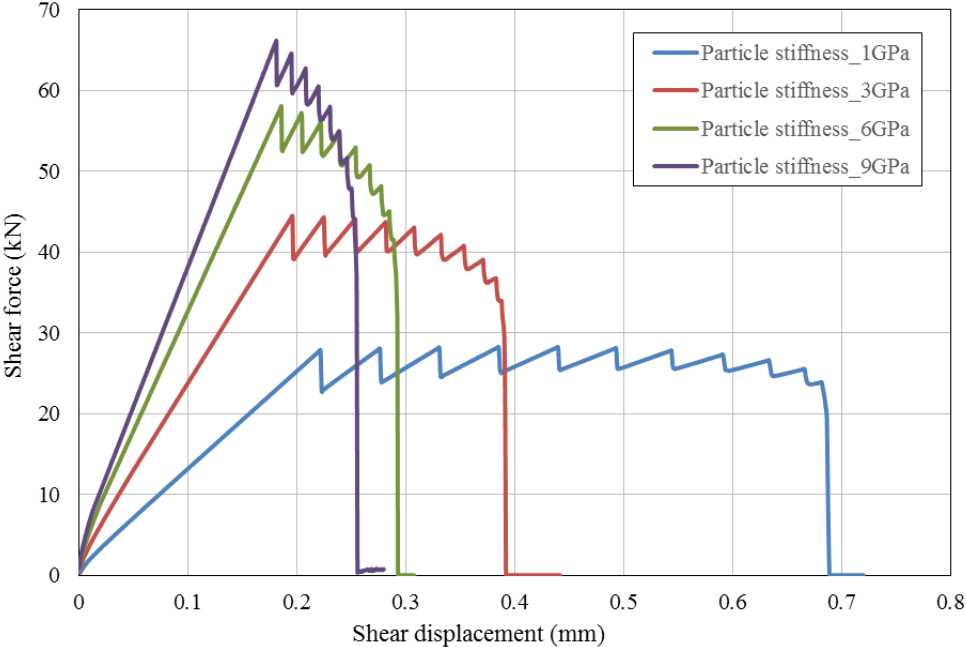
Figure 7.9 Effect of particle stiffness on the shear force and shear displacement
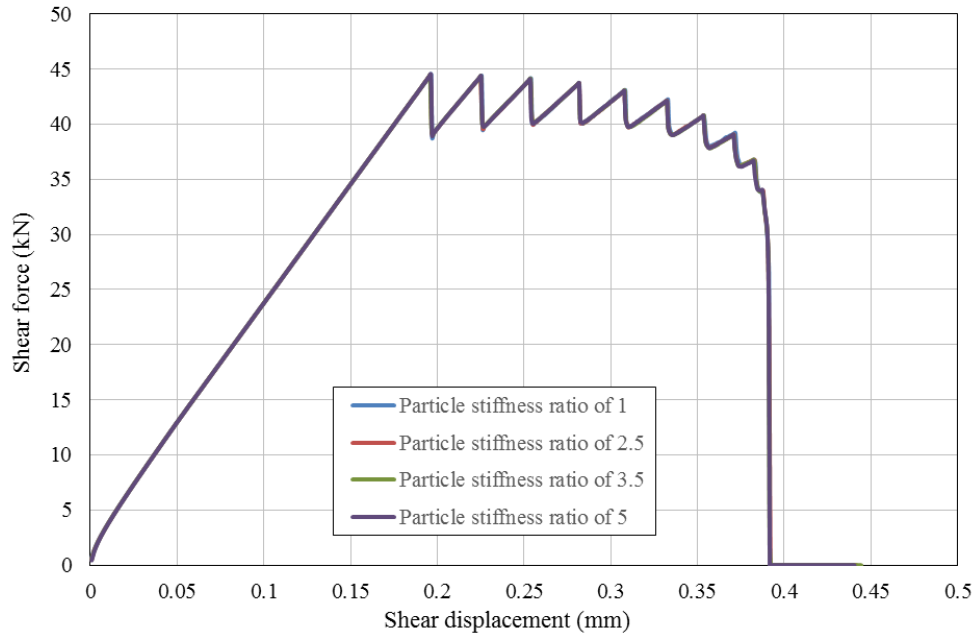
Figure 7.10 Effect of particle stiffness ratio on the shear force and shear displacement

7.4.2 Effect of friction between particles

In PFC, after the parallel bonds are broken, the force acting on the particle contact is set to a residual value that depends on the compressive normal force at the contact and the coefficient of friction. Friction between particles can suppress independent particle movement such as rotation or slippage, and then increase the shearing resistance. Besides, it has been reported that friction between particles affects post-peak behavior (Itasca, 2008).

In this study, the effect of particle friction is investigated by changing the friction coefficient μ between 0.12 and 0.48. Figure 7.11 indicates that the first peak shear force is affected by the bonding strength, the friction force and the force given by the neighboring particles. As the number of mobilized bonds increase, the increase in peak shear force becomes more obvious with the friction coefficient. Furthermore, ignoring the effect of parallel bonds and particle overlaps, the residual shear force increases proportionally with the increase in particle friction.
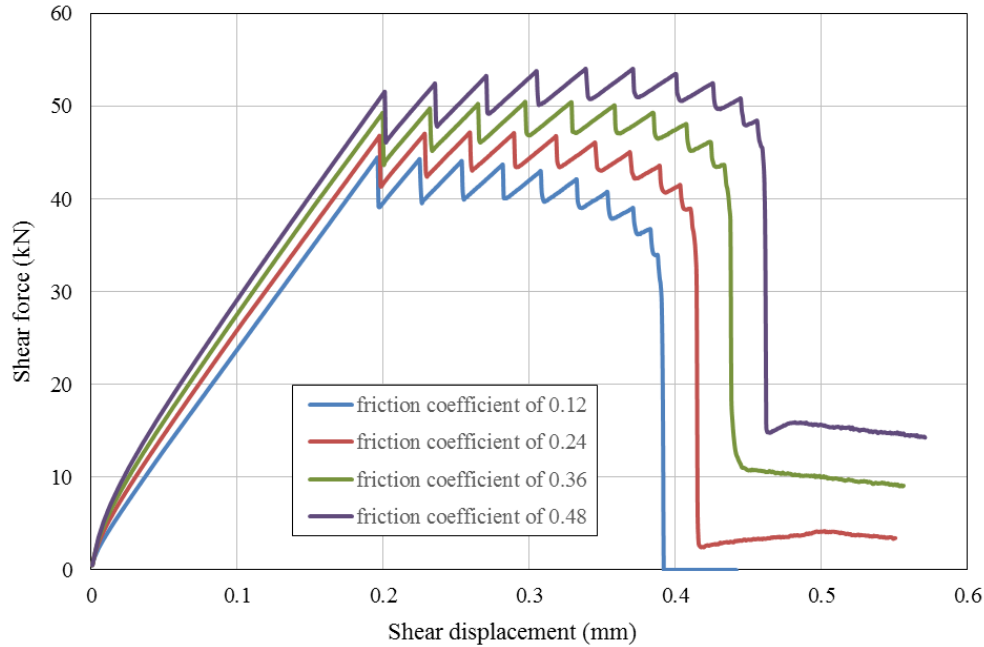
Figure 7.11 Effect of the coefficient of friction on the shear force and shear displacement

7.4.3 Effect of bond strength

As shown in Table 7.1, the shear and normal bonding strength ($\bar{\tau}_c$ and $\bar{\sigma}_c$) are set to be 2.0 MPa for the base case. Then, both the shear and normal bonding strengths are increased by 0.5, 1.5 and 2.0 times to study the impact of bond strength. The direct shear test results are shown in Figure 7.12. It shows that both the peak shear force and shear displacement at peak increase proportionally with the increase in bond strength.

The shear to normal bonding strength ratio ($\bar{\tau}_c / \bar{\sigma}_c$) is another very important parameter that characterizes the macro strength and behavior. For example, by increasing this ratio, shear bond rupture will be suppressed because of the increased shear bonding strength which lead to more normal bond ruptures. Diederichs (2000) also shows that the shear to normal bonding strength ratio can control the macro peak strength of the material. In this study, the effect of shear to normal bonding strength ratio on the direct shear testing behavior is also investigated by varying it from 1.0 to 9.0. The normal bonding strength is kept constant as 2.0 MPa. As can be seen in Figure 7.13, both the peak shear force and shear displacement at peak increase significantly with this ratio. Since all the bonds are failed in shear for this special configuration, increasing the bonding strength ratio increases the shear bonding strength, and eventually leads to a higher peak shear force.

134
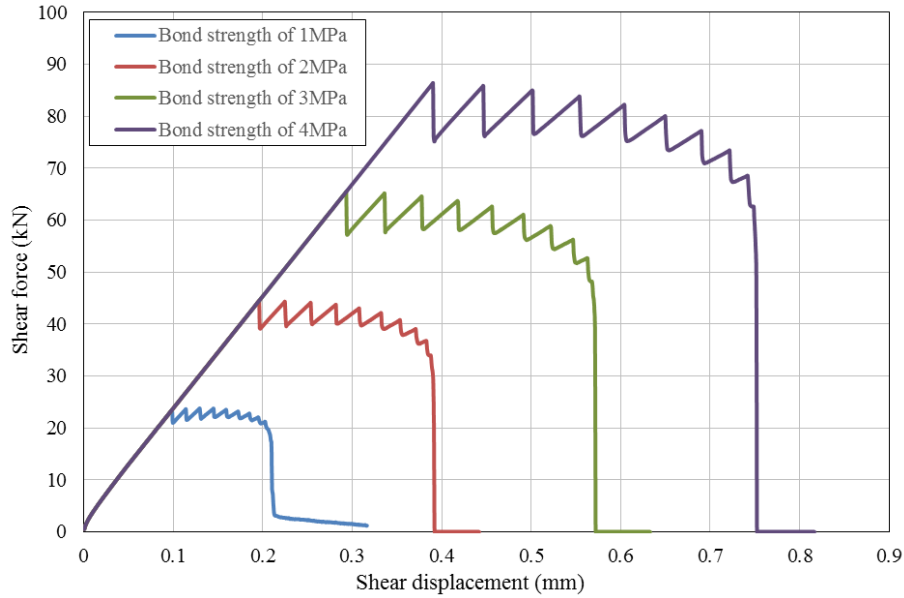
Figure 7.12 Effect of bond strength on the shear force and shear displacement
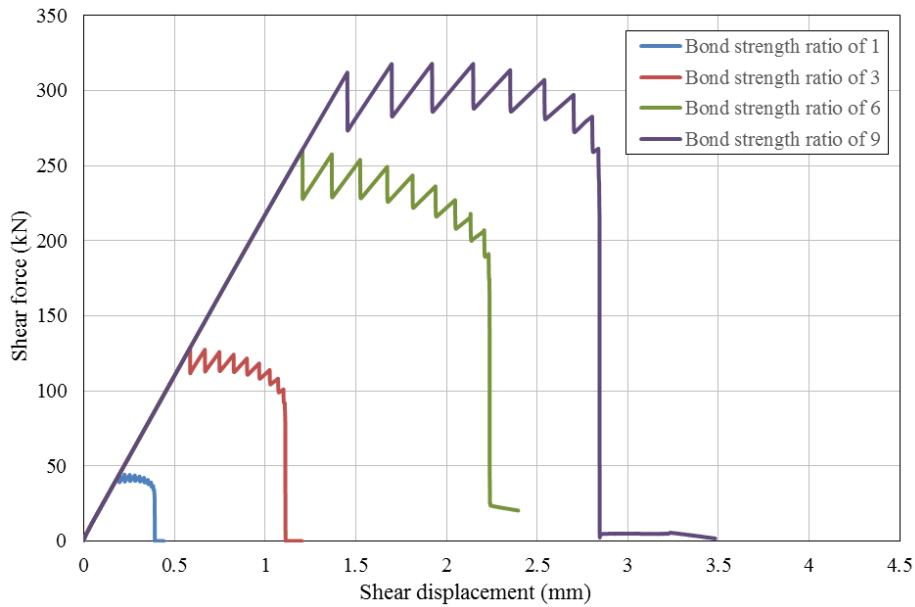
Figure 7.13 Effect of shear to normal bonding strength ratio on the shear force and shear displacement

7.4.4 Effect of bond stiffness

The effect of bond stiffness is studied by setting the normal bond stiffness $\bar{k}^n$ equals to 1.0 GPa, 3.0 GPa, 6.0 GPa, and 9.0 GPa. It is evident from Figure 7.14 that both the peak shear force and shear displacement at peak force decrease with increase in bond stiffness. In addition, the

macroscopic response is also investigated numerically with normal to shear bond stiffness ratios ($\bar{k}^n / \bar{k}^s$) of 0.1, 0.5, 1.0, and 2.0. The outcome of this study is shown in Figure 7.15, which shows that both the peak shear force and shear displacement corresponding to peak force increase with the increase in bond stiffness ratio.
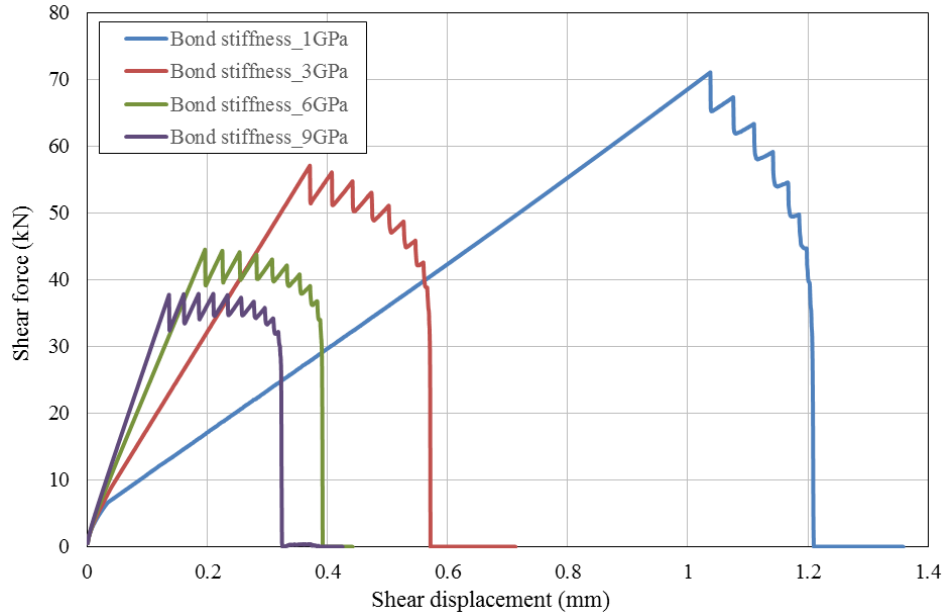
Figure 7.14 Effect of bond stiffness on the shear force and shear displacement
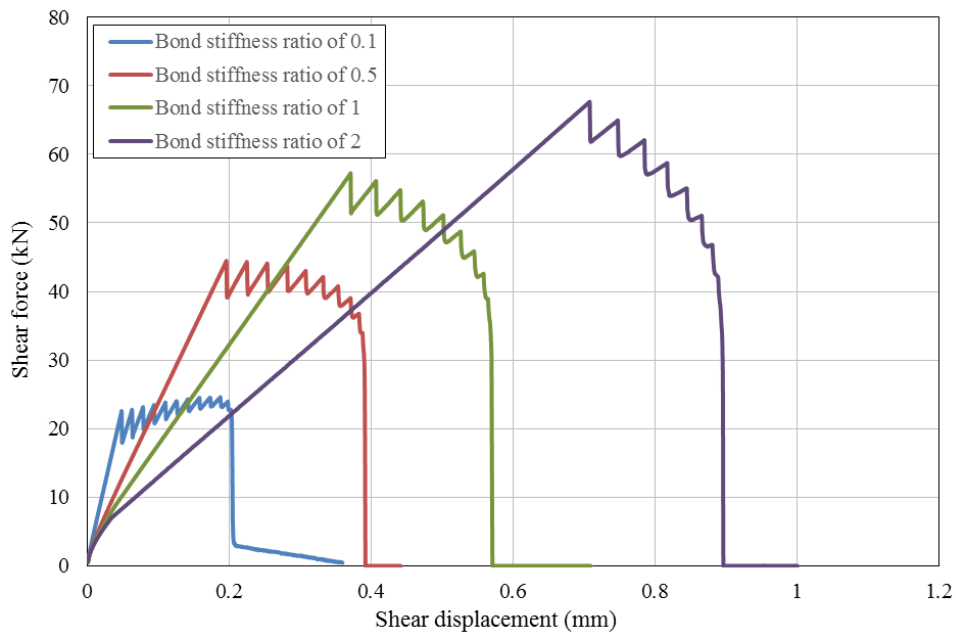
Figure 7.15 Effect of bond stiffness ratio on the shear force and shear displacement

7.4.5 Discussion

The particle-clump model used for the parametric sensitivity study is a special linear configuration. The peak shear force and shear displacement at peak are found to increase proportionally with the bond strength. Also, the residual shear force is found to increase proportionally with the particle friction coefficient.

For a whole assembly of particles, although the shear force and shear displacement would not increase proportionally with the micro parameters, the trends as shown in the parametric sensitivity study can be used for reference in the calibration in the subsequent section.

Firstly, the slope of shear force versus shear displacement plot before peak is affected by the particle stiffness, bond stiffness and bond stiffness ratio. With the increase in particle stiffness, the slope and peak shear force can be significantly increased. However, the increase in parallel bond stiffness reduces both the peak shear force and shear displacement at peak significantly, although the slope increases somewhat. For the bond stiffness ratio, while the slope decreases with the increase of it, the peak shear force and shear displacement at peak increase with the bond stiffness ratio.

Then, the parallel bond strength can be adjusted to capture the peak shear force. With negligible effect on the slope, both the peak shear force and shear displacement at peak increase with the increase of bond strength. It should be noted that the bonding strength ratio can be adjusted to change the cracking and failure mode. Furthermore, the friction coefficient is another micro parameter that affects the peak shear force. However, adjusting the friction coefficient is usually used to capture the residual shear force and post-failure behavior.

The calibration procedure is based on a systematic trial-and-error method and a comparison of laboratory and numerical simulation results. However, the parametric sensitivity study shows that different micro parameters have different effects on the macro responses of simulated direct shear testing. Therefore, understanding and identifying these trends can contribute to an efficient calibration process with minimal number of iterations.

7.5 Numerical direct shear testing

After the investigation of progressive failure mechanism in the micro modeling and the effect of micro parameters on the direct shear behavior, the numerical conglomerate samples similar to those prepared in the laboratory are generated and tested in direct shear testing. The sample generation and test procedures are described in details below. The numerical and laboratory results are compared and discussed.

7.5.1 Sample generation

In the laboratory, the artificial conglomerate sample was prepared with steel balls and Portland cement. In PFC^{2D}, the circular discs and parallel bonds are chosen to produce a similar numerical sample. Like the laboratory tests, four groups of numerical conglomerates are prepared for direct shear tests in this study. The numerical sample represents the longitudinal cross section of the conglomerate samples from the laboratory. For the densest packing configuration, the maximum allowable circular discs that can fit into the longitudinal cross section of the conglomerate sample (63.5 mm × 127 mm) are counted, and the generated porosity of the numerical sample is 17%, which corresponds to the porosity of 38.5% of the laboratory sample. The dimensions and the particle sizes of numerical samples are kept the same as those of laboratory samples, as shown in Table 7.2.

Table 7.2 The dimensions and particle sizes of numerical samples

Numerical samples	Diameter/Length of sample (mm)	Diameter of particles used (mm)
Group 1	63.5/127	4.8
Group 2	63.5/127	3.2
Group 3	63.5/127	Half of 3.2 mm and half of 4.8 mm
Group 4	63.5/127	4.8

In sample generation, a group of particles initially at 0.6 times of their final sizes are generated inside a rectangular container bounded by frictionless walls. Then, all the particles are expanded to their final sizes based on the desired porosity, as shown in Figure 7.16(a). The particle stiffness, initial friction coefficient and particle density are specified.

The particles are placed in the given space randomly. To reduce the overlaps and locked-in forces within the assembly, a small constant stress is applied by specifying the velocities of all the walls.

138

The stresses and strains are computed by taking the average wall forces divided by appropriate areas. The strains in both the *x*- and *y*-directions are computed using the following relationship (Itasca 2008):

$$\varepsilon = \frac{L - L_0}{\frac{1}{2}(L + L_0)} \qquad [7.1]$$

where L is the current sample length in the corresponding direction, and L_0 is the original sample length in that direction.

Throughout the loading process, the confining stress is kept constant by adjusting the wall velocities using a numerical servomechanism called "once per cycle". The numerical servo-control is used to adjust the wall velocities to reduce the difference between the measured stress and the specified stress.

Finally, after the locked-in forces are reduced and the assembly is at the equilibrium state (Figure 7.16(b)), the parallel bonds are installed at the contact points among the particle to mimic the cementation in the laboratory (Figure 7.16(c)). The parallel bond stiffness and bonding strength are specified.

(a)　　　　　　　　　(b)　　　　　　　　　(c)
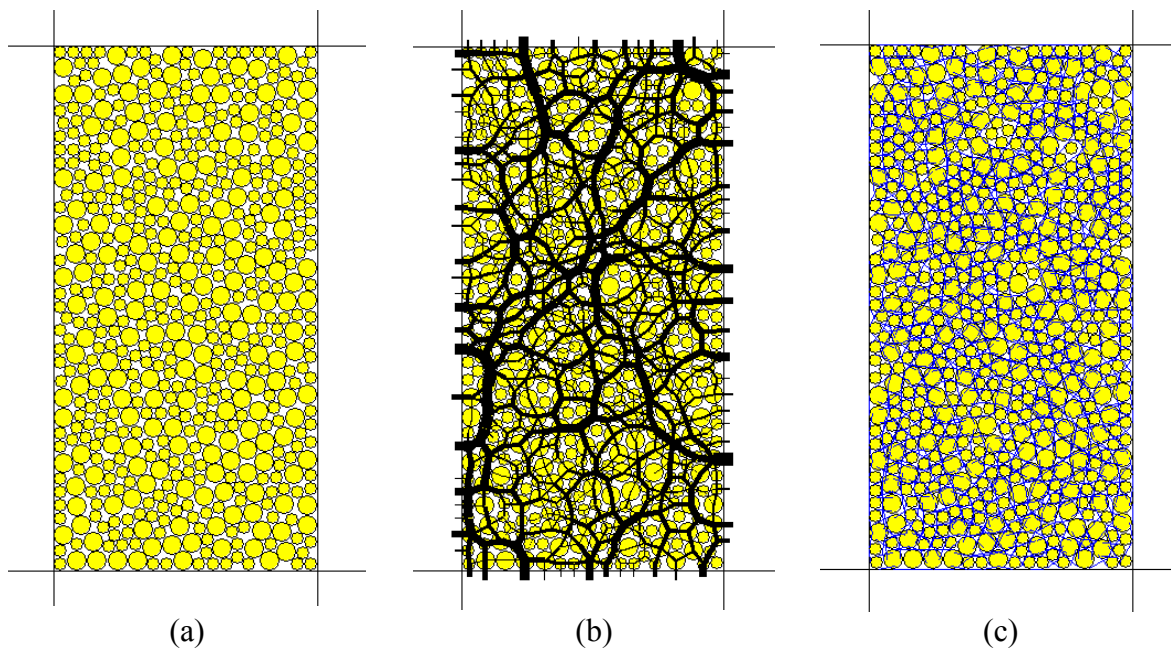
Figure 7.16 Sample generation procedure: (a) Particles generated randomly at a given space; (b) An equilibrium state assembly (contact force in black color); (c) Parallel bond installation (bond in blue color).

7.5.2 Computing and installing the normal stress

Like the laboratory tests, vertical stress is applied on the top wall in the numerical testing. For each group of numerical conglomerates, four samples are tested under the normal stresses of 0.5, 2, 5, and 10 MPa. The required normal stresses on the wall are kept constant by the servo-mechanism as discussed above.

To conduct the direct shear test, the original lateral walls are deleted and are substituted by Wall 3 to Wall 8 as shown in Figure 7.17. The gap between the top and bottom shear boxes is 0.2 mm. Walls 7 and 8 are created to avoid any particles escaping from the shear boxes during shearing.
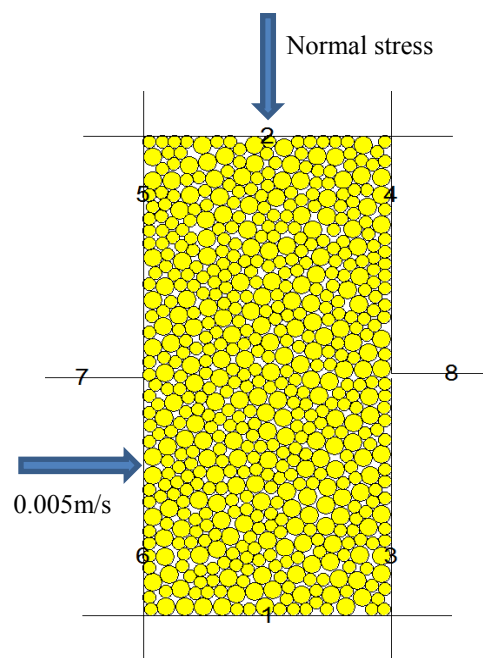
Figure 7.17 The configuration of numerical sample before shearing

7.5.3 Shearing of the specimen

After establishing the initial testing condition, the samples are ready for shearing. The velocity applied on Walls 3 and 6 as shown in Figure 7.17 is specified using a FISH function. It applies velocity to the wall in such a way that the final specified velocity is achieved in definite chunks containing a finite number of steps. The purpose of this approach is to avoid any initial damage to the sample due to the application of sudden high velocity at the start of the test (Itasca 2008). The

ultimate velocity applied is equal to 0.005 m/s. The shear strength, shear displacement and normal displacement are monitored and recorded during the tests.

The shear and tensile cracks are also monitored, which are developed due to parallel bond failure. The developed cracks can be used to track the shearing process. They are good indicators for investigating the progressive failure mode of the bonded particles assembly. While the shear cracks are shown in blue color, the tensile cracks are shown in red color in Figure 7.18. Obviously, the dominate cracks developed are shear cracks in the direct shear test. The initial shear crack is developed at 60% of the peak shear strength. The number of cracks increases with the increase in shear stress. After reaching the peak shear strength, both the shear and tensile cracks develop very fast as shown in the figure. This progressive failure mode greatly affects the numerical simulation results, which will be explained in detail in next section.
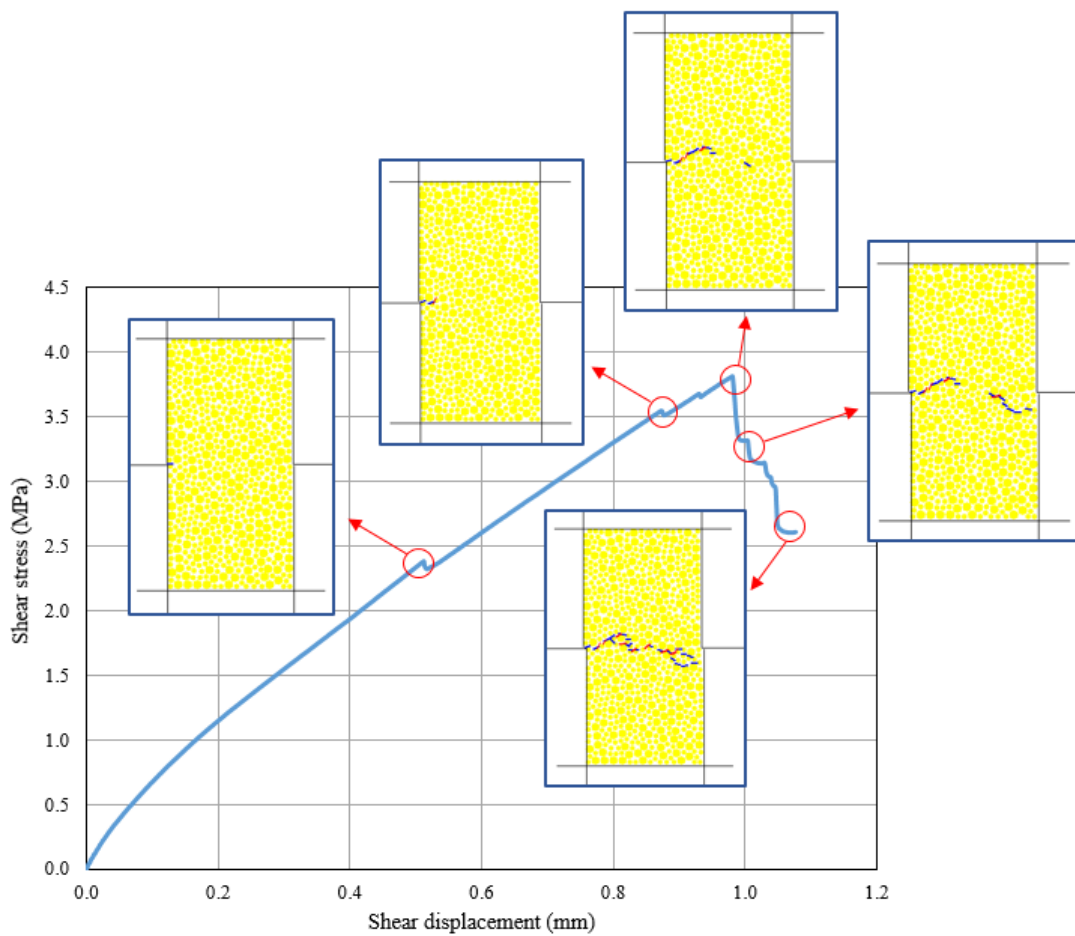
Figure 7.18 The progressive failure of group 3 numerical sample in direct shear testing under 0.5 MPa normal stress

7.5.4 Calibration of micro parameters

In micro modeling, by specifying the microscopic parameters for particles and bonds, the macroscopic behavior of numerical samples can be calculated. Comparing with the physical samples in the laboratory, no cement fills the pore space among particles in the numerical model. Therefore, the micro parameters in the micro modeling should represent the effect of both particles and cement. In this section, calibration of micro parameters is carried out with PFC^{2D} to incorporate the effect of cementation into the particle contact properties.

Based on the results from the parametric sensitivity study in Section 7.4, the micro parameters for four groups of numerical samples are calibrated separately by matching their macro responses in the direct shear testing to the corresponding laboratory results. The calibrated micro parameters are summarized in Table 7.3. It shows variations of several parameters among the numerical samples with different particle sizes.

Table 7.3 Calibrated micro parameters for all groups of numerical samples

Numerical samples	Particle properties				
	Particle diameter d (mm)	Normal stiffness k^n (GPa)	Stiffness ratio k^n/k^s	Friction coefficient μ	Density kg/m^3
Group 1	4.8	2.0	2.5	0.24	7850
Group 2	3.2	3.0	2.5	0.48	7850
Group 3	4.8 / 3.2	2.7	2.7	0.48	7850
Group 4	4.8	2.0	2.5	0.24	7850
Numerical samples	Parallel bond properties				
	Normal stiffness $\bar{k}^n$(GPa)	Stiffness ratio $\bar{k}^n/\bar{k}^s$	Shear strength $\bar{\tau}_c$(MPa)	Normal strength $\bar{\sigma}_c$(MPa)	Bond-radius multiplier $\bar{\lambda}$
Group 1	6.0	0.5	14.0	2.0	1.0
Group 2	6.0	0.5	2.0	2.0	1.0
Group 3	6.0	0.5	4.5	1.6	1.0
Group 4	6.0	0.5	13.0	2.0	1.0

With proper micro parameters input, a close agreement between numerical and laboratory results at different normal stresses is expected. Consider group 1 samples as an example, the laboratory and numerical testing results are compared by examining the failure envelopes, shear stress versus shear displacement plots, and normal displacement versus shear displacement plots, as shown in Figures 7.19 to 7.21. The comparison indicates a close match between numerical and laboratory results for group 1 samples. In addition, the numerical and laboratory results for the other three groups of samples also match very well, are shown in Table 7.4. The difference in shear strength between numerical and laboratory results is within 10%, when normal stress is equal to or larger than 2 MPa.

Table 7.4 The laboratory and numerical results for the direct shear testing

Numerical and artificial samples	Normal stress (MPa)	Shear strength (MPa)	
		Laboratory	Numerical
Group 1	0.5	3.96	3.69
	2	6.49 / 6.04	6.14
	5	10.39	11.05
	10	18.08	18.41
Group 2	0.5	2.84	3.62
	2	5.86	6.43
	5	11.72	11.62
	10	18.56 / 18.13	18.54
Group 3	0.5	2.78	3.34
	2	5.86	5.89
	5	11.35 / 10.79	10.58
	10	19.00	18.88
Group 4	0.5	2.71	3.58
	2	5.98 / 5.80	6.01
	5	10.67	11.06
	10	17.60	17.61
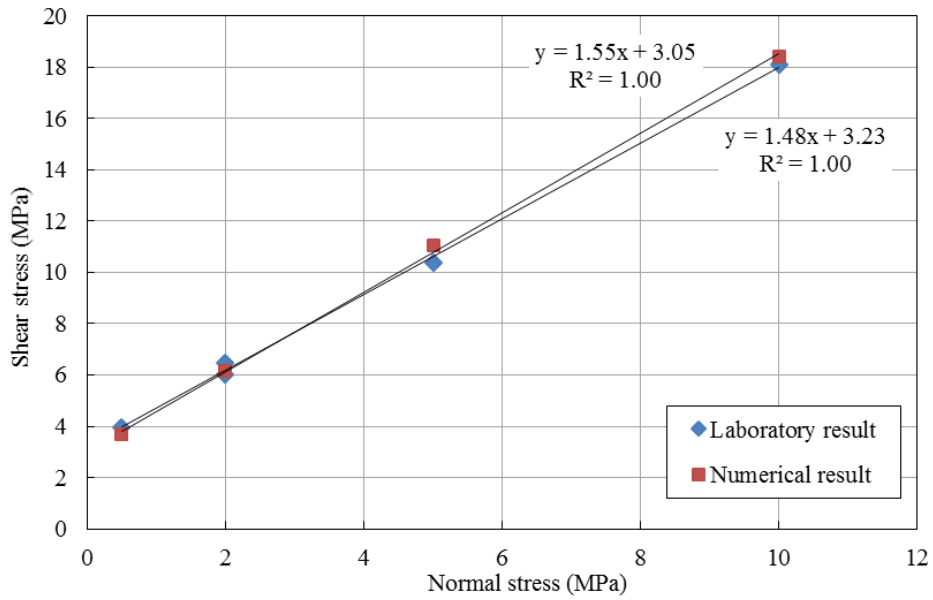
Figure 7.19 The laboratory and numerical failure envelopes of group 1 conglomerates
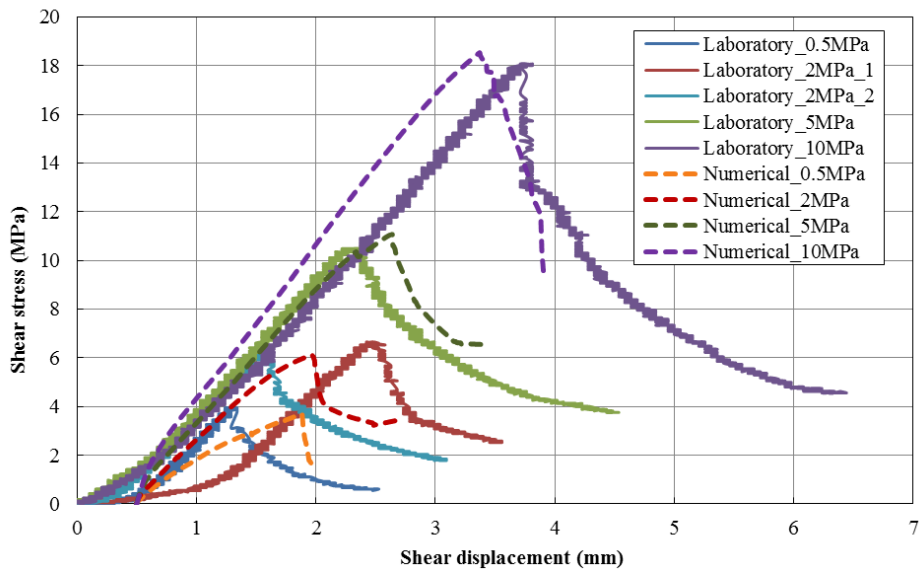
Figure 7.20 The laboratory and numerical shear stress versus shear displacement plots of group 1 conglomerates
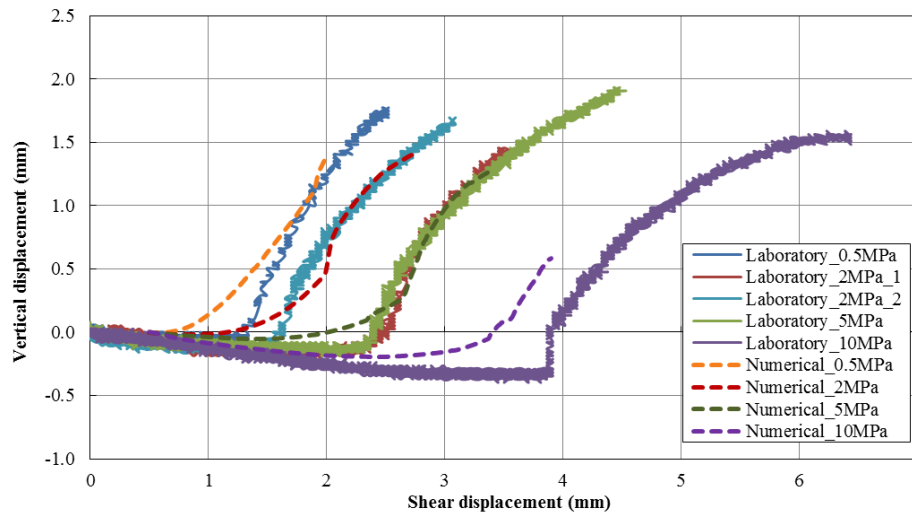
Figure 7.21 The laboratory and numerical normal displacement versus shear displacement plots of group 1 conglomerates

7.5.5 Discussion on the calibration results

For the laboratory results, as presented in Chapter 4, with the same or similar micro parameters, the macro responses of artificial conglomerates with different sizes of balls are similar. However, in the numerical model with different particle sizes, the calibrated micro parameters are not all the same. For example, as shown in Table 7.3, the particle stiffness for group 1 numerical samples is 2 GPa, while the particle stiffness for group 2 and group 3 numerical samples are 3 GPa and 2.7 GPa, respectively. This difference is not due to the change of micro mechanical properties between different sizes of particles physically. It is due to progressive failure at particle contacts in the micro model. The progressive failure mechanism is particle size dependent, as shown in the particle-clump testing results in section 7.3.2.

In the laboratory experiments, the steel balls used have very high stiffness and results in much less progressive failure phenomenon, comparing with numerical simulation. In addition, the cement in the pores among the steel balls assembly has very low stiffness, which leads to a large shear displacement during shearing.

As shown in the parametric sensitivity study, the progressive failure phenomenon decreases significantly with the increase in particle stiffness. However, because there is no cement in the pore space among the particles in the numerical model, the particle stiffness in the micro modeling

145

cannot be set higher than the stiffness of steel ball. Steel balls and cement are modelled by DEM particles and parallel bonds. The stiffness of the sample is dominated by the stiffness of the particles. If the same stiffness of steel is used in the micro modeling, the shear displacement at peak would be very small due to the high stiffness. The particle stiffness in the micro modeling should represent both the stiffness of steel balls and cement in the real sample. This explains why the calibrated particle stiffness is much lower than that of the steel balls. Furthermore, the relatively low particle stiffness used in the micro modeling leads to an apparent progressive failure mode.

Besides the particle stiffness, both the particle friction coefficient and the bonding strength in the micro modeling should represent the effect of both steel balls and cement in the laboratory. Thus, they have different values in the numerical simulation from those measured in the laboratory.

As shown in Table 7.4, with the micro parameters calibrated for each group of numerical samples, the numerical and laboratory results under different normal stresses match very well.

7.6 Summary

In this chapter, a numerical investigation was conducted to study the micro mechanical behavior of cemented granular material, and to test whether the proposed theoretical relationship can provide the micro mechanical properties that can capture the macro behavior with PFC^{2D}.

In the micro modeling, there is no cementing material filling the pore space among particles. Therefore, the particle properties in the micro modeling should represent both the effect of steel balls and cement in the physical samples. Similarly, the bonding strength in the micro modeling should represent both the bonding strength between the steel balls and cement, and the strength of cement. Furthermore, in the numerical conglomerates, after the parallel bond breakage, no cement matrix exists and the particles are free to rotate as per the specified friction. Any additional forces and moments are transferred only by the inter-particle contacts. However, in the artificial conglomerates, even after overcoming the bonds, cement is present and affects the overall mechanical response of the sample by restricting particle rotation, and redistributing forces and moments (Akram 2010). Therefore, the micro parameters for numerical samples are calibrated to incorporate the effect of cementation into the particle contact properties. For each group of numerical samples, the numerical and laboratory results under different normal stresses for direct shear tests reach a close match with the calibrated micro parameters.

For different groups of numerical conglomerates, the calibrated micro parameters are not all the same. This difference is mainly due to the progressive failure mechanism in the micro model, which is particle size dependent. As shown in the numerical investigation of shearing of an assembly of particles, the same peak strength is obtained for the clump-clump model due to uniformly shearing. The same shear force versus shear displacement plots are achieved for the samples with different particle sizes. For the particle-clump testing model, there are several peaks due to non-uniform shearing. Furthermore, different peak shear forces and different shapes of curves are obtained for samples with different particle sizes. Since progressive failure is size dependent, it is necessary to calibrate the micro parameters for each case.

Overall, the numerical model shows that the micro mechanical parameters provided by the proposed theoretical relationship can capture the macro response with micro modeling.

Chapter 8: Summary, Conclusions and Recommendations

8.1 Summary

The main objective of this research is to investigate the relationship between micro and macro mechanical properties of cemented granular material. Currently, it is widely accepted that shear bonding strength between soil particles is the same as the cohesion in the Mohr Coulomb failure criterion. Normal bonding strength equals to Brazilian tensile strength or direct tensile strength. However, the normal and shear bonding strength between particles and cementing agent is found to be smaller than the corresponding macro parameters mentioned above, using a simplified physical model and published data. Further investigation is warranted on the relationship between micro and macro mechanical properties of cemented granular material.

Regular packing of rigid and uniform rods is used to develop the theoretical relationship between the micro and macro strength. Two extreme regular packing conditions, namely, densest and loosest packings, have been studied. Based on static force equilibrium, the micro peak resisting force at contact points is related to the local externally applied forces. Subsequently, by considering groups of rods along the direct shear failure surface, the micro bonding strength and inter-particle friction angle are correlated to the macro cohesion and peak friction angle, respectively.

To study the mechanical behavior of cemented granular material and obtain the parameters involved in the theoretical relationship, artificial conglomerate samples are prepared with steel balls and Portland cement. Four groups of conglomerates are made to study the effect of particle size, uniform or non-uniform particle size distribution and cementing strength on the mechanical behavior of cemented granular material. Two groups of cement paste samples are also prepared.

Direct shear, uniaxial/triaxial and Brazilian tensile tests have been conducted to study the mechanical behavior and obtain the macro mechanical properties of testing samples. Innovative testing programs are designed to determine the inter-particle friction angle and movement criterion. Post-failure analysis is carried out on samples from direct shear and Brazilian tensile tests with 3D laser scanning technique. The micro bonding strength, contact area coefficient and movement coefficient are obtained.

With the measured/calculated parameters, the relationship between micro and macro mechanical properties in Eq. 3.46 and Eq. 3.47 has been verified in Chapter 6. Equation 3.46 represents the relationship between the inter-particle friction angle and macro peak friction angle. Since particle rotation is prohibited in cemented granular material, the macro peak friction angle of cemented granular material is found to be directly related to the inter-particle friction angle and micro dilation. Equation 3.47 represents the relationship between micro bonding strength and the macro cohesion. Through the analysis of the term B, this relationship is found related to the porosity of particles skeleton. With a constant shear bonding strength, the macro cohesion would increase with the porosity of the particle skeleton.

Based on measured micro properties, the calculated cohesions from the theoretical relationship are about 0.84 to 1.05 times of the measured cohesions from direct shear tests. The calculated peak friction angles are about 10% to 15% higher than the measured values from direct shear tests. It is practically impossible to reach the particle arrangement assumed in the theoretical relationship which seems to be the main reason for the discrepancy between calculated and observed responses.

To investigate the micro mechanical behavior of cemented granular material, and to test the accuracy of the proposed theoretical relationship with numerical simulation, different numerical samples are generated and tested in direct shear testing with PFC^{2D}. At first, two simple models are created with two rows of particles to study the progressive failure mechanism, which is found to be size dependent. Since there is no cementing material filling the pore space among particles in the micro modeling, the micro properties input should represent both the effects of steel balls and cement in the physical samples. Based on the trends obtained in the parametric sensitivity study, the micro parameters of four groups of numerical conglomerates are calibrated by matching their macro responses in the direct shear testing to the corresponding laboratory results. The numerical conglomerates are created similarly to those prepared in the laboratory.

With the calibrated micro parameters, the numerical and laboratory results under different normal stresses for direct shear testing reach a close match for each group of samples. However, for numerical samples with different particle sizes, the calibrated micro parameters are not all the same. The main reason for this difference is due to the size dependent effect of the progressive failure mechanism in the micro modeling. Overall, the numerical model shows that the proposed

theoretical relationship provides the micro mechanical parameters that can capture the macro responses.

8.2 Conclusions

The following conclusions can be made from this research:

- The stress-strain behavior of artificial conglomerate is brittle under low confining stress. It is because the bonding between steel ball and cement contributes more to the strength than the friction between particles under low confining stress. On the other hand, the stress-strain behavior could become more ductile due to the increased contribution of friction to the strength, if the confining stress is higher.

- The volumetric contraction of artificial conglomerate is evident due to the presence of steel balls. The dilation curves under different normal stresses are nearly parallel to each other for different artificial conglomerate groups. Therefore, the variation of normal stress only changes the onset of dilation but does not affect its magnitude.

- The predominant failure surface is found to lie along the steel ball-cement contact in all tested artificial conglomerate samples. The bonding strength between the steel balls and cement is therefore weaker than that of the cement matrix as per the principle of least work.

- The effect of particle size and uniform/non-uniform particle size distribution on the strength and mechanical behavior is very limited for the artificial conglomerates being tested in this study, which were prepared with the densest steel ball assembly.

- An innovative method is designed to determine the inter-particle friction angle of spherical particles, which is simple and effective.

- Three-dimensional scanning technique is effective in studying the failure surface and the micro properties of cemented granular material.

- The relationship between micro inter-particle friction angle and macro peak friction angle in Eq. 3.46 is considered valid for the artificial conglomerates being tested and can be used to correlate the micro and macro friction angle of the cemented granular material in this study.

- The calculated theoretical cohesion using Eq. 3.47 is found in agreement with the measured cohesion. Thus, Eq. 3.47 can be used to represent the relationship between micro bonding strength and cohesion of the artificial conglomerates being tested in this study.

- The calculated cohesion and friction agree with the measured values in the laboratory experiments, which indicates the existence of a relationship between the micro and macro mechanical properties. The macro parameters of cemented granular material can be calculated with measured micro properties using the derived theoretical relationship, and the micro bonding strength and inter-particle friction for the tested material can be calculated with the measured macro parameters, as shown in the verification.

- The macro cohesion of cemented granular material should be larger than the micro bonding strength for the cemented granular material, when there is not a significant amount of voids in the material. Presently, shear bonding strength is usually assumed to be the same as the cohesion, which results in the overestimation of the micro bonding strength.

- Due to the absence of cementing material filling the pore spaces among particles in the micro model, the micro parameters should represent both the effect of particles and cement in the physical samples. With the calibrated micro parameters, the numerical and laboratory results under different normal stresses are in good agreement.

- The progressive failure mechanism in the micro modeling is size dependent. Different calibrated micro parameters can be obtained for numerical samples with different sizes of particles. In the numerical simulation, the progressive failure phenomenon can be reduced by increasing the stiffness of particles. However, the particle stiffness in the micro modeling should represent both the stiffness of particles and cement in the laboratory.

- The micro mechanical parameters provided by the proposed theoretical relationship can capture the macro response with the micro modeling. The accuracy of derived theoretical relationship is verified with numerical simulation.

8.3 Recommendations

Recommendations for future work are as follows:

- The developed theoretical relationship between micro and macro mechanical properties is based on two extreme packing conditions with spherical particles and uniform rod (for 2 D

analysis) size distribution. This relationship can be further improved by considering the packing condition with different void ratios, the effect of particle shape, and the effect of particle size distribution.

- In the derivation of the theoretical relationship, all bonds between the rods and the cementing agent are assumed to be broken at the same time, and the bonding strength and friction between rods are also assumed to fail simultaneously. These assumptions can be further investigated and studied using the Principle of Least Work.

- The proposed theoretical relationship between micro and macro mechanical properties has been verified based on experimental results of artificial conglomerate made by steel balls and Portland cement. Further experimental work can be performed using materials that are more representative of natural cemented granular material (e.g., use cemented Ottawa sand to model sandstone). Further, the effect of particle shape, particle surface roughness, and the effect of grain crushing needs to be considered, if applicable. Thin section analysis and microscopy analysis is recommended to investigate the particle surface properties before preparing the artificial samples.

- High-quality cementing material should be used in future experimental study. The cementing material purchased from specific cement manufacturer should be sampled and tested randomly to ensure consistency of material. Moreover, the difference of selected water to cement ratios of cementing material should be large enough to investigate the effect of cementing strength on the relationship between micro and macro mechanical properties. Cemented granular material can be tested at different porosities to investigate the effect of void ratio on the relationship of micro and macro mechanical properties. Furthermore, samples with different sizes should be prepared and tested to investigate the scaling effect on the relationship of micro and macro mechanical properties.

- Numerical simulation with other DEM software can be conducted to investigate the effect of micro properties on the macro mechanical behavior of cemented granular material. The results can be compared with the PFC modeling results.

- In order to apply the relationship between micro and macro mechanical properties and improve the understanding of many practical problems, such as sand production in petroleum oil wells, several factors should be considered and simulated in the experimental study, such as the effect of reservoir temperature, capillary force, seepage force, and cyclic loading.

Bibliography

Akram, M.S. (2010). "Physical and numerical investigation of conglomeratic rocks." PhD thesis. The University of New South Wales, Sydney, Australia.

Akram, M.S., and Sharrock, G.B. (2010). "Physical and numerical investigation of a cemented granular assembly of steel spheres." International Journal for Numerical and Analytical Methods in Geomechanics, 34(18), 1896-1934.

Amini, Y., and Hamidi, A. (2014). "Triaxial shear behavior of a cement-treated sand–gravel mixture." Journal of Rock Mechanics and Geotechnical Engineering, 6, 455-465.

Amini, Y., Hamidi, A., and Asghari, E. (2014). "Shear strength-dilation characteristics of cemented sand-gravel mixtures." International Journal of Geotechnical Engineering, 8(4), 406-413.

Asghari, E., Toll, D.G., and Haeri, S.M. (2003). "Triaxial behavior of a cemented gravelly sand, tehran alluvium." Journal of Geotechnical and Geoenvironmental Engineering, 21(1), 1–28.

ASTM D5607-08. (2008). "Standard test method for performing laboratory direct shear strength tests of rock specimens under constant normal force," ASTM International, West Conshohocken, PA.

ASTM D3967-08. (2008). "Standard test method for splitting tensile strength of intact rock core specimens," ASTM International, West Conshohocken, PA.

Bahador, S., and Jong, H.C. (2006). "Effect of preconditioning of concrete under accelerated test." 31st Conference on Our World in Concrete & Structures, Ci-premier Pte Ltd, Singapore, Article Id: 100031015.

Barton, M.E., Mockett, L.D., and Palmer, S.N. (1993). "An engineering geological classification of the soil/rock borderline materials between sands and sandstones." The Engineering Geology of Weak Rock, J.C.Cripps, J.M.Coulthard, M.G.Culshaw, A.Forster, S.R.Hencher, C.F.Moon, eds., A.A. Balkema, Rotterdam, 125-138.

Baud, P., Zhu, W., and Wong, T. (2000). "Failure mode and weakening effect of water on sandstone." Journal of Geophysical Research, 105(B7), 16371-16390.

Bell, F.G. (1978). "The physical and mechanical properties of the fell sandstones," Northumberland, England. Engineering Geology, 12, 1-29.

Bernabe, Y., Fryer, D.T., and Hayes, J.A. (1992). "The effect of cement on the strength of granular rocks." Geophysical Research Letters, 19(14), 1511-1514.

Bica, A.V.D., Bressani, L.A., Vendramin, D., Martins, F.B., Ferreira, P.M.V., and Gobbi, F. (2008). "Anisotropic shear strength of a residual soil of sandstone." Canadian Geotechnical Journal, 45(3), 367-376.

Bishop, A.W. (1954). "Discussion on A.D.M.Penman (1953)." Geotechnique, 4(1), 43-45.

Bishop, A.W., and Henkel, D.J. (1957). The measurement of soil properties in the triaxial test. Edward Arnold LTD, London.

Boggs, S. (2006). Principles of sedimentology and stratigraphy. Pearson Prentice Hall, Upper Saddle River, New Jersey.

British Standard 5930. (1981). "The code of practice for site investigations." British Standards Institution, London.

Caquot, A. (1934). Equilibre des massifs a frottement interne. Gauthier-Villars, Paris, France.

Cho, N., Martin, C.D., and Sego, D.C. (2007). "A clumped particle model for rock." International Journal of Rock Mechanics and Mining Sciences, 44(7), 997-1010.

Cho, N. (2008). "Discrete element modeling of rock pre-peak fracturing and dilation." PhD thesis. University of Alberta, Edmonton, Canada.

Christoffersen, J., Mehrabadi, M. M., and Nemat-Nasser, S. (1981). "A micromechanical description of granular material behavior." Journal of Applied Mechanics, 48, 339-344.

Clough, G.W., Rad, N.S., Bachus, R.C., and Sitar, N. (1981). "Cemented sands under static loading." Journal of the Geotechnical Engineering Division, 107(6), 799-817.

154

Consoli, N., Viana da Fonseca, A., Cruz, R., and Heineck, K. (2009). "Fundamental parameters for the stiffness and strength control of artificially cemented sand." Journal of Geotechnical and Geoenvironmental Engineering, 135(9), 1347-1353.

Contreras, I., Grosser, A.T., and Ver Strate, R.H. (2008). "The use of the fully-grouted method for piezometer installation." Geotechnical News, 26, 30-37.

Coop, M.R., and Atkinson, J.H. (1993). "The mechanics of cemented carbonate sands." Geotechnique, 43(1), 53–67.

Cooper, A. (2011). Biophysical chemistry. Royal Society of Chemistry, United Kingdom.

Cundall, P.A., and Strack, O.D.L. (1979). "A discrete numerical model for granular assemblies." Geotechnique, 29(1), 47-65.

Cundall, P. A. (1980). "UDEC- A generalized distinct element program for modeling jointed rock." Report No. PCAR-I-80, U.S. Army, European Research Office, London.

Cundall, P. A. (1988). "Formulation of three dimensional distinct element model Part-l. A scheme to detect and represent in a system composed of many polyhedral blocks." International Journal of Rock Mechanics and Mining Sciences & Geomechanics Abstracts, 25 (3), 107-116.

Cundall, P. A., and Hart, R. D. (1993). "Numerical modeling of discontinua." Comprehensive Rock Engineering: Principles, Practice & Projects (Volume 2), J. A. Hudson, ed., Pergamon Press, Oxford, 231-243.

Das, A., Tengattini, A., Nguyen, G., and Einav, I. (2013). "A micromechanics based model for cemented granular materials." Constitutive Modeling of Geomaterials, Q. Yang, J. Zhang, H. Zheng, Y. Yao, eds., Springer, Berlin, 527-534.

Dehler, W., and Labuz, J.F. (2007). "Stress path testing of an anisotropic sandstone." Journal of Geotechnical and Geoenvironmental Engineering, 133(1), 116-119.

Delenne, J.-Y., Topin, V., and Radjai, F. (2009). "Failure of cemented granular materials under simple compression - Experiments and numerical simulations." Acta Mechanica, 205, 9-21.

Diederichs, M.S. (2000). "Instability of hard rock masses: the role of tensile damage and relaxation." PhD thesis. University of Waterloo, Waterloo, Canada.

Ding, X., and Zhang, L. (2014). "A new contact model to improve the simulated ratio of unconfined compressive strength to tensile strength in bonded particle models." International Journal of Rock Mechanics and Mining Sciences, 69, 111-119.

Dittes, M., and Labuz, J. (2002). "Field and laboratory testing of St. Peter sandstone." Journal of Geotechnical and Geoenvironmental Engineering, 128(5), 372-380.

Dobereiner, L. (1984). "Engineering geology of weak sandstones." PhD Thesis, Imperial College, London.

Dobereiner, L., and Freitas, M.H. (1986). "Geotechnical properties of weak sandstones." Geotechnique, 36(1), 79-94.

Dyke, C.G., and Dobereiner, L. (1991). "Evaluating the strength and deformability of sandstones." Quarterly Journal of Engineering Geology, 24, 123-134.

Einav, I. (2007). "Breakage mechanics—Part II: modelling granular materials." Journal of the Mechanics and Physics of Solids, 55(6), 1298–1320.

Essam, I., and Wally, A. (2007). "Effect of water injection on sand production associated with oil production in sandstone reservoirs." Middle East Drilling and Technology Conference, Society of Petroleum Engineers, Cairo, Egypt, 1-9.

Fu, Y. (2005). "Experimental quantification and DEM simulation of macro behaviors of granular materials using x-ray tomography imaging." PhD thesis. Louisiana State University, Baton Rouge, USA.

Gil, I., Roegiers, J. C., Hart, R., and Shimizu, Y. (2005). "Modeling the mechanical properties of Antler sandstone using a discrete element model." The 40th U.S. Symposium on Rock Mechanics (USRMS), Anchorage, USA.

Goodman, R.E. (1993). Engineering Geology: Rock in Engineering Construction. Wiley, New York.

Gu, X.F., Seidel, J.P., and Haberfield, C.M. (2003). "Direct shear test of sandstone-concrete joints." *International Journal of Geomechanics, 3(1-2), 21-33.*

Hadizadeh, J., and Law, R. (1991). "Water-weakening of sandstone and quartzite deformed at various stress and strain rates." *International Journal of Rock Mechanics and Mining Sciences & Geomechanics Abstracts, 28(5), 431-439.*

Haeri, S.M., Yasrebi, S., and Asghari, E. (2002). "Effects of cementation on the shear strength parameters of tehran alluvium using large direct shear test." *Proceedings of 9th Congress of IAEG, Durban, South Africa, 519–525.*

Haeri, S.M., Hosseini, S.M., Toll, D.G., and Yasrebi, S.S. (2005). "The behavior of an artificially cemented sandy gravel". *Geotechnical & Geological Engineering, 23(5), 537-560.*

Haeri, S., Hamidi, A., Hosseini, S., Asghari, E., and Toll, D. (2006). "Effect of cement type on the mechanical behavior of a gravely sand." *Geotechnical and Geological Engineering, 24, 335-360.*

Han, G., and Dusseault, M.B. (2002). "Quantitative analysis of mechanisms for water-related sand production." *International Symposium on Formation Damage Control, Society of Petroleum Engineers, Lafayette, Louisiana, USA, 361-372.*

Harsh, S., Shen, Z., and Darwin, D. (1990). "Strain-rate sensitive behavior of cement paste and mortar in compression." *ACI Material Journal, 87(5), 508-516.*

Heap, M.J., Baud, P., Meredith, P.G., Bell, A.F., and Main, I.G. (2009). "Time-dependent brittle creep in Darley Dale sandstone." *Journal of Geophysical Research, 114(B7), B07203.*

Holt, R. M. (2001). "Particle vs laboratory modelling of in-situ compaction." *Physics and Chemistry of the Earth (A), 26 (1-2), 89-93.*

Holt, R.M., Doornhof, D., and Kenter, C.J. (2003). "Use of discrete particle modeling to understand stress-release effects on mechanical and petrophysical behavior of granular rocks." *Numerical Modeling in Micromechanics via Particle Methods: International PFC Symposium, Gelsenkirchen, Germany, 269-276.*

Horii, H., and Nemat-Nasser, S. (1986). "Brittle failure in compression: splitting, faulting and brittle-ductile transition." Philosophical Transactions of the Royal Society of London (Series A)-Mathematical Physical and Engineering Sciences, 319(1549), 337-374.

Horne, M.R. (1965). "The behavior of an assembly of rotund, rigid, cohesionless particles. I and II." Proceedings of the Royal Society of London. Series. A, Vol. 286, pp. 62-97.

Hsieh, Y.M., Li, H.H., Huang, T.H., and Jeng, F.S. (2008). "Interpretations on how the macroscopic mechanical behavior of sandstone affected by microscopic properties—Revealed by bonded-particle model." Engineering Geology, 99(1-2), 1-10.

Huang, J.T., and Airey, D.W. (1998). "Properties of artificially cemented carbonate sand." Journal of Geotechnical and Geoenvironmental Engineering, 124(6), 482–499.

Hyett, A.J., Bawden, W.F., and Reichert, R.D. (1992). "The effect of rock mass confinement on the bond strength of fully grouted cable bolts." International Journal of Rock Mechanics and Mining & Geomechanics Abstracts, 29(5), 503-524.

Ismail, M.A., Joer, H.A., Sim, W.H., and Randolph, M.F. (2002). "Effect of cement type on shear behavior of cemented calcareous soil." Journal of Geotechnical and Geoenvironmental Engineering, 128(6), 520–529.

Itasca Consulting Group, Inc. (2008). "PFC2D (Particle Flow Code in 2 Dimensions), Version 4.0." Itasca, Minneapolis, USA.

Jeng, F.S., Weng, M.C., Lin, M.L., and Huang, T.H. (2004). "Influence of petrographic parameters on geotechnical properties of tertiary sandstones from Taiwan." Engineering Geology, 73(1-2), 71-91.

Jiang, M., Sun, Y., and Xiao, Y. (2012). "An experimental investigation on the mechanical behavior between cemented granules." Geotechnical Testing Journal, 35(5), GTJ104408.

Jiang, M., Zhang, W., Sun, Y., and Utili, S. (2013). "An investigation on loose cemented granular materials via DEM analyses." Granular Matter, 15(1):65-84.

Kainat, M. (2014). *"Initial imperfections of high strength UOE manufactured steel piles and their effects on pipe buckling." PhD thesis. University of Alberta, Edmonton, Canada.*

Kongsukprasert, L., Tatsuoka, F., and Tateyama, M. (2005). *"Several factors affecting the strength and deformation characteristics cement-mixed gravel." Soils and Foundations, 45(3), 107–124.*

Kruyt, N.P., Millet, O., and Nicot, F. (2015). *"Deformation analysis of granular materials at micro and macro scales." Geomechanics from Micro to Macro, K. Soga, K. Kumar, G. Biscontin, M. Kuo, eds., Taylor & Francis group, London, 753-757.*

Li, X., Yu, H.S., and Li, X.S. (2009). *"Macro–micro relations in granular mechanics." International Journal of Solids and Structures, 46, 4331–4341.*

Louis, L., David, C., and Robion, P. (2003). *"Comparison of the anisotropic behavior of undeformed sandstones under dry and saturated conditions." Tectonophysics, 370, 193-212.*

Marketos, G., and Bolton, M.D. (2007). *"A DEM study of compaction band formation." Bifurcations, Instabilities, Degradation in Geomechanics, G. E. Exadaktylos, I. G. Vardoulakis, eds., Springer, Berlin, 155-171.*

Marri, A. (2010). *"The mechanical behavior of cemented granular materials at high pressures." PhD thesis. University of Nottingham, Nottingham, United Kingdom.*

Matsuoka, H. (1974). *"A microscopic study on shear mechanism of granular materials." Soils and Foundations, 14(1), 29-43.*

Menendez, B., Zhu, W., and Wong, T. (1996). *"Micromechanics of brittle faulting and cataclastic flow in Berea sandstone." Journal of Structural Geology, 18(1), 1-16.*

Muhuri, S.K., Dewers, T.A., Scott, T.E., and Reches, Z. (2004). *"Interseismic fault strengthening and earthquake-slip instability: friction or cohesion?" Geology, 31(10), 881-884.*

Nakagawa, S., and Myer, L.R. (2001). *"Mechanical and acoustic properties of weakly cemented granular rocks." Rock Mechanics in the National Interest: Proceedings of the 38th Annual U.S. Rock Mechanics Symposium, D. Elsworth, J.P. Tinucci, K.A. Heasley, eds., A.A. Balkema, Rotterdam, 3-10.*

Nardelli, V., and Coop, M.R. (2015). "An experimental investigation of the micromechanical behavior of cemented sand particles." *Geomechanics from Micro to Macro*, K. Soga, K. Kumar, G. Biscontin, M. Kuo, eds., Taylor & Francis group, London, 1013-1017.

Nemat-Nasser, S. (2000). "A micromechanically-based constitutive model for frictional deformation of granular materials." *Journal of the Mechanics and Physics of Solids*, 48, 1541-1563.

Nespereira, J., Blanco, J.A., Yenes, M., and Pereira, D. (2010). "Irregular silica cementation in sandstones and its implication on the usability as building stone." *Engineering Geology*, 115(3-4), 167–174.

Newland, P.L., and Allely, B.H. (1957). "Volume changes in drained triaxial tests on granular materials." *Geotechnique*, 7(1):17-34.

Nova, R., Castellanza, R., and Tamagnini, C. (2003). "A constitutive model for bonded geomaterials subject to mechanical and/or chemical degradation." *International Journal for Numerical and Analytical Methods in Geotechnics*, 27, 705-732.

Oda, M., and Konishi, J. (1974). "Microscopic deformation mechanism of granular material in simple shear." *Soils and Foundations*, 14(4), 25-38.

Oda, M. (1974). "A mechanical and statistical model of granular material." *Soils and Foundations*, 14(1), 13-27.

Pettijohn, F.J., Potter, P.E., and Siever, R. (1965). *Geology of sand and sandstone*. Indiana University Print Plant, Bloomington.

Pettijohn, F.J., Potter, P.E., and Siever, R. (1987). *Sand and sandstone*. Springer, Berlin.

Potyondy, D. O.and Cundall, P.A. (2004). "A bonded particle model for rock." *International Journal of Rock Mechanics and Mining Sciences*, 41(8), 1329-1364.

Rahmati, H. (2013). "Micromechanical study of borehole breakout mechanism." PhD thesis. University of Alberta, Edmonton, Canada.

Ray, S.K., Sarkar, M., and Singh, T.N. (1999). "Effect of cyclic loading and strain rate on the mechanical behavior of sandstone." *International Journal of Rock Mechanics and Mining Sciences, 36(4), 543-549.*

Reviron, N., Reuschle, T., and Bernard, J.D. (2009). "The brittle deformation regime of water-saturated siliceous sandstones." *Geophysical Journal International, 178(3), 1766-1778.*

Riedel, J.J., and Labuz, J.F. (2007). "Propagation of a shear band in sandstone." *International Journal for Numerical and Analytical Methods in Geomechanics, 31(11), 1281-1299.*

Rowe, P.W. (1962). "The stress-dilatancy relation for static equilibrium of an assembly of particles in contact." *Proceedings of the Royal Society, 269, 500-527.*

Rowe, P.W., Barden, L., and Lee, I.K. (1964). "Energy components during the triaxial cell and direct shear tests." *Geotechnique, 14(3), 245-261.*

Saxena, S.K., and Lastrico, R.M. (1978). "Static properties of lightly cemented sand." *Journal of Geotechnical and Geoenvironmental Engineering, 104(12), 1449-1465.*

Schnaid, F., Prietto, P.D.M., and Consoil, M.H.T. (2001). "Characterization of cemented sand in triaxial compression." *Journal of Geotechnical and Geoenvironmental Engineering, 127(10), 857-867.*

Shen, Z., Jiang, M., and Thornton, C. (2016). "DEM simulation of bonded granular material. Part I: Contact model and application to cemented sand." *Computers and Geotechnics, 75, 192-209.*

Skoczylas, F., Burlion, N., and Yurtdas, I. (2007). "About drying effects and poro-mechanical behavior of mortars." *Cement & Concrete Composites, 29(5), 383-390.*

Singh, S.K. (1989). "Fatigue and strain hardening behavior of graywacks from the flag stuff formation." *Engineering Geology, 27(2), 171-180.*

Taheri, A., Sasaki, Y., Tatsuoka, F., and Watanabe, K. (2012). "Strength and deformation characteristics of cement-mixed gravelly soil in multiple-step triaxial compression." *Soils and Foundations, 52(1), 126-145.*

Taylor, D.W. (1948). *Fundamentals of soil mechanics. John Wiley & Sons, New York.*

Tobita, Y., and Oda, M. (1999). *"Friction based deformation and strength behaviors of granular soils." Mechanics of Granular Materials: An Introduction, M. Oda, K. Iwashita, eds., A.A. Balkema, Rotterdam, 50-55.*

Tronvoll, J., Papamichos, E., Skjaerstein, A., and Sanfilippo, F. (1997). *"Sand production in ultra-weak sandstones: is sand control absolutely necessary?" Latin American and Caribbean Petroleum Engineering Conference, Society of Petroleum Engineers, Rio de Janeiro, Brazil, SPE 39042.*

Urquhart, L.C. (1959). *Civil Engineering Handbook. McGraw-Hill Book Company, New York.*

Wang, Y.H., and Leung, S.C. (2008). *"Characterization of cemented sand by experimental and numerical investigations." Journal of Geotechnical and Geoenvironmental Engineering, 134(7), 992-1004.*

Weng, M.C., Jeng, F.S., Huang, T.H., and Lin, M.L. (2005). *"Characterizing the deformation behavior of Tertiary sandstones." International Journal of Rock Mechanics and Mining Sciences, 42(3), 388-401.*

Williams, A.F., and Pells, P.J.N. (1981). *"Side Resistance Rock Sockets in Sandstone, Mudstone, and Shale." Canadian Geotechnical Journal, 18(4), 502-513.*

Yang, S., and Jiang, Y. (2010). *"Triaxial mechanical creep behavior of sandstone." Mining Science and Technology (China), 20(3), 339-349.*

Yang, S., and Jing, H. (2011). *"Strength failure and crack coalescence behavior of brittle sandstone samples containing a single fissure under uniaxial compression." International Journal of Fracture, 168(2), 227-250.*

Yurtdas, I. Burlion, N., and Skoczylas, F. (2004a). *"Experimental characterization of the drying effect on uniaxial mechanical behavior of mortar." Materials and Structures, 37(3), 170-176.*

Yurtdas, I. Burlion, N., and Skoczylas, F. (2004b). *"Triaxial mechanical behavior of mortar: Effects of drying." Cement and Concrete Research, 34(7), 1131-1143.*

Appendix A

To understand the bonding and debonding mechanism of cemented granular material, such as sandstone, a summary of sand and sandstone in several aspects is provided in this appendix, including the formation, classification and mechanical properties.

A.1 Introduction to sand

A.1.1 Formation and classification of sand

Sand is formed primarily by the disintegration of quartz-bearing plutonic rocks (Pettijohn et al. 1965). Through the transportation by wind and water, most sand deposits are in the form of beaches, dunes, deserts, and deltas. The size and shape of sand particles are inherited from the source rock, but also heavily influenced by the effects of weathering and transportation. For example, while quartz sand that is recently weathered from granite will be angular, desert sand that is transported long distance by wind will be rounded. Besides, the depositional environment and the subsequent geological events also affect the state and the structure or fabric of sand. Sand is so variable that rarely two sand particles are the same, so the classification methods of sand usually only focus on one characteristic.

(1) Classification method based on size difference

In the United States, based on the Krumbein phi scale, sand is commonly divided into five sub-categories according to size: very fine sand (1/16 - ⅛ mm diameter), fine sand (⅛ mm - ¼ mm), medium sand (¼ mm - ½ mm), coarse sand (½ mm - 1mm), and very coarse sand (1 mm - 2mm) (Urquhart 1959).

According to the British Soil Classification System (British Standard: 5930 1981), sand particles are divided into three groups based on size: fine sand (0.06 - 0.2mm), medium sand (0.2 - 0.6mm) and coarse sand (0.6 - 2mm).

(2) Classification method based on differences in behavior

Another usual classification method of sand is dividing it into dense sand and loose sand. However, this method is not only based on the density of sand, which is highly variable depending on grain size, moisture content and particle arrangement. Actually, this classification method is mostly

163

according to the difference in behavior of sand. Dense sand tends to expand in volume or "dilate" upon shearing, while loose sand tends to decrease in volume or "contract".

Besides, it is worth to mentioning that the Relative Density Index $D_r = \frac{e_{max}-e}{e_{max}-e_{min}}$ is not sufficient to characterize the behavior of sand. As shown in Figure A.1, when two sand samples with the same void ratio are loaded under different confining stresses, the dense sample under higher stress would present "loose behavior". Therefore, besides void ratio, pressure should also be considered when studying the behavior of sand.
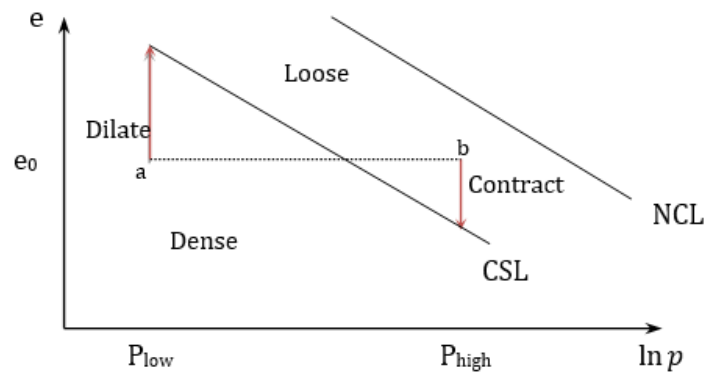
Figure A.1 The influence of confining pressure on sand behavior

A.2 Introduction to sandstone

A.2.1 Formation of sandstone

Because of weathering and erosion, the parent rock of sandstone is disintegrated into mineral grains. Then, mineral grains are transported and deposited as sand. A layer or layers of sand accumulates as the result of sedimentation, either from water (as in a stream, lake or sea) or from air (as in the desert). Typically, sedimentation occurs by sand settling from suspension. With sufficient accumulation of sand particles, the sand becomes sandstone when it is compacted by the pressure of the overlying deposits and cemented by the precipitation of minerals within the pore spaces between sand grains. The whole rock cycle may have been repeated numerous times as sandstones were eroded and reconstituted again and again which contributed the constituent grains to sediments that were redeposited and form new sandstone again (Boggs 2006, Goodman 1993, Pettijohn et al. 1965).

A.2.2 Components of sandstone

Sandstone consists of three main components: framework grains, matrix and cementing agent.

(1) Framework grains

Framework grains are silicate grains and are detrital in origin. The size of framework grains is in the range of 1/16 to 2 mm. Depending on the different mineral compositions, the framework grains can be classified into three different categories.

    a. Quartz framework grains are the dominant minerals in most sedimentary rocks. They have exceptional physical properties, such as hardness and chemical stability.

    b. Feldspathic framework grains are the second most abundant minerals in sandstone.

    c. Lithic framework grains are individual mineral grains weathered from any fine-grained or coarse-grained igneous, metamorphic or sedimentary rocks (Boggs 2006).

Besides, the framework grains also include some accessory minerals, which only account for less than 1%~2% in sedimentary rocks. Common accessory minerals include micas, olivine, pyroxene, and corundum. Accessory minerals are heavier in density than common rock-forming minerals, such as quartz and feldspar (Boggs 2006).

(2) Matrix

Matrix is a kind of very fine material (clay or silt), which is present within interstitial pore space between the framework grains.

(3) Cement

Cement is the material that binds the framework grains together. They may be either silicate minerals or carbonate minerals. Quartz is the most common silicate mineral that acts as cement, while calcite cement is the most common carbonate cement. There are also some other kinds of cementing minerals, like hematite, limonite, feldspars, anhydrite, gypsum, barite, clay minerals, and zeolite minerals (Boggs 2006).

A.2.3 Classification of sandstone

(1) Mature sandstone and immature sandstone (Goodman 1993)

A sand grain has a long history involving numerous cycles of petrogenesis, erosion and redeposition. As the number of cycle increases, the weaker and more weatherable constituents are lost, and the residual grains, mainly quartz, become more rounded. A rock composed almost entirely of rounded quartz grains is said to be mature. Mature sandstone tends to be sorted texturally, with relatively uniform gradation. For example, orthoquartzite as shown in Figure A.2 (a) is a kind of mature sandstone, which exhibits rounded grains and almost entirely of quartz.

The sandstone composed of sub-angular quartz grains, with feldspars and ferromagnesian minerals and possibly lithic fragments is said to be immature. The immature sandstone is not uniformly graded, such as greywacke as shown in Figure A.2 (b), which consists of angular grains of different size grades and variable composition (Goodman 1993). Besides, while clay is a common constituent of immature sandstone, it accounts for very small proportion in the mature sandstone.

<div align="center">(a)   (b)</div>
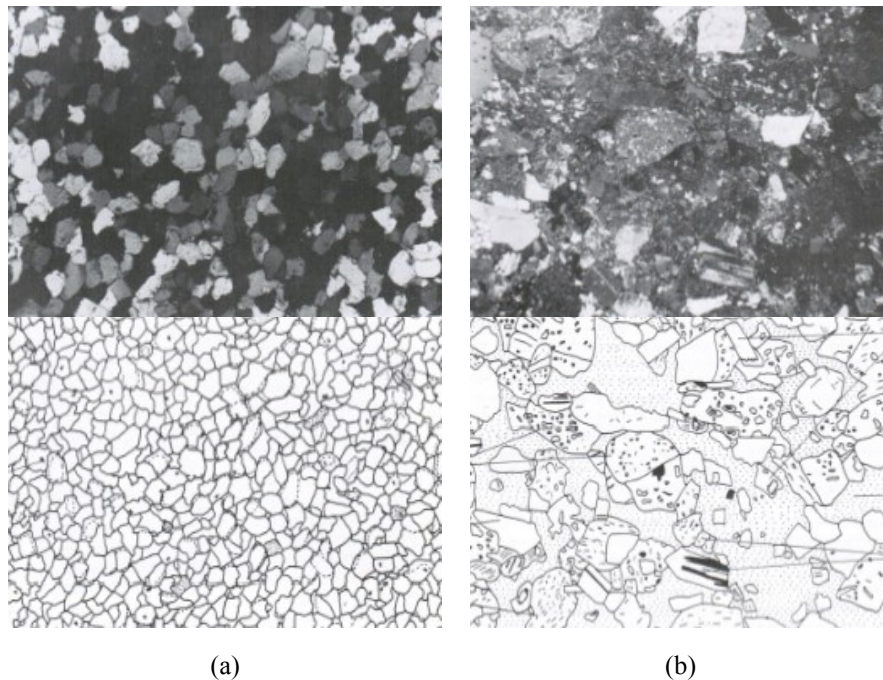
Figure A.2 Textural contrasts between (a) Orthoquartzite and (b) Greywacke. (Goodman 1993)

(2) The classification system by Pettijohn

Sandstones are divided into those with less than 15% detrital matrix and those with more than 15% by Pettijohn in 1954. Detrital matrix refers to the clastic portion of the finer material in the pores

of the sandstone framework, excluding precipitated cement, water and organic material (Pettijohn et al. 1965).

Sandstone with more than 15% detrital matrix is called greywacke, which includes feldspathic greywacke and lithic greywacke. Sandstone with less than 15% detrital matrix is called arenite. Compositional names for the arenites are as follows:

 a. Arkose is the sandstone with less than 75% quartz and more feldspar than rock fragments.

 b. Orthoquartzite is the sandstone composed of more than 95% quartz.

 c. Lithic sandstone is the sandstone with more rock fragments than feldspar. (Pettijohn et al. 1965)

(3) Dott (1964) Classification Scheme

Dott's classification scheme is based on the mineralogy of framework grains, and on the type and amount of matrix existed among the framework grains. Dott set the boundary between arenite and wacke at 15% clay matrix. He also divided the framework grains in sandstones into three major categories: quartz, feldspar and lithic grains as follows.

 a. Arenite is the sandstone that has less than 15% clay matrix among the framework grains, including quartz arenite, feldspathic arenite and lithic arenite.

 b. Wacke is the sandstone that contains more than 15% clay matrix among the framework grains, including quartz wacke, feldspathic wacke and lithic wacke (Boggs 2006).

A.2.4 Mechanical properties of sandstone

(1) Deformation of sandstone

Deformation is one of the most important geotechnical engineering property. It is the relative displacement caused by external load, body force or temperate changes. Deformation can be measured in the laboratory in terms of axial strain, volumetric strain, lateral strain, and shear strain, with triaxial compression test, triaxial extension test, uniaxial compression test (UCS), and direct shear test and so on.

The deformation properties of St. Peter sandstone were investigated with laboratory testing (Dittes and Labuz 2002). The variations of lateral strain and axial strain with axial stress were measured

with uniaxial compression tests. The Young's modulus and Poisson's ratio are found in the range of 0.4~2.0 GPa and 0.2~0.33, respectively. The dilate behavior of St. Peter sandstone was also evaluated by direct shear test, which decreased with the increase of applied normal stress. While the macro dilation angle at failure is equal to 45° at 19 kPa normal stress, it is equal to 21° under 152 kPa normal stress (Dittes and Labuz 2002).

Through cycles of loading and unloading, the elastic and plastic components of volumetric strain and shear strain were obtained with triaxial tests and simple shear tests for Tertiary sandstone (Weng et al. 2005). It was found that the elastic volumetric deformation was non-linear and tended to dilate throughout the shearing process, while the plastic volumetric deformation compacted at first and then dilated. For the shear strain, when the stress path approached the failure envelope, the elastic shear strain increased relative linearly whereas the plastic component increased significantly. The Young's modulus for Tertiary sandstone is found to be in the range of 5~12 GPa. Reviron et al. (2009) also conducted triaxial compression tests to investigate the brittle deformation behavior of the water-saturated siliceous sandstone. Similarly, the volumetric strain was observed to increase firstly due to compaction, and then decreased because of dilation when approaching the peak stress. It is noted that the dilatant part of the differential stress vs. volumetric strain curve becomes smaller with the increment of effective stress. This behavior is similar to sand.

Based on the literature review, the Young's modulus of sandstone is found in the range of 0.5~36 GPa (Dittes and Labuz 2002, Yang and Jing 2011). The Passion's ratio is found in the range of 0.1~0.38 (Gu et al. 2003, Riedel and Labuz 2007) and the macro dilation angle is in the range of 18°~40°.

(2) Failure modes and strength of sandstone

The mechanical response of sandstone is potentially influenced by pressure, temperature and strain rate (Horii and Nematnasser 1986). Baud et al. (2000) found that the strain rate affects the mechanical behavior of Darley Dale sandstone in the range of 2×10^{-6} to $5 \times 10^{-5} s^{-1}$ and the failure modes of dry samples are qualitatively like those of water-saturated samples.

Brittle fracture and cataclastic ductile flow are two prime failure modes of sandstone. Brittle fracture can be divided into two types: axial splitting failure and faulting. While axial splitting of

samples occurs at zero confining pressure, faulting usually happens when the confining pressure is low or moderate. Sandstone located in Linyi City, China, failed in axial splitting failure mode in the UCS test (Yang and Jing 2011), and the axial stress dropped dramatically to zero and the intact sample was fractured into many small blocks. The water-saturated Bentheim sandstone deformed in the brittle faulting regime under triaxial compression conditions (Reviron et al. 2009). The effect confining pressure was found to be in the range of 2 to 50 MPa resulting in a peak strength ranging from 70 to 224 MPa. Using the triaxial rheology experiment, the strength of sandstone collected from Xiangjiaba Project in southwestern China under different confining pressures (3, 5 and 7 MPa, respectively) was determined. The results show that the compressive strength of sandstone (164~210 MPa) increased significantly with increasing confining pressure. A cone shear failure mode of the sample was observed at confining pressure of 5 MPa. This may be due to the effect of friction between the bottom surface of the sample and the loading plate, which limited the lateral expansion of the sample (Yang and Jiang 2010).

Samples would fail in the mode of cataclastic ductile flow under high confining pressures and low temperatures. This failure mode is manifested by damage in the form of distributed micro cracks, pore collapse and grain crushing (Menendez et al. 1996). For the Berea and Darley Dale sandstones under dry condition, the results obtained from triaxial compression tests show that the failure mode was obviously shear localization with the confining pressure ranging from 10 to 50 MPa, and through a transition regime, the failure mode of these two kinds of sandstones tended to be cataclastic flow when the confining pressures were above 100 MPa (Baud et al. 2000). Figure A.3 shows two different failure modes of Darley Dale sandstone under different confining pressures. The solid symbol in the figures denotes dry samples and the open symbol denotes water-saturated samples.
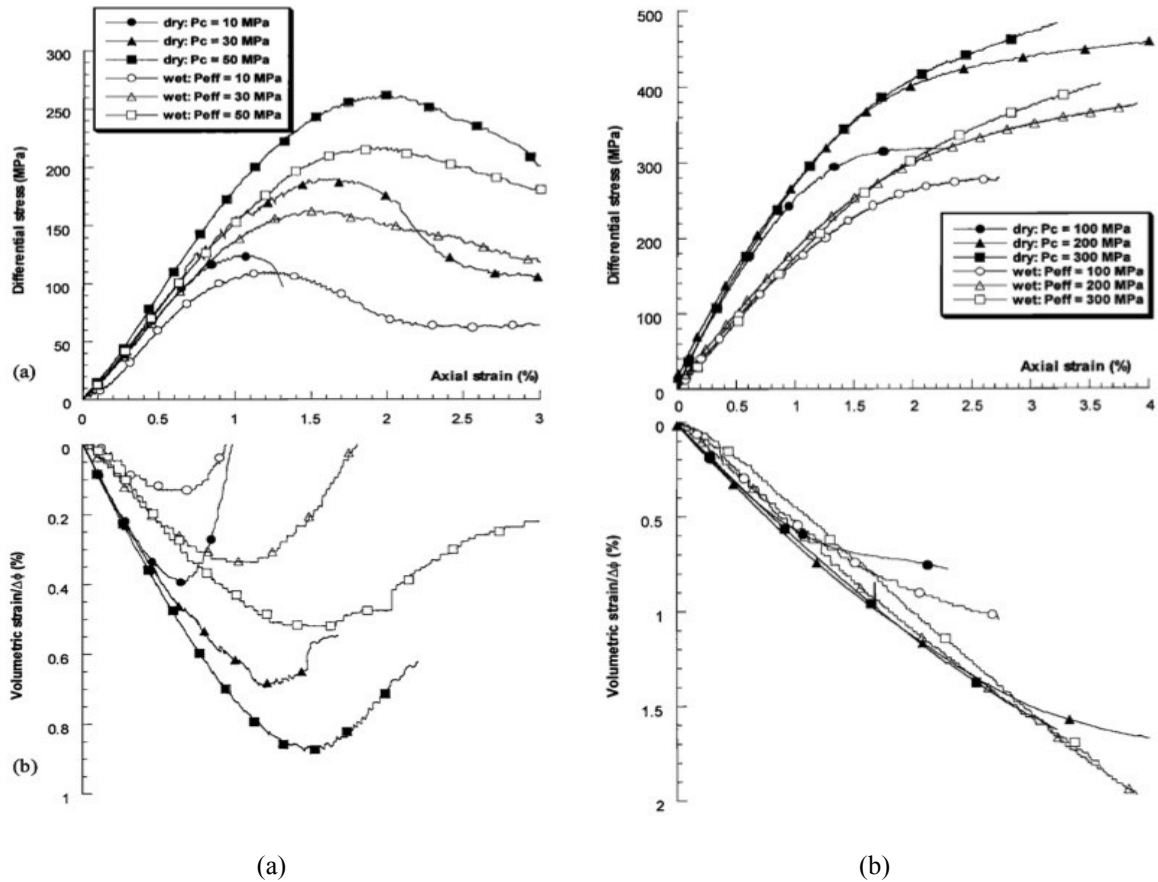
Figure A.3 Differential stress and volumetric stain are plotted versus axial strain for Darley Dale sandstone: (a) The brittle fracture regime; (b) The cataclastic flow regime. (Baud et al. 2000)

According to the literature review, the uniaxial compression strength of sandstone is in the range of 2.5~86 MPa (Weng et al. 2005, Williams and Pells 1981). The friction angle is in the range of 30~55° (Dehler and Labuz 2007).

(3) Anisotropic behavior of sandstone

In the laboratory, specimens obtained with different orientations to the bedding plane are usually used to study the anisotropic behavior of sandstone. Drained and undrained triaxial compression tests were conducted on the Botucatu sandstone from southern Brazil to investigate the influence of anisotropy on shear strength and yield surface (Bica et al. 2008). For the drained experiments, the yield surface obtained from the test when axial stress was parallel to the bedding is much larger than that when axial stress was normal to the bedding. Correspondingly, under undrained condition and confining pressure ranging from 50 to 400 kPa, the peak shear strength for the specimen that

axial stress applied parallel to bedding is approximately 100 to 170 kPa larger than that of specimens with axial stress applied normal to bedding (Figure A.4).
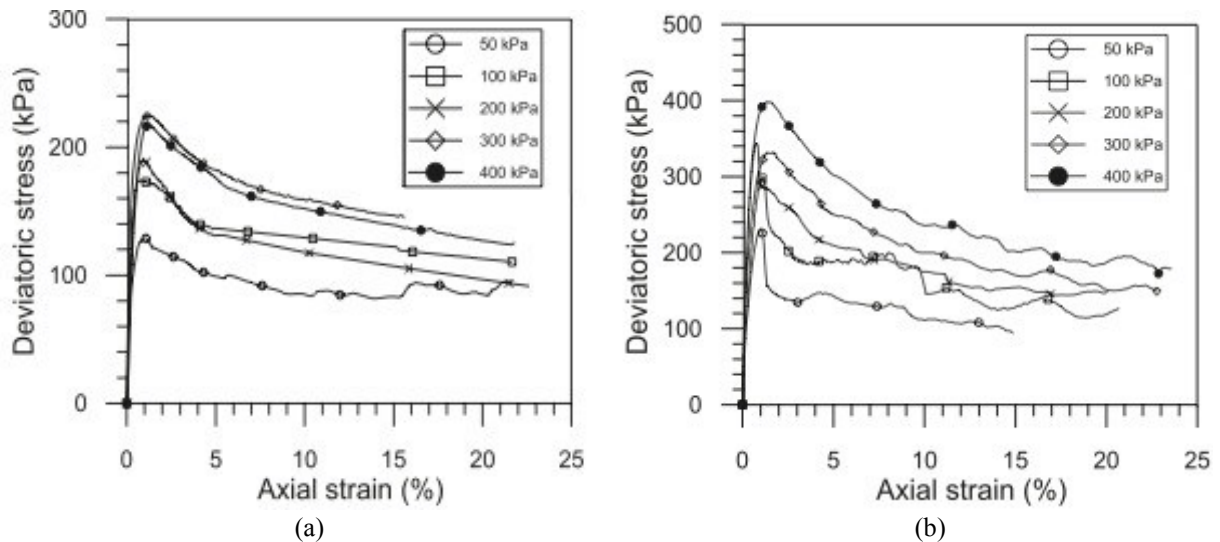
Figure A.4 Stress-strain curves of undisturbed Botucatu sandstone from undrained triaxial tests: (a) Axial stress was applied normal to the bedding; (b) Axial stress was applied parallel to the bedding (Bica et al. 2008)

Anisotropic behavior of Berea sandstone (Dehler and Labuz 2007) was also verified by four different stress path experiments: compression loading, compression unloading, extension loading, and extension unloading. Laboratory results show that the internal friction angle was almost the same for compression and extension tests (55°) when the axial stress was applied parallel to bedding. However, for the axial stress perpendicular to bedding, the internal friction angle was different for compression (50°) and extension (44°). Furthermore, the UCS was found to be 46 MPa for axial stress normal to bedding, while the UCS for axial stress parallel to bedding was only 36 MPa. Besides, through analyzing the anisotropic behaviors of the Bentheim and Rothbach sandstones, Louis et al. (2003) stated that the anisotropic behavior of sandstones is controlled by the anisotropic pore shape and the matrix.

(4) Water-weakening effect of sandstone

The strength of sandstone is generally reduced in the presence of water. Baud et al. (2000) conducted triaxial compression experiments on Berea, Darley Dale, Boise, and Gosford sandstones (with porosity of 21%, 13%, 35%, and 11%, respectively) to compare the water-weakening effect in brittle failure regime and cataclastic flow regime. Results show that in the brittle regime, the

reduction in strength when water was present ranged from 5% to 17 %. In the cataclastic ductile flow regime, the yield strength was lowered by 20~69% in saturated conditions when compared with those dry samples under similar pressure conditions. As shown in Figure A.3, the strength of Darley Dale sandstone in the brittle regime and cataclastic flow regime was reduced by 12~17% and 26~30% in the presence of water, respectively. The water-weakening effect in cataclastic flow regime is explained by the reduction of the specific surface energy, whereas the lowered brittle strength is due to reductions of both the specific surface energy and friction coefficient.

Depending on the component and microstructure of the sandstone, the water-weakening effect is quite variable, ranging from zero effect (Hadizadeh and Law 1991) to 69% reduction (Baud et al. 2000) in strength. The Bentheim sandstone (Reviron et al. 2009) is homogeneous quartz-rich sandstone, and the grains are mainly monocrystalline quartz grains (95%) with quartz overgrowth at the edges, which binds the quartz grains together. By comparing the experiment results obtained on dry samples and water-saturated samples of Bentheim sandstone, no noticeable effect of the presence of water on the critical stress level was observed. Similar phenomenon was also observed in Fontainebleau sandstone that contains more than 99% quartz. It is declared that clay minerals play an important role in the water-weakening effect. The presence of clay minerals will reduce local permeability in the argillaceous sandstone, which controls the mobility of water in the pores. Moreover, friction of saturated clay minerals may drop by 40~80% compared to the value in dry condition, which leads to the friction reduction in the argillaceous sandstone.

(5) Creep behavior of sandstone

Creep is a form of time-dependent deformation. Mechanical creep behavior of sandstone is very important because it can be used for evaluating the long-term stability in geotechnical engineering and in understanding tectonic movements. Lots of tests have been performed in the laboratory to study the creep behavior of sandstone. Yang and Jiang (2010) conducted short-term tests and triaxial creep tests to study the mechanical creep behavior of sandstone. The multi-stage stress triaxial creep tests were conducted firstly through short-term tests under different confining pressures (3, 5 and 7MPa, respectively) and then 4 to 6 stress increments were applied in the long term test with confining pressure of 3 MPa lasting 438.96 hours. Primary creep, steady-state creep and tertiary creep regions were observed in the tests. It is worth mentioning that deformation in the tertiary creep stage accounted for 51.3% of the total creep strain, but the time in this stage only

accounted for 9.34% of the total creep time. Tertiary creep of rock is associated with crack growth and it occurs when the crack density reaches a critical value. Creep can lead to failure of the sandstone at a much lower stress than the short-term strength. For example, when a confining pressure of 5 MPa was applied, the compressive strength decreased from 180.7 MPa for short-term test to 160 MPa for creep test.

With multi-stage testing technique, brittle creep behavior of water-saturated samples of Darley Dale sandstone was investigated under different confining pressures (Heap et al. 2009). The results demonstrate that creep strain rate is heavily dependent on the applied differential stress. At higher effective confining pressure, creep strain rate can be reduced by multiple orders of magnitude.

Appendix B

Presently, shear bonding strength is usually assumed to be the same as the cohesion, and the normal bonding strength equals to the Brazilian tensile strength or direct tensile strength. In order to investigate these commonly accepted relationships between the micro and macro parameters, the normal and shear bonding strength of the synthetic conglomerate is calculated using published experiment results (Akram 2010).

B.1 Preparation of samples

In order to study the mechanical behavior of synthetic conglomerates, cylindrical, circular and rectangular shaped samples were prepared for the uniaxial/ triaxial, Brazilian tensile and direct shear tests, respectively. The dimensions of synthetic conglomerates and cement paste samples are summarized in Table B.1.

Table B.1 Dimensions of synthetic conglomerates and cement paste samples (Akram 2010)

Synthetic conglomerates	Diameter/length or thickness (mm)	Cement paste samples	Diameter/length or thickness (mm)
Uniaxial/Triaxial	94/188	Uniaxial/Triaxial	94/188
Brazilian	94/47	Brazilian	94/47
Direct shear	100×100/36	-	-

Numbers of balls used in different conglomerates are shown in Table B.2. The porosity of all synthetic conglomerates is 39.7%. The sample making procedure is shown in Figure B.1, and a thin layer of cement paste with a uniform thickness (3 mm) was left on top of each sample. The microstructure of synthetic conglomerates is shown in Figure B.2.

Table B.2 Numbers of balls used in different synthetic conglomerates (Akram 2010)

Description	Uniaxial/ Triaxial test samples	Brazilian tensile test samples	Direct shear test samples
The number of balls (4.75mm)	14000-14020	3500-3515	3840-3865

Figure B.1 Sample preparation steps (Akram 2010)
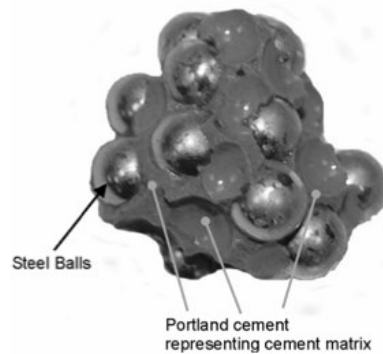
Figure B.2 Microstructure of the synthetic conglomerates (Akram 2010)

B.2 Experiments conducted and the corresponding results

B.2.1 Experiment results of cement paste samples

The experiment results of cement paste samples are shown in Table B.3. The Mohr Coulomb failure criterion with tension cut-off was used to obtain the strength parameters (Figure B.3).

Table B.3 Summary of experiment results on cement paste samples (Akram 2010)

Tests	No. of samples	Average peak strength (MPa)
Uniaxial	11	12.76
Triaxial (2MPa)	2	24.60
Triaxial (5MPa)	3	32.98
Triaxial (10MPa)	2	43.80
Brazilian tensile	3	1.36
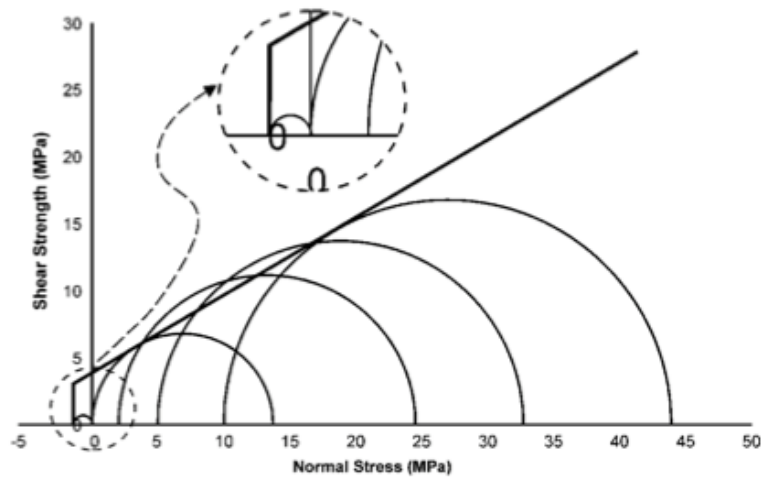
Figure B.3 Plotting of laboratory results to yield Mohr Coulomb strength parameters of cement paste samples (friction angle of 30.4°, cohesion of 3.98 MPa and tensile cut-off at 1.36 MPa) (Akram 2010)

B.2.2 Experiment results of synthetic conglomerates

The experimental results of uniaxial/triaxial and Brazilian tensile tests of synthetic conglomerates are shown in Table B.4. Similarly, the Mohr Coulomb failure criterion was applied to obtain the cohesion and friction angle of synthetic conglomerates (Figure B.4).

Table B.4 Summary of experiment results on synthetic conglomerates (Akram 2010)

Tests	No. of samples	Average peak strength (MPa)
Uniaxial	8	2.98
Triaxial (5MPa)	3	25.48
Triaxial (10MPa)	3	42.70
Brazilian tensile	6	0.16

Besides, six synthetic conglomerates were tested in direct shear at normal stresses of 0.5, 1.0 and 2.0 MPa. Shear displacement, vertical displacement and shear force were monitored throughout the test. Vertical displacement was plotted against the shear displacement to determine the macro dilation angle during shearing. The experiment results of direct shear testing are shown in Table B.5.

176

Table B.5 Summary of direct shear testing results of synthetic conglomerates (Akram 2010)

| Normal load (MPa)	Shear strength (MPa)
0.5	7.88
1.0	12.57
2.0	21.20
Cohesion (MPa)	3.56
Apparent angle of friction (°)	83.90
Mean angle of dilation (°)	46.08
Angle of friction (°)	37.82
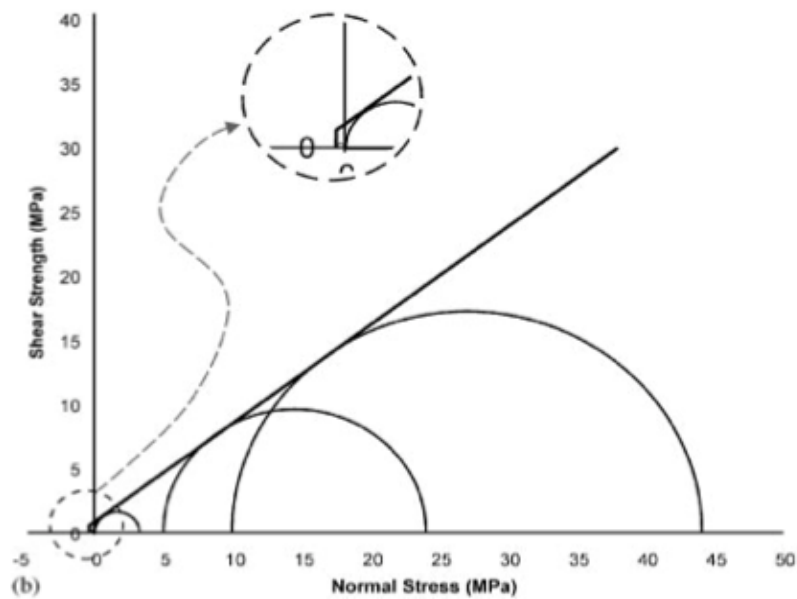
Figure B.4 Plotting of laboratory results to yield Mohr Coulomb strength parameters of conglomerates (friction angle of 37.3∘, cohesion of 0.75 MPa and tensile cutoff at 0.16 MPa) (Akram 2010)

B.3 Calculation of the bonding strength

For the synthetic conglomerate, both the tensile strength of cement and the normal bonding strength between steel balls and cement contribute to the granular sample's tensile strength. Similarly, based on the Mohr Coulomb criterion, the cohesion of the synthetic conglomerate consists of the cohesive strength of cement and shear bonding strength between steel balls and

cement. Since the strength of synthetic conglomerates and Portland cement paste samples is known, the normal and shear bonding strength could be obtained based on the above-mentioned relationships.

B.3.1 Normal bonding strength

The normal bonding strength between steel balls and cement can be calculated using Brazilian tensile testing results and the following relationship:

$$\sigma_t = \frac{\sigma_c \, A_C}{A} + \frac{\sigma_m \, A_B}{A} \qquad\qquad [B.1]$$

where σ_t is the tensile strength of synthetic conglomerate (0.16 MPa), σ_c is the tensile strength of Portland cement paste sample (1.36 MPa), σ_m is the normal bonding strength between steel ball and cement, A_C is the area occupied by the cement-cement contact on the failure surface, A_B is the area occupied by the steel ball-cement contact on the failure surface, and A is the total area of failure surface of the synthetic conglomerate.

Here, the failure surface of the synthetic conglomerate is assumed to be a flat surface with half balls on the top. The calculation procedure of the areas A_C, A_B, and A are shown below.

The cross-sectional area of the sample's failure surface is A_1=94×47=4418 mm^2

The number of balls on the failure surface is around n=200, as shown in Figure B.5.

The area occupied by steel ball-cement contact is A_B=n×2πr^2=200×2×π× (4.75/2)^2=7088 mm^2

The area occupied by cement is A_C=A_1-n×πr^2=4418-200×π× (4.75/2)^2=874 mm^2

The total area of failure surface is A= A_C+ A_B =7962 mm^2

Then, substituting all the known values into the Eq. B.1:

$$0.16 = \frac{1.36 \times 874}{7962} + \frac{\sigma_m \times 7088}{7962}$$

The normal bonding strength is obtained, which is $\sigma_m = 12$ kPa.

Obviously, the obtained normal bonding strength is much smaller than the Brazilian tensile strength of synthetic conglomerates. Also, the normal bonding strength is smaller than the direct

tensile strength gained from the Mohr Coulomb failure criterion (shown in Figure B.4), which is

$\sigma_t' = c/\tan \phi = 0.75/\tan (37.3°)=0.98$ MPa.

Figure B.5 The failure surface of the synthetic conglomerate after Brazilian tensile testing (Akram 2010)

B.3.2 Shear bonding strength

Similar to the calculation of normal bonding strength, the shear bonding strength can be obtained with the following relationship:

$$\tau = c + \sigma \tan \phi = \frac{\tau_c \, A_C}{A} + \frac{\tau_m \, A_B}{A} + \sigma \tan \phi \qquad [B.2]$$

where τ is the shear strength of synthetic conglomerate, c is the cohesion of synthetic conglomerate, τ_c is the cohesion of Portland cement paste sample (3.98MPa), τ_m is the shear bonding strength between steel ball and cement, and A_C, A_B, and A are the same as defined above.

(1) Calculation of the shear bonding strength based on direct shear testing results

The cross-sectional area of the sample's failure surface is $A_1=100×100=10000$ mm^2

The number of balls on the failure surface is around n=500, as shown in Figure B.6.

The area occupied by steel ball-cement contact is $A_B=n×2\pi r^2 =500×2×\pi×(4.75/2)^2=17720$ mm^2

The area occupied by cement is $A_C=A_1-n×\pi r^2=10000-500×\pi×(4.75/2)^2=1140$ mm^2

The total area of failure surface is $A= A_C+A_B =18860$ mm^2

And, the cohesion of synthetic conglomerates from direct shear testing is c=3.56 MPa

Then, substituting all the known values into the Eq. B.2:

179

$$3.56 = \frac{3.98 \times 1140}{18860} + \frac{\tau_m \times 17720}{18860}$$

The shear bonding strength obtained is $\tau_m = 3.53\ MPa$.

Figure B.6 Failure surface of the lower half of the synthetic conglomerate after direct shear testing
(Akram 2010)

(2) Calculation of the shear bonding strength based on triaxial compression test results

As the synthetic conglomerates were crushed in the triaxial compression testing, it is impossible to check the failure surface. However, the friction angle of the synthetic conglomerates is known (ϕ =37.3°), and the angle between the imaginary failure plane and minor compressive stress direction can be estimated, which is θ=45°+ϕ/2=63.7°. The long axis of the imaginary failure plane is equal to b=94 mm/cosθ=212 mm.

Then, the area of the sample's failure surface is A_1=π×a×b=π×(94/2) ×(212/2)=15651mm^2.

The number of balls n on the failure surface is estimated, which is in the range of 690~860. Then, the average value n=780 is adopted.

The area occupied by steel ball-cement contact is A_B=n×2πr^2 =780×2×π×(4.75/2)^2=27644 mm^2

The area occupied by cement is A_C=A_1-n×πr^2=15651-780×π×(4.75/2)^2=1829 mm^2

The total area of the failure surface is A= A_C+A_B =29473 mm^2

The cohesion of synthetic conglomerates from triaxial compression testing is c=0.75 MPa

Then, the Eq. B.2 can be written as:

$$0.75 = \frac{3.98 \times 1829}{29473} + \frac{\tau_m \times 27644}{29473}$$

The shear bonding strength can be obtained, which is $\tau_m = 0.54\ MPa$

Because the measured cohesions from triaxial compression testing and direct shear testing are inconsistent, the obtained shear bonding strength is different. However, the calculated shear bonding strengths are both smaller than the corresponding measured cohesions. This analysis shows that the commonly accepted relationships between the micro bonding strength and macro parameters may not be reliable and further investigation is warranted.

Appendix C

In order to investigate the micro mechanical behavior of cemented granular material, and to test the accuracy of the proposed theoretical relationship with numerical simulation, different numerical samples are generated and tested in direct shear testing with PFC^{2D}. In this appendix, a brief introduction to the PFC^{2D} Particle-Flow model is presented.

C.1 Calculation cycle

The calculation cycle in PFC^{2D} is based on a time-stepping algorithm as illustrated in Figure C.1. At the start of each time step, the set of contacts is updated from the known particle and wall positions. The force-displacement law is then applied to each contact to update the contact forces based on the relative motion between the two entities at the contact and the contact constitutive model. Next, the law of motion is applied to each particle to update its velocity and position based on the resultant force and moment arising from the contact forces and body forces acting on the particle. Also, the wall positions are updated based on the specified wall velocities. The calculations performed in each of the two boxes of Figure C.1 can be done in parallel.
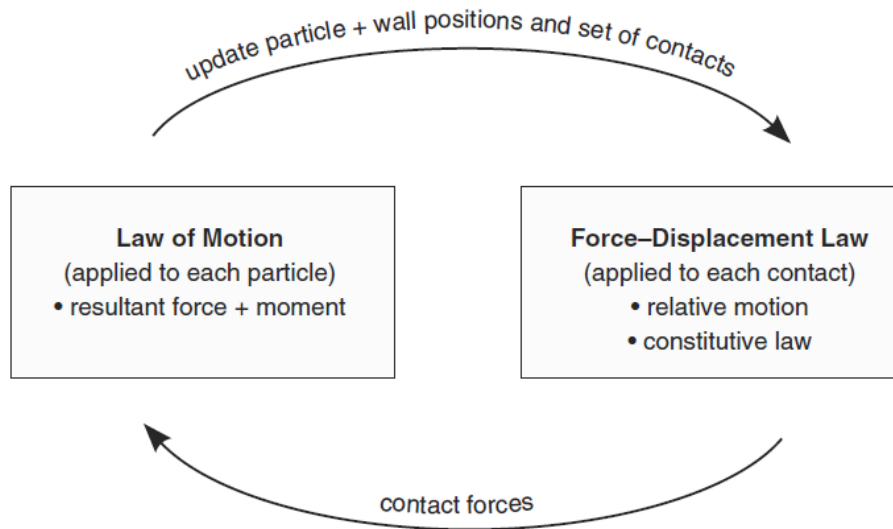

Figure C.1 Calculation cycle in PFC^{2D} (Itasca, 2008)

C.2 Some basic assumptions

In PFC^{2D}, some of the basic assumptions are (Itasca, 2008):

- The particles are treated as rigid bodies with a finite mass. All particles are circular.

- The contacts occur over a vanishingly small area (i.e., at a point).

- Behavior at the contacts uses a soft-contact approach, where the rigid particles are allowed to overlap one another at contact points.

- The magnitude of the overlap is related to the contact force via the force-displacement law, and all overlaps are small in relation to particle sizes.

- Bonds can exist at contacts between particles. Bonds can carry a load and can break. The particles at a bonded contact need not overlap.

The deformation of a packed-particle assembly, or a granular assembly such as sand, is described well by the assumption of particle rigidity, because the deformation results primarily from the sliding and rotation of the particles as rigid bodies and the opening and interlocking at interfaces rather than from individual particle deformation. The addition of bonds between the particles in the assembly corresponds with the addition of real cement between the grains of a sedimentary rock, such as conglomerate or sandstone (Potyondy and Cundall 2004).

In this study, PFC^{2D} is selected since it is shown to be an efficient tool to model granular material. It is able to model the behavior of cemented granular material by bonding every particle to its neighbors. For the numerical conglomerate sample, the steel balls and cementing material used in the artificial conglomerate sample can be represented by the rigid particles and parallel bonds in PFC^{2D}. Furthermore, similar to the artificial conglomerate sample, the deformation of numerical conglomerate sample could exhibit damage-formation processes under increasing load as the bonds are broken progressively.

C.3 Slip model and inter-particle friction

The slip behavior along unbonded particles in PFC^{2D} is defined by the friction coefficient μ at the contact, which corresponds to the inter-particle friction angle ϕ_μ.

As shown in Figure C.2, whenever two particles (particles A and B) overlap, a contact is formed at the center of the overlap region along the line joining the particle centers ($x_i^{(c)}$), and two linear springs are inserted along with a slider in the shear direction. The contact force vector, F_i (which

represents the action of particle A on particle B), can be resolved into normal and shear components with respect to the contact plane as:

$$F_i = F_i^n + F_i^s \qquad [C.1]$$

where F_i^n and F_i^s denote the normal and shear component vectors, respectively.

The magnitude of the normal contact force is calculated by:

$$F^n = K^n U^n \qquad [C.2]$$

where U^n is the overlap and K^n is the normal stiffness at the contact, which is given by:

$$K^n = \frac{k_n^{(A)} k_n^{(B)}}{k_n^{(A)} + k_n^{(B)}} \qquad [C.3]$$

with $k_n^{(A)}$ and $k_n^{(B)}$ being the normal stiffnesses of particle A and B, respectively.
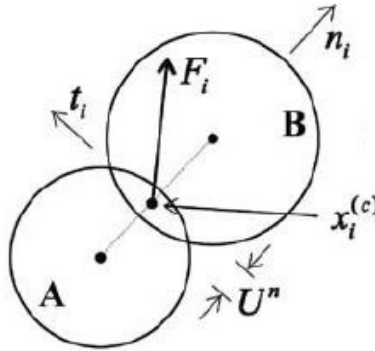
Figure C.2 Notation used to describe particle-particle contact (Potyondy and Cundall 2004)

The shear force component is computed in an incremental fashion. When the contact is formed, the total shear contact force F^s is initialized to zero. Each subsequent relative shear displacement increment results in an increment of elastic shear force that is added to the current value. The increment of elastic shear force is given by:

$$\Delta F^s = -k^s \Delta U^s \qquad [C.4]$$

where ΔU^s is the shear displacement increment and k^s is the shear stiffness at the contact, which is given by:

$$k^s = \frac{k_s^{(A)} k_s^{(B)}}{k_s^{(A)} + k_s^{(B)}}$$

[C. 5]

with $k_s^{(A)}$ and $k_s^{(B)}$ being the shear stiffnesses of particle A and B, respectively.

The relative displacement increment during the time-step Δt is given by $\Delta U_i = V_i \Delta t$, where V_i is the contact velocity given by:

$$V_i = \left(\dot{x}_i^{(c)}\right)_B - \left(\dot{x}_i^{(c)}\right)_A = \left(\dot{x}_i^{(B)} + e_{ijk}\omega_3^{(B)}\left(x_k^{(c)} - x_k^{(B)}\right)\right) - \left(\dot{x}_i^{(A)} + e_{ijk}\omega_3^{(A)}\left(x_k^{(c)} - x_k^{(A)}\right)\right)$$

[C. 6]

$\dot{x}_i$ and ω_3 are the particle translational and rotational velocity, respectively, and e_{ijk} is the permutation symbol. The relative shear displacement increment vector is given by:

$$\Delta U_i^s = V_i^s \Delta t = (V_i - V_i^n)\Delta t = \left(V_i - V_j n_j n_i\right)\Delta t$$

[C. 7]

The slip on contacts occurs when the magnitude of the resolved shear force exceeds the frictional strength. The slip model, acting in parallel with granular behavior, provides no normal strength in tension and allows slip to occur by limiting the shear force. If the overlap U^n is less than or equal to zero (a gap exists), then both normal and shear forces are set to zero; otherwise, slip is accommodated by computing the contact friction coefficient as follows:

$$\mu = \min\left(\mu^{(A)}, \mu^{(B)}\right)$$

[C. 8]

where $\mu^{(A)}$ and $\mu^{(B)}$ are the friction coefficients of particle A and B.

The contact is checked for slip conditions by calculating the maximum allowable shear contact force:

$$F_{max}^s = \mu|F_i^n|$$

[C. 9]

If $|F_i^s| > F_{max}^s$, then slip is allowed to occur during the next calculation cycle by setting:

$$F_i^s = \mu F_i^n \qquad\qquad [C.10]$$

C.4 Particle-Cement behavior and parameters

PFC^{2D} allows particles to be bonded together at the contacts. Two standard bonding behaviors are embodied in contact bonds and parallel bonds. The contact bond can transmit only a force, while the parallel bond can transmit both a force and a moment.

A contact bond can be envisioned as a pair of elastic springs (or a point of glue) with constant normal and shear stiffnesses acting at the contact point. These two springs have specified shear and tensile normal strengths, commonly refer to normal contact bond strength and shear contact bond strength. If the magnitude of the tensile normal contact force equals or exceeds the normal contact bond strength, the bond breaks, and both the normal and shear contact forces are set to zero. If the magnitude of the shear contact force equals or exceeds the shear contact bond strength, the bond breaks, but the contact forces are not altered, provided that the shear force does not exceed the friction limit, and provided that the normal force is compressive (Itasca 2008).

Parallel bond can be envisioned as a set of elastic springs with constant normal and shear stiffnesses, uniformly distributed over a rectangular cross-section lying on the contact plane and centered at the contact point in PFC^{2D}. Parallel bonds reproduce the effect of additional material (e.g., cementation) deposited after the particles are in contact. These bonds establish an elastic interaction between particles that acts in parallel with the slip or contact-bond behaviors. Thus, the existence of a parallel bond does not preclude the possibility of slip. Relative motion at the contact causes a force and a moment to develop within the bond material as a result of the parallel-bond stiffnesses. This force and moment act on the two bonded particles, and can be related to maximum normal and shear stresses acting within the bond material at the bond periphery. If either of these maximum stresses exceeds its corresponding bond strength, the parallel bond breaks (Itasca 2008).

A parallel bond is defined by the following five parameters: normal and shear stiffness, $\bar{k}^n$ and $\bar{k}^s$; normal and shear strength, $\bar{\sigma}_c$ and $\bar{\tau}_c$; and bond-radius multiplier $\bar{\lambda}$. Such that parallel bond radius is:

$$\bar{R} = \bar{\lambda}\min\left(R^{(A)}, R^{(B)}\right) \qquad\qquad [C.11]$$

where $R^{(A)}$ and $R^{(B)}$ are the radius of particle A and B as shown in Figure C.3.

186

The total force and moment associated by the parallel bond are denoted by $\bar{F}_i$ and $\bar{M}_3$, which represent the action of the parallel bond on particle B of Figure C.3. The force vector can be resolved into normal and shear components with respect to the contact plane as:

$$\bar{F}_i = \bar{F}_i^n + \bar{F}_i^s \qquad [C.12]$$

where $\bar{F}_i^n$ and $\bar{F}_i^s$ denote the normal and shear component vectors, respectively.
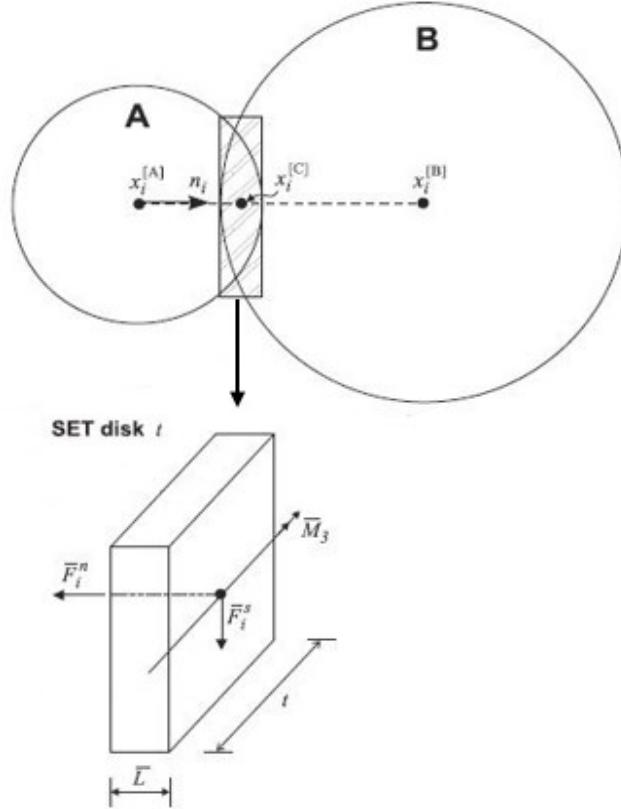

Figure C.3 Parallel bond depicted as a finite-sized piece of cementitious material

When the bond is formed, $\bar{F}_i$ and $\bar{M}_3$ are initialized to zero. Each subsequent relative displacement and rotation increment at the contact results in an increment of elastic force and moment that is added to the current values. The elastic force and moment increments occurring over a time-step of Δt are calculated by:

$$\begin{cases} \Delta \bar{F}_i^n = (-\bar{k}^n A \Delta U^n) n_i \\ \Delta \bar{F}_i^s = -\bar{k}^s A \Delta U_i^s \\ \Delta \bar{M}_3 = -\bar{k}^n I \Delta \theta_3 = -\bar{k}^n I \, (\omega_3^{(B)} - \omega_3^{(A)}) \Delta t \end{cases} \qquad [C.13]$$

187

where A is the bond cross-section area

I is the moment of inertia of parallel bond

θ is the increment of rotation, and

ω is the rotational velocity.

These quantities are given by:

$$\begin{cases} A = 2\bar{R}t \\ I = \frac{2}{3}t\bar{R}^3 \end{cases}$$ [C. 14]

The maximum tensile and shear stresses acting on the parallel bond are calculated by the beam theory to be:

$$\begin{cases} \sigma_{max} = \dfrac{-\bar{F}^n}{A} + \dfrac{|\bar{M}_3|}{I}\bar{R} \\ \tau_{max} = \dfrac{|\bar{F}_i^s|}{A} \end{cases}$$ [C. 15]

If the maximum tensile stress exceeds the tensile strength ($\sigma_{max} \geq \bar{\sigma}_c$) or the maximum shear stress exceeds the shear strength ($\tau_{max} \geq \bar{\tau}_c$), then the parallel bond breaks and its contributions to force and moment are no longer considered.

C.5 Clumped particle model

If significant regions of a model contain many neighboring particles that are moving with essentially the same velocity, a savings in computation time can be achieved by combining the particles in such regions into clumps, each of which will then move as a rigid body. The particles comprising the clump remain at a fixed distance from each other, and contacts internal to the clump are skipped during the calculation cycle. However, contacts with particles external to the clump are not affected. Particles within a clump may overlap to any extent, and contact forces are not generated between these particles. Thus, a clump acts as a rigid body that will not break apart, regardless of the forces acting upon it. In this sense, a clump differs from a group of particles that are bonded to one another (Itasca, 2008).

The basic mass properties of a clump are its total mass, m, location of the center of mass, $x_i^{[G]}$, and moments and products of inertia, I_{ii} and I_{ij}. For a general clump comprised of N_p balls, each of which has mass $m^{[p]}$, radius $R^{[p]}$ and centroid location $x_i^{[p]}$, the mass properties are defined by the following equations:

$$m = \sum_{p=1}^{N_p} m^{[p]} \qquad [C.16]$$

$$x_i^{[G]} = \frac{1}{m} \sum_{p=1}^{N_p} m^{[p]} x_i^{[p]} \qquad [C.17]$$

$$I_{ii} = \sum_{p=1}^{N_p} \left\{ m^{[p]} \left(x_j^{[p]} - x_j^{[G]} \right) \left(x_j^{[p]} - x_j^{[G]} \right) + \frac{2}{5} m^{[p]} R^{[p]} R^{[p]} \right\}; \; (j \neq i) \qquad [C.18]$$

$$I_{ij} = \sum_{p=1}^{N_p} \left\{ m^{[p]} \left(x_i^{[p]} - x_i^{[G]} \right) \left(x_j^{[p]} - x_j^{[G]} \right) \right\}; \; (j \neq i) \qquad [C.19]$$

The moments and products of inertia are defined with respect to a reference frame that is attached to the clump at its center of mass and aligned with the global axis system. In general, this will be a non-principal set of axes (i.e., $I_{ij} \neq 0$).

Besides, the motion of a clump is determined by the resultant force and moment vectors acting upon it. Because the clump is treated as a rigid body, its motion can be described in terms of the translational motion of a point in the clump and the rotational motion of the entire clump. The translational motion of the center of mass is described in terms of its position x_i, velocity $\dot{x}_i$, and acceleration $\ddot{x}_i$. The rotational motion of the clump is described in terms of its angular velocity ω_i, and angular acceleration $\dot{\omega}_i$.

The equation for translational motion can be written in the vector form:

$$F_i = m(\ddot{x}_i - g_i) \qquad [C.20]$$

in which F_i is the resultant force, the sum of all externally applied forces acting on the clump. m is the total mass of the clump, and g_i is the body force acceleration vector arising from gravity loading. The resultant force is computed by

$$F_i = \tilde{F}_i + \sum_{p=1}^{N_p}\left(\tilde{F}_i^{[p]} + \sum_{c=1}^{N_c} F_i^{[p,c]}\right) \qquad [C.21]$$

in which $\tilde{F}_i$ is the externally applied force acting on the clump, $\tilde{F}_i^{[p]}$ is the externally applied force acting on particle (p), and $F_i^{[p,c]}$ is the force acting on particle (p) at contact (c).

The equation for rotational motion can be written in the vector form:

$$M_i = \dot{H}_i \qquad [C.22]$$

in which M_i is the resultant moment about the center of mass, and $\dot{H}_i$ is the time rate-of-change of the angular momentum of the clump. The resultant moment is computed by

$$M_i = \widetilde{M}_i + \sum_{p=1}^{N_p}\left(\widetilde{M}_i^{[p]} + \epsilon_{ijk}\left(x_j^{[p]} - x_j^{[G]}\right)F_k^{[p]} + \sum_{c=1}^{N_c}\epsilon_{ijk}\left(x_j^{[c]} - x_j^{[p]}\right)F_k^{[p,c]}\right) \quad [C.23]$$

in which $\widetilde{M}_i$ is the externally applied moment acting on the clump, $\widetilde{M}_i^{[p]}$ is the externally applied moment acting on particle (p), $F_k^{[p]}$ is the resultant force acting on particle (p) at its centroid, and $F_k^{[p,c]}$ is the force acting on particle (p) at contact (c).

Eq. C.22 is referred to a local coordinate system that is attached to the clump at its center of mass. For such a system, the time rate-of-change of the angular momentum can be written as

$$\dot{H}_i = \alpha_i I_{ii} - \alpha_j I_{ij} + \epsilon_{ijk}w_j(w_k I_{kk} - w_l I_{kl}); (j \neq i, l \neq k) \qquad [C.24]$$

where $\alpha_i = \dot{\omega}_i$.

The equations of motion, given by Eq. C.20 and Eq. C.22, are integrated using a centered finite difference procedure involving a time-step of Δt. The quantities $\dot{x}_i$ and ω_i are computed at the

mid-intervals of $t \pm n\Delta t/2$, while the quantities x_i , $\ddot{x}_i$, $\dot{\omega}_i$, F_i and M_i are computed at the primary intervals of $t \pm n\Delta t$.

As shown in the above paragraphs, one of the big differences between bonded particles and clumped particles is the particle rotation mechanism. As shown in Figure C.4, particles in the bonded material have rotational velocities, while rotational velocities of particles in clumped assembly are fixed. Only the clumped body itself can have rotational velocities. Hence, by taking the clump logic, excessive particle rotation is restricted but moment loading can still be properly simulated (Cho et al. 2007).
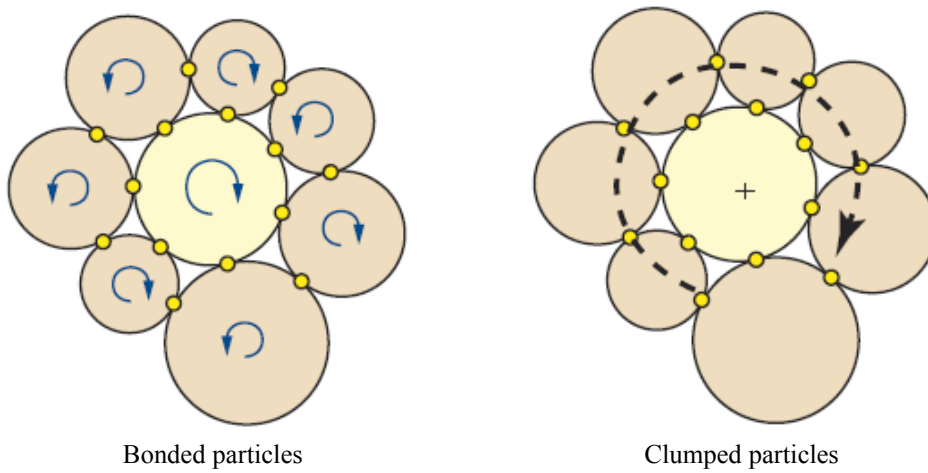

Bonded particles   Clumped particles

Figure C.4 Particle rotation mechanisms in bonded and clumped particles (Cho et al. 2007)